

Long-term Retention of Small, Volatile Molecular Species within Metallic Microcapsules

by

James Paul Hitchcock

BSc (Hons) MSc (Distinction)

**Supervisors: Dr Olivier Cayre and Professor Simon Biggs and Professor David
York**

A report is submitted for the Institute of Particle Science and Engineering

The University of Leeds

For the degree of

DOCTOR OF PHILOSOPHY

30th September 2015

The candidate confirms that the work submitted is his own and that appropriate credit has been given where reference has been made to the work of others.

This copy has been supplied on the understanding that it is copyright material and that no quotation from the thesis may be published without proper acknowledgement.

© 2015 The University of Leeds and James Hitchcock

The right of James Hitchcock to be identified as Author of this work has been asserted by him in accordance with the Copyright, Designs and Patents Act 1988.

Acknowledgements

I would like to start by thanking my supervisors Dr Olivier Cayre and Professor Simon Biggs and Professor Dave York for their guidance and support during my PhD. Their expertise, enthusiasm and depth knowledge of the state of the art helped me understand the science more deeply and build the framework of knowledge needed for my PhD. Without Olivier offering me an interesting MSc project within the Institute of Particle Science and Engineering, I may never have had an opportunity undertake a PhD. Thanks for taking a chance on me Olivier and thanks very much for allowing me to explore many of my own ideas so freely.

I would also like to acknowledge the support of my industrial sponsor Proctor and Gamble and my industrial supervisor Dr Elaine Baxter, her deep knowledge of the subject and infectious drive to push the technology forward helped me remain focused on the task in hand, nine patents can't be bad. I would also like to acknowledge the match funding that came in through the EPSRC, without which the PhD would not have been possible.

There are so many other people whom I have worked alongside during my PhD who have played a role in helping me to become the researcher I am today and made my time at Leeds a great pleasure; Dr Tim Hunter, Dr Soyeb Manga, Dr Alison Tasker, Dr Chris Hodges, Andy Leeson and Dr Grace Yow, to name but a few.

Finally, I would like to give a big thank you to my Mum and Dad (Sue and Chris), my Sister Liz and Brother Tom. They have provided a massive amount of support during my time at Leeds University, it's great to know that they are there to run things by and ask advice when I need it. Without the push, money and help with applications for university back in 1990 from my Mum and Dad I would never have got my degree in Physics and therefore would not have had the opportunity to take my Masters in nanotechnology which led to the PhD. If the technology goes on to have an impact in, for example targeted cancer treatments, my family can all know that they played a very large part.

Abstract

The efficient encapsulation of active ingredients within formulated products and their controlled, targeted delivery to the sites of action, is very important to a range of industries such as pharmaceuticals, agrochemicals, home and personal care and cosmetics to name but a few. By successfully stopping the release of active chemicals and triggering their release where and when they are needed, product efficiency can be improved which reduces the required dose, lowering costs, environmental impact and/or side effects. Such active chemicals include pharmaceutical drugs, pesticides, fragrant and flavour oils, enzymes, vitamins.

Encapsulation and full retention of small molecular weight actives is a particularly challenging task that remains unsolved by current technologies used in industry and academia. In particular, certain everyday product formulations provide difficult environments in which preventing active leakage through capsule walls is not feasible. For example, a continuous phase that can fully dissolve an encapsulated active will typically force full release over a fraction of the intended lifetime of a product. This is due to the inherent porosity of polymeric membranes typically used as capsule wall materials in current technologies. In this work, a method for preventing undesired loss of encapsulated actives under these extreme conditions using a simple three step process is developed. The developed methodology forms an impermeable metal film around polymer microcapsules, prevents loss of small, volatile oils within an ethanol continuous phase for at least 21 days while polymeric capsules lose their entire content in less than 30 min under the same conditions. Polymer shell–oil core microcapsules are produced using a well known cosolvent extraction method to precipitate a polymeric shell around the oil core. Subsequently, metallic catalytic nanoparticles are physically adsorbed onto the microcapsule polymeric shells. Finally, this nanoparticle coating is used to catalyse the growth of a secondary metallic film. Specifically, this work shows that it is possible to coat polymeric microcapsules containing a model oil system or typical fragrance oil with a continuous metal shell. It also shows that the coverage of nanoparticles on the capsule surface can be controlled, which is paramount for obtaining

a continuous impermeable metal film. In addition, control over the metal shell thickness is demonstrated without altering the capability of the metal film to retain the encapsulated oils.

In addition, a method to grow a continuous, non-porous metallic film directly onto nanoparticle stabilised Pickering emulsion droplets is demonstrated, negating the need for an underlying polymeric shell.



Contents

Acknowledgements	3
Abstract	4
Contents	6
List of Figures	12
1 Introduction	23
1.1 The challenge.....	23
1.2 General solution.....	26
1.3 This work.....	27
1.4 Thesis structure.....	29
1.5 Aims and objectives.....	29
1.6 Potential research impact.....	30
2 Microencapsulation and small volatile molecules	32
2.1 Limitations of encapsulation of small volatile molecules.....	32
2.1.1 Limitations of current methods of encapsulation.....	33
2.2 Amorphous / crystalline metals or inorganic crystalline films at colloidal particle interfaces.....	37
2.2.1 Metal and inorganic crystalline nanoparticles at liquid-liquid interfaces; Pickering emulsions, colloidosomes and 2D interfaces.....	38
2.2.1.1 Metal NPs at 2D liquid-liquid interfaces.....	38
2.2.1.2 Metal nanoparticle Pickering emulsions and colloidosomes.....	39
2.2.1.3 Adsorption/incorporation of metal and inorganic crystalline nanoparticles on/in microcapsule and particle interfaces.....	41
2.2.2 Growth of continuous metal 2D films on electrically insulated surfaces.....	43
2.2.3 Continuous metal films on solid colloidal particles.....	46
2.2.4 Continuous metal films on microcapsule and emulsion droplet surfaces.....	48

2.3	Remaining challenges to overcome	50
3	Materials and Methodologies.....	52
3.1	Chemicals.....	52
3.2	Equipment.....	55
3.2.1	Atomic force microscopy (AFM)	55
3.2.2	Quartz Crystal Microbalance QCM D300:.....	57
3.2.3	Spin and dip -coating	58
3.2.4	Dynamic light scattering.....	59
3.2.5	Optical and electron microscopy	59
3.2.6	Focus Ion Beam (FIB)	60
3.2.7	Sample Microtoming	60
3.2.8	Gas Chromotography (GC).....	60
3.2.9	Mastersizer.....	61
3.3	Methodologies/ Synthesis	63
3.3.1	Synthesis of polymeric capsules with oil core.....	63
3.3.2	Preparation of Platinum Nanoparticles (Pt-NPs).....	64
3.3.3	Adsorption of nanoparticles at polymeric microcapsule or emulsion droplet interface	64
3.3.3.1	Adsorption of Pt-NPs at room temperature onto a polymeric microcapsules or emulsion droplet interfaces	64
3.3.3.2	Adsorption of Pt-NPs directly onto emulsion droplet interfaces.....	65
3.3.4	General metallic film growth procedure.....	65
3.3.4.1	Gold film growth on polymeric microcapsules:	65
3.3.4.2	Gold film growth on dip-coated 2D interfaces	66
3.3.4.3	Gold film growth on Pt-NP stabilised emulsion droplets.....	66
3.3.5	Core release testing using gas chromatography (GC)	66
3.3.5.1	Testing for the release of hexyl salicylate using gas chromatography	
	66	

3.3.5.1	Testing for release of hexadecane from metal coated emulsion droplets using gas chromatography	67
3.3.6	Florescent dye gold encapsulation.....	68
3.4	General calculations.....	69
3.4.1	Colloidal surface areas from size distribution data.....	69
3.4.2	Image-J analysis NP adsorption density and size analysis	70
3.4.3	Maximum percentage surface coverage of hexagonally close packed spheres	70
3.4.4	Number of NPs per unit volume	72
3.4.5	Expected inter-nanoparticle spacing on a microcapsule interface assuming 2D hexagonal packing	73
3.4.6	Polymeric microcapsule core shell size ratios	76
4	Model capsule choice.....	78
4.1	Model Capsule Selection and Characterisation	78
4.1.1	Choice of toluene core, PEMA shell microcapsules as a model system	79
4.1.2	Capsule core/shell volume ratios and dispersion surface area.....	80
4.1.2.1	Solutions to the final volume problem.....	82
4.1.2.2	Calculating the dispersion surface area	87
4.2	Conclusion	91
5	Adsorption of catalytic NPs on relevant polymer substrates.....	93
5.1	Synopsis.....	93
5.2	Introduction.....	94
5.3	Nanoparticle characterisation	95
5.3.1	PVP stabiliser concentration vs resulting Pt-NP dispersion size.....	95
5.3.2	Ratios of free PVP to Pt-NPs.....	98
5.4	Adsorption characteristics of Pt-NPs on model spin coated and dip coated polymeric films (2D)	101
5.4.1	Characterisation of spin coated PEMA film used in QCM work	101

5.4.2	Energy and rate of adsorption of Pt-NPs onto polymeric thin films using QCM	102
5.4.3	Excess polymer stabiliser in the NP suspension can influence NP adsorption density onto the polymer film	106
5.4.4	The effect of Pt-NP concentration on resulting adsorption density.....	111
5.4.4.1	QCM Studies.....	112
5.4.4.2	TEM Studies	113
5.4.5	Rate of adsorption using QCM	120
5.4.6	Determination of the Langmuir adsorption equilibrium constant and adsorption energy.....	121
5.5	Analysis of Pt-NP adsorption density on 3D capsule interface	129
5.5.1	NP surface density vs NP concentration using TEM (3D)	129
5.5.1.1	Corrections applied for curvature of the capsules	130
5.5.1.2	NPs adsorption densities on polymer shell microcapsules as a function of bulk concentration.	133
5.5.2	NP Packing Density Analysis	138
5.5.3	Pt-NP adsorptions density, morphology and polymeric stabiliser conformation.	142
5.6	Conclusion	147
6	Secondary metallic film morphology, growth and properties	151
6.1	Synopsis	151
6.2	Metal film morphology on 2D model polymeric substrates	153
6.2.1	AFM analysis of 2D film thickness and roughness as a function of temperature and time	156
6.4	Metal film morphology on microcapsule 3D surfaces.....	162
6.4.1	Further evidence of Gold film growth mechanism.....	162
6.4.2	Measuring metal film thickness from microtome capsules	164
6.4.2.1	Dealing with the four variables associated with microtome samples	165

6.4.2.2	Finding a mean shell thickness using microtome	167
6.4.3	Microcapsule gold film thickness as a function of plating solution concentration (PEMA/Toluene core capsules)	172
6.6	Oil core release and gold film thickness as a function of temperature (Hexyl salicylate core capsules).....	177
6.6.1	Oil core release study (Hexyl salicylate core capsules).....	177
6.6.2	Gold film thickness as a function of temperature (Hexyl salicylate core capsules)	179
6.7	Conclusion	180
7	Metal films grown directly on emulsion droplet surfaces	183
7.1	Synopsis	183
7.2	Pickering emulsions formed using high purity Pt-NP dispersions	184
7.2.1	Reducing the emulsion size distribution to increase droplet stability	185
7.2.2	Pickering emulsion ‘aging’	187
7.2.2.1	Is limited coalescence occurring in our system?	189
7.2.2.2	What is the mechanism for multi-layered stable film growth?.....	190
7.2.3	Proof of a complete non porous metallic shell	192
7.2.3.1	Ethanol stability test using GC	192
7.2.3.2	Oil soluble fluorophore encapsulation in an ethanol continuous phase	193
7.4	Further improvement using ultrasonic homogenisation?.....	195
7.6	Conclusions.....	200
8	Appendix 1 - Future work.....	202
8.1	Potential Papers.....	202
8.2	Pharmaceuticals	203
8.3	Advanced materials photonics/plasmonics and metal micro foam composites.....	204
8.4	Metal bubbles for low density materials with unusual thermal	205
8.5	Minimising the use of secondary metal	206
8.5.1	Smooth thin films	206

8.5.2	Amorphous/crystalline nonporous glasses as shells	206
8.6	Alternative metals shell synthesis	207
8.6.1	Alternative combinations / methods	207
8.6.2	Nickel-Boron hard low friction microcapsules/particles	209
8.8	Variable flow buoyancy pinning using a controlled flow environment	210
8.9	pH encapsulation using a W/O/W Metal microcapsule	Error! Bookmark not defined.
8.10	Self-healing materials	211
9	Appendix 2 - Paper	212
10	References	221

List of Figures

Figure 1 Diagram showing some of the many industrial applications of micro encapsulation.	23
Figure 2. Schematic diagrams (a-d) and corresponding optical and electron microscopy images (a ₁ -d ₁) of the different phases from emulsion droplet to metal coated capsule (a) emulsion droplet, (b) capsule, (c) capsule with adsorbed NPs, (d) metal (Au) coated capsule, (a _i) emulsion droplet (optical microscopy), (b _i) capsule (TEM), (c _i) capsule with adsorbed NPs (TEM), (d _i) Metal coated capsule (SEM). The micrographs presented correspond to different samples and are chosen to illustrate the evolution of the systems over the different steps.	28
Figure 3 TEM micrograph of a gold nano-crystalline film [45].	38
Figure 4 Crown ether ligands.	39
Figure 5 (a) chloroform phase covered with an aqueous gold dispersion (red), (b) after the addition of chloroform solution of crown ether ligand a gold nanocrystalline film forms on the surface of the plastic container and the water/chloroform interface [47].	39
Figure 6 Schematic diagram of the synthesis of nanoparticle surfactants and the resulting stabilised emulsions [49].	40
Figure 7 TEM images of AuNP Pickering emulsions formed by method developed by Tian et al. [50].	40
Figure 8 CIT-Au studded polymeric capsules [55].	42
Figure 9 Modified image of chemical structure of the reactive surfactant, acrylate cross-linker and photoinitiator and (b) schematic diagram of the whole process to fabricate microcapsules containing metal nanoparticles and (e,f) TEM images of an individual capsule [54].	43
Figure 10 Schematic graph showing how the presence of a catalyst lowers the activation energy of a reaction allowing it to occur under ambient background thermal conditions [57].	44
Figure 11 (a) TEM micrograph showing the gold deposited on the Pt colloidal particles. The gold deposits were produced by ELP for 10 s. (b) shows the same position of (a) after the removal of gold deposits by bromine/tetraethylammonium bromide/acetonitrile solution [64].	46

Figure 12 Schematic illustration of the fabrication of PMMA-Ni core-shell composite microspheres by electrostatic polyelectrolyte adsorption and the subsequent electroless plating [70].....	47
Figure 13 SEM images of hollow Ag spheres.	48
Figure 14 scheme for the synthesis of liquid filled metal microcapsules [72].....	49
Figure 15 Schematic representation of the fabrication of metal-coated soybean oil droplets and cryogenic SEM of the resulting capsules [74].	50
Figure 16 Schematic diagram showing the general principles of AFM and an SEM image of the end of a tip	55
Figure 17 Schematic diagram showing the general principles of QCM	57
Figure 18 Schematic diagram of an array of hexagonal close packed spheres.....	74
Figure 19 Schematic diagrams (a-d) and corresponding optical and electron microscopy images (e-h) of the different phases from emulsion droplet to gold coated capsule (a) emulsion droplet, (b) capsule, (c) capsule with adsorbed NPs, (d) Gold coated capsule, (e) emulsion droplet (optical microscopy), (f) capsule (TEM), (g) capsule with adsorbed NPs (TEM), (h) Gold coated capsule (SEM) (inset gold coated capsule under visible light). Red box highlights the part of the process discussed in this chapter.....	78
Figure 20 SEM image of dry Toluene core /PEMA shell capsules.	80
Figure 21 Shows low angle laser light scattering (LALLS) (Mastersizer) size distribution data for Tol/PEMA capsules. The first 3 data points were measured by adding the emulsion directly after homogenization into the Mastersizer [3.2.9]. The rest samples were taken from normal procedure over the first 10 hours of solvent extraction. The inset shows the actual size distribution by volume for the first 4 points.....	81
Figure 22 Graph showing the experimentally measured initial emulsion size distribution and the final capsule size distribution after the solvent extraction phase is complete. The dotted lines represent size distribution data calculated from the measured initial size distribution and show calculated size distributions for 100%DCM loss, 100%DCM and 50% toluene loss, 100%DCM and 85% toluene loss and 100%DCM and 99% toluene loss.....	83
Figure 23 (a) ~100nm thin microtomed samples of metal coated Toluene core / PEMA shell capsules showing core /shell structure and (b) an SEM image of the	

block from which the microtomes were taken showing voids in the cores of sliced capsules and depressed cores relative to the original slice position.....	86
Figure 24 Schematic diagram showing the ratio of the core diameter to the total capsule diameter for a capsule which has lost volume, during the co-solvent extraction phase [3.4.6], which is equivalent to 100% loss of DCM and 85% loss of Toluene [eq. 13].	86
Figure 25 Show the fully formed PEMA/Toluene capsule size distribution as a percentage of sample volume and number.	88
Figure 26 Graph of total capsule surface area as a function of percentage of original synthesis volume.	90
Figure 27 Schematic diagrams (a-d) and corresponding optical and electron microscopy images (e-h) of the different phases from emulsion droplet to gold coated capsule (a) emulsion droplet, (b) capsule, (c) capsule with adsorbed NPs, (d) Gold coated capsule, (e) emulsion droplet (optical microscopy), (f) capsule (TEM), (g) capsule with adsorbed NPs (TEM), (h) Gold coated capsule (SEM) (inset gold coated capsule under visible light). Red box highlights the part of the process discussed in this chapter.	94
Figure 28 Shows a TEM micrograph of the Pt-NPs adsorbed onto a PEMA coated TEM grid [3.2.3].	96
Figure 29 shows a graph of Pt-NP size as a function of PVP concentration. Several Pt-NP dispersions were made up using different concentrations of PVP polymeric stabilizer. Error bars show the standard deviation for each size distribution.	97
Figure 30 Graph of PVP weight % used in Pt-NP synthesis [ref] verses the number of Pt-NPs (black squares) and mean NP diameter (red diamonds).	99
Figure 31 Graph of PVP weight % used in Pt-NP synthesis verses the ratio of number of NPs to number of PVP chains in the dispersion.	100
Figure 32 Showing an AFM micrograph of the 3 example sections across a PEMA/Glass slide boundary. The glass slide was revealed by scoring with a scalpel blade. The graph shows the corresponding height data for multiple sections across the boundary. Lines of best fit were generated by the least squares method from the height data for the glass slide and the PEMA surface for each section. The height difference was measured for each section and these measurements were averaged.	102

Figure 33 QCM adsorption data showing the adsorption of Pt-NPs (Pt-NPs synthesized with 0.0015wt% PVP [3.3.2])	104
Figure 35 QCM Pt-NP adsorption data showing the effect of multiple wash cycles on the adsorbed Pt-NPs film. Pt-NPs are introduced at 9 mins. Labels 1-6 show the effect of 6 consecutive wash cycles. The temporary trough in the frequency data upon each wash is due to the pressure wave caused by the replacement of the bulk phase (Pt-NPs synthesized with 0.0015wt% PVP [3.3.2])	105
Figure 36 QCM data showing how the concentration of stabiliser used in the synthesis of Pt-NPs affects the resulting 2D adsorption density on PEMA films. The red dotted line represents the frequency change for pure PVP.....	107
Figure 37 TEM micrographs of NPs on PEMA coated TEM grids showing the resulting NP surface density using Pt-NPs made with different concentrations of PVP stabiliser (a) $5 \times 10^{-4} \text{M}$, (b) $2 \times 10^{-5} \text{M}$, (c) $1.5 \times 10^{-6} \text{M}$, (d) $3.8 \times 10^{-7} \text{M}$ (equivalent to 2-0.0015wt% respectively). All samples were dip coated for 60 minutes.	108
Figure 38 TEM data showing how the concentration of stabiliser used when synthesising the Pt-NP dispersions relates to the resulting 2D adsorption density on PEMA dip coated films [3.2.3].	109
Figure 39 QCM adsorption data for different concentrations of Pt-NPs onto spin coated PEMA [3.2.3]. The key represents percentage dilution of the original dispersion. The nanoparticles used were synthesised using $3.8 \times 10^{-7} \text{M}$ PVP (0.0015wt%) [3.3.2].	112
Figure 40 QCM adsorption data for different concentrations of the Pt-NPs suspension onto spin coated PEMA. The nanoparticles used were synthesised using $3.8 \times 10^{-7} \text{M}$ PVP (0.0015wt%) [3.3.2].	113
Figure 41 – TEM micrographs of Pt-NP adsorption densities after 60 minutes for different concentrations of the original Pt-NP dispersion at a concentration of $4.6 \times 10^{15} \text{L}^{-1}$ (a-d) 1%, 10%, 50%, 100% of the original concentration respectively (PVP concentration used in synthesis $3.8 \times 10^{-7} \text{M}$ PVP (0.0015wt%) [3.3.2].	114
Figure 42 Pt-NP surface density vs Pt-NP suspension concentration for samples shown in shown in Figure 41 (Dip coated TEM grids). The inset shows the	

equivalent QCM data (same data as shown in Figure 39 but Y-axis shows the additive inverse frequency change).	115
Figure 43 Graph showing spherical hard particle diameter and Polymeric diameter of gyration as a function of diffusion coefficient. Equations eq. 21 and eq. 23 were used to calculate diffusion coefficient for hard spheres and polymeric chains respectively. PVP molecular masses were converted to radius of gyration using equation eq. 30.....	118
Figure 44 QCM data showing the adsorption rates for different concentrations of the original Pt-NP dispersion at a concentration of $4.6 \times 10^{15} \text{ mL}^{-1}$ (PVP concentration used in Pt-NP synthesis $3.8 \times 10^{-7} \text{ M}$ PVP (0.0015wt%) [3.3.2]).	120
Figure 45 Graph showing rate of adsorption vs concentration of Pt-NP suspension concentration. Adsorption rates were calculated by taking the maximum gradient of the isotherms in Figure 44.....	121
Figure 46 Shows the shape of curve expected for a typical Langmuir isotherm	123
Figure 47 QCM data showing the adsorption isotherms for different concentrations of Pt-NPs (100% concentration equates to 4.6×10^{15} Pt-NPs mL^{-1} . The nanoparticles used were synthesised using $3.8 \times 10^{-7} \text{ M}$ PVP (0.0015wt%) [3.3.2]).	124
Figure 48 QCM adsorption data for low (red squares) and high (blue triangles) concentrations of Pt-NP suspensions. The black diamonds show a typical pressure wave for pure water. The dotted lines show what the adsorption isotherms when corrected for the influence of the ‘pressure wave’	125
Figure 49 shows a plot of the rate constant as a function of dispersion concentration. The line of best fit is calculated by the ‘least squares’ method.....	126
Figure 50 TEM micrograph of a NP coated PEMA capsule highlighting the NP variation across the capsule centre.	130
Figure 51 Graph showing how the NP density were corrected for sphere curvature [ref] and sphere transparency. The dotted blue line plots the surface area relative to a flat surface as a function of sphere radius, the circles show an actual example of the apparent NP surface density count as a function of sphere radius and the squares show the same data corrected for sphere curvature. The schematic diagram over which the graph sits is there to aid understanding.	

The arrow and circle represent the capsule and viewing angle respectively.	133
Figure 52 shows representative TEM micrographs of the resulting Pt NPs loaded microcapsules when adding an increasing concentration of Pt NP suspensions to the microcapsules. From (a) to (d) the number of Pt-NP added to the continuous phase was as follows: (a) 1.55×10^{15} , (b) 3.10×10^{15} , (c) 1.26×10^{16} , (d) 1.59×10^{16} . 1%wt of the original capsule synthesis were used [3.3.1]. Insets to (a) and (d) show corresponding gold coated capsules (note that both these images were obtained using different electron beam intensity in order to adjust the required contrast between the polymer and gold areas, the location of the gold on the surface was verified via EDX).....	134
Figure 53 EDX trace showing the presence of gold on the surface of the capsules	134
Figure 54 Graph showing Pt-NP adsorption densities on the polymeric microcapsule surfaces as a function of the number of Pt-NP concentration (black diamonds). The (red squares) show the equivalent adsorption data for 2D model substrates from Figure 42.	135
Figure 55 Schematic diagram representing a sphere and a square of equal surface area	136
Figure 56 Graph showing number of Pt-NPs available per unit surface area of capsules introduced as a function of Pt-NPs introduced to each sample (red squares) and the measured Pt-NP adsorption densities on the polymeric microcapsule surfaces as a function of Pt-NPs dispersion concentration (black diamonds).	137
Figure 57 Graph showing the number of NP's per μm^2 needed to achieve hexagonal close packing (HCP) relative to the coverage we are getting. The measured mean size of the NPs using TEM was used to calculate the packing.....	138
Figure 58 Scaled schematic diagram showing how hexagonal packed sphere separation relates to 2D surface area coverage (a) HCP – 91% surface coverage and (b) 5.6% surface coverage generated from equation eq. 29	139
Figure 59 Shows a TEM image of 5.6% surface coverage on a capsule. Note that the image shows both the top and bottom surface. Most NPs appear to be separated from their neighbors instead of being butted up against them.	140
Figure 60 Show a scale 'model' of 3 Pt-NPs hexagonally packed at a core separation which represents 5.6% Pt core surface coverage. In this example each Pt core	

is stabilised by a single 40KDa PVP chain. The ratio of PVP chain length to Pt core diameter is 108:3.	141
Figure 61 Shows the same NPs adsorbed onto a PEMA coated TEM grid [ref technique] allowing closer inspection. We see a somewhat regular spacing around each adsorbed NP.....	141
Figure 62 DLS [3.2.4] size data for Pt-NPs showing the percentage of the dispersion by number, volume and intensity.	142
Figure 63 molecular structure of PVP monomer	143
Figure 64 shows some simple, approximately to scale, models of possible Pt-NP core / PVP stabiliser confirmations. For these scale models, the ratio of NP core diameter to PVP chain length used is 3:108 (3nm mean diameter, 108nm length polymer chain). The length of an extended PVP chain can be calculated, we know that each monomer consists of 2 C-C bonds which are each ~0.14nm long. Therefore, the length of the extended polymer is 0.3x360 ~108nm.....	144
Figure 65 Schematic diagrams (a-d) and corresponding optical and electron microscopy images (e-h) of the different phases from emulsion droplet to gold coated capsule (a) emulsion droplet, (b) capsule, (c) capsule with adsorbed NPs, (d) Gold coated capsule, (e) emulsion droplet (optical microscopy), (f) capsule (TEM), (g) capsule with adsorbed NPs (TEM), (h) Gold coated capsule (SEM) (inset gold coated capsule under visible light). Red box highlights the part of the process discussed in this chapter.....	152
Figure 66 SEM image of spin-coated PEMA film on a glass substrate with a gold film grown on top. The arrows show (A) a relatively light scrape with a plastic pipette tip removes only the gold film and (B) light scraping with a scalpel removes both the PEMA and the gold film. The PEMA film is ~3nm thick [5.4.1].	154
Figure 67 shows how AFM height profiles were analysed to measure the thickness of the metal films (a) shows the data for a single profile (b) shows two new line made when the profile was split (c) the equation of each new line was found and (d) the mid-point of the divide and the average of the inverse of the two lines gradient was used to generate a third line.	155
Figure 68 Graph showing how mean secondary metal film thickness varies with time and temperature..	156

Figure 69 Graph of mean metal film thickness as a function of temperature at 10, 30 and 60 seconds plating time.	157
Figure 70 Graph showing how mean secondary metal film surface roughness varies with time	158
Figure 71 showing how mean secondary metal film thickness varies with roughness.	158
Figure 72 AFM images showing increasing roughness and ‘grain’ size with time (a-d) height profiles in plan for times 0.5, 10, 60 and 600sec respectively, (e-h) 3D projections of the same samples.	160
Figure 73 shows a schematic diagram of the proposed mechanism for secondary metallic film growth on a NP film.....	161
Figure 74 shows SEM evidence for grain size variation on a broken capsule. The grain size increases from the interior out and initial secondary metal grain size appears to be comparable to the dimensions of the original adsorbed Pt-NP film. Inset shows 2D model Pt-NP adsorption density of the equivalent Pt-NP film used.	163
Figure 75 shows an SEM micrograph of a freeze fractured capsule showing how the gold film edges can fold and twist which prevents accurate measurement of thickness	164
Figure 76 TEM image of a 100nm thick microtome slice through metal coated capsules set in an epoxy resin block [3.2.7].....	165
Figure 77 TEM images of microtomed capsules from the same sample showing a range of apparent secondary metallic film thicknesses. A range such as this can be found within a single sample due to the polydisperse capsule size and random capsule slice position.	166
Figure 78 Schematic diagrams representing shell roughness and shell thickness between capsules, the two variables which have the action of spreading the theoretical thickness frequency distribution for a single ‘microtome’ shell.	166
Figure 79 Schematic diagram showing that the observed film thickness of an ideal metal coated capsule depends on how far from the diameter the capsule is sliced.	167
Figure 80 Theoretical shell thickness frequency distribution for spheres of radii 100 and 40nm both with a 5nm shell.	169
Figure 81 shows experimental frequency distribution data for a polydisperse microtome capsule sample.....	170

Figure 82 SEM images of different slices of a block of capsules set in epoxy resin. The red dots in show capsules in a different volume of the sample that have been cut through the diameter	171
Figure 83 Frequency distribution of gold film thickness of a sample of microcapsules formed in a 0.73M gold salt plating solution. The two distributions compare data from 100nm thick microtomed capsules samples [3.2.7] and thickness measurements taken directly from FIB [3.2.6].....	172
Figure 84 Typical wide field TEM micrograph of ~100nm thick microtome gold coated capsules in epoxy resin [3.2.7].	173
Figure 85 Microtome data showing gold film thickness as a function of gold salt concentration used on the electroless plating solution.	174
Figure 86 shows the calculated gold film thickness at 100% conversion of gold salt, plotted as a function of introduced gold salt concentration (red diamonds) and is overlaid on the actual measured gold film thicknesses for the different gold salt concentrations (black squares). The inset shows the same graph but with the calculated film thickness corrected for a 2/3 loss of capsules during the synthesis wash cycles.	175
Figure 87 Hexyl salicylate release profile from PMMA capsules (◆) and gold coated PMMA capsules (x), placed in 4:1 ethanol:water at 40°C. The level of encapsulated oil released from mechanically fractured gold coated capsules (after residing in ethanol:water mixture for 7 days) is indicated by ▲. Inset – An SEM image of a mechanically fractured gold coated PMMA capsule with hexyl salicylate core. These data were not collected experimentally by myself but are part of the overall effort of our research group to demonstrate this technology on polymer microcapsules, however they have been published in the article placed in appendix [87] [Appendix section 10].....	178
Figure 88 Thickness of metal shell as a function of plating temperature (◆), measured from microtome images using TEM, and release of core as a function of plating temperature (4:1 ethanol:water mixture for 7 days at 40°C) (X). Inset – A TEM image showing a microtomed capsule from which shell thicknesses are measured. These data were not collected experimentally by myself but are part of the overall effort of our research group to demonstrate this technology on polymer microcapsules, however they have been published in the article placed in appendix	179

Figure 89 Optical microscopy of Pt-NP stabilised hexadecane emulsion droplets (pre secondary metal growth stage). Homogenised at 15Krpm for 2 min and then gentle agitated by hand for 30 seconds [3.3.3.2].	185
Figure 90 Optical microscopy of Pt-NP stabilised emulsion droplets. Images show emulsion droplets homogenized at a) 15Krpm 5 min and b) 23Krpm for 5 min.	186
Figure 91 SEM micrograph of (a) a representative gold coated emulsion droplet showing pinholes in the metal film and (b) a zoomed in micrograph of one of the pin holes and (c) a wide field image of the capsules.	186
Figure 92 Optical microscopy showing the difference in capsule size and morphology when left on the carousel for 24 hours in excess NP dispersion – multi-layering and size distribution becomes larger.	188
Figure 93 shows a single Pt-NP stabilized emulsion droplet that has undergone limited coalescence. The stabilizing NP film clearly shows some multi-layering ..	188
Figure 94 Show optical micrographs of multilayer Pt-NP films which have built up over a period of 48 hours at a hexadecane / Pt-NP dispersion interface. The photograph of the vial shows the vial from which the film was taken.	190
Figure 95 Gas chromatography data showing stability in ethanol/water (80/20) for 7 days. Red squares show the percentage loss hexadecane into the ethanol after 7 days. The blue point shows subsequent 94% release on mechanical breakage by crushing [3.3.5.1].	192
Figure 96 (a,b) stabilised emulsion under visible and UV light, (b,c) crystalline coated microcapsules under visible and UV light and (e,f) crushed capsules under visible and UV light.	194
Figure 97 TEM micrographs of collapsed Pt-NP colloidosomes formed by ultrasonic probe homogenization [3.3.3.2].	196
Figure 98 shows an optical micrograph of the ultrasonic probe homogenized colloidosomes [3.3.3.2] coated with gold [3.3.4.3]. The insets show the relative size of emulsions formed via homogenisation with ultraturrax at 15Krpm and 23Krpm.	197
Figure 99 SEM micrograph of a capsule from the sample shown in Figure 98. All the capsules cracked open under vacuum.	198
Figure 100 (a) Schematic diagram showing the proposed gold film growth mechanism, (a1, a2 and a3) are to scale and show a TEM micrograph of the underlying	

Pt-NP film, an SEM image of the interior gold surface and an SEM micrograph of the external surface of the gold film respectively. (b) and (c) show to scale zoomed micrographs of the Pt-NP film and the interior gold film surface. 199

Figure 100 Microscopy images of the film of NP's formed at an air water interface after several weeks. Very robust, appears to be more than one NP thick. Maybe NP's behave differently at an oil-water (liquid-liquid) interface than they do at a water-polymer (liquid-solid) interface NB move this to future work bubble section I have an experiment running to show growth at and oil water interface 205

Figure 101 Schematic diagram for a variable flow buoyancy pinning using a controlled flow environment..... 210

1 Introduction

1.1 The challenge

The efficient encapsulation of active chemicals with an associated controlled (and targeted) delivery is increasingly important to a range of industries [1-6] [Figure 1]. The targeted delivery of actives using microcapsules provides potential benefits for many applications, for example in pharmaceutical or agrochemical formulations by lowering the required dose in the final product. This has obvious cost benefits and importantly, lower doses can reduce or eliminate detrimental side effects. Whilst microencapsulation techniques are increasingly used for specific actives such as fragrances in personal care products, insecticides in agrochemicals, nutraceuticals in foods, and drugs in pharmaceuticals, there remain significant limitations for both the types of actives that can be encapsulated, and the characteristics of the release profile that can be achieved.

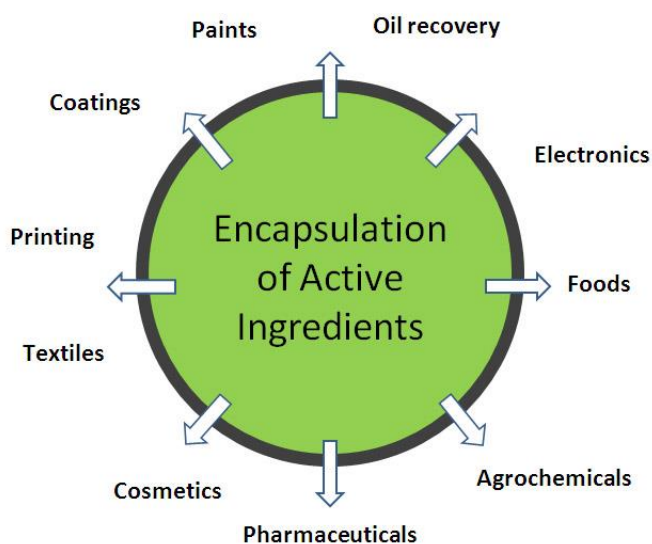


Figure 1 Diagram showing some of the many industrial applications of micro encapsulation.

Numerous methodologies for encapsulating and delivering specific actives (cancer drugs, pesticides etc) have been reported in the academic literature [2, 7-13]. The

proposed methodologies have yielded increasingly functional microcapsules but often the complexity of the synthesis processes involved is a significant barrier to the implementation of these advanced delivery technologies in every day products. A particular area requiring improvement concerns the encapsulation and delivery of small molecules to which most typical microcapsule membranes (i.e. polymeric / particulate / lipid-based membranes) are highly permeable. In particular, small volatile compounds present a significantly difficult challenge when designing methods for controllably delivering such actives within formulated products. This is of specific relevance to the incorporation of fragrances and other small actives in personal care, cosmetics and home care products, for example. It is also important in a wide range of other areas (pharmaceuticals, foods) where the delivery of small actives (e.g. drugs, vitamins) is important. Arguably, the key challenge to using microencapsulation as an efficient delivery route for such small, volatile actives is the ability to retain them within the carrier capsule without (a) leaching and (b) potentially damaging interaction with the environment. In this work, a method was proposed that tackled this challenge by creating a microcapsule which is able to retain an encapsulated active in a continuous phase, in which the capsules are dispersed, that can also dissolve the encapsulated active.

Several methods exist for significantly reducing the release rate of small, volatile actives from microcapsules and those have been applied on the basis of standard laws of diffusion through membranes. Fickian laws of diffusion [equation eq. 1] are typically used to describe the diffusion rate of an active ingredient permeating across a membrane as a function of time [14]. In the case of diffusion of an encapsulated active through a shell into the continuous phase, the following equation can be used as a basis for understanding the microcapsule characteristics that control the release rate.

$$d_c/d_t = A * H * D \frac{C_{int} - C_{ext}}{x} \quad \text{eq. 1}$$

Where:

A Surface area

H Partition coefficient

D	Diffusion coefficient
C	Active concentration
x	Shell thickness

According to equation 1, the diffusion rate, d_c/d_t , can be significantly reduced by minimising the relative solubility of the dispersed phase within the continuous phase [12]. Reducing the concentration difference between the capsule core and the continuous phase can also lead to drastically slower diffusion rates, but this does, of course, obviate the value of encapsulation. Thicker capsule shells will also have a beneficial effect but typically at the cost of reducing the volume of the capsule core, leading to smaller encapsulation efficiencies [12].

Such measures are often considered / applied but typically do not lead to complete retention of active species. In particular, when the active ingredients are highly volatile, the diffusion rates tend to be dictated by the volatility of the species and are typically very high [15]. The successful long-term encapsulation of volatile molecules requires different materials than currently used (organic shells) to create impermeable barriers that can arrest the diffusion of actives from the capsule core. For example, polymeric materials produce diffusion coefficients in the order of $10^{-8} \text{ cm}^2 \cdot \text{s}^{-1}$ for highly volatile small molecules [16]. These relatively high diffusion coefficients render most currently implemented encapsulation methods inappropriate to achieve full retention of such actives, particularly in an environment that is capable of dissolving them. For example, microcapsules for which the release of a specific active is tested (e.g. a dye with suitable solubility characteristics) typically demonstrate a full release of the encapsulated species within days, more often within hours [12, 17, 18]. On this basis, the author is not aware of any methodology described in the literature that has demonstrated the encapsulation, long-term (i.e. more than a few days), retention and subsequent delivery of small (i.e. $< 250 \text{ g} \cdot \text{mol}^{-1}$), volatile molecules.

1.2 General solution

The peculiar requirements of highly volatile small molecules suggests that membrane materials such as amorphous/crystalline metals or inorganic crystals with very low diffusion coefficients ($10^{-15} \text{ cm}^2 \text{ s}^{-1}$) may be required in this case [19, 20]. Films of these materials are considered impermeable due to their crystalline nature [21]. Whilst some atomic species can over time permeate through a crystalline metal surface, [22] a hydrocarbon chain larger than the atomic spacing and interstitial spacing within the crystal is unable to move through the lattice. Thus, metal films in the order of tens of nanometres in thickness are able to render the movement of small volatile molecules across the membranes negligible over the relevant timescales (i.e. those of product manufacturing, storage and use). Enabling the encapsulation of such small compounds could have very significant impact across many industries where active retention during product storage and triggered release during use (through mechanical action in this case) would be beneficial.

Deposition of metal films from solution via standard electroplating techniques was considered an appropriate method due to the electric isolation of each microcapsule. Therefore an electroless deposition technique was used. Electroless deposition is a term first used by Brenner et al. [23] to describe the reduction of metal ions to metal atoms to form metal films without using an external source of electric current. This form of reduction is especially useful when attempting to form films on surfaces which are electrically isolated and is therefore suited to the creation of metallic films on individual microcapsules/emulsion droplets within a continuous phase.

1.3 This work

This work reports a simple method to encapsulate low molecular weight volatile oils, as a proof of concept for the use of metallic microcapsule shells.

The method described uses an oil-in-water emulsion as the precursor for a polymeric microcapsule. Extraction of a co-solvent from the oil dispersed phase induces precipitation of a polymer initially dissolved in the oil and formation of a polymer shell for the resulting microcapsules [24, 25]. This method typically allows for the production of systems with good control over shell thickness. However, such microcapsules are not suitable for long-term retention of small, volatile actives.

The prepared polymer microcapsules dispersed in water are the basis for the next steps in the procedure, which creates impermeable microcapsule shells through the electroless deposition of a metal film. The second step in the procedure consists of metallic nanoparticle adsorption onto the microcapsule polymeric shells. In a third step this nanoparticle coating is used to catalyse the growth of a secondary metallic film reduced in-situ from the continuous phase [26]. Here the catalytic nanoparticles on the surface of the polymer microcapsules reduce the energy barrier for the metal salt reduction and thereby serve to localise the reduction of the metal salt on the microcapsule surface, which also drastically limits, and potentially negates, precipitation of solid metal in the continuous phase. Figure 2 shows a schematic diagram of the complete production process (a-d) and corresponding optical and electron micrographs of examples of microcapsules produced in each stage (a_i-d_i).

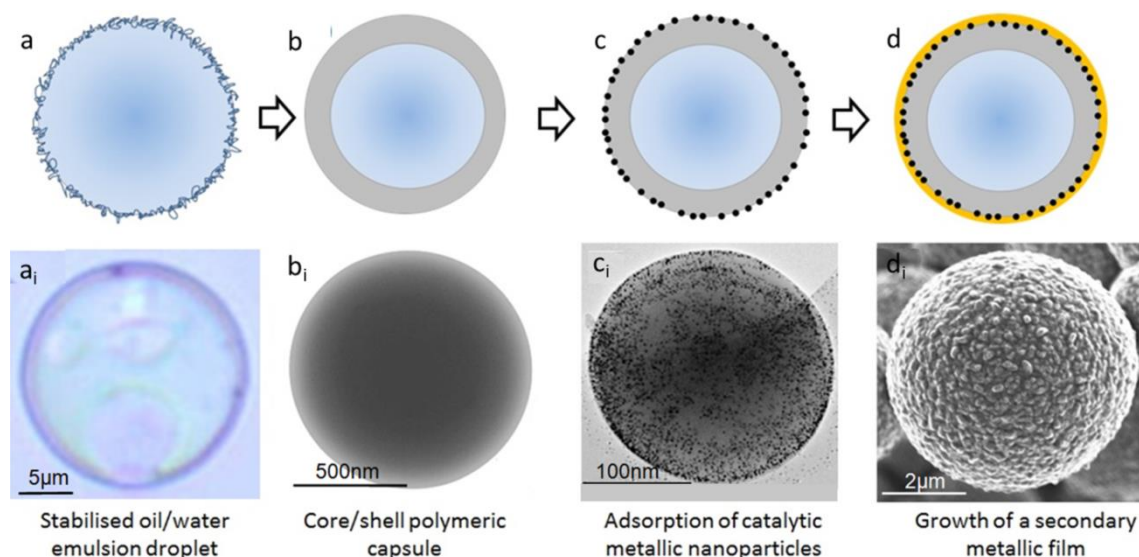


Figure 2. Schematic diagrams (a-d) and corresponding optical and electron microscopy images (a₁-d₁) of the different phases from emulsion droplet to metal coated capsule (a) emulsion droplet, (b) capsule, (c) capsule with adsorbed NPs, (d) metal (Au) coated capsule, (a_i) emulsion droplet (optical microscopy), (b_i) capsule (TEM), (c_i) capsule with adsorbed NPs (TEM), (d_i) Metal coated capsule (SEM). The micrographs presented correspond to different samples and are chosen to illustrate the evolution of the systems over the different steps.

The combination of the two metals for this work was chosen on the basis of existing methodologies for electroless deposition of metal films as described in the literature. Commonly authors have described the use of platinum or gold NPs as the catalyst for the electroless deposition processes which justifies our choice to base the development of this technology on using Pt-NPs as the catalyst followed by the growth of the gold film. We know this is a potential challenge with respect to translating the methodology to commercial products because of the costs associated with using these metals in the manufacturing process. Alternative metal combinations have also been demonstrated but control of the metal film characteristics is currently less advanced. Our research group is separately focusing some effort in developing this methodology for more cost effective metal combinations such as palladium, catalysing the growth of continuous copper or nickel secondary films.

1.4 Thesis structure

Chapters 1-3 provide an introduction, literature review and materials and methodologies sections respectively. The schematic diagram, Figure 2a-d, showing the different stages from the formation of a liquid core gold coated polymeric capsule forms the basis for chapters 4-7 of this thesis. Chapter 4 focuses on characterising and understanding the formation of the oil core / polymeric shell microcapsules with a view to understanding core / shell volume ratios and dispersion surface areas so that expected primary NP surface densities and secondary gold film thickness can be calculated. In chapter 5 an analysis of the NP adsorption kinetics of the catalytic Pt-NPs is made. Chapter 6 goes on to look at the secondary metallic film growth mechanism and general morphology. Chapter 7 introduces and discusses a method for growing metal films directly on emulsion droplets and chapter 8 lists, with some discussion, potential future work.

1.5 Aims and objectives

The aim of this work is to develop a reliable, reproducible route to making nonporous microcapsules which are able to indefinitely retain small volatile molecules. In order to achieve this goal, complete metal films are to be grown around liquid core, polymer shell microcapsule chassis.

On the basis of the methodology explained in section 1.3 above, the specific objectives of the work are based on the different steps involved in this method and are as follows:

Synthesise robust microcapsules which contain highly volatile cores via solvent extraction as a template for metal film deposition. Characterise the resulting capsules and understand the process of formation so that variables such as core/shell ratio, core volume and sample surface area can be calculated and used in the rest of the work.

Synthesise and characterise NPs dispersions which show good catalytic activity for the electroless deposition of metal. Optimise the adsorption characteristics of catalytic NPs onto both the capsule polymer shell and 2D model systems and demonstrate an ability

to control the nanoparticle surface density on the polymer, which plays a critical role in ensuring that the subsequent metal coating is continuous and impermeable. Analyse both the equilibrium adsorption and kinetic adsorption data using standard Langmuir adsorption theories and use these to determine a consistent value of the Langmuir adsorption equilibrium constant for the nanoparticle – polymer interaction.

Use the catalytic NPs to grow, characterise and show control over secondary continuous metal films using electroless deposition. Analyse secondary metal film growth on both the 3D microcapsule surface and 2D model polymeric films. Show control over the metal morphology using variables such as reaction temperature, time, plating solution constitution and NP surface density.

Finally, demonstrate the metal coated polymer microcapsules ability to encapsulate, over long time scales, low molecular weight, volatile molecules within a continuous phase that can dissolve the encapsulated molecules.

1.6 Potential research impact

This technology will initially be applied within personal care products at Procter and Gamble (P&G) however, the ability to encapsulate small volatile molecules may also make it extremely useful in other areas such as, agrochemicals, coatings, paints, self-healing materials and pharmaceutical drug delivery (e.g. targeted cancer treatments). In addition to being able to encapsulate small molecules, the ability to build spherical metallic thin films with control over both the sphere size and shell thickness opens up a number of very interesting potential applications. At present, Industry has some difficulty making good quality homogenous metallic foams for light materials for use in the space industry as metal aerogels. This technology could solve a number of the issues which industry presently encounters. In addition to this, if metal shells were to be grown on polymeric particles with a tight size distribution the possibility of creating meta-materials with highly unusual plasmonic / photonic properties could open up.

Permanent encapsulation and retention of small volatile molecules has not yet been shown in industry or academia. As such, the industrial sponsors of this PhD, P&G,

have filed a total of 9 patents on the technology. Leeds University has a licence free agreement to utilise all potential applications outside the small list of applications P&G have described in the patents. The intention is to form a platform technology within the university to exploit the technology and form links with other departments both at Leeds, other institutions and industries. This has the potential to generate new positions at Leeds and allow the team to realise some of the technologies described previously and others, as yet to be thought of.

2 Microencapsulation and small volatile molecules

Microencapsulation is a technology which enables the protection of active materials which can be liquid, solid or gaseous within a protective shell or matrix. The isolated active can then be released via, for example, a chemical, pH, solvent or shear stress activated trigger or the active can simply diffuse through the shell over time.

A variety of successful encapsulation methods have been used including coacervation, spray drying, inclusion complexation [27], co crystallization, freeze drying, fluidised bed coating, liposome entrapment and microencapsulation formation via emulsification [28]. Each of these techniques can be further divided into many subcategories. Several of these techniques are discussed later in this review and their various merits for encapsulation of small volatile molecules are assessed.

2.1 Limitations of encapsulation of small volatile molecules

By definition, microcapsules are small and therefore surface area volume ratios are very large. Actives in the core have a large surface area of shell through which to penetrate. In addition to this, shell thicknesses are generally in the order of a few microns or less and therefore any small molecule which successfully adsorbs on to the interior shell interface has only a short distance to diffuse through the shell itself.

Significant reductions in diffusion rates from emulsified cores can be achieved by reducing the relative solubility of the dispersed phase into the continuous phase. However, the use of two highly immiscible liquids will have very limited effect on the diffusion rates of highly volatile small molecules. Altering the solubility of the 'core' material relative to the shell or encapsulating matrix affects the diffusion rate and therefore the permeability. However, if the vapour pressure of the active material is

sufficiently high, it can become the dominant driving force for diffusion and overcome the relative solubility barrier [29].

In addition to relative solubility, wetting at the interface between the shell and the dispersed phase also plays a part. Zieringer et al. significantly delayed release of small actives to several weeks by enveloping an aqueous core in a fluoropolymer (PFPE) shell using microfluidics [30]. The multiple inert carbon-fluorine bonds create a low energy surface which is not susceptible to polarisation and therefore solvents such as water will not wet the surface well forming a barrier to molecules dissolved in the core.

Wang et al. used ethyl cellulose microcapsules to significantly prolong the release of encapsulated lavender oil by size exclusion [31]. However, the encapsulation of volatile aqueous or oil soluble molecules requires a sufficiently non porous shell/matrix capable of slowing, or arresting entirely, the rate of diffusion of the active compound. It is therefore generally not sufficient to only alter the relative solubility of the core, shell and continuous phase or use shells with low core wettability when dealing with highly volatile small molecules. Instead it is necessary to form a physical barrier using a material with a low diffusion coefficient such as an atomically amorphous/crystalline metal or other inorganic crystal.

2.1.1 Limitations of current methods of encapsulation

Spray drying involves the hydration of a ‘carrier’ material which is then homogenised with the material to be encapsulated. An atomising spray is then used to create small droplets which are then heated to drive off water and other solvents, leaving dry capsules/particles [28]. Spray cooling, whereby the atomised particles are cooled and the water is driven off using a low pressure environment, can be used to improve the efficiency of encapsulation of relatively small molecules. However, high vapour pressure small molecules tend to be driven off with the water.

Fluidized bed coating requires solid particles of the active material to be ‘fluidized’ in a high temperature environment. The encapsulating material is dissolved in a suitable solvent and then atomized and injected into the fluidized bed. The encapsulate adsorbs and spreads onto the particle surface and the solvent is then driven off by the hot air

[32]. The resulting capsules tend to be relatively large and the technique is not appropriate for the small high vapour pressure molecules because of the high temperature.

Co-crystallization requires the atomisation of a melted crystal such as sucrose syrup. The melt is then reduced in temperature in a low moisture environment. Active materials such as flavourings can be added at the time of ‘spontaneous crystallisation’. The crystal incorporates the flavour by modifying its crystalline structure to incorporate active molecules or entrapping them in porous crystalline aggregates [32]. This encapsulation method is subject to the same limitations as the previously mentioned techniques. Beristain et al. showed that the efficiency of encapsulation of volatile molecules was comparable to those achieved using spray drying [33].

Liposome entrapment was originally used for drug delivery in the pharmaceutical industry but is increasingly finding use in food encapsulation [34]. When dissolved in water, amphiphilic molecules containing lipophilic hydrocarbon chains connected to hydrophilic head groups will spontaneously self-assemble. Lipid bilayer/monolayer sheets, tubes or spheres can form. The structure depends on variables such as the hydrophilic/phobic balance between the head and tail groups, length/size of the tail/head groups and number of hydrocarbon tail groups. It’s possible to entrap dissolved active molecules within these spherical liposomes. Liposomes tend to be biocompatible and their permeability and stability can be varied by changing the lipid type [35]. Sugars and large polar molecules can be successfully encapsulated. However, these films form in an aqueous environment by lowering the Gibbs free energy of the system and are usually thermodynamically unstable. Constituent molecules swap from bilayer to bulk and vice versa, in addition to molecules within the layer being able to move within the 2D surface. There is therefore inherent porosity which limits their use as capsules for high vapour pressure small molecules.

Complexation has been successfully used to encapsulate highly volatile molecules such as methyl iodide [36]. ‘Host’ molecules are designed to form a temporary complex with a ‘guest’ species. This selective molecular recognition and encapsulation usually means that the ratio of guest: host is 1:1 and therefore encapsulating efficiencies are relatively low. Hosts are guest species specific and therefore encapsulation of mixtures of

different small molecules is not possible. In addition, release mechanisms are complex [27].

Encapsulation via emulsification

Emulsification technologies require at least, two immiscible liquids. The two phases, usually oil and water based, are homogenised together. Droplets of one of the phases become dispersed in the other continuous phase. Oil in water (O/W) or water in oil (W/O) emulsions can be formed. More complex multiple emulsions such as oil in water in oil (O/W/O) are also possible [37].

In order to create emulsions that are thermodynamically stable and do not easily coalesce ‘emulsifiers’ such as surfactants, polymeric stabilisers or particles are used. Potential surfactants can be cationic (e.g. Hexadecyltrimethyl Ammonium Bromide (CTAB)), anionic (e.g. Anionic Sodium Dodecyl Sulfate (SDS)) or non-ionic (e.g. Polyoxyethylene 40 Stearate (PE40S)). An example of a polymeric stabiliser might for example be Polyvinylalcohol (PVA).

Most systems are based on using an organic core. Which phase becomes the dispersed phase is dependent on variables such as the phase volume ratio, the form of the stabiliser and the phase the emulsifier is dissolved in.

Encapsulation methods based around emulsification are very flexible; there are a wide variety of different techniques which can be employed:

Colloidosomes are formed when particles are used to stabilise an oil/water boundary and are then linked together in some way to form a particle 2D network. This technique allows for a great deal of control over permeability. Variables such as particle size, degree of chemical crosslinking of the particles or degree of fusing via sintering can be used to control pore sizes [38]. Tailoring the properties of the particles that are used can allow for the creation of responsive capsule shells. Particles which swell or have surface polymers which extend or contract in different pH or temperate environments can be used to form shells with variable porosity [39]. Bollhost et al. attempted to tailor inter-particle nano-pores in sub-micron Pickering emulsions and colloidosomes with a view to release via size exclusion [40]. To the best of my knowledge none of the groups who

have used metallic or inorganic particles to enhance the encapsulation capabilities have succeeded in significantly slowing release. Even if non-porous crystalline metal or inorganic nanoparticles (NPs) are used to form colloidosomes, the inherent porosity due to interstitial particle spacing allows for all small volatiles to diffuse. To date it appears that no group has demonstrated a sufficiently good sintering or blocking of interstitial sites with a secondary non-porous material.

Liquid core / polymer shell microcapsules can be formed by a variety of techniques. Surfactants or polymeric stabilisers are generally used to stabilise the emulsion while the polymeric shell forms, for example, Vincent et al. used water soluble Polyvinyl alcohol (PVP) [25, 41].

- *Polymer precipitation by phase separation* describes two approaches to forming a polymeric shell:
 - Polymerisation induced phase separation is achieved by dissolving a monomer in the organic core and initiating polymerisation of that monomer within the core. The growing polymer becomes immiscible in the oil phase and precipitates to form a shell.
 - Solvent extraction and evaporation involves dissolving a polymer in an organic core composed of a mixture of poor solvent and good volatile solvent. The volatile solvent evaporates forcing the polymer to precipitate and migrate to form a shell. Polymer wetting between phases is important since good wetting allows the polymer to spread and form a full shell [42].
- *Polycondensation interfacial polymerisation* is achieved by dissolving a monomer and an initiator in two incompatible phases. The monomers polymerise and precipitate at the interface to produce a shell. An example of this is nylon or polyurethane.
- *Layer-by-layer polyelectrolyte deposition* involves the alternate electrostatic adsorption of oppositely charged polyelectrolytes to build up a polymeric layer on an emulsion droplet/particle [43, 44].

Small volatile molecules are able to diffuse through polymeric microcapsule shells and therefore, over relatively short time frames, microcapsules synthesised using the techniques described above will leak. (An exception to this is the previously mentioned work by Zieringer et al. which significantly limits the wettability of the internal shell surface by the encapsulate and therefore prevents the core entering the polymeric matrix in the first place effectively arresting diffusion [30]).

2.2 Amorphous / crystalline metals or inorganic crystalline films at colloidal particle interfaces

As discussed previously, the permanent encapsulation of highly volatile small molecules requires the formation of a physical barrier using a material with a low diffusion coefficient such as amorphous/crystalline metals or other inorganic crystals.

There are several examples in the literature of the use of non-porous amorphous/crystalline metals or other inorganic crystalline nanoparticles in the formation of films at colloidal particles interfaces. There are far less examples of the formation of continuous films of amorphous/crystalline metals or other inorganic crystals on colloidal systems and there are even fewer examples of the formation of continuous metal films around colloidal systems liquid cores. The existing art in this area is described in this section.

First the formation of metal and inorganic crystalline nanoparticles at liquid-liquid interfaces is discussed, including the formation of Pickering emulsions and colloidosomes. The adsorption or incorporation of non-porous nanoparticles on/in microcapsule and particle interfaces is then examined.

The growth of continuous metal films on electrically insulated surfaces and the application of continuous metal films to solid colloidal particle interfaces are then considered. Finally the deposition of continuous metal films on liquid core microcapsules and emulsion droplet surfaces is discussed.

2.2.1 Metal and inorganic crystalline nanoparticles at liquid-liquid interfaces; Pickering emulsions, colloidosomes and 2D interfaces

2.2.1.1 Metal NPs at 2D liquid-liquid interfaces

Rao et al. successfully developed a technique for creating a nano-particulate metal film at an aqueous/organic interface [45]. By separating a metal salt which is soluble in the organic phase and a water soluble reducing agent in the aqueous phase, reduction of the metal salt was limited to the aqueous/organic interface only. Metal ions are reduced to atomic nuclei and then nucleate and grow to form a nano-particulate film. The nanoparticle arrays have a good size distribution and can hexagonally close pack (HCP) to create self-assembled monolayers (SAM). The SAM can easily be removed from the interface and observed via TEM [Figure 3].

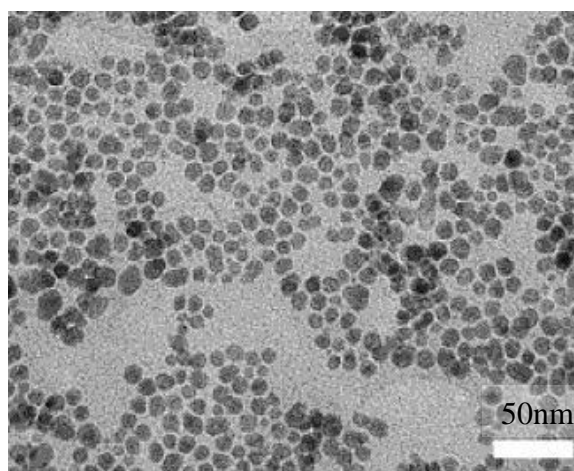


Figure 3 TEM micrograph of a gold nano-crystalline film [45].

Increasing the concentration of gold and reducing agent can result in multilayers of nanoparticles, the loss of HCP and less-uniform size distributions. The choice of metal precursor, reducing agent and organic solvent is crucial to forming stable films. By varying the starting conditions, hydrosol or organosol nanoparticle dispersions can be made to form in either of the two phases [46]. In addition, nanoparticle films can be

readily extracted to aqueous or organic layers as a dispersion by adding suitable capping agents.

Lee et al. succeeded in using various crown ether ligands [Figure 4] to drive dispersed gold nanoparticles to an aqueous/organic interface [47]. The crown ether is dissolved in a chloroform organic phase with a gold nanoparticle dispersion being in the aqueous phase [Figure 5a]. The crown ether ligands are able to mediate the self-assembly of a gold nanoparticle film forms at the organic/aqueous interface [Figure 5b].

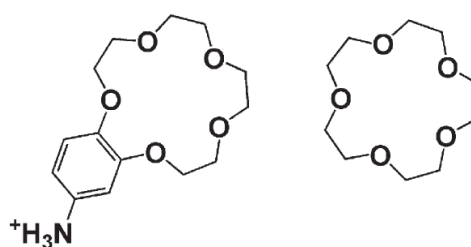


Figure 4 Crown ether ligands.



Figure 5 (a) chloroform phase covered with an aqueous gold dispersion (red), (b) after the addition of chloroform solution of crown ether ligand a gold nanocrystalline film forms on the surface of the plastic container and the water/chloroform interface [47].

2.2.1.2 Metal nanoparticle Pickering emulsions and colloidosomes

Yamanaka et al. formed Pickering emulsions stabilised with mercaptocarboxylated Au nanoparticles. AuNPs are first formed using a phase transfer method using Tetrakis(decyl)ammonium bromide (TDAB) as the phase transfer agent. MPDA is then

used as a stabiliser. The AuNPs obtained are then sufficiently surface active to stabilise a water in oil emulsion [48].

Larson-Smith et al. used thiol-terminated polyethylene glycol (PEG) chain stabilised gold nanoparticles to form hexadecane core Pickering emulsions [49] [Figure 6].

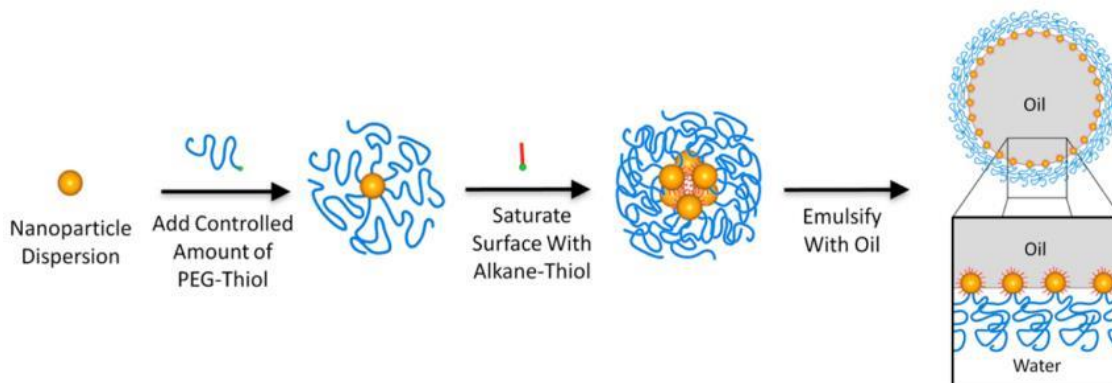


Figure 6 Schematic diagram of the synthesis of nanoparticle surfactants and the resulting stabilised emulsions [49].

Tian et al. formed Pickering emulsions by homogenising an aqueous citrate-stabilised AuNP dispersion with an organic phase of polystyrene with thiol terminal groups (PS-SH) dissolved in toluene. Emulsion droplets are stabilised by the formation of AuNPs with grafted PS-SH on their surface at the liquid-liquid interface [Figure 7] [50].

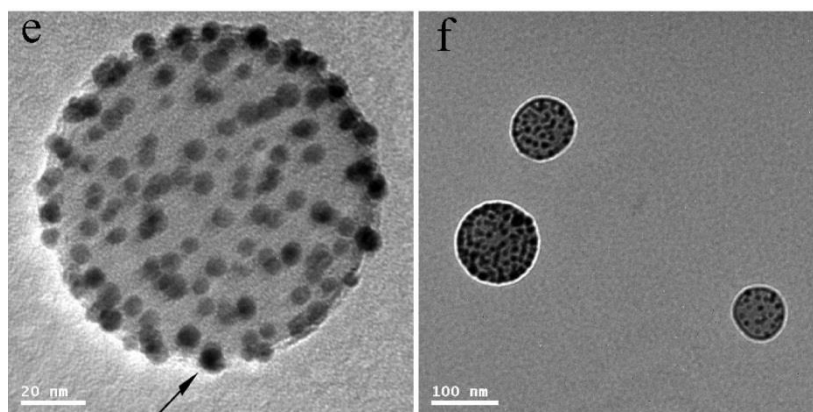


Figure 7 TEM images of AuNP Pickering emulsions formed by method developed by Tian et al. [50].

2.2.1.3 Adsorption/incorporation of metal and inorganic crystalline nanoparticles on/in microcapsule and particle interfaces

Non-porous metal NPs and other inorganic crystalline NPs have also been successfully adsorbed or incorporated onto or into microcapsule shells and particle cores and interfaces. Methodologies typically involve a two-step process. Microcapsules are first formed and then NPs are adsorbed or incorporated onto or into the microcapsule by a form of in situ reduction of pre-adsorbed metal ions or electrostatic adsorption of charged NPs onto a charged microcapsule interface [51-54]. Alternately NPs in the continuous phase can be destabilised by, for example, the introduction of a salt or change of pH forcing them to precipitate out of the dispersion onto the colloidal interfaces [55]. In addition, NPs can be incorporated into the 'core' phase of the forming colloidal system - for example as a stable dispersion in the emulsified phase thereby trapping the NPs in the forming colloidal particle.

Kozlovskaya et al. [51] used a layer-by-layer technique to create polyelectrolyte microcapsules onto which Au ions can be adsorbed and subsequently reduced in situ to form AuNPs and Geest et al. alternately adsorbed a positive polyelectrolyte (poly(allylamine hydrochloride) (PAH)) and negatively charged AuNPs onto emulsion drop interfaces in order to build up a polymer/NP multi-layered microcapsules [52]. Antipov et al. used a layer by layer technique to build up alternate Poly(sodium 4-styrenesulfonate) (PSS) and poly(allylamine hydrochloride) (PAH) films on melamine formaldehyde (MF) latexes. The deposited film is easily oxidised and acts as a reducing agent for the Ag^+ ions in the continuous phase. The result is a nanoparticulate Ag film on the capsule surface [53].

Cayre et al. successfully destabilised a nanoparticle dispersion using pH in order to adsorb NPs at a microcapsule interface [55]. Poly(methylmethacrylate) (PMMA) microcapsules were formed by a cosolvent extraction method in the presence of citrate stabilised gold nanoparticles (CIT-Au). A short time into the homogenisation step an acid was added to the continuous phase containing the NPs. The addition of the acid acted to decrease the charge density on the surface of the CIT-Au by protonating the

adsorbed citrate ions. The nanoparticles therefore became less hydrophilic and precipitated out on the newly formed polymeric capsule surface resulting in a CIT-Au studded polymeric capsule [Figure 8]. The acid was added after the homogenisation step to promote the formation of a large surface area for NP adsorption over inter NP aggregation.

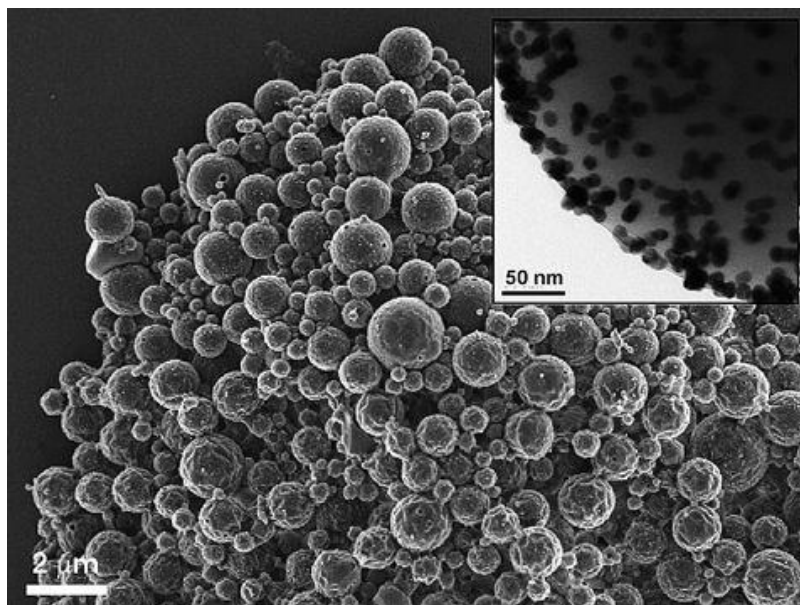


Figure 8 CIT-Au studded polymeric capsules [55]

Liu et al., demonstrated a clever one pot synthesis of NP encrusted thin filmed polymeric microcapsules. An oil phase containing amphiphilic polyhedral oligomeric silsesquioxane (which itself contained thiol groups (PTPS)), a trimethylolpropane triacrylate (TMPTA) and a photoinitiator were homogenised with an aqueous phase containing a gold salt to produce an oil in water emulsion [54]. The amphiphilic PTPS acted as a stabiliser (hydrophobic alkyl chains and hydrophilic PEG chains). Exposure of the emulsion to UV light photo initiated the polymerisation of the thiol groups on the TMPTA forming a crosslinked polymer wall. At the same time radicals generated by photoinitiation reduced Au ions which diffused to the interface causing them to nucleate and grow into AuNPs [Figure 9].

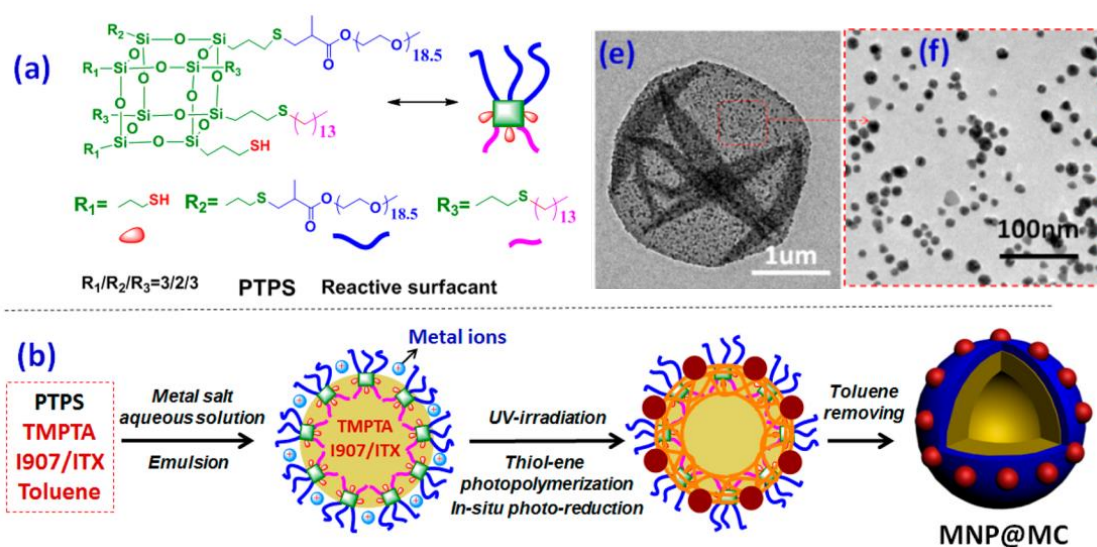


Figure 9 Modified image of chemical structure of the reactive surfactant, acrylate cross-linker and photoinitiator and (b) schematic diagram of the whole process to fabricate microcapsules containing metal nanoparticles and (e,f) TEM images of an individual capsule [54].

The use of metal or inorganic crystalline nanoparticles in the formation of Pickering emulsions or colloidosomes or the adsorption of the same particles as a film on to preformed microcapsule template has, to date, not endowed the resulting microcapsules with the ability to permanently encapsulate small volatile molecules. Even if the NPs are efficiently hexagonally close-packed within the films they provide and inherent porosity due to the spaces between NPs. Therefore unless a secondary non-porous material is added to/grown in the interstitial sites between the particles, small volatile molecules are still able to diffuse.

2.2.2 Growth of continuous metal 2D films on electrically insulated surfaces

There are many examples of successful deposition of homogeneous crystalline metallic films onto both metallic and non-metallic 2D surfaces [56]. The electronics industry, for example, uses many techniques such as sputter coating and electro-deposition for depositing metals on solid surfaces; however these techniques are not suitable for deposition on microcapsules due to the liquid continuous phase and the electric isolation.

The reduction of metal ions to metal atoms resulting in the formation of a metal film via electroless deposition on the other hand does not require an external source of electric current [56]. This form of reduction is especially useful when attempting to form continuous films on surfaces which are electrically isolated.

In order to direct the reduction of the metal to be plated onto a non-conducting surface, such as a polymeric shell or emulsion droplet surface, a heterogeneous catalyst needs to be present. Catalysts are usually noble metals such as Platinum, Palladium or Gold. The energy barrier to the reduction without the catalyst needs to be sufficiently high as to significantly limit the reduction of the metal ions in the bulk. Therefore highly active reducing agents are inappropriate.

Noble metals have long been known to display excellent catalytic properties, in the main, due to their good surface adsorption energy which promotes physisorption of reactants and their inert nature which restricts the more permanent chemisorption of species which might restrict catalytic activity.

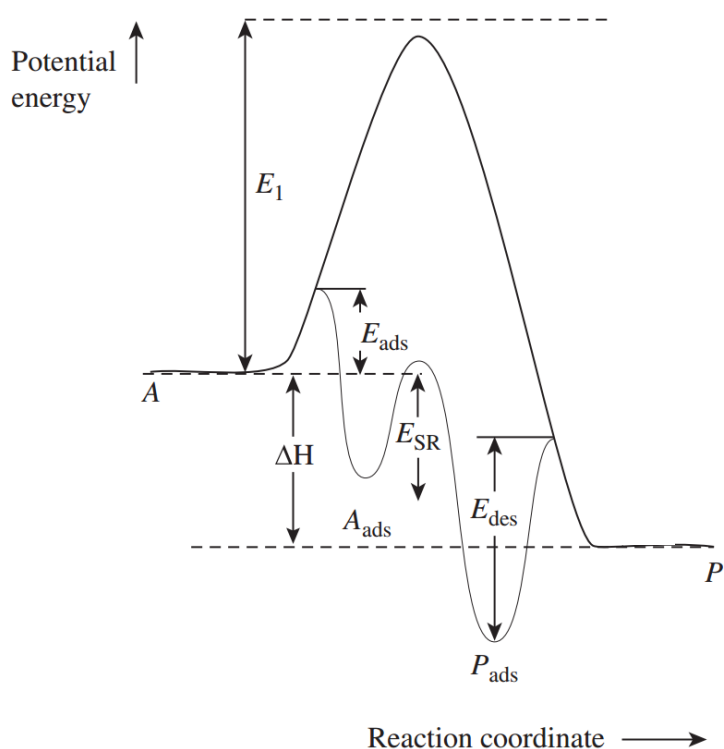


Figure 10 Schematic graph showing how the presence of a catalyst lowers the activation energy of a reaction allowing it to occur under ambient background thermal conditions [57].

Figure 10 shows a schematic diagram of the general energy states of a reaction with and without a catalyst. The reactant (A) reacts to make the product (P) with an activation energy (E_1) and enthalpy of reaction (ΔH). The reactant is able to adsorb onto the catalyst surface to form a new state (A_{ads}) which itself has an activation energy barrier (E_{ads}). The adsorption of the reactant often leads to dissociation or weakening of the bonds within reactant molecules allowing the reaction to occur more quickly [58]. The adsorbed reactant is then able to transform, via a surface reaction process into a product (P), this step also has an activation energy (E_{sr}). Finally the product is able to desorb with a third activation energy (E_{des}) [57]. In some cases more than one of the reactants adsorb onto the surface of the catalyst, diffuse across the surface towards each other and react to form the product which then needs relatively little energy to desorb from the surface.

Whichever route the catalysed reaction uses, the general principle involves the breakdown of the original uncatalysed reaction process into several transitions each with lower energy barriers and therefore the reaction can occur more quickly under ambient background thermal conditions.

Electroless deposition is a term which appears to be used interchangeably in the literature to describe 3 different metallic film formation mechanisms substrate catalysed, autocatalytic and galvanic replacement [59].

Both substrate catalysed and autocatalytic deposition require the plating solution to contain both a metal salt and a reducing agent. During autocatalytic deposition the metal being deposited is in itself a catalyst for the reduction of the metal salt and therefore relatively thick layers can be produced. Film thicknesses are limited in substrate catalysed reduction processes because once the surface gets covered by the secondary metal the catalytic activity drops off significantly. During Galvanic displacement the substrate atoms provide electrons to the metal salt and in doing so detach from the metal lattice and become ions themselves [59].

Metallic nanoparticles are widely studied for their use as catalysts [60-63]. Horiuchi et al. showed that platinum nanoparticles act as a good catalyst for the electroless deposition (ELP) of homogeneous crystalline gold films [64].

Polyvinylpyrrolidone (PVP) is used to stabilise platinum nanoparticles (Pt-NPs) in water. It is Horiuchi's belief that the Pt-NPs have a negative surface charge and can therefore be directed to a positively charged surface. A polystyrene surface was dipped into a stearyl trimethyl ammonium chloride (STAC) aqueous solution to create a positively charged surface. The surface was then dipped into the Pt-NPs, washed and subsequently dipped into a gold plating solution containing a metal salt and reducing agent.

TEM microscopy confirmed that gold growth preferentially occurred around the Pt-NP [Figure 11]. It is not understood why the gold appears to grow more on some NPs than others.

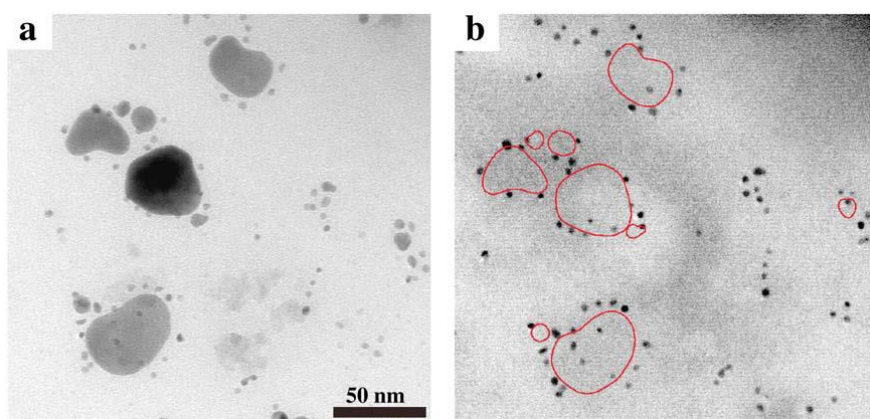


Figure 11 (a) TEM micrograph showing the gold deposited on the Pt colloidal particles. The gold deposits were produced by ELP for 10 s. (b) shows the same position of (a) after the removal of gold deposits by bromine/tetraethylammonium bromide/acetonitrile solution [64].

The process demonstrated by Horiuchi et al. has both catalytic and autocatalytic elements. Platinum is used as a catalyst for the primary gold film growth which envelopes the NPs - after this the gold continues to grow via autocatalytic ELP.

2.2.3 Continuous metal films on solid colloidal particles

Most examples, in the existing literature, of continuous metal films being grown on colloidal systems are grown on solid colloidal particles [65-69]. Lin et al. grew Ni shells on polyelectrolyte-modified PMMA beads using direct Ni^+ ion adsorption and reduction

[70]. PMMA beads were first surface modified with ammonia solution to provide a negative surface charge. Cationic and anionic polyelectrolytes were then sequentially adsorbed to create a negatively charged polyelectrolyte surface onto which Ni^+ ions were added. The particles were then placed in a nickel plating solution which reduced the Ni^+ ions. A Ni film grew via an autocatalytic process on the polymeric bead surface [Figure 12].

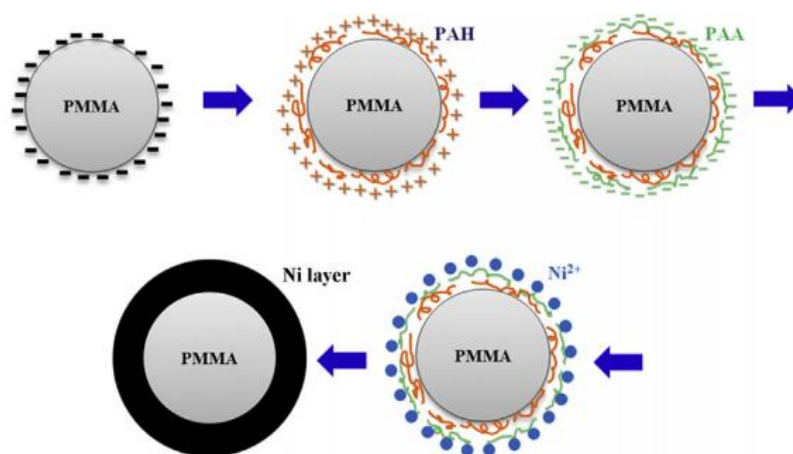


Figure 12 Schematic illustration of the fabrication of PMMA-Ni core-shell composite microspheres by electrostatic polyelectrolyte adsorption and the subsequent electroless plating [70].

Karagoz et al. reported a process for generating variable thickness of metal deposits on polymer microspheres via electroless plating [66]. The technique was used to successfully coat polymeric beads with Ni, Cu and Ag. Metal complexes were formed on triethylenetetramine (TETA) functionalised crosslinked poly(glycidyl methacrylate) (PGMA) microspheres by immersing them in aqueous solutions of the respective metal salts. The metals chelated, with TETA surface groups, were reduced to atomic metal on the addition of hydrazinium formate or hydrazine. The resulting metal 'seeded' surface then acted as nucleation points for further growth of the metal in standard plating solutions of the respective metals.

Wang et al. produced size-controllable monodisperse hollow silver microspheres [71]. Beeswax was melted and homogenized with an aqueous solution of CTAB and silver salt. CTAB stabilised emulsion droplets of melted beeswax were produced. As the wax cooled, hydroquinone was used as a reducing agent to form solid wax spheres studded with atomic silver. Silver nitrate was then reduced in the presence of the wax cores and the existing surface silver caused an autocatalytic reaction whereby the silver grew

preferentially on the surface. Finally the capsules were heated in an alcoholic solution to remove the wax core leaving a silver shell [Figure 13].

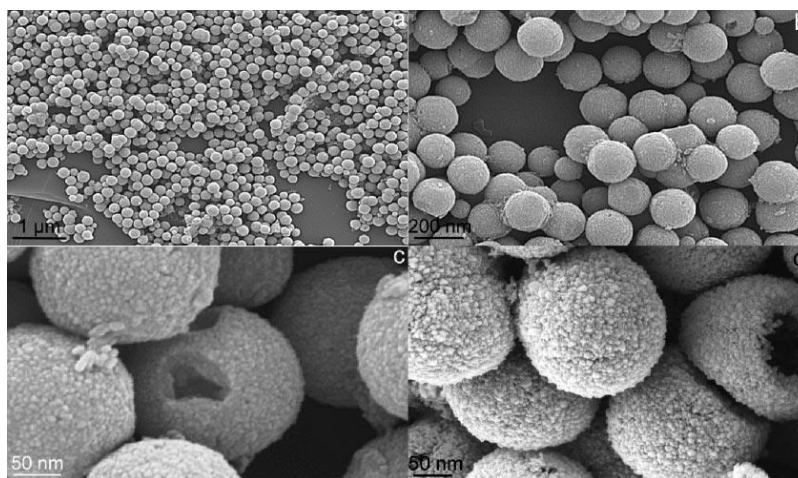


Figure 13 SEM images of hollow Ag spheres.

The fact that the waxy molecules were removed from the core indicates the porosity of the shell to relatively large polymeric molecules. Therefore, this renders this technology incapable of encapsulating high vapour pressure small molecules.

2.2.4 Continuous metal films on microcapsule and emulsion droplet surfaces

Very few papers report metal encapsulation of liquid core microcapsules or emulsion droplets and none demonstrate the use of metal films to permanently encapsulate small volatile actives. Two recent papers report the successful deposition of continuous metal films on liquid core microcapsules [72, 73].

In the first example, Patchan et al. sequentially adsorbed polyelectrolyte, tin and palladium ions onto polymeric microcapsules before the target surface was suitable for metal deposition [72].

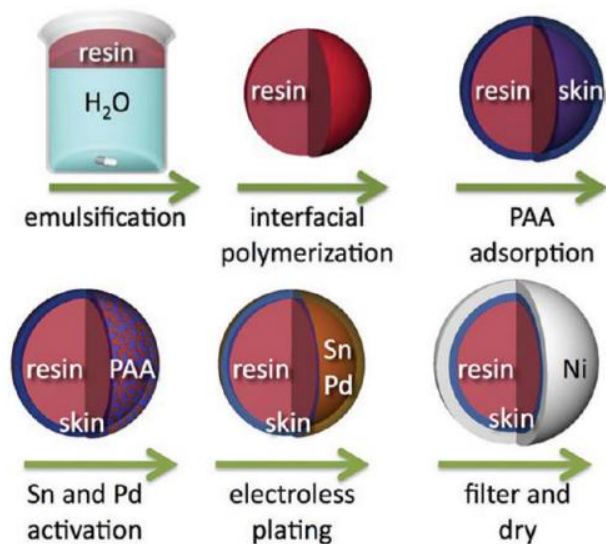


Figure 14 scheme for the synthesis of liquid filled metal microcapsules [72].

Interfacial polymerisation was used to produce liquid core polymer shell microcapsules. The capsules were then placed in a solution of poly(acrylic acid) (PAA) which adsorbed onto excess amine groups left over from the interfacial polymerisation. The microcapsules were then placed into a SnCl_2 solution, washed and immersed in an acidic PdCl_2 solution. The Sn^{2+} deposited on the negatively charged PAA surface then reduced Pd^{2+} ions from solution to create Sn^{4+} and Pd^0 . The atomic Pd then acted as a catalyst for the electroless deposition of Ni from a standard Ni plating solution [Figure 14].

In the second example, Nocera et al. described a method that involves the doping of a polydopamine membrane (surrounding an oil core) with metal ions followed by the reduction of the ions and growth of a silver film [74] [Figure 15].

A soybean core phase was homogenised in an aqueous phase containing Tris(hydroxymethyl)aminomethane (Tris), dopamine hydrochloride, potassium permanganate and a surfactant to stabilise the forming droplets (Tween 20). After two hours a polydopamine film formed on the surface of the soybean droplet. The resulting microcapsules exhibited a highly negative surface charge (-60mV).

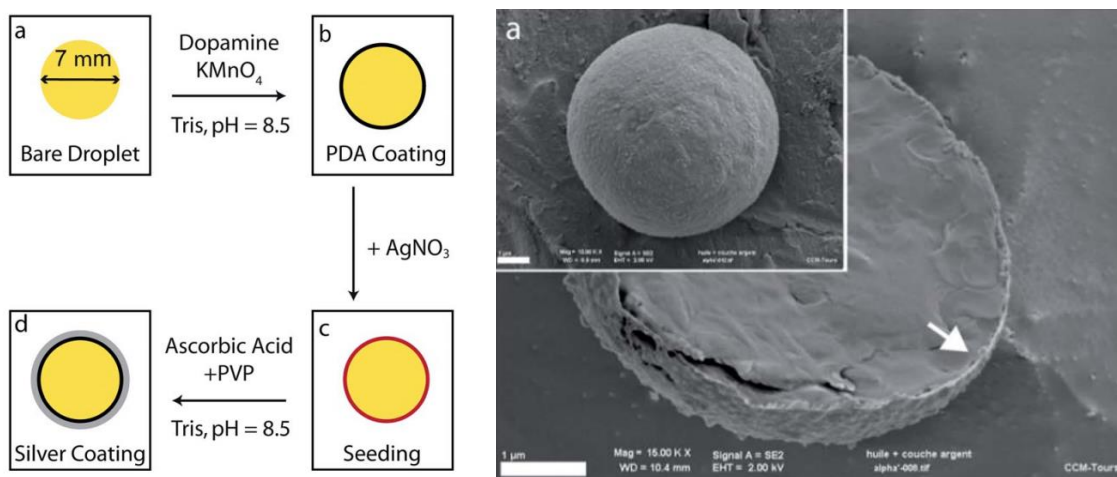


Figure 15 Schematic representation of the fabrication of metal-coated soybean oil droplets and cryogenic SEM of the resulting capsules [74].

The capsules were then re-dispersed in a solution of silver nitrate. The positive silver ions adsorbed electrostatically to the negatively charged polydopamine layer. Some of the silver ions were reduced by the redox behaviour of the polydopamine film. In order to grow a ‘complete’ film of silver on the nanoparticulate ‘seed’ layer ascorbic acid was added to the continuous phase.

The primary aim of these experiments was to create core-shell structures with specific optical properties; the authors did not investigate the permeability of the metal films.

2.3 Remaining challenges to overcome

These examples can enable some of the challenges associated with encapsulating small molecules to be overcome. For example the fluorinated polymer wall demonstrated by Zieringer et al [30] may be used in some instances where the continuous phase is aqueous.

In a particular challenge, our industrial collaborators are requiring to encapsulate a small volatile fragrance oil in a continuous phase containing 70% ethanol. Required timescales corresponding to this products stability can reach 2-3 years taking into account manufacturing, transport, storage and final use of the product. This is the case for new perfumes which P&G are developing.

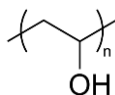
The examples given above are unlikely to solve this particular challenge. There is a need for shell materials with lower diffusion coefficients that retain the actives on these timescales. A solution to this is presented here and is summarised in section 0.

3 Materials and Methodologies

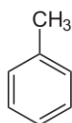
3.1 Chemicals

Water: All solutions were prepared using ultra-pure Milli-Q water (resistivity ~18M Ω cm)

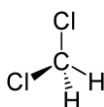
Polyvinylalcohol (PVOH): Sigma Aldrich; 88/8 product code: 81383; Batch code: 1312300/51408043 (*Emulsion stabiliser*)



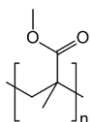
Toluene: Fisher Chemicals; product code: T/2250/17; batch code: 1016822



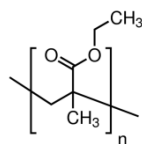
Dichloromethane (DCM): Acros Organics; product code: 383780010; batch code: 0807683 (*Good solvent for PMMA*)



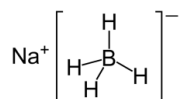
Polymethylmethacrylate (PMMA): Sigma Aldrich; product code: 18223-0; batch code: MKBB7676 (*Polymer*)



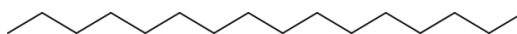
Poly(ethylmethacrylate) (PEMA): Sigma Aldrich; average Mw ~515,000 (*Polymer*)



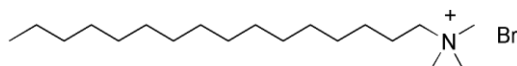
Sodium Borohydride: Sigma Aldrich; product code: 101088565



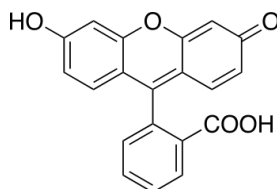
Hexadecane - Fisher Chemical; product code: H/0350/17; Batch code: 1147348



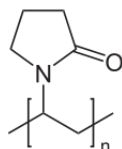
Cetyltrimethylammonium bromide: (CTAB) 98%, Sigma Aldrich



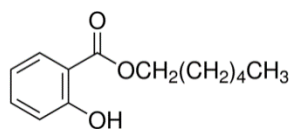
Fluorescein: Sigma Aldrich



Polyvinylpyrrolidone (PVP) 40KDa Sigma Aldrich



Hexyl salicylate: 99% Sigma Aldrich



Gold(III) chloride hydrate: Sigma Aldrich 99.999% trace metals basis 254169-5G

Chloroplatinic acid hydrate: Sigma Aldrich 99.9% trace metals basis 520896-5G

Hydrogen peroxide solution: Sigma Aldrich 35wt% 349887-500mL

3.2 Equipment

3.2.1 Atomic force microscopy (AFM)

AFM (Veeco BioScope 2) was used to look at the secondary metallic film morphology and thickness of spin-coated polymeric substrates.

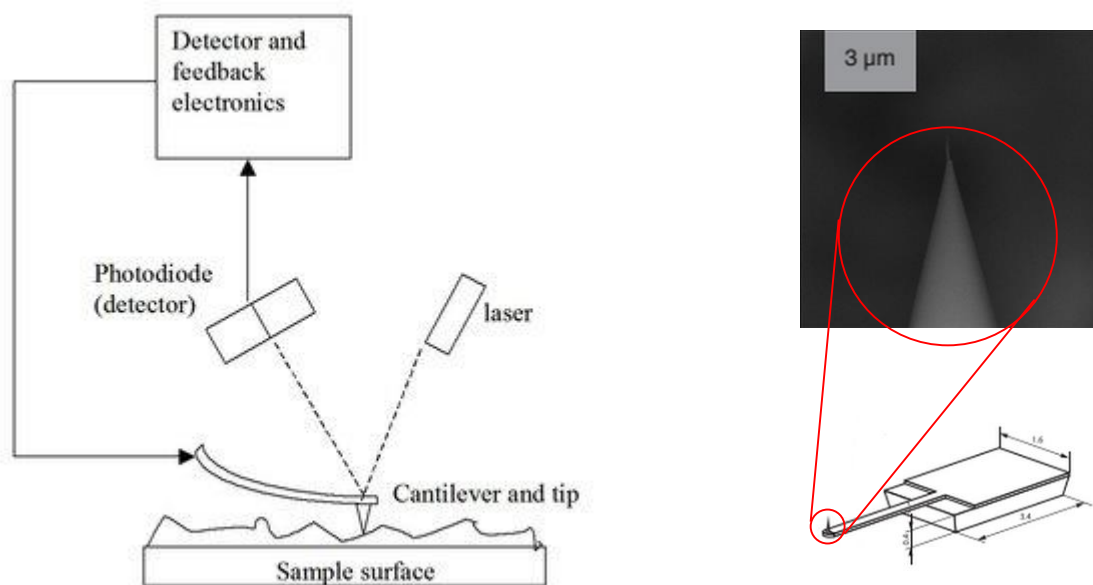


Figure 16 Schematic diagram showing the general principles of AFM and an SEM image of the end of a tip

A fine SiO_2 cone shaped tip is grown on the end of a Silica cantilever. A laser is aligned to reflect off the top of the cantilever onto a photodiode detector. The tip is coarsely brought into close proximity of the sample by electric motor and then into contact with the sample via piezoelectric crystal [Figure 16].

A further two piezoelectric crystals are used to move the tip laterally across the sample in the horizontal plane. As the contact with the surface changes the deflection on the can cantilever changes which alters the signal to the detector and, via an electronic feedback loop, a piezoelectric crystal alters the height of the tip in order to bring the signal on the

detector back to the original position. Using the vertical and horizontal drive signals a 3D raster scan of the surface can be obtained.

The cantilever was operated in tapping mode. The piezoelectric crystal drives the lever to resonate at or near one of its resonant frequencies. The interaction of the tip with the surface causes the amplitude of oscillation to decrease. A piezoelectric adjusts the height of the lever to maintain the resonant frequency. This height adjustment is used to build up a raster image of the surface from the individual scan lines.

To characterise metallic film thickness and morphology the metal on polymer on glass substrates were first, gently scored using a scalpel. It was shown via AFM that although gentle scoring cut through both the polymeric spin coated film and the gold film, the glass slide remained unaffected. AFM was then used to scan the scored area and sections across the break in the film were taken. Multiple sections were then averaged out to find a mean film depth. Similar characterisation of the bare polymeric spin-coated films was also undertaken.

Film roughness was measured by comparing scan area with the measured surface area within that scan area. The roughness was the ratio between flat and measured sample surface area. Multiple measurements were then taken in the areas around the score marks and averaged to find a mean roughness.

3.2.2 Quartz Crystal Microbalance QCM D300:

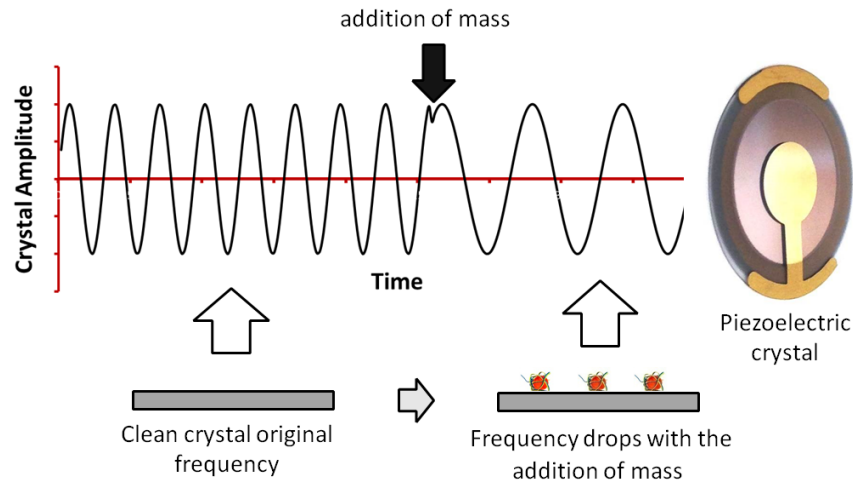


Figure 17 Schematic diagram showing the general principles of QCM

Quartz Crystal Microbalance (QCM) experiments were performed using a Q-Sense D300. The QCM was used to assess the adsorption of polymers and nanoparticles onto spin coated polymeric films [section 3.2.3]. The QCM uses a quartz crystal resonator to measure mass adsorption onto the crystal interface. The crystal is placed into a chamber into which liquids can be injected and an oscillating electrical signal is sent across the crystal and tuned to set up a resonance within the crystal. The frequency changes when mass adsorbs to the crystal surface from the liquid phase [Figure 17]. The frequency change can be correlated to the mass change using Sauerbrey's equation [eq. 3].

$$\Delta f = -\frac{2f_0^2 \Delta m}{A\sqrt{\rho_q \mu_q}} \quad \text{eq. 2}$$

$$\Delta m = \frac{-A\sqrt{\rho_q \mu_q}}{2f_0^2} \Delta f \quad \text{eq. 3}$$

Where:

f_o	Resonant frequency (Hz)
Δf	Frequency change (Hz)
Δm	Mass change (g)
A	Piezoelectrically active crystal area (Area between electrodes, cm^2)
ρ_q	Density of quartz ($\sim 2.643 \text{ g/cm}^3$)
μ_q	Shear modulus of quartz for AT-cut crystal ($\sim 2.947 \times 10^{11} \text{ g}\cdot\text{cm}^{-1}\cdot\text{s}^{-2}$)

Before each run piping was renewed and the system was rinsed with Milli-Q water several times and then was allowed to settle for 20 minutes prior to the injection of the dispersion / solution to be tested. In some cases a wash cycle, which consisted of a simple rinse with 5mL of Milli-Q water, was used to rinse excess surface active material from the bulk of the QCM chamber. Where necessary, details of concentrations and times of operation are described within the results section.

All Δf values were measured for the third overtone of the crystals fundamental frequency near 15MHz at room temperature (20°C).

3.2.3 Spin and dip -coating

A spin coating machine (WS-400B-6NPP/LITE) was used to deposit thin films of polymer onto both SiO_2 QCM crystals and glass slides. Surfaces to be spin coated were cleaned with a soap solution, rinsed thoroughly with Milli-Q water, dried with compressed air and then washed in 100% ethanol and dried again with compressed air. To keep the surfaces free of dust, samples were stored in a sample holder with lid.

The spin-coater was set to spin at 200rpm for 2 minutes. As soon as the spin-coater was up to speed (2-3seconds), 1mL of the coating solution, in most cases PEMA in DCM, was then deposited via a glass pipette onto the substrate at a concentration of 0.1wt% in DCM (1gL^{-1}).

Glass slides were then scored with a glass cutter across the middle of the spin-coated area (middle of the slide) and divided into two equal samples each with spin-coated polymer up to the end cut.

In order to coat TEM grids with PEMA. Grids were dipped into the same solution of PEMA in DCM (0.1wt% in DCM (1gL^{-1})) for ~ 1 second and were then touched onto a tissue to remove excess PEMA solution and allowed to dry for 1hour.

3.2.4 Dynamic light scattering

A NanoSeries Zetasiser (Malvern Nano-ZS) which was fitted with a He-Ne laser source (633nm wavelength, 4mW power) was used to measure nanoparticle size distributions and Zeta potentials.

When light hits particles that are small compared to the wavelength of the incident radiation, the incident light scatters in all directions. This is called Rayleigh scattering and is a result of the incident electromagnetic field setting up the same oscillation in the polarisable charges with the particle. The particle therefore becomes a small radiating body.

If a monochromatic and coherent light source, such as a laser, is shone on a dispersion of small particles, the light from all the particles constructively and destructively interferes and a speckled pattern is formed. The scattered light patterns' intensity varies over time due to the change in position of the particles due to Brownian motion. Information about the time scale of movement of the particles is to be found within this intensity fluctuation. A variation of the Stokes–Einstein equation can then be used to calculate particle size.

3.2.5 Optical and electron microscopy

The morphology of the microcapsules was studied using an Olympus BX51 optical microscope with a Colorview 2 digital camera. 'Cell D' imaging software was used to

record the images. A LEO 1530 Gemini field emission gun scanning electron microscopy (FEGSEM) and using a FEI Tecnai TF20 field emission transmission gun electron microscopy (FEGTEM) fitted with a HAADF detector and Gatan Orius SC600A CCD camera were also used. Prior to TEM analysis, samples were dispersed on a TEM grid (holey carbon film, 400 Cu Mesh from Agar Scientific). Chemical compositions of the metal-coated microcapsules were analysed using an Oxford Instruments INCA 350 energy dispersive x-ray spectroscopy (EDX) with 80mm X-Max SDD detector, within the FEGTEM and FEGSEM instruments. To analyse metal shell thickness, cross sections of the capsules were taken using microtome, prior to being studied by FEGTEM and analysed using the image processing software, (imageJ). Where necessary, details of specific sample preparation are described in the results section.

3.2.6 Focus Ion Beam (FIB)

An FIE Nova200 Duelbeam SEM/FIB was used to etch away parts of samples to reveal internal structure. Where necessary, details of specific sample preparation are described in the results section.

3.2.7 Sample Microtoming

Microtomed samples of capsules were produced by exchanging the aqueous continuous phase for ethanol via centrifuge and allowing the sample to dry. The dry capsules were then mixed into Struers Epofix and the epoxy resin and allowed to solidify. An agar scientific Y515ZA was then used to cut the sample into 80-100nm thick slices, which were then mounted onto TEM grids.

3.2.8 Gas Chromatography (GC)

GC was used to measure release from metal coated emulsion droplets and metal coated polymeric capsules. In all our polymeric capsule release experiments, the metal-coated capsules were compared against standard polymer-shell capsules. An equal portion of polymer capsules was removed from the sample undergoing the coating procedure. The polymer capsules were subjected to the same washing steps as the metal coated capsules to ensure equivalent losses of encapsulated oil (although minimal over the timescale of the experiment) from the capsule cores through the various stages of the process. Release rates in different solvent conditions were measured using gas chromatography as follows.

In a typical experiment, a known volume of metal-coated polymeric capsules was centrifuged to remove the supernatant. A corresponding sample of polymer-shell capsules was also centrifuged to remove the supernatant. Each sample was dispersed in 2 ml Milli-Q water and heated to 40°C. 8 ml absolute ethanol at 40°C was added to each sample and the capsules were redispersed and placed in a water bath at 40°C. 1 ml of each agitated suspension was taken at known time intervals over a period of 21 days. The extracted capsule samples were centrifuged at 7000 rpm for 1 min and the supernatant analysed via GC.

Samples were run on a Perkin Elmer Clarus 580GC using the following method and column:

GC column: Elite-1 capillary column, length 30m, internal diameter 0.25mm. The column temperature was programmed from 50°C to 300°C at 20°C/min at a flow rate of 2ml/min.

All data was compared against a calibration curve of the encapsulated oil determined in the same continuous phase of 4:1 ethanol:water mixture.

Metal coated emulsion droplets were treated in the same way as described above but no comparison was made to release from the bare Pt-NP stabilised emulsion droplets because of the instability of the Pickering emulsions in ethanol.

3.2.9 Mastersizer

A Malvern hydro 2000SM Mastersizer was used in conjunction with a Malvern 'Small Volume Sample Dispersion Unit' to measure size distributions of microcapsules via low angle laser light scattering (LALLS).

3.3 Methodologies/ Synthesis

3.3.1 Synthesis of polymeric capsules with oil core

Both Toluene and hexyl salicylate were used as an oil to be encapsulated. PEMA (5g) was dissolved in DCM (81g). The oil to be encapsulated (14g) was added and mixed until a single phase formed. This was used as the emulsion dispersed phase. CTAB (0.28g) was dissolved into 100ml of Toluene saturated Milli-Q water to form the emulsion continuous phase. The dispersed phase (7 ml) and continuous phase (7 ml) were added to a glass vial and emulsified (using IKA T25 Ultra-Turrax) at 15000 rpm for 2 min.

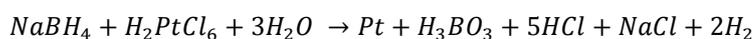
The emulsion was then stirred magnetically at 400 rpm while a further 86ml of continuous phase was poured in slowly. The diluted emulsion was then stirred at 400 rpm for 24 hours at room temperature to allow capsule formation to occur – this stage allows for extraction of DCM into the continuous phase and subsequent evaporation, which forces precipitation of the polymer onto the emulsion droplet surface.

The resulting capsules underwent three washing steps via centrifugation (Heraeus Megafuge R16) at 4000 rpm for 5 min, during which the supernatant was removed and replaced with fresh Milli-Q water. Finally, the capsules were redispersed in 50 ml Milli-Q water. Colloidal stability of the prepared capsules was verified over the timescale of the procedure through light scattering measurements.

In order to slow the initial solvent extraction phase to assess, for example, ‘initial’ emulsion size distributions for the toluene core capsules, for some experiments the CTAB aqueous phase was saturated with both Toluene and DCM prior to homogenisation. 100mL of the CTAB solution was made up and 4mL of Toluene and DCM were added. The vial was sealed with a lid, shaken by hand and allowed to stand. 7mL of the solution was taken via pipette when needed and the vial was resealed.

3.3.2 Preparation of Platinum Nanoparticles (Pt-NPs)

$H_2PtCl_6 \cdot 6H_2O$ (0.23 g) was added to PVP 40Kda (100 mL, 1.56 μ M (0.0015wt%) in some cases) and stirred to dissolve. $NaBH_4$ (0.4 mL of 5 mM solution (0.189g in 10mL water and take 3mL)) was added to the platinum salt-PVP solution with vigorous stirring for 2 minutes. The solution immediately turned dark brown suggesting formation of solid platinum as illustrated in equation eq. 4, and was left to stand overnight for the formation of Pt-NPs to complete.



eq. 4



For some experiments Pt-NPs were synthesised using a range of concentrations of PVP. Details of these experiments can be found in the particular chapter.

3.3.3 Adsorption of nanoparticles at polymeric microcapsule or emulsion droplet interface

3.3.3.1 Adsorption of Pt-NPs at room temperature onto a polymeric microcapsules or emulsion droplet interfaces

Adsorption of Pt-NPs at room temperature onto polymeric microcapsules or emulsion droplet interfaces was achieved by using Pt-NPs synthesised using the lower 0.0015wt% PVP stabiliser [paragraph 3.3.2]. 2% of the capsule dispersion [synthesis described in section 3.3.1] were added to the PVP-Pt nanoparticle suspension (5 ml), and mixed for 10 min on a carousel. Immediately after, the capsules were washed by centrifugation at 4000 rpm for 5 minutes, three times. The capsules were subsequently redispersed in 30 ml Milli-Q water.

3.3.3.2 Adsorption of Pt-NPs directly onto emulsion droplet interfaces

Adsorption of Pt-NPs at room temperature onto emulsion droplet interfaces was also achieved by using Pt-NPs synthesised using the lower 0.0064wt% PVP stabiliser [paragraph 3.3.2]. 0.1mL Hexadecane was added to 10mL of Pt-NP dispersion and was homogenised at 15-24Krpm for 2 minutes using an Ultra-Turrax IKA T25 or for 30 seconds at 30% power using an ultrasonic probe (Sonic Dismembrator Ultrasonic Processor, Model #FB-505 (From Fisher Scientific)). In some cases emulsions were allowed to 'age' prior to washing by placing the unwashed emulsion on a carousel for 24 hours. Samples were allowed to cream for 1 hour after which a hypodermic needle was used to extract the water containing the excess Pt-NPs below the creamed layer. 60mL of deionised water was then added followed by gentle stirring by hand to homogenise (not shaking). This wash cycle was repeated 3 times.

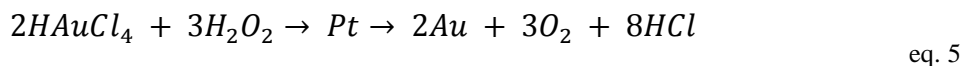
3.3.4 General metallic film growth procedure

3.3.4.1 Gold film growth on polymeric microcapsules:

HAuCl_4 (1 ml, 40 mM), hydrogen peroxide (1 ml, 60 mM) and poly(vinyl pyrrolidone) (1 ml, x mM) (used in this procedure as a polymeric stabiliser to provide colloidal stability to the resulting microcapsules) formed the electroless plating solution. Pt-loaded polymer capsules (9 ml (0.6% of original synthesis)) were added dropwise to the solution and stirred vigorously for 5 min during which the gold ions were reduced to solid gold as shown in equation eq. 5. The capsules were subsequently washed by centrifugation at 4000 rpm for 5 minutes, three times.

3.3.4.2 Gold film growth on dip-coated 2D interfaces

The same plating solution was used to dip-coat 2D interfaces such as spin-coated PEMA on glass (where necessary, variation from this sample preparation are described in the results section).



3.3.4.3 Gold film growth on Pt-NP stabilised emulsion droplets

After the final stage of cleaning of the Pt-NP stabilised emulsion droplets [section 3.3.3] the Pickering emulsions/colloidosomes were topped up with 15mL PVP (0.2wt% aqueous solution of 40kDa), 3mL 40mM solution of Gold (III) chloride hydrate ($\text{HAuCl}_4 + \sim 3\text{H}_2\text{O}$) and 3mL H_2O_2 reducing agent (60mM) and were shaken gently by hand for 2 minutes and then washed via centrifuge (Eppendorf Minispin Plus 1min 7000rpm)

3.3.5 Core release testing using gas chromatography (GC)

3.3.5.1 Testing for the release of hexyl salicylate using gas chromatography

In all our release experiments, we compared the metal-coated capsules against standard polymer-shell capsules. An equal portion of polymer capsules was removed from the sample undergoing the coating procedure. The polymer capsules were subjected to the same washing steps as the metal coated capsules to ensure equivalent losses of encapsulated oil (although minimal over the timescale of the experiment) from the capsule cores through the various stages of the process. Release rates in different solvent conditions were measured using gas chromatography as follows.

In a typical experiment, a known volume of metal-coated capsules was centrifuged to remove the supernatant. A corresponding sample of polymer-shell capsules was also centrifuged to remove the supernatant.

Each sample was dispersed in 2 ml Milli-Q water and heated to 40°C. 8 ml absolute ethanol at 40°C was added to each sample and the capsules were redispersed and placed in a water bath at 40°C. This procedure was chosen for compliance with industry standard tests. 1 ml of each agitated suspension was taken at known time intervals over a period of 21 days. The extracted capsule samples were centrifuged at 7000 rpm for 1 min and the supernatant analysed via GC.

Samples were run on a Perkin Elmer Clarus 580GC using the following method and column:

GC column: Elite-1 capillary column, length 30m, internal diameter 0.25mm. The column temperature was programmed from 50°C to 300°C at 20°C/min at a flow rate of 2ml/min.

All data was compared against a calibration curve of the encapsulated oil determined in the same continuous phase of 4:1 ethanol:water mixture.

3.3.5.1 Testing for release of hexadecane from metal coated emulsion droplets using gas chromatography

In a typical experiment, a known volume of hexadecane oil core was metal encapsulated [3.3.4.3].

Each sample was dispersed in 2 ml Milli-Q water and heated to 40°C. 8 ml absolute ethanol at 40°C was added to each sample and the capsules were redispersed and placed in a water bath at 40°C. 1 ml of each agitated suspension was taken at known time intervals over a period of 7 days. The extracted capsule samples were centrifuged at 7000 rpm for 1 min and the supernatant analysed via GC.

After 7 days the samples were centrifuged and pipetted onto a glass slide and the ethanol was allowed to evaporate. A second glass slide was then used to crush the 'dry' capsules and the crushed capsule / hexadecane oil core mix was carefully washed back

into a vial using 40mL of ethanol. This sample was then centrifuged at 7000 rpm for 1 min and the supernatant analysed via GC.

Samples were run on a Perkin Elmer Clarus 580GC using the following method and column:

GC column: Elite-1 capillary column, length 30m, internal diameter 0.25mm. The column temperature was programmed from 50°C to 300°C at 20°C/min at a flow rate of 2ml/min.

All data was compared against a calibration curve of the encapsulated oil determined in the same continuous phase of 4:1 ethanol:water mixture.

3.3.6 Florescent dye gold encapsulation

Perylene, an oil soluble fluorophore, was dissolved in hexadecane and used as the oil phase to form gold coated capsules via the standard technique described above [3.3.4.3]. The continuous phase was then exchanged for an ethanol phase and left for 24hours. The capsules were then crushed with a glass slide and observed in visible and ultraviolet light.

3.4 General calculations

3.4.1 Colloidal surface areas from size distribution data

In order to calculate, for example, the surface area of a given sample one requires both the size distribution data and a total volume. The total surface area contribution at a particular size range (size bin limit) can then be calculated. These surface area contributions at the different size bin limits can be added together to find the total surface area of a sample. The surface area of known volumes of homogenised capsule dispersions can therefore be found [eq. 6].

Total surface area contributions from all size bin limits:

Where:

- d_{Lim} Bin limit diameter
- V_{cap} Particle volume at bin limit
- S_{Lim} Surface area of capsule at bin limit
- $V_{\%}$ Percentage volume contribution at bin limit
- V_T Final volume of dispersed phase
- V_{Lim} Actual volume contribution at bin limit
- n_{Lim} Number of capsules at bin limit
- S_{Lim} Total surface area of capsules at bin limit

$$V_{cap} = 4/3\pi(d_{Lim}/2)^3$$

$$S_{Lim} = 4\pi(d_{Lim}/2)^2$$

$$V_{Lim} = \frac{V_{\%}}{100} * V_T$$

$$n_{Lim} = \frac{V_{Lim}}{V_{cap}} = \frac{6V_{\%}V_T}{100\pi(d_{Lim})^3}$$

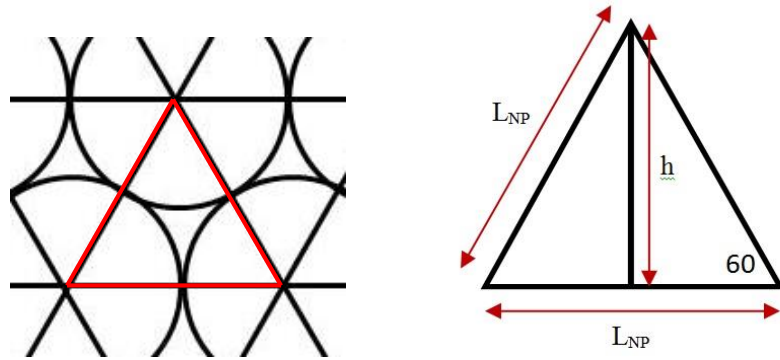
$$S_{Lim} = n_{Lim}S_{Lim} = \frac{6V_{\%}V_T 4\pi(d_{Lim}/2)^2}{100\pi(d_{Lim})^3} = \frac{6V_{\%}V_T}{100d_{Lim}}$$

$$S_{Total} = \sum_{d_{Lim}=0}^{\infty} \frac{6V_{\%}V_T 4\pi(d_{Lim}/2)^2}{100\pi(d_{Lim})^3} = \sum_{d_{Lim}=0}^{\infty} \frac{6V_{\%}V_T}{100d_{Lim}} \quad \text{eq. 6}$$

3.4.2 Image-J analysis NP adsorption density and size analysis

Image analysis software (Image-J) was used to analyse nanoparticle adsorption densities. Raw transmission electron microscope images were first adjusted for contrast. The threshold size was then set to a surface area 2-49 nm² and the circularity was set to 0.2-1.00. The resulting image was then made binary and the particles were automatically analysed to record the apparent cross sectional area of nanoparticles. In order to convert this to particle size, the surface area was used as an approximation of the Pt-NPs cross sectional surface area, assuming it was a perfect sphere. This surface area was then used to calculate equivalent particles diameters and a size distribution for the dispersion.

3.4.3 Maximum percentage surface coverage of hexagonally close packed spheres



The the maximum surface area coverage of hexagonally packed spheres is given by the ratio of spheres surface inside the equilateral triangle to the surface area of the triangle itself. Therefore:

Surface area of triangle side length 1:

$$\Delta_s = \frac{1}{2} \text{base} * \text{height} = \frac{1(\sqrt{1^2 - 0.5^2})}{2} = 0.433 \quad \text{eq. 7}$$

Surface area of 'sphere' inside the triangle:

$$\phi_s = 3(\pi 0.5^2 (60/360)) = 0.393 \quad \text{eq. 8}$$

Ratio of ϕ_s to Δ_s is equal to maximum possible surface area coverage:

$$\phi_s / \Delta_s = 0.393 / 0.433 = 0.91 \cong 91\% \quad \text{eq. 9}$$

3.4.4 Number of NPs per unit volume

Where:

M_s Mass of platinum salt used [3.3.2]

M_p Mass of platinum used

V_{aq} Volume of aqueous dispersion

D_{Pt} Density of platinum

V_{Pt} Therefore volume of atomic platinum per unit volume

r_{NP} Average radius of NPs in the dispersion

V_{NP} Average volume of a NP

N_{NP} Number of NPs per unit volume

Mass platinum atoms per unit volume $\frac{M_p}{V_{aq}}$

$$Density = Mass/Volume$$

Therefore volume of atomic platinum per unit volume (V_{Pt}):

$$V_{Pt} = \frac{M_p}{V_{aq} D_{Pt}}$$

$$V_{NP} = \frac{4}{3} \pi (r_{NP})^3$$

$$N_{NP} = \frac{V_{Pt}}{\left(\frac{4}{3} \pi (r_{NP})^3\right)}$$

$$N_{NP} = \frac{M_p}{V_{aq} D_{Pt}} \bigg/ \left(\frac{4}{3} \pi (r_{NP})^3\right)$$

$$N_{NP} = \frac{3M_p}{4\pi V_{aq} D_{Pt} (r_{NP})^3} \quad \text{eq. 10}$$

For the standard Pt-NP dispersion synthesised and used in this work, 0.23 g of $\text{H}_2\text{PtCl}_6 \cdot 6\text{H}_2\text{O}$ therefore 0.14g of platinum. Using the equations above [eq. 10] we find that the concentration of NPs per mL of dispersion works out at 4.6×10^{15} NPs per mL.

In section 3.4.4 in which the Langmuir adsorption equilibrium constant and adsorption energy are determined, the concentration of Pt-NP is expressed as a molarity. Using eq. 11 we get a concentration of $7.67 \times 10^{-6} \text{M}$.

Where:

c Molarity (M)

N Number of molecules (or in this case particles) present

N_A Avogadro number ($6 \times 10^{23} \text{mol}^{-1}$)

V Volume (L)

$$c = N / N_A V \quad \text{eq. 11}$$

3.4.5 Expected inter-nanoparticle spacing on a microcapsule interface assuming 2D hexagonal packing

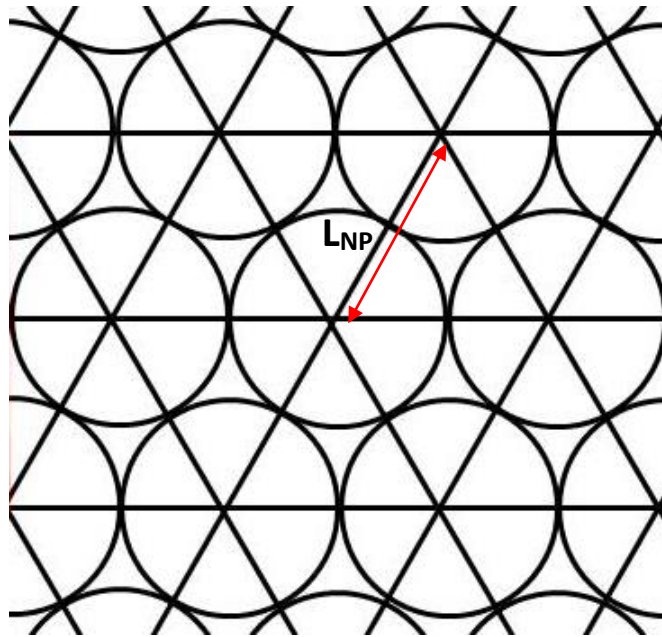


Figure 18 Schematic diagram of an array of hexagonal close packed spheres.

Where:

n_{NP} Number of NP's per unit area of capsule surface (surface density)

L_{NP} Inter-nanoparticle spacing

n_t Number of triangles per unit area

s_t Surface area of a triangle

n_t Number of triangles per unit area

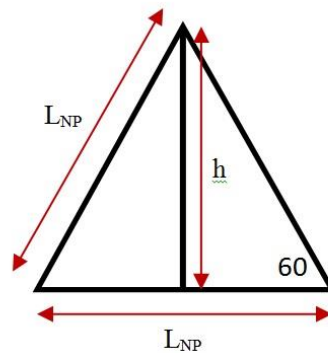
S_{cap} Total surface area of capsules introduced

$$n_{NP} = N_{NP} / S_{cap}$$

Ratio of whole circles to whole triangles per unit area is 1:2 [Figure 18] therefore the number of triangles per unit area twice number of NPs per unit area.

$$n_{NP} = 2n_t$$

$$s_t = \frac{1}{2} L_{NP} h$$



$$h^2 + \left(\frac{L_{NP}}{2}\right)^2 = L_{NP}^2$$

$$h = \sqrt{\frac{3L_{NP}^2}{4}}$$

$$s_t = \frac{1}{2} L_{NP} \sqrt{\frac{3L_{NP}^2}{4}} = L_{NP}^2 \sqrt{\frac{3}{16}}$$

$$n_t = \frac{1}{s_t}$$

$n_{NP} = 2n_t$ therefore:

$$\frac{n_{NP}}{2} = \frac{1}{s_t} = \frac{1}{L_{NP}^2 \sqrt{\frac{3}{16}}}$$

$$n_{NP} = \frac{2}{\left(L_{NP}^2 \sqrt{\frac{3}{4}}\right)}$$

$$n_{NP} L_{NP}^2 = \frac{2}{\left(\sqrt{\frac{3}{4}}\right)} = 4 \sqrt{\frac{1}{3}}$$

$$L_{NP} = 2 \sqrt{\frac{\sqrt{\frac{1}{3}}}{n_{NP}}}$$

eq. 12

3.4.6 Polymeric microcapsule core shell size ratios

Where:

M_{DCM}	DCM mass in core solution
M_{Tol}	Toluene mass in core solution
M_{PEMA}	PEMA mass in core solution
V_{DCM}	DCM volume in original core solution
V_{Tol}	Toluene volume in original core solution
V_{PEMA}	PEMA volume in original core solution
ρ_{DCM}	Density of DCM
ρ_{Tol}	Density of toluene
ρ_{PEMA}	Density of PEMA
$\%_{DCM}$	% of DCM remaining after solvent extraction phase
$\%_{Tol}$	% of Toluene remaining after solvent extraction phase
$\%_{PEMA}$	% of PEMA remaining after solvent extraction phase
V_{core}	Final core volume

V_{cap}	Final capsule volume
r_{core}	Final core radius
r_{cap}	Final capsule radius

$$\rho_{DCM} = M_{DCM}/V_{DCM} \quad \rho_{Tol} = M_{Tol}/V_{Tol} \quad \rho_{PEMA} = M_{PEMA}/V_{PEMA}$$

$$V_{core} = 0.01 \left(\frac{\%_{DCM} M_{DCM}}{\rho_{DCM}} + \frac{\%_{Tol} M_{Tol}}{\rho_{Tol}} \right)$$

$$V_{cap} = 0.01 \left(\frac{\%_{DCM} M_{DCM}}{\rho_{DCM}} + \frac{\%_{Tol} M_{Tol}}{\rho_{Tol}} + \frac{\%_{PEMA} M_{PEMA}}{\rho_{PEMA}} \right)$$

$$V = \frac{4}{3} \pi r^3$$

Therefore core and capsule radius are given by:

$$r_{core} = \sqrt[3]{\frac{0.03}{4\pi} \left(\frac{\%_{DCM} M_{DCM}}{\rho_{DCM}} + \frac{\%_{Tol} M_{Tol}}{\rho_{Tol}} \right)}$$

$$r_{cap} = \sqrt[3]{\frac{0.03}{4\pi} \left(\frac{\%_{DCM} M_{DCM}}{\rho_{DCM}} + \frac{\%_{Tol} M_{Tol}}{\rho_{Tol}} + \frac{\%_{PEMA} M_{PEMA}}{\rho_{PEMA}} \right)}$$

Core shell ratio:

$$\frac{r_{core}}{r_{cap}} = \frac{\frac{\%_{DCM} M_{DCM}}{\rho_{DCM}} + \frac{\%_{Tol} M_{Tol}}{\rho_{Tol}}}{\frac{\%_{DCM} M_{DCM}}{\rho_{DCM}} + \frac{\%_{Tol} M_{Tol}}{\rho_{Tol}} + \frac{\%_{PEMA} M_{PEMA}}{\rho_{PEMA}}} \quad \text{eq. 13}$$

4 Model capsule choice

In order to characterize the resulting structures from each of the steps in the procedure, such as predicted nanoparticle adsorption densities or secondary metal film thicknesses, one needs to first define the polymeric microcapsule model system. This short chapter describes the model capsule system chosen for this work, and the characterization of key capsule properties such as oil core/ polymer shell volume ratios and colloidal surface areas.

4.1 Model Capsule Selection and Characterisation

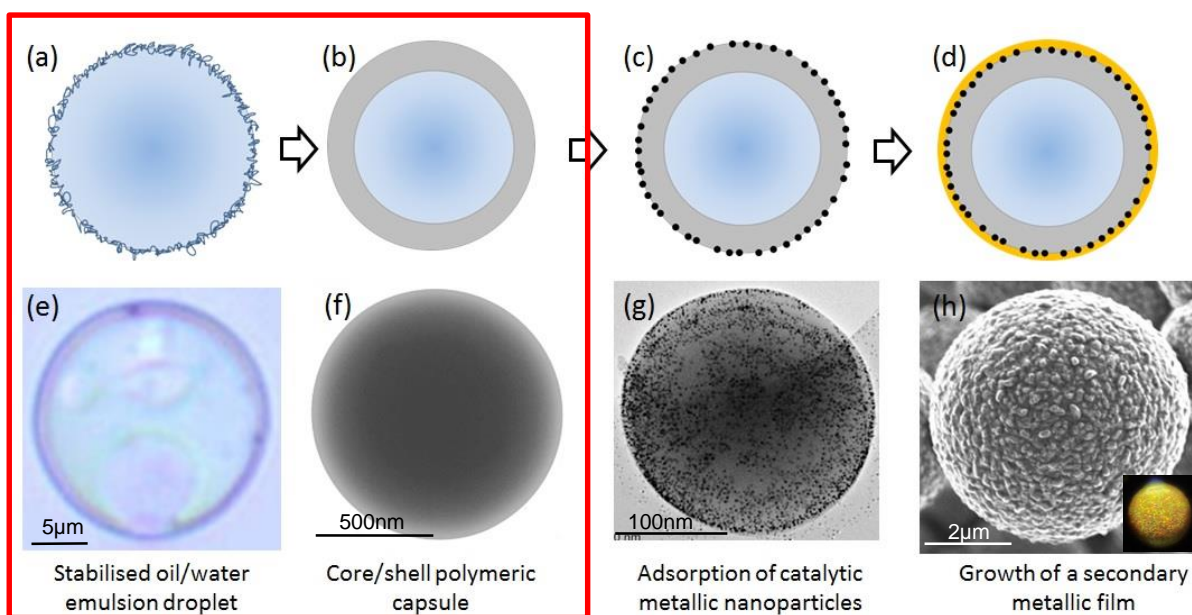


Figure 19 Schematic diagrams (a-d) and corresponding optical and electron microscopy images (e-h) of the different phases from emulsion droplet to gold coated capsule (a) emulsion droplet, (b) capsule, (c) capsule with adsorbed NPs, (d) Gold coated capsule, (e) emulsion droplet (optical microscopy), (f) capsule (TEM), (g) capsule with adsorbed NPs (TEM), (h) Gold coated capsule (SEM) (inset gold coated capsule under visible light). Red box highlights the part of the process discussed in this chapter.

The model system chosen was a toluene core, PEMA shell microcapsule (Tol/PEMA) formed by a solvent extraction method [Figure 19] [See section 3.3.1 for details of

synthesis]. A core phase made up of a solution of Toluene and PEMA in DCM is homogenised with water containing a CTAB stabiliser. The resulting emulsion droplets are then stirred in an open container to allow the water soluble DCM, which acts as a good solvent for the PEMA, to diffuse into the water and then evaporate. As the core shrinks, its constitution changes from DCM rich to Toluene rich forcing the PEMA to precipitate and form a shell around the Toluene drop, in which it is not soluble.

4.1.1 Choice of toluene core, PEMA shell microcapsules as a model system

Tol/PEMA microcapsules were chosen as a model system for several reasons. One of the aims of this thesis is to demonstrate ‘permanent’ encapsulation of highly volatile small molecules, toluene is an appropriate small volatile molecule. Also, understanding the kinetics and having some control over the adsorption of the NP catalyst and subsequent secondary metal film growth were two primary aims of this thesis. There was therefore a requirement for robust capsules which keep their shape throughout several processing steps. The proportions of toluene, DCM and PEMA used in the initial core solution [3.3.1] result in the production of thick shelled microcapsules with relatively inflexible interfaces providing a robust interface for NP adsorption. Figure 20 shows an SEM micrograph of the dry capsules. The capsules keep their spherical shape on drying in a vacuum.

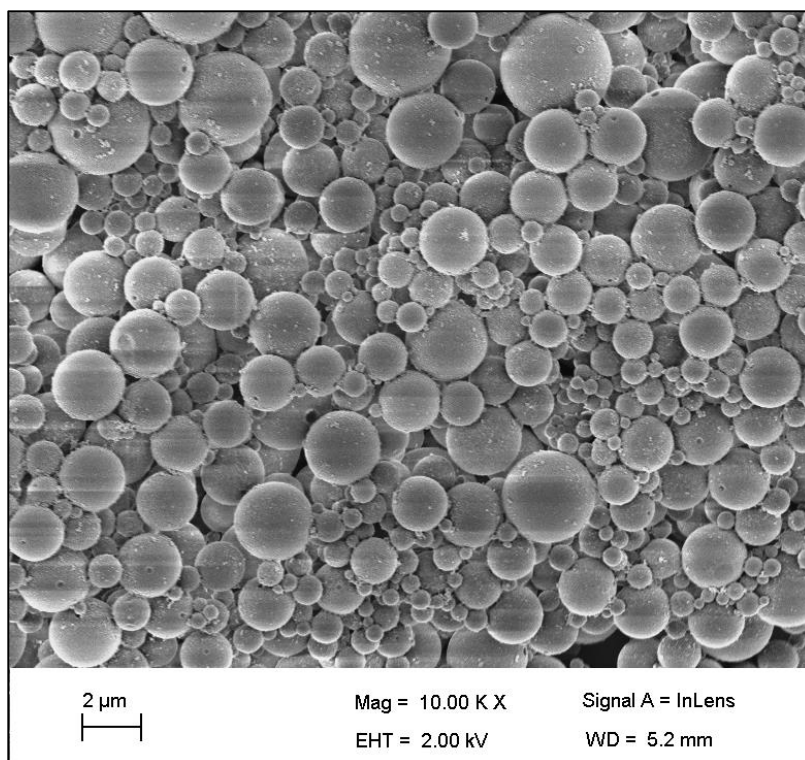


Figure 20 SEM image of dry Toluene core /PEMA shell capsules.

In addition to this, the ability to use a short-chain surfactant (CTAB) as the stabiliser for the emulsion allows for a wide range of possible of catalytic nanoparticle adsorption techniques. The hydrophilic charged head group allows for the adsorption of oppositely charged primary catalytic NPs or allows the charge to be reversed by using, for example, layer-by-layer polyelectrolyte techniques. The short chain surfactant also creates no steric hindrance to the adsorption of surface active polymerically stabilised catalytic NPs.

4.1.2 Capsule core/shell volume ratios and dispersion surface area

In order to calculate, for example, catalytic NP adsorption densities or secondary metal film thicknesses it is necessary to have some understanding of the process of formation and final structure of the core shell capsules, such as, expected core / shell volume ratios or capsule surface areas.

To measure the surface area of the capsules two pieces of information are required; the final capsule size after capsule formation and the final total volume.

Figure 21 shows the mean size distribution as a function of time for capsules measured from the start of the solvent evaporation phase. The size distribution was measured over a period of 9 hours. It should be noted that the continuous phase was pre saturated with both DCM and Toluene prior to homogenisation in an attempt to slow the initial solvent evaporation phase in order to capture the initial size distribution prior to shrinkage [3.3.1].

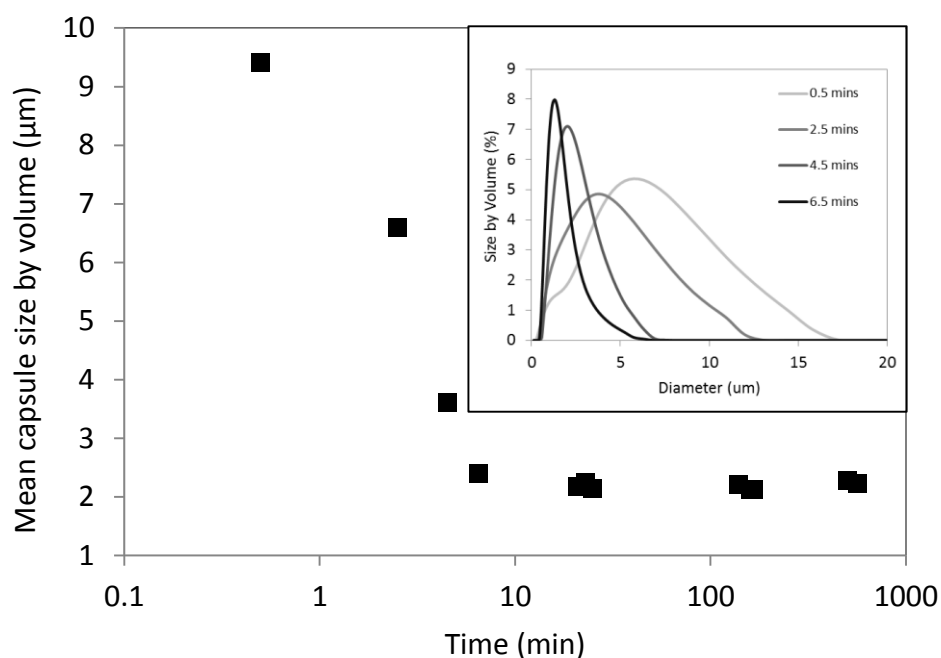


Figure 21 Shows low angle laser light scattering (LALLS) (Mastersizer) size distribution data for Tol/PEMA capsules. The first 3 data points were measured by adding the emulsion directly after homogenization into the Mastersizer [3.2.9]. The other samples were taken from normal procedure over the first 10 hours of solvent extraction. The inset shows the actual size distribution by volume for the first 4 points.

We can see from Figure 21 that the emulsion droplets initially reduce in size from $\sim 9\mu\text{m}$ to $\sim 2\mu\text{m}$ across the first 10 minutes of the solvent extraction phase. The capsules then remain at this size until the end of the synthesis. Accurate final size distribution data is therefore easy to obtain.

Obtaining an accurate figure for the final volume of the sample is however non trivial. We know that the capsules shrink during the dilution phase of the synthesis as the DCM evaporates into the continuous phase forcing the PEMA to precipitate and form a shell. We also know that because the highly volatile DCM is both soluble in the forming PEMA shell and the aqueous continuous phase 100% of the DCM is released from the forming capsule over the 24hour solvent evaporation phase. However, for the following reasons we cannot simply make the assumption that the final volume is the original volume of polymer plus the original volume of Toluene:

Toluene is, to a small extent, soluble in water (0.52 g/L (20 °C)) and therefore a relatively small proportion of the Toluene will also be lost during the DCM extractions phase which in turn may affect the final volume of the capsules.

As the relatively thick polymeric shell precipitates out around the shrinking oil core it may inhibit complete size reduction down to the volume of the poor solvent (toluene) plus the polymer (PEMA). If the forming shell arrests the reduction in size, because the 100% of the DCM will leave by diffusion, it is possible that water ingress occurs to make up the volume.

4.1.2.1 Solutions to the final volume problem

The initial core volume is precisely known and therefore if we could precisely know the initial size distribution after homogenisation but prior to solvent extraction we could use the initial size distribution and initial volume to calculate the number of emulsion droplets in the sample. We could then make the reasonable assumption that the dispersion remains stable throughout the solvent extraction phase and therefore the number of particles does not change. We would then be able to use the total number of particles and the final size distribution to calculate the final volume and surface area.

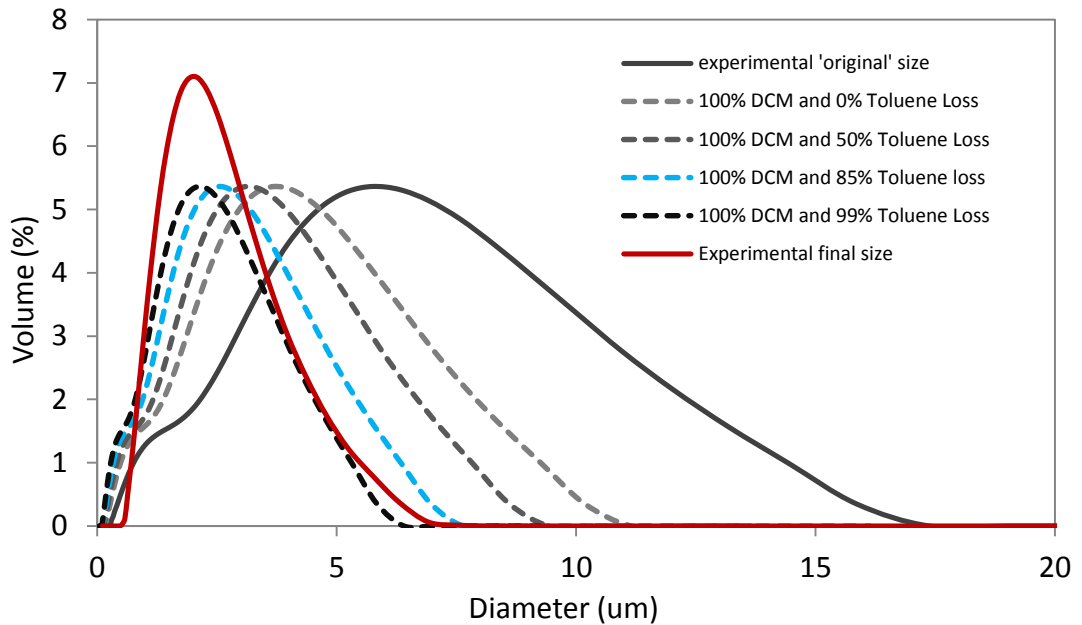


Figure 22 Graph showing the experimentally measured initial emulsion size distribution and the final capsule size distribution after the solvent extraction phase is complete. The dotted lines represent size distribution data calculated from the measured initial size distribution and show calculated size distributions for 100%DCM loss, 100%DCM and 50% toluene loss, 100%DCM and 85% toluene loss and 100%DCM and 99% toluene loss.

Figure 22 shows the experimentally measured initial emulsion size distribution by volume and the final capsule size distribution after the solvent extraction phase is complete by volume. The dotted lines represent size distribution data calculated from the measured initial size distribution and show calculated size distributions for 100%DCM loss, 100%DCM and 50% toluene loss, 100%DCM and 85% toluene loss and 100%DCM and 99% toluene loss. The projected size distributions are calculated in the following way. Each bin limit within the size distribution undergoes the following mathematical transformation.

Where:

d_1 Initial bin limit diameter

V_1 Initial particle volume at bin limit

Δ_{core} Chosen percentage reduction in volume of core phase

V_2 Final particle volume at bin limit

d_2 Final bin limit diameter

$$V_1 = 4/3\pi(d_1/2)^3 \quad \text{eq. 14}$$

$$V_2 = \pi/75 (100 - \Delta_{core})(d_1/2)^3 \quad \text{eq. 15}$$

$$d_2 = \left(1 - \frac{\Delta_{core}}{100}\right) \left(\frac{d_1}{2}\right)^3 \quad \text{eq. 16}$$

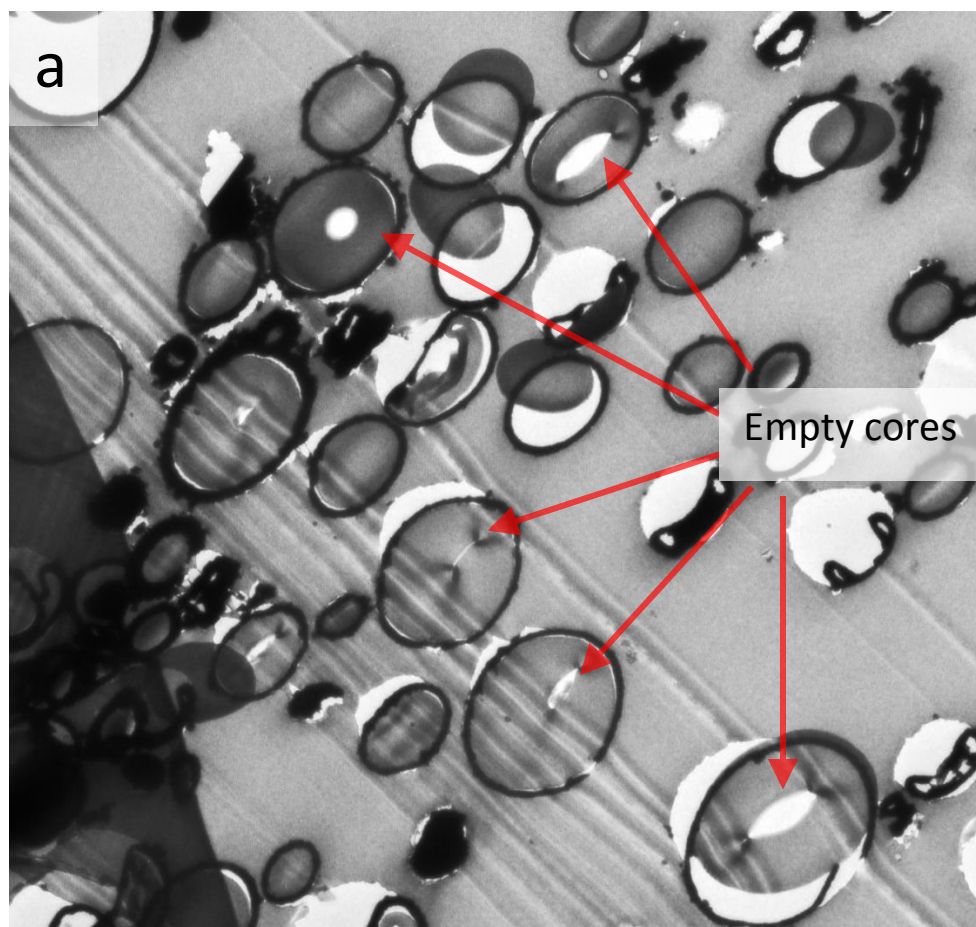
The new diameter (d_2) is then allocated to the original volume percent (V_1) at the original diameter (d_1).

We can see from Figure 22 that only the size distribution for 100%DCM and 99% toluene loss fits with the final size distribution found experimentally. The implication is therefore that ~100% of the core has diffused out during the solvent extraction phase and therefore we should be left with capsules which have no core and are 100% PEMA. However there are several pieces of data that contradict this finding.

1. TEM microtomes of the capsules show the presence of a small core in a high proportion of the capsules. Figure 23a shows ~100nm thin slice of capsules set in epoxy resin [3.2.7]. Small cores are clearly visible in a number of the capsules. It should be noted that the cores are small enough to be not visible in all capsules because of the core position relative to the shell and the random microtome slice position though the core.
2. When the surface from which the microtomed samples were taken was observed by SEM, voids were visible where, it could be argued, liquid cores had evaporated away [Figure 23b]. If the cores were made up of 100% solid PEMA one would not expect to see core/shell structure. In addition to this, all cores appear to have shrunk somewhat creating depressions. Although further work would be required to

confirm the following, it is likely that core shrinkage would not be observed if the cores were 100%PEMA. One possible explanation of the core shrinkage is that the PEMA shell remains solvated to some extent by the core solvent and, when cut open, releases the remaining solvent forcing the PEMA shell to loose mass and volume.

3. Gas chromatography was used to measure the release of toluene from the fully formed capsules and showed that ~15% of the toluene remains present in the capsules. We can see from Figure 22 (dotted blue line) that at 100% DCM and 85% toluene loss the projected size distribution is larger than the measured final size distribution. We therefore know that our measured initial size distribution of the capsules must be too large. This increase in size distribution must occur in the time between the homogenisation step and the measurement via LALLS (mastersizer). For example, it could be due to some level of emulsion droplet coalescence when the dispersion is pumped through the machine.



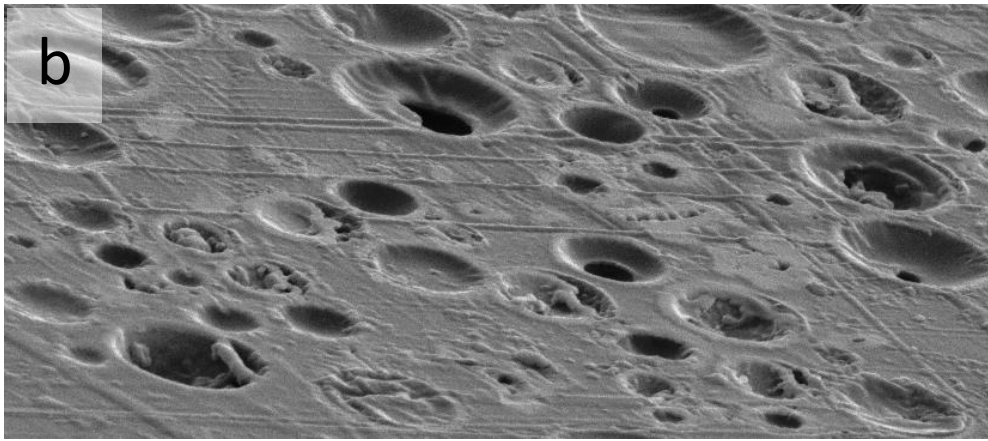


Figure 23 (a) ~100nm thin microtomed samples of metal coated Toluene core / PEMA shell capsules showing core /shell structure and (b) an SEM image of the block from which the microtomes were taken showing voids in the cores of sliced capsules and depressed cores relative to the original slice position

Figure 24 is a schematic diagram showing the ratio of the core diameter to the total capsule diameter for a capsule which has lost volume, during the co-solvent extraction phase [3.3.1], 100% of the DCM and 85% loss of Toluene. Assuming the remaining PEMA and Toluene phase separate into a perfect core shell structure and there is zero water ingress, it can be seen that the core diameter should be 71% of the total capsule diameter. It is worth noting that the predicted core/shell ratio calculated using eq. 13, at 100% DCM and 85% Toluene loss [Figure 24], appears to be larger than the core/shell ratio pictured in Figure 23a. We know from the GC measurements that 15% of the Toluene remains. One explanation for this could be incomplete PEMA/Toluene phase separation. This lends weight to the explanation given previously for the observed partial collapse of the cores in Figure 23b.

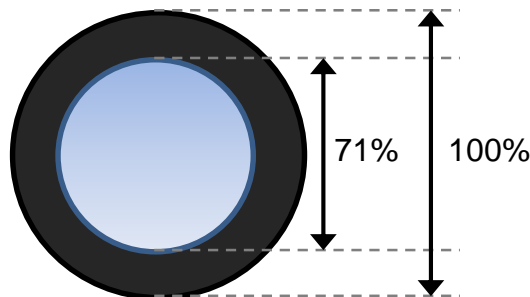


Figure 24 Schematic diagram showing the ratio of the core diameter to the total capsule diameter for a capsule which has lost volume, during the co-solvent extraction phase [3.4.6], which is equivalent to 100% loss of DCM and 85% loss of Toluene [eq. 13].

It is known that the final size distribution is correct and, from GC, that 15% of the toluene remains present in the core after capsule formation. It is therefore concluded that the final total volume of capsule must be at least as big as 100% of the original PEMA plus 15% of the original toluene.

It is therefore known that the minimum final volume is ~8% of the original core volume used in the synthesis. In our case 7mL of core solution is used and therefore the total minimum volume of capsules after the co-solvent extraction has taken place should be ~0.56mL. This volume was used in all future calculations.

4.1.2.2 Calculating the dispersion surface area

Now that a figure for final size and final volume has been agreed upon the total surface area of our sample can be calculated.

Figure 25 shows the size distribution of our capsule dispersion by both volume and number percent. The first thing to note is that both curves are not perfect normal distributions but are in fact skewed towards larger capsules. Therefore taking the 'mode' or peak of these graphs as the mean is incorrect as the mean occurs at a somewhat larger size than the mode. However, even if correct values for the mean are found, two problems remain. Firstly, which of the two graphs, size by volume% or size by number %, should the mean be taken from? Secondly, is it acceptable to take the mean diameter as representative of the whole sample? In other words, do the capsules which are smaller than the mean contribute to the total surface area in a mirrored way to the capsules which are larger? As surface area is proportional to the square of the diameter the two surface areas on either side of the mean do not mirror each other and therefore using the mean size is not an accurate way of measuring the total surface area.

The mastersizer instrument is capable of calculating surface area from the measured size distribution. However, for the purpose of understanding the characteristics of our distributions specifically these calculations were carried out separately as highlighted below.

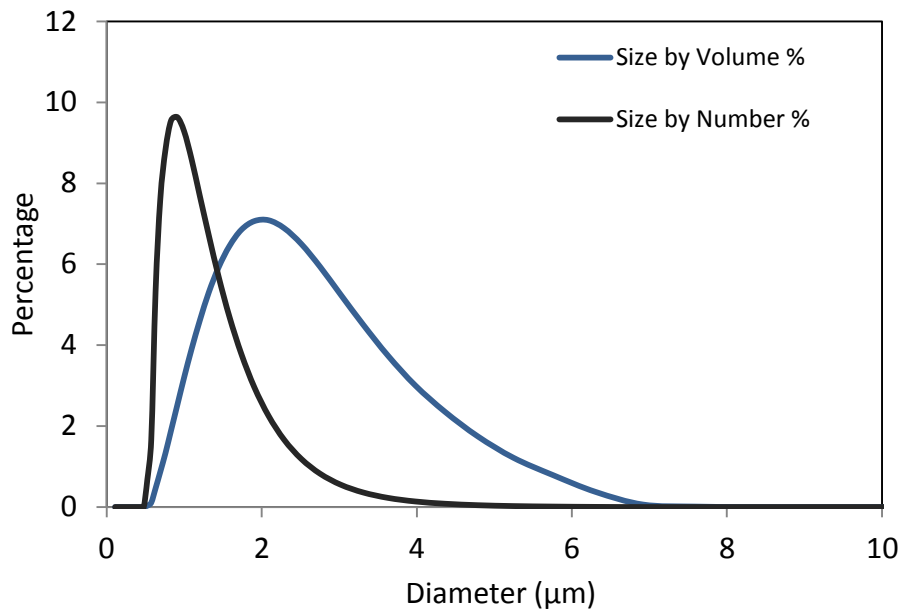


Figure 25 Show the fully formed PEMA/Toluene capsule size distribution as a percentage of sample volume and number.

A more accurate way of using the size distribution data is to calculate the total sample surface area by calculating the surface area contribution from each of the bin limits within the size distribution by volume percent and then totalling up all the surface area contributions to find the total sample surface area.

Total surface area contributions from all size bin limits:

Bin limit diameter d_{Lim}

Particle volume at bin limit V_{cap}

$$V_{cap} = 4/3\pi(d_{Lim}/2)^3$$

Surface area of capsule at bin limit S_{Lim}

$$S_{Lim} = 4\pi(d_{Lim}/2)^2$$

Percentage volume contribution at bin limit $V_{\%}$

Final volume of dispersed phase V_T

Actual volume contribution at bin limit V_{Lim}

$$V_{Lim} = \frac{V_{\%}}{100} * V_T$$

Number of capsules at bin limit n_{Lim}

$$n_{Lim} = \frac{V_{Lim}}{V_{cap}} = \frac{6V_{\%}V_T}{100\pi(d_{Lim})^3}$$

Total surface area of capsules at bin limit S_{Lim}

$$S_{Lim} = n_{Lim}S_{Lim} = \frac{6V_{\%}V_T 4\pi(d_{Lim}/2)^2}{100\pi(d_{Lim})^3} = \frac{6V_{\%}V_T}{100d_{Lim}}$$

$$S_{Total} = \sum_{d_{Lim}=0}^{\infty} \frac{6V_{\%}V_T 4\pi(d_{Lim}/2)^2}{100\pi(d_{Lim})^3} = \sum_{d_{Lim}=0}^{\infty} \frac{6V_{\%}V_T}{100d_{Lim}} \quad \text{eq. 17}$$

Error! Reference source not found. shows a plot, generated from the equation above [eq. 17], of total capsule surface area as a function of percentage of original sample used. For comparison, plots showing what the relationship between these two variables would be if we used the mean size by volume and the mean size by number in our calculations.

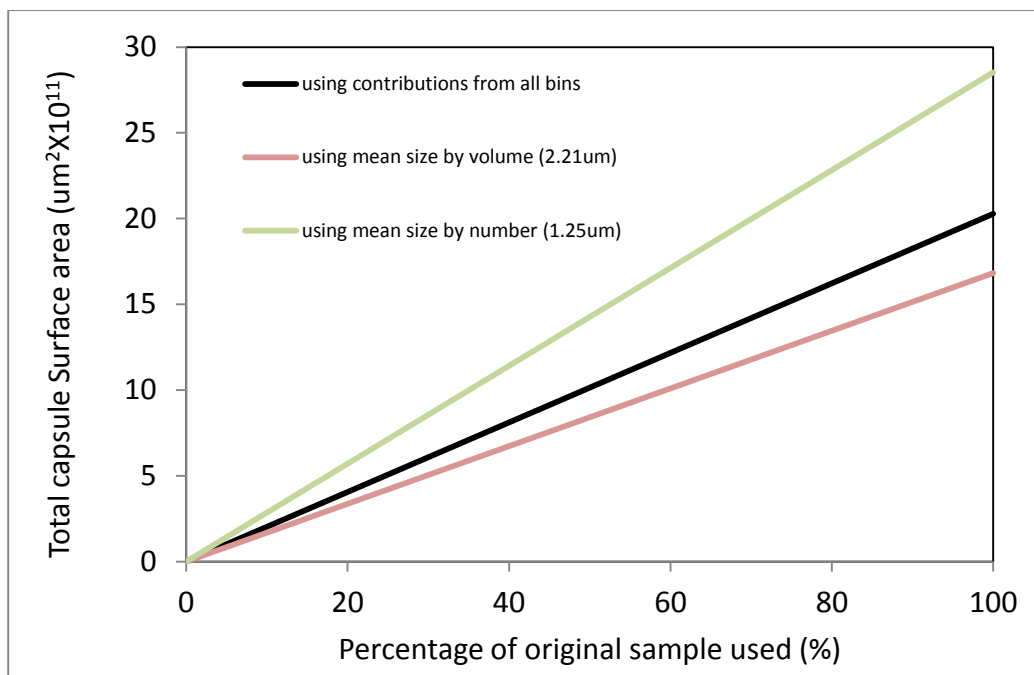


Figure 26 Graph of total capsule surface area as a function of percentage of original synthesis volume.

We can see from the graph that 100% of the original sample has a surface area of $2.03 \times 10^{12} \mu\text{m}^2$ which is just over 2 m^2 . In the original synthesis of the capsules 7 mL of core solution was homogenized with 7 mL of the CTAB solution which was subsequently diluted to 100 mL with CTAB solution. We calculate that the oil phase reduces in volume by $\sim 92\%$ therefore the total final volume of the capsules are dispersed in is $\sim 93.6 \text{ mL}$. However actual measured final total volumes were $\sim 92 \text{ mL}$ because of water evaporation over the 24hour solvent extraction phase. Therefore the surface area per mL of capsule dispersion should be approximately $2.2 \times 10^{10} \mu\text{m}^2 \text{ mL}^{-1}$.

This figure represents a good approximation for the surface area of the microcapsules post solvent extraction phase prior to washing via centrifuge [3.3.1]. The washing phase involves 3 wash cycles to remove excess CTAB from the original synthesis. In section 6.3.3 it is proved that the surface area is at least $2/3$ smaller than expected from these calculations. Although it is likely we disproportionately lose the small capsules during the centrifuge phase, these calculations use the capsule size distribution post wash cycle and are therefore representative of the sample.

Subsequent calculations involving capsules surface area should then take into account the potential loss of capsules throughout the washing process therefore correlations

made for the subsequent steps of the process should fit within the range defined by the minimum ($7.3 \times 10^9 \mu\text{m}^2\text{mL}^{-1}$) and maximum ($2.2 \times 10^{10} \mu\text{m}^2\text{mL}^{-1}$) surface areas.

4.2 Conclusion

Toluene core PEMA shell capsules were successfully synthesised using a cosolvent extraction method. Tol/PEMA microcapsules were chosen as a model system for our studies firstly because Toluene was an appropriate small volatile molecule for release studies and secondly the capsules formed relatively thick, robust shells (at least 29% of the capsule radius [Figure 24]) which keep their shape throughout several processing steps and form a suitable interface for subsequent metal film growth.

TEM microtomes of the capsules show the presence of a small core in a high proportion of the capsules [Figure 23a]

When the surface from which the microtomed samples were taken was observed by SEM not only were voids visible where, it could be argued, liquid cores had evaporated away but all cores appeared to have collapsed somewhat creating depressions. One explanation of the core shrinkage is that the PEMA shell remains solvated, to some extent, by the core solvent and, when cut open, releases the remaining solvent forcing the PEMA shell to lose mass and volume.

Gas chromatography showed that ~15% of the toluene remained present in the capsules after synthesis. Given 85% loss of Toluene, it is calculated that that the core diameter should be 71% of the total capsule diameter. The minimum possible final volume is 8.1% of the original core volume used in the synthesis (in the case of this synthesis is ~0.4mL).

This volume was used along with the final measured size distribution to calculate total final sample surface area. According to these figures the final sample [3.3.1] has a surface area of $\sim 2.03 \times 10^{12} \mu\text{m}^2$ which is just over 2m^2 . However, subsequent experiments showed that $\sim 2/3$ of the capsules were being lost during wash cycles and therefore correlations made for the subsequent steps of the process should fit within the range defined by the minimum ($7.3 \times 10^9 \mu\text{m}^2\text{mL}^{-1}$) and maximum ($2.2 \times 10^{10} \mu\text{m}^2\text{mL}^{-1}$) surface areas.

The use of toluene as the capsule core allowed us to demonstrate the presence of an, albeit small, volume of encapsulated oil. Therefore these capsules provide a suitable basis for investigating the ability of the method described in the introduction to successfully grow a metal shell on the surface. As will be demonstrated in section 6.4 the amount of core oil encapsulated may not provide sufficient evidence to demonstrate the expected release characteristics. Therefore subsequent studies also looked at using less soluble oil to encapsulate.

5 Adsorption of catalytic NPs on relevant polymer substrates

5.1 Synopsis

The focus of this chapter is the adsorption of the catalytic NPs onto the polymeric microcapsule surface [Figure 27]. In the method we have developed for permanent encapsulation of small, volatile species, we use platinum nanoparticles (Pt-NPs) to catalyse the growth of a homogeneous polycrystalline gold film via electroless deposition [see sections 3.3.3 and 3.3.4 for full methodology]. As mentioned previously, the critical step in this procedure is ability of the catalytic nanoparticles to adsorb efficiently on the surface to be metal-coated. Indeed, surface adsorption homogeneity, surface density and energy of adsorption of the primary catalytic nanoparticles are important variables which affect the quality of subsequent secondary metallic film. Therefore, a good understanding of Pt-NP adsorption kinetics and some level of control over the adsorption density is paramount for the permanent encapsulation of the desired species. In addition, catalysts for electroless deposition tend to be Noble metals such as Pt, Pd and Au and are expensive; therefore, efficient use will play an important role in the cost-effectiveness of the process.

PVP stabilised Pt-NPs are particularly suitable for this work. Platinum is known to be a very good catalyst for the growth of gold via electroless deposition [64] and because catalytic activity is proportional to available surface area Pt in its nano-particulate form is very efficient per unit mass. In addition to this, PVP has an ability to physisorb to a broad range of interfaces as a result of the polarity of the polymer [75] (including polymeric, charged surfaces and some liquid/liquid interfaces). However, PVP also provides good steric hindrance when used as a stabiliser for the platinum NP cores. This allows for the creation of stable Pt-NP dispersions that are highly surface active and show good catalytic activity for the reduction of gold.

5.2 Introduction

In this chapter we use quartz crystal microbalance (QCM) and transmission electron microscopy (TEM) to explore Pt-NP adsorption density as a function of several variables, such as NP concentration in the continuous phase, temperature and adsorption time.

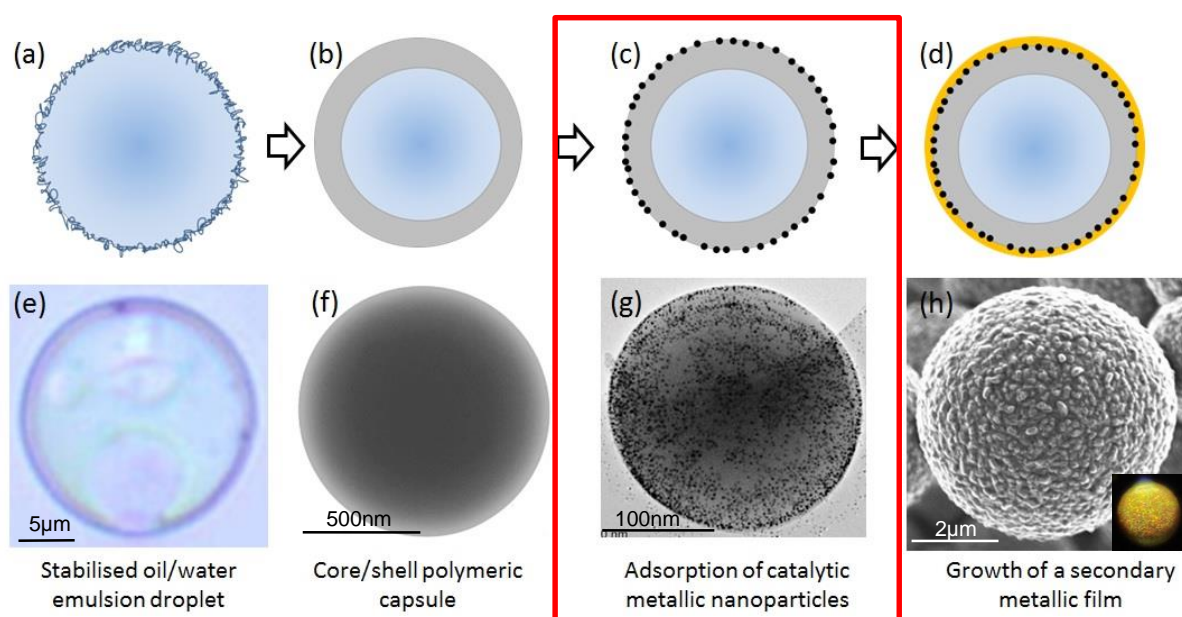


Figure 27 Schematic diagrams (a-d) and corresponding optical and electron microscopy images (e-h) of the different phases from emulsion droplet to gold coated capsule (a) emulsion droplet, (b) capsule, (c) capsule with adsorbed NPs, (d) Gold coated capsule, (e) emulsion droplet (optical microscopy), (f) capsule (TEM), (g) capsule with adsorbed NPs (TEM), (h) Gold coated capsule (SEM) (inset gold coated capsule under visible light). Red box highlights the part of the process discussed in this chapter.

Firstly, the effect of polymeric stabiliser concentration on Pt-NP synthesis and their resulting diameter is briefly explored. From this study a specific set of nanoparticles were chosen to subsequently use for adsorption onto the polymer substrates.

Nanoparticle adsorption onto 2D polymer substrates (used as a model surface for the polymer microcapsules) was then characterised to guide the choices made for experimental conditions when adsorbing nanoparticles to the 3D capsule surface. In particular, NP adsorption kinetics was explored in detail in this part of the chapter. For these experiments, polymeric thin films were spin coated onto quartz crystals [3.2.3]

and dip coated onto TEM grids [3.2.3]. These respective polymer substrates were then characterised and NP adsorption was monitored with QCM [3.2.2] and TEM [3.2.5].

This chapter is broken down into three main sections, firstly the nanoparticles were characterised using TEM. Secondly, 2D spin coated polymeric films were used as a model system to study the adsorption kinetics of the Pt-NPs using QCM and TEM. Finally, TEM was used to measure Pt-NP adsorption density directly onto 3D microcapsule interface. PEMA/Toluene core/shell capsules were used for the 3D studies [3.3.1].

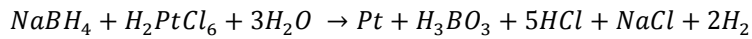
5.3 Nanoparticle characterisation

5.3.1 PVP stabiliser concentration vs resulting Pt-NP dispersion size

It is important to characterise and understand the synthesised Pt-NPs prior to using the dispersion in the adsorption experiments. This part of the work therefore was designed to understand what level of control one can have on the synthesis of the catalytic nanoparticles and to focus on one specific particle size to be used for the subsequent experiments involving the adsorption of the nanoparticles onto the polymer substrates.

In particular, the influence of polymer stabiliser concentration on the characteristics of the resulting nanoparticles was of interest.

Platinum nanoparticles were synthesised by adding known quantities of a polymeric stabiliser (Polyvinylpyrrolidone (PVP)) into a platinum salt solution (chloroplatinic acid) and adding a reducing agent (Sodiumborohydride) [3.3.2]. Platinum ions from the salt are reduced to atomic platinum. The atomic platinum then nucleates and grows into nanoparticles which are subsequently sterically stabilised by the PVP polymer chains. Equation eq. 18 shows the chemical equation for the process.



eq. 18

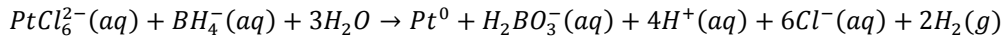


Figure 28 shows a TEM micrograph of the Pt-NPs adsorbed onto a PEMA coated TEM grid. The Pt-NPs are shown to be somewhat spherical in shape and are approximately 3nm in diameter.

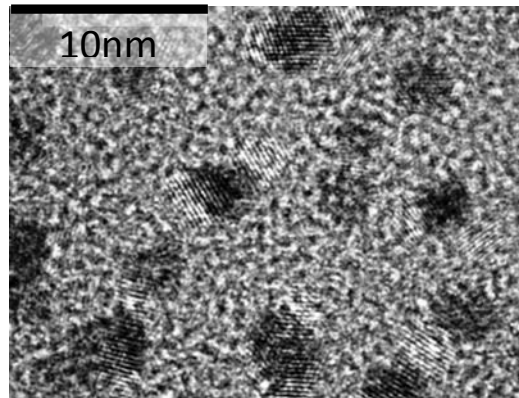


Figure 28 Shows a TEM micrograph of the Pt-NPs adsorbed onto a PEMA coated TEM grid [3.2.3].

Figure 29 shows a graph of Pt-NP size as a function of PVP concentration. Several Pt-NP dispersions were made up using different concentrations of PVP polymeric stabiliser. The Pt-NPs were then adsorbed onto dip coated TEM grids [3.2.3] and micrographs of the nanoparticles were analysed using image-J [3.4.2].

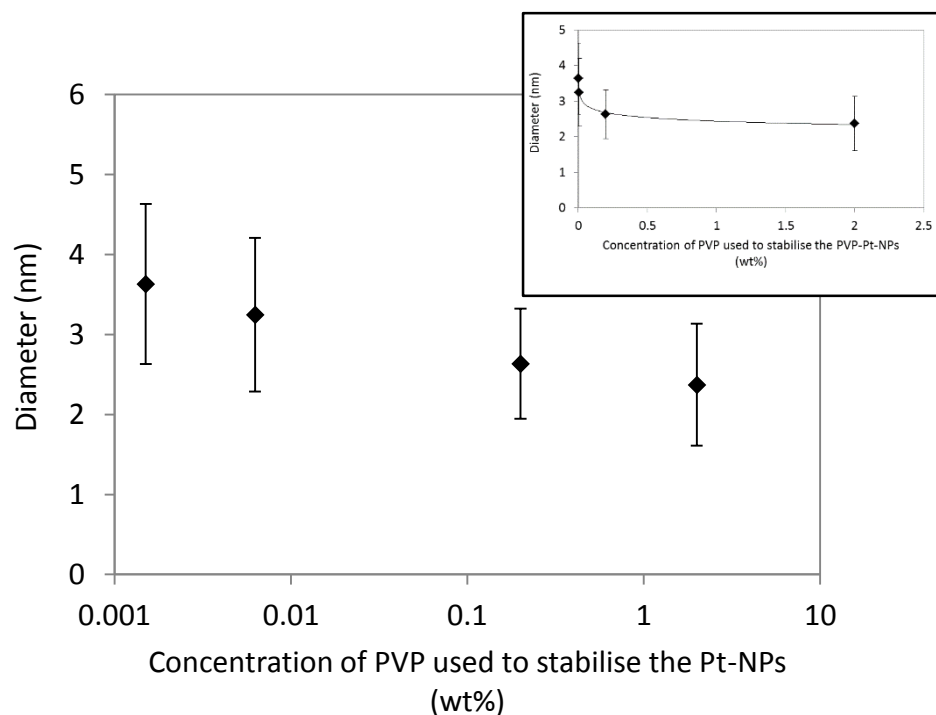


Figure 29 shows a graph of Pt-NP size as a function of PVP concentration. Several Pt-NP dispersions were made up using different concentrations of PVP polymeric stabilizer. Error bars show the standard deviation for each size distribution.

The NP core diameters appear to be inversely proportional to the log of the concentration of PVP used to stabilise the NP dispersion. The higher concentration of polymer chains appears to be able to stabilise more nucleating NPs resulting in an increased number of smaller NPs. This relationship between polymeric stabilizer concentration and resulting NP mean size is found in the literature [76]. Pt-NP dispersions remained stable and monodisperse for this entire range of different PVP stabilise concentrations. To date these dispersions have remained stable for a period of 8 months at $\sim 20^{\circ}\text{C}$ showing little or no sign of flocculation / precipitation. It should be noted that Pt-NPs synthesised using lower than 0.0015wt% of PVP stabiliser were not stable. A large proportion of the Pt precipitated out of dispersion in a matter of hours forming a dark ‘sludge’ at the bottom of the vial.

5.3.2 Ratios of free PVP to Pt-NPs

Calculations of the ratio of number of NPs to number of polymeric chains show that most examples of polymerically stabilised NP synthesis in the literature introduce a great deal more polymer chains than the number of NPs they are synthesising [64, 77, 78]. Table 1 shows several examples from the literature of resulting ratio of number of polymer chains to number of NPs found in the respective polymer stabilized NP synthesis. The number of polymer chains was calculated from the volume of polymer solution used and the molarity using Avogadro's number. The number of NPs was calculated by converting the mass of metal in the metal salt used into a volume and dividing though by the volume of a single NP of mean diameter.

Author	Stabilising Polymer	Number of polymer chains	Nanoparticle type	Diameter of NP (nm)	Number of NPs produced	Ratio Polymer chains to NPs
Jiang et al	PDDA	$1.2 \times 10^{+21}$	Platinum	2	$4.2 \times 10^{+18}$	$2.8 \times 10^{+02}$
Pastoriza-Santos	PVP	$4.6 \times 10^{+21}$	Gold	3	$3.5 \times 10^{+18}$	$1.3 \times 10^{+03}$
Pastoriza-Santos	PVP	$4.6 \times 10^{+21}$	Silver	3	$6.4 \times 10^{+15}$	$7.1 \times 10^{+05}$
Horiuchi et al	PVP	$1.5 \times 10^{+19}$	Platinum	3	$1.7 \times 10^{+16}$	$8.8 \times 10^{+02}$

Table 1 Shows several examples from the literature of resulting ratio of number of polymer chains to number of NPs found in the respective polymer stabilized NP synthesis [64, 77, 79].

If we take the lowest ratio of 280:1 from the examples in Table 1 and look at the polymer chain molecular mass (40KDa) and the resulting NP diameters, it is clear that no more than a few polymer chains could possibly fit around the NP cores. A 40KDa chain of PVP has a diameter of gyration of approximately 11.4nm. (see section 5.5.3 for calculation of R_g), therefore few chains would be able to fit around a 2nm platinum NP. These geometrical limitations apply to all of the examples in Table 1. On this basis it is highly likely that excess polymer is left over from the synthesis.

Procedures for the synthesis of polymerically stabilised nanoparticles typically do not remove the excess polymer present in the bulk prior to use and therefore any free polymer may affect the subsequent adsorption of the nanoparticles onto the polymeric capsule shells.

Understanding the ratio of free PVP polymer to Pt-NPs is therefore important. It should help us form NP dispersions which are more surface active, give insight into why dispersions becomes unstable at a given stabiliser concentration and may provide information to help us describe NP morphology and potentially NP growth mechanisms.

In order to find the approximate ratio of PVP chains to Pt-NPs in the synthesised dispersions, we need the following information; size distribution of the NPs, the mean polymeric PVP chain length and the mass of Platinum and PVP introduced in the original synthesis.

If we assume 100% conversion of platinum salt to platinum during the NP synthesis we can then use the mass of Pt introduced and the measured mean size of the metallic NP cores from TEM to calculate the number of NPs in the resulting dispersion (This procedure is described in detail in section [3.4.4]). The number of polymer chains can easily be calculated from the molar mass of polymer introduced during the NP synthesis and the mass of a single mean polymeric chain, which in our case is 40KDa. The evolution of the particle average size (as determined by TEM observations) and the number of particles in the sample can then be plotted on the same graph as a function of the number of PVP chains introduced in the synthesis [Figure 30].

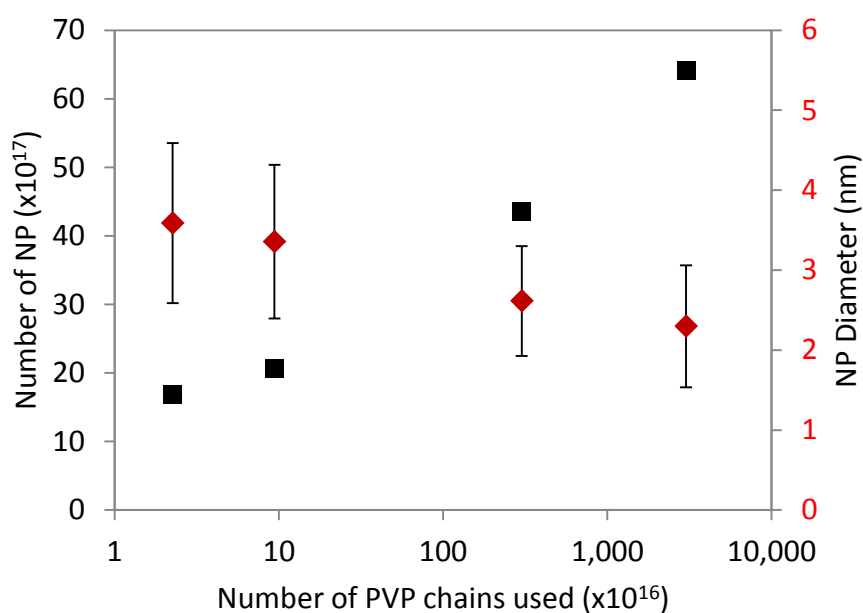


Figure 30 Graph of PVP weight % used in Pt-NP synthesis [ref] versus the number of Pt-NPs (black squares) and mean NP diameter (red diamonds).

Figure 30 shows that as the mean size of Pt-NP decreases with increasing PVP concentration the corresponding number of Pt-NP and therefore the dispersion concentration, NPs per unit volume, increases.

It is also possible to plot $\log(10)$ of concentration of PVP used in the different syntheses against $\log(10)$ of the ratio of number of NPs to number of PVP chains, which gives a straight line which passes through a concentration of $\sim 0.02\text{wt}\%$ PVP at a ratio of 1:1 [Figure 31].

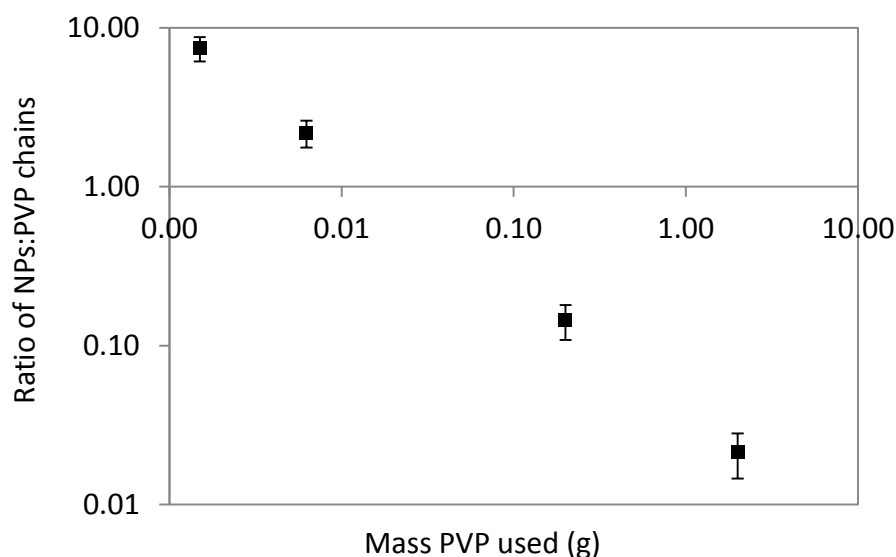


Figure 31 Graph of PVP weight % used in Pt-NP synthesis versus the ratio of number of NPs to number of PVP chains in the dispersion.

Irrespective of the confidence we have in the linearity of the log-log plot and where that line crosses the y-axis, the implication of this is that at the two lowest PVP concentrations used there are less PVP chains in the system than NP cores (assuming all of the platinum salt used in the synthesis becomes NPs).

In this synthesis, only three possible outcomes of the reaction taking place are possible. a) a proportion of the NPs are being stabilised by single PVP chains, b) sufficient Pt remains unstable and is precipitated out allowing the remaining Pt-NPs to be stabilised by 1 or more PVP chains or c) even though stoichiometrically we are using an excess of reducing agent (3.75:1 NaBH_4 :Pt salt) all the platinum is for some reason not being reduced.

5.4 Adsorption characteristics of Pt-NPs on model spin coated and dip coated polymeric films (2D)

The spin coated Poly(ethyl methacrylate) (PEMA) films [3.2.3] were first characterised by AFM to ensure smooth continuous homogeneous films were present. Known concentrations of Pt-NPs were then injected into a chamber above an oscillating quartz crystal and analysed via QCM by measuring the change in frequency of the quartz crystal as the Pt-NPs adsorbed and the crystals effective mass changed [3.2.2].

5.4.1 Characterisation of spin coated PEMA film used in QCM work

PEMA was used as the polymeric shell on the chosen model microcapsule system onto which nanoparticles were adsorbed and metal films were grown [3.3.1]. Therefore PEMA was also used as a model polymer substrate to carry out adsorption studies in the QCM on a 2-dimensional substrate.

Firstly, PEMA films were spin coated onto a glass slide [3.2.3] and their thickness was measured via AFM. Under AFM, which has a height resolution of approximately 1nm, the glass slide surface appeared to be completely flat. We wanted the spin coated PEMA film to be as flat as possible and therefore decided to make the film thin (less than 10nm) in order that its upper surface, as closely as possible, mapped the underlying flat glass. We also required the PEMA to be a complete homogeneous film.

Multiple scalpel score lines were indented through the polymer films to expose the bare surface to facilitate thickness measurements. Subsequently, thicknesses of the polymer films were measured with the AFM between the exposed underlying glass slide and the top of the polymer film.

Figure 32 shows an AFM micrograph of the 3 example sections across a PEMA/Glass slide boundary. The glass slide was revealed by scoring with a scalpel blade. The graph shows the corresponding height data for multiple sections across the boundary. Lines of best fit were generated by the least squares method from the height data for the glass

slide and the PEMA surface for each section. The height difference was measured for each section and these measurements were averaged.

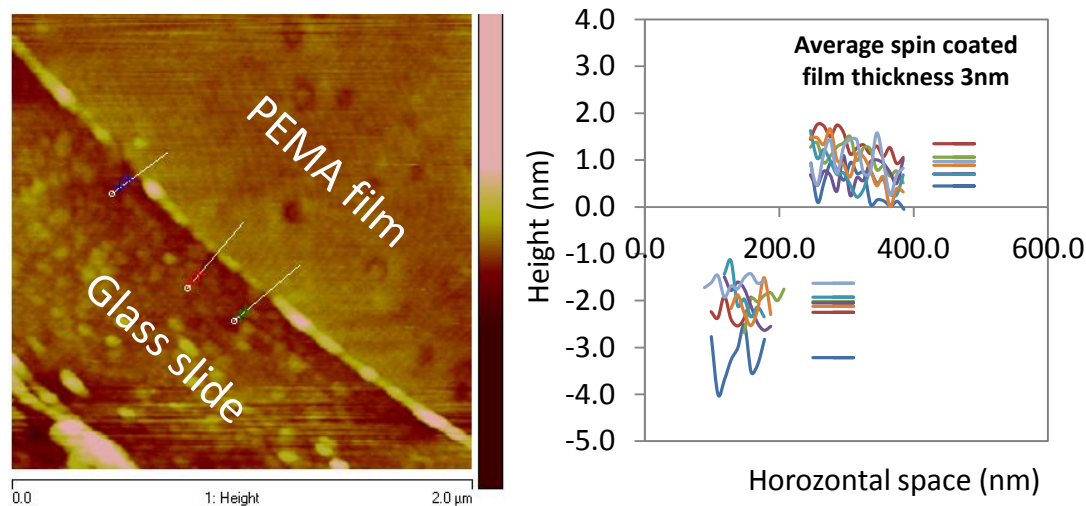


Figure 32 Showing an AFM micrograph of the 3 example sections across a PEMA/Glass slide boundary. The glass slide was revealed by scoring with a scalpel blade. The graph shows the corresponding height data for multiple sections across the boundary. Lines of best fit were generated by the least squares method from the height data for the glass slide and the PEMA surface for each section. The height difference was measured for each section and these measurements were averaged.

Films were shown to be flat with a roughness of the order of less than a nanometer and mean film thickness was measured at ~3 nm [Figure 32]. Films were also shown to be largely uniform.

5.4.2 Energy and rate of adsorption of Pt-NPs onto polymeric thin films using QCM

The same PEMA films were also spin coated onto SiO₂ QCM crystals. An assumption was made that the film was the same as the film on the glass slides described previously [5.4.1] because 1) the QCM crystal surface is designed to be very flat, 2) the QCM crystal surface is essentially made of the same material as the glass slide (SiO₂) and 3) spin coating thickness is generally not a function of surface area.

The crystals were subsequently used as a 2D model system for the 3D PEMA shell microcapsules. Pt-NPs were introduced as a dispersion into the QCM and the corresponding frequency change was recorded.

The QCM uses a quartz crystal resonator to measure mass adsorption onto the crystal interface. The crystal is placed into a chamber into which liquids can be injected and an oscillating electrical signal is sent across the crystal and tuned to set up a resonance within the crystal. The frequency change is proportional to the adsorbed mass and can be correlated to the mass change using Sauerbrey's equation:

$$\Delta f = -\frac{2f_0^2 \Delta m}{A\sqrt{\rho_q \mu_q}} \quad \text{eq. 19}$$

$$\Delta m = \frac{-A\sqrt{\rho_q \mu_q}}{2f_0^2} \Delta f \quad \text{eq. 20}$$

Where:

- f_0 – Resonant frequency (Hz)
- Δf – Frequency change (Hz)
- Δm – Mass change (g)
- A – Piezoelectrically active crystal area (Area between electrodes, cm²)
- ρ_q – Density of quartz (~2.643 g/cm³)
- μ_q – Shear modulus of quartz for AT-cut crystal (~2.947x10¹¹ g·cm⁻¹·s⁻²)

Figure 33 shows a graph of QCM frequency as a function of time. The QCM chamber was first filled with water and the frequency was allowed to settle. The Pt-NP dispersion was then introduced to the crystal surface at a concentration of 4.6x10¹⁵ L⁻¹ (100% of original dispersion concentration [3.3.2]). A rapid frequency change was observed followed by a plateauing of the signal. The frequency change is due to the NPs adsorbing on the PEMA surface and that adsorption reaching equilibrium in less than a

minute after which no further adsorption takes place (Figure 43 shows that equilibrium is reached in less than a minute for all NP concentrations used (2.8×10^{16} - $4.6 \times 10^{15} \text{L}^{-1}$ (6-100%)).

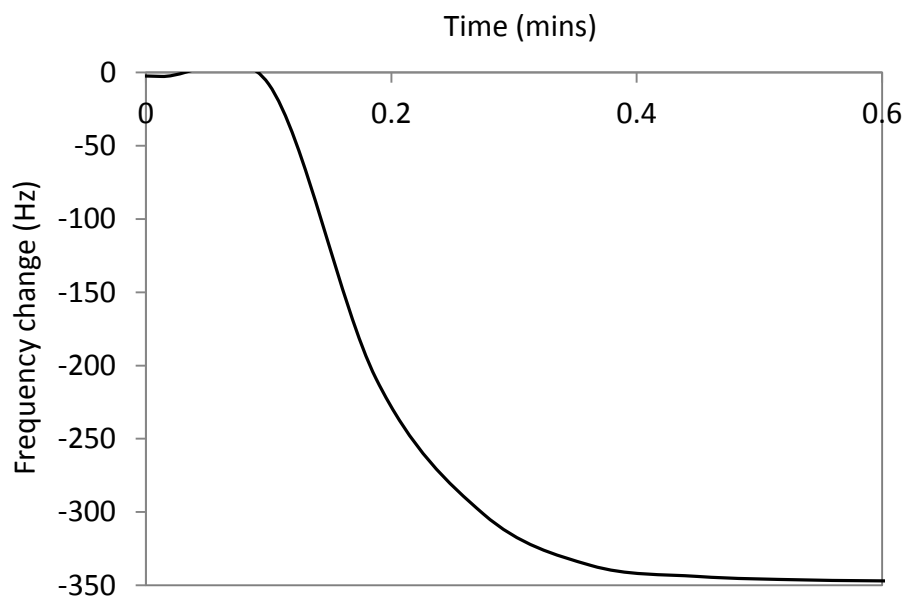


Figure 33 QCM adsorption data showing the adsorption of Pt-NPs (Pt-NPs synthesized with 0.0015wt% PVP [3.3.2])

Figure 34 shows the effect of multiple wash cycles on the system in equilibrium shown in Figure 33. Pt-NPs are adsorbed on a QCM crystal previously coated with a thick layer of PEMA. In this experiment, Pt-NPs are introduced to the QCM cell above the coated crystal at $t = 9$ minutes at which point a drop in frequency is observed as the Pt-NPs adsorb to the polymeric surface. Labels 1-6 show the effect of 6 consecutive wash cycles after the initial NP adsorption. Each wash cycle is simply the introduction of 5mL of fresh Milli-Q water [3.2.2].

After the first wash an increase in frequency and therefore a loss of mass from the crystal is observed. This is probably due to loosely adsorbed NPs being removed. However all subsequent wash cycles show a comparatively small frequency change. The temporary trough in the frequency data upon each wash is due to the pressure wave caused by the replacement of the bulk phase. This graph demonstrates that once a first wash with pure water is applied (mimicking a centrifugal washing step in the process where the Pt NPs are adsorbed on the surface of microcapsules), only minimal changes

in frequency (and thus in mass adsorbed) are recorded. Wash cycle 6, involved continual flow of water onto the crystal for several minutes, after which no change in frequency was observed demonstrating that the total adsorbed mass remains stable throughout this process.

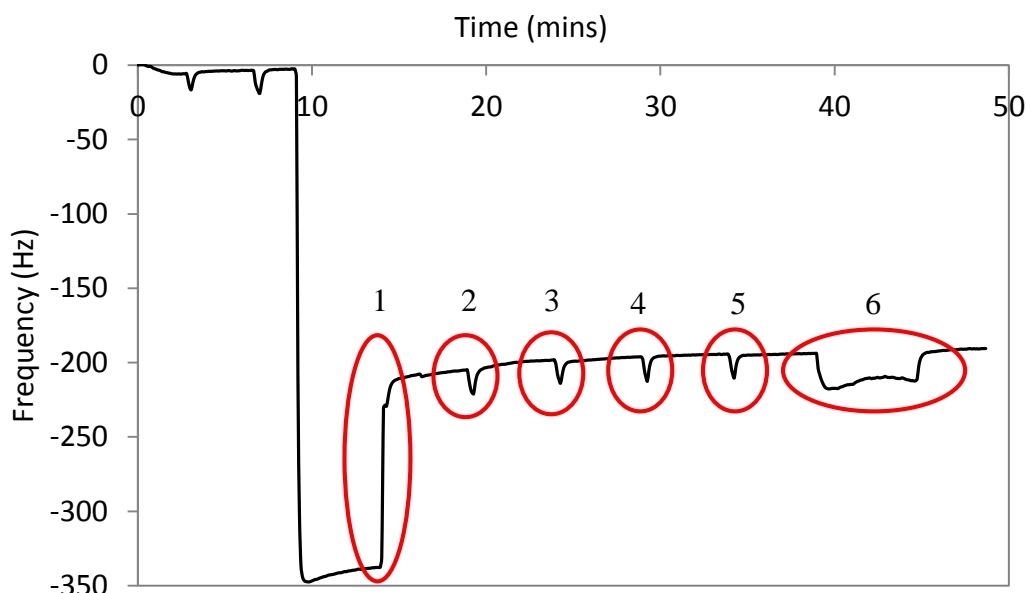


Figure 34 QCM Pt-NP adsorption data showing the effect of multiple wash cycles on the adsorbed Pt-NPs film. Pt-NPs are introduced at 9 mins. Labels 1-6 show the effect of 6 consecutive wash cycles. The temporary trough in the frequency data upon each wash is due to the pressure wave caused by the replacement of the bulk phase (Pt-NPs synthesized with 0.0015wt% PVP [3.3.2])

In order to use the Pt-NPs as a catalyst for the growth of a secondary metallic film we require high surface adsorption densities with good adsorption energies of many times kT in order that the NPs remain attached during wash cycles. Figure 34 shows that the Pt-NPs reach equilibrium in less than a minute, stay attached over long time frames and remain attached though multiple wash cycles. It is clear therefore that the Pt-NPs adsorb sufficiently strongly to sustain the washing steps applied in our procedures.

The same Pt-NPs were subsequently used in further experiments with the aim of exploring how much control towards particle adsorption densities could be achieved using this particular system.

5.4.3 Excess polymer stabiliser in the NP suspension can influence NP adsorption density onto the polymer film

There have been suggestions in the recent literature that the catalytic activity of NP adsorbed onto a solid surface can be dependent upon the concentration of the polymer stabiliser in the original NP synthesis. For example, Horuchi et al. use PVP stabilised Pt-NPs to grow 2D gold films. In this article the authors mention the use of a reduced concentration of PVP in the NP synthesis to enhance the NPs catalytic activity [64]. Their corresponding explanation is that the PVP stabiliser increasingly acts to block the catalytic surface of the Platinum. However, excess PVP left over from the synthesis may also affect the resulting surface adsorption density. The Pt-NP surface density is not measured in the paper.

The growth of a secondary metal film onto the polymer microcapsules in our developed method is likely to depend highly on both the catalytic activity of the Pt-NPs and the density of the catalytic nanoparticles on the microcapsule surface. Therefore, we closely studied the influence the polymer concentration in the NP synthesis has on the adsorbed particle density using both QCM and TEM studies.

4.5.3.1 QCM studies

Batches of NPs were synthesised using different concentrations of polymeric stabiliser from 2 to 0.0015wt% [3.3.2]. The different dispersions were introduced to spin coated PEMA polymeric films on QCM crystals and allowed to adsorb for 60 minutes before a wash cycle was run [3.2.2]. The resulting frequency change was then noted. The values quoted in the following graph are that of the equilibrium frequency change after 3 wash cycles.

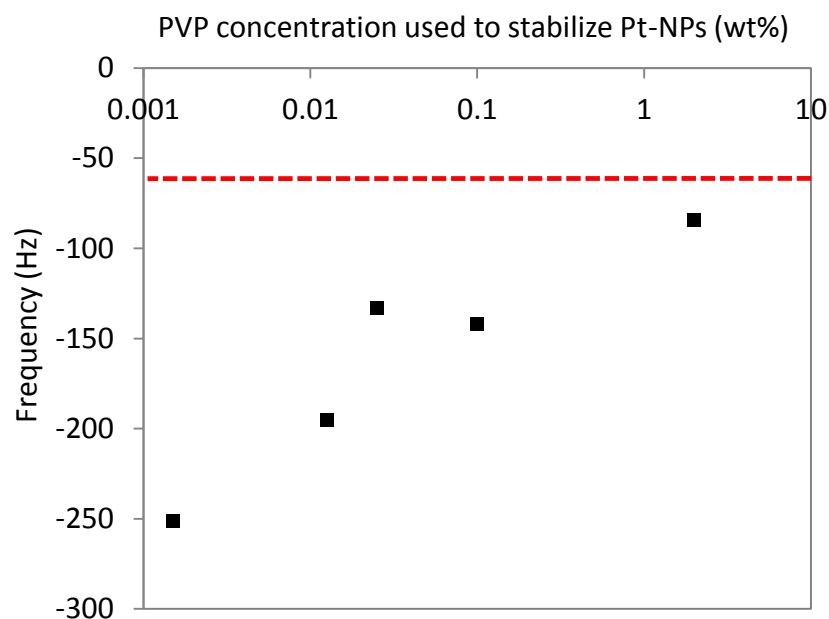


Figure 35 QCM data showing how the concentration of stabiliser used in the synthesis of Pt-NPs affects the resulting 2D adsorption density on PEMA films. The red dotted line represents the frequency change for pure PVP.

QCM data shows that the concentration of stabiliser used in the synthesis of the Pt-NP dispersions drastically affects the resulting equilibrium 2D adsorption density on the PEMA films [Figure 36]. Lower concentrations of polymeric stabiliser in the particle synthesis lead to an increased frequency change and therefore increased adsorbed particle mass. It is worth noting here that the contribution of the denser Pt to the frequency change is much higher than that of the polymer. At the highest polymer concentration of 2wt%, which is commonly used in the literature for the synthesis of such NP systems [Table 1], the adsorbed mass becomes similar to the adsorption of pure polymer (designated in Figure 35 by the red dotted line) suggesting that only few Pt NPs are therefore adsorbed under these conditions.

4.5.3.2. TEM Studies

This trend was also confirmed through a different series of experiments that studied the density of adsorbed nanoparticles onto polymer-coated carbon grids via TEM. In order to perform these experiments, TEM grids were first dip-coated in a PEMA solution

[3.2.3]. The PEMA coated TEM grids were then dried for 1 hour and dipped for 60 minutes in the different Pt-NP dispersions which were themselves synthesized at different PVP concentrations. Figure 35 shows the resulting TEM micrographs of Pt-NP adsorption densities and Figure 37 shows a graph of the Pt-NP surface density as a function of concentration of polymer used in the NP synthesis for the same samples.

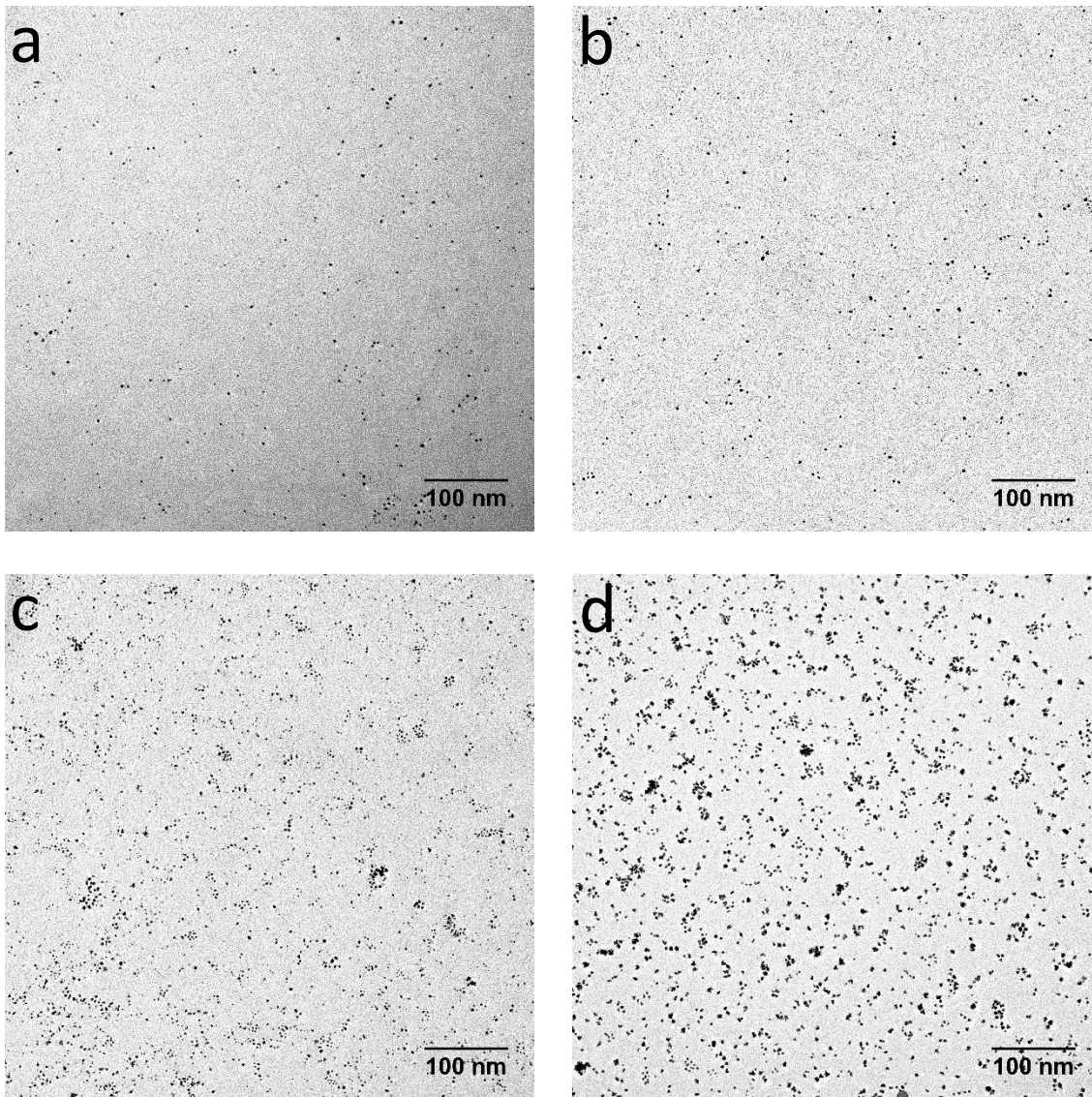


Figure 36 TEM micrographs of NPs on PEMA coated TEM grids showing the resulting NP surface density using Pt-NPs made with different concentrations of PVP stabiliser (a) $5 \times 10^{-4} \text{M}$, (b) $2 \times 10^{-5} \text{M}$, (c) $1.5 \times 10^{-6} \text{M}$, (d) $3.8 \times 10^{-7} \text{M}$ (equivalent to 2-0.0015wt% respectively). All samples were dip coated for 60 minutes.

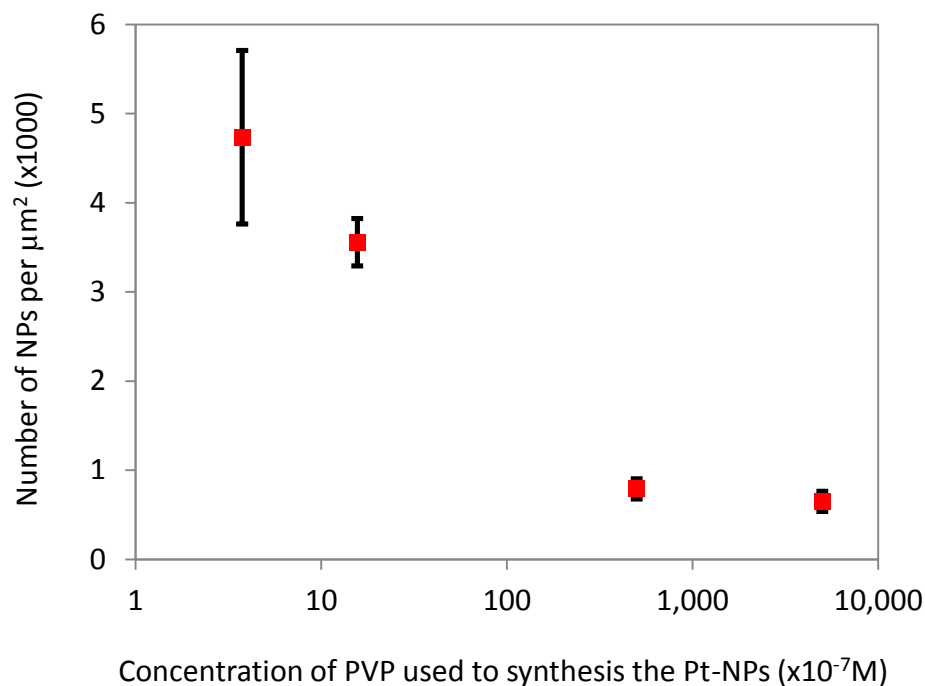


Figure 37 TEM data showing how the concentration of stabiliser used when synthesising the Pt-NP dispersions relates to the resulting 2D adsorption density on PEMA dip coated films [3.2.3].

Both the TEM micrographs [Figure 36] and the graph in Figure 37 show clearly that Pt-NPs synthesized with the higher concentrations of PVP stabiliser result in lower adsorption densities.

We know from QCM that multiple wash cycles do not remove adsorbed Pt-NPs from a PEMA interface [Figure 34]. Therefore both PVP and the Pt-NPs adsorb at the PEMA interface with energy many times that of the inherent thermal energy associated with the particle (kT). Under the conditions of these experiments and those for our capsule synthesis, both the Pt-NPs and the bare PVP chains can be considered permanently attached to the PEMA surface [Figure 35].

We know from our QCM studies that adsorption of all dispersions made with different concentrations of PVP reach plateaus in less than 1 minute. We can therefore confidently say that in these adsorption experiments 60 minutes is sufficient to saturate the film.

We also know that in all cases TEM grids were dipped into a large excess of Pt-NP dispersion Pt-NPs are therefore still available in the bulk after films had saturated (dispersions also remained dark after QCM and TEM grids are fully coated and therefore Pt-NPs are still present in the dispersion). The variation in adsorption density observed in the QCM data and TEM images is therefore not due to depletion of the Pt-NPs from the bulk.

The PVP clearly has a strong affinity for the PEMA surface however, in an aqueous environment; steric hindrance restricts adsorption of more PVP polymeric chains. The same mechanism allows them to stabilize the metallic platinum nanoparticle cores. This steric hindrance means that it is likely that once an approximate monolayer of bare PVP or Pt-NP has adsorbed at the interface, further adsorption is restricted by the PVPs loops and tails which extend into the bulk.

On the basis of the high adsorption energy of both bare PVP and Pt-NPs and their ability to restrict further adsorption of either species through steric hindrance, it seems likely that the observed change in NP adsorption density in Figure 35 Figure 36 and Figure 37 is due to a change in ratio of adsorbed bare PVP and adsorbed Pt-NP.

Figure 36a-d all show 2D polymer films saturated with a combination of bare PVP and PVP stabilized Pt-NPs, however, the hydrocarbon PVP chains do not provide much contrast between the carbon and PEMA film and are therefore largely invisible.

Figure 36a shows an interface covered with low concentration of NPs and comparatively a high concentration of free PVP chains. Oppositely, Figure 36d shows an interface covered with a higher concentration of NPs and consequently a lower concentration of free PVP chains.

It is worth noting that this relationship cannot solely be explained by a variation in adsorbed mass due to either changes in the conformation of the PVP in the bulk at different concentrations or changes in allowable relaxation times for polymers adsorbed at the interface. At low concentration the adsorbing PVP chains should have more time to relax onto the surface before adjacent adsorption sites are taken up with polymer. They are therefore able to take up more surface area per polymer chain thus partially restricting further adsorption of PVP. We would therefore expect to see a somewhat reduced frequency change at saturation for low concentration PVP. As yet unpublished QCM data from Leeson et al [80] showed that there was indeed a small frequency

change of approximately ~10Hz between high and low concentrations of PVP when the surface was saturated. This observed difference is however small compared to the change in frequency we observe (frequency change varied from ~80Hz to ~250Hz for the different concentrations [Figure 35]). Polymer relaxation times at interfaces tend to take place over time periods of at least an order of magnitude greater than the adsorption times observed in these data [31]. One might predict therefore that at much lower concentrations than were looked at in these experiments the effect of polymer relaxation may become more pronounced.

Excess PVP in the resulting NP dispersion will act to lower the Pt-NP adsorption density. It therefore seems likely that the variation in catalytic activity described by Horuchi et al [64] is largely due to excess PVP left over from the Pt-NP synthesis and not blocking of the platinum NP cores by excess PVP. In addition to this, given PVPs steric hindrance to self-adsorption, the maximum surface density of PVP on the Pt-NP core surface would be limited to an approximate monolayer and not increase significantly with increasing concentration of PVP in the continuous phase.

In summary then, if one requires a high surface density of Pt-NPs, care should be taken during the NP synthesis to limit the excess PVP in the resulting dispersion.

5.4.4 The effect of Pt-NP concentration on resulting adsorption density

QCM and TEM were also employed to measure the resulting NP adsorption as a function of Pt-NP dispersion concentration. In order to limit the excess PVP in the system, for this work, we used NPs synthesised with $3.8 \times 10^{-7} \text{M}$ (0.0015wt%) PVP stabiliser.

The hypothesis for the following experiment is as follows: if both the bare PVP and the Pt-NPs diffuse towards the polymer surface at the same rate, if one reduces the concentration of both species, the time taken to reach an adsorption equilibrium should increase but the final adsorbed mass should not vary. However, if the diffusion of one of the species is more rapid, at lower dispersion concentrations, the more rapidly diffusing species should dominate the adsorption process. Here we test this question by changing

the concentration of the Pt-NP dispersion by estimating the ratio of bare PVP to Pt-NPs adsorbed at the interface at equilibrium.

In order to test this hypothesis, we run adsorption isotherms of the NP suspension for different dilutions (with Milli-Q water) of the original Pt-NPs suspension in the QCM and record the frequency change as a function of time. Figure 38 shows the typical variations of frequency change observed as a function of time upon addition of the PVP-stabilised Pt-NPs to the PEMA polymer-coated crystal.

5.4.4.1 QCM Studies

Figure 38 shows QCM frequency change against time for different suspension concentrations of Pt-NPs and Figure 39 shows the total change in frequency at equilibrium for each of the Pt-NP adsorption isotherms.

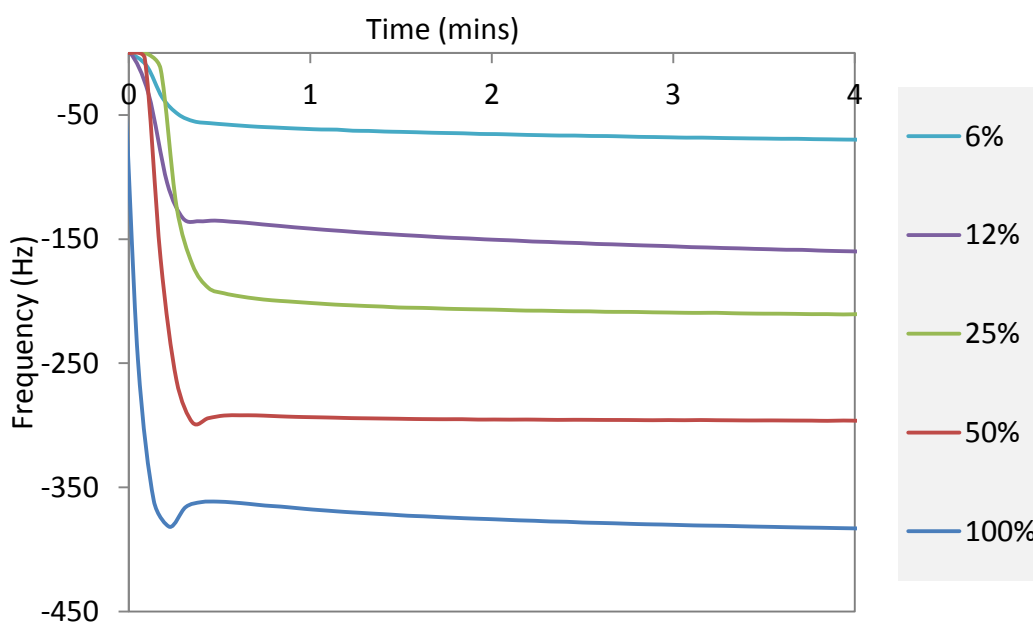


Figure 38 QCM adsorption data for different concentrations of Pt-NPs onto spin coated PEMA [3.2.3]. The key represents percentage dilution of the original dispersion. The nanoparticles used were synthesised using $3.8 \times 10^{-7} \text{M}$ PVP (0.0015wt%) [3.3.2].

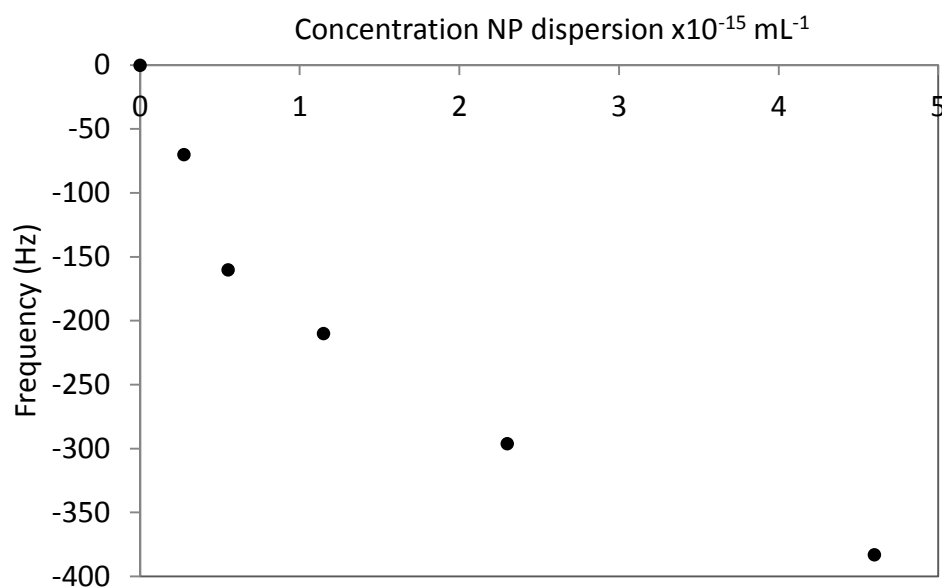


Figure 39 QCM adsorption data for different concentrations of the Pt-NPs suspension onto spin coated PEMA. The nanoparticles used were synthesised using $3.8 \times 10^{-7} \text{ M}$ PVP (0.0015wt%) [3.3.2].

The total resulting frequency change and therefore the adsorbed mass increase with increasing Pt-NP suspension concentration. From Figure 38, one can notice that the initial rate of adsorption within the first 20s increases with increasing Pt-NP suspension concentration. Additionally, both figures demonstrate that a larger frequency change is achieved when the suspension concentration is increased.

5.4.4.2 TEM Studies

Figure 40 shows the resulting TEM micrographs of PEMA substrates placed in contact with different concentrations of Pt-NP suspensions [3.2.3] and Figure 41 shows a plot of concentration versus Pt-NP adsorption density calculated from the micrographs represented in Figure 40. The concentrations used are the same as the those used in the QCM work. The TEM micrographs clearly show that the NPs adsorption density at equilibrium is increasing with increasing Pt-NP suspension concentration and the Figure 41 plot shows that the surface density increases with Pt-NP suspension concentration but reaches a plateau. The inset in Figure 41 shows the equivalent adsorption data from the QCM. Both the QCM and the TEM data show increasing Pt-NP adsorption density with Pt-NP suspension concentration.

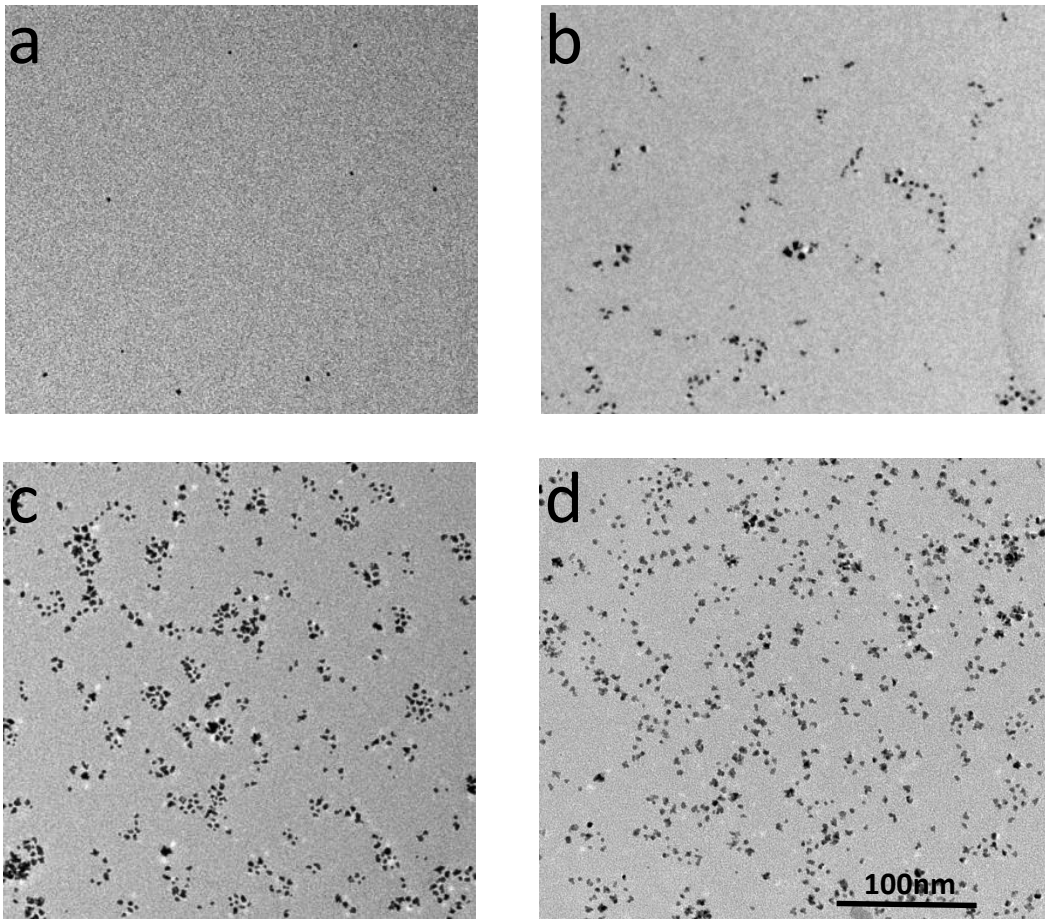


Figure 40 – TEM micrographs of Pt-NP adsorption densities after 60 minutes for different concentrations of the original Pt-NP dispersion at a concentration of $4.6 \times 10^{15} \text{ L}^{-1}$ (a-d) 1%, 10%, 50%, 100% of the original concentration respectively (PVP concentration used in synthesis $3.8 \times 10^{-7} \text{ M}$ PVP (0.0015 wt%) [3.3.2]).

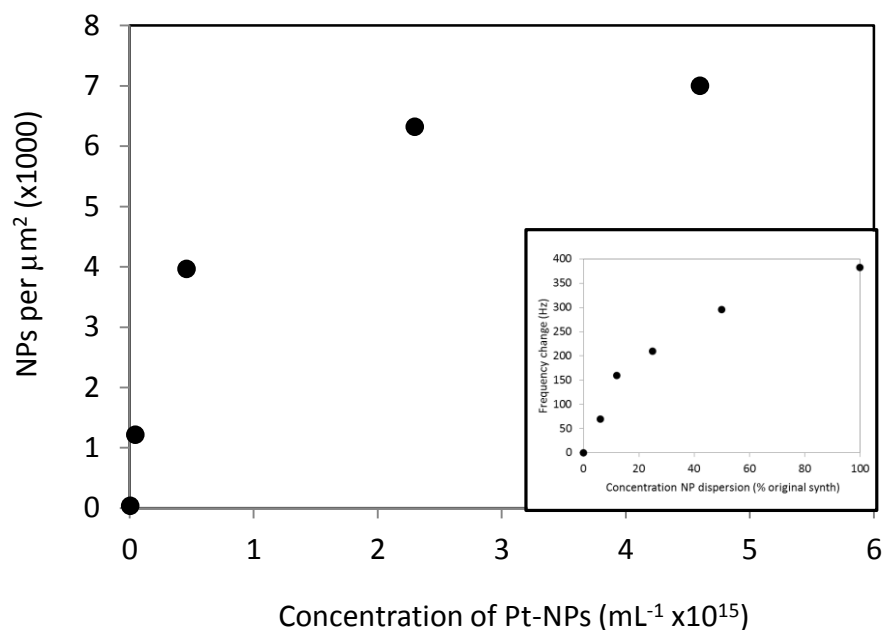


Figure 41 Pt-NP surface density vs Pt-NP suspension concentration for samples shown in shown in Figure 40 (Dip coated TEM grids). The inset shows the equivalent QCM data (same data as shown in Figure 38 but Y-axis shows the additive inverse frequency change).

A likely explanation for the observed data is that the free excess PVP chains in the NP dispersion are not only blocking potential NP adsorption sites but, even though the ratio of Pt-NPs to PVP remains constant in the bulk, as the suspension concentration is lowered the adsorption rate of the PVP increases faster than that of the Pt-NP adsorption rate. Therefore the lower the dispersion concentration the higher the resulting ratio of adsorbed PVP to Pt-NPs at equilibrium.

The diffusion rates of the two species are different; the Pt-NPs are likely to be somewhat larger than the free polymer chains and therefore diffuse more slowly. The Stokes-Einstein equation shows that, for hard spherical particles, the diffusion constant is inversely proportional to the radius of the diffusing particle and therefore through Stokes-Einstein-Sutherland equation is inversely proportional to the diffusion rate [eq. 21].

Stokes–Einstein–Sutherland equation:

$$D = \frac{k_B T}{6\pi\eta r} \quad \text{eq. 21}$$

Where:

- D Diffusion coefficient (m^2s^{-1})
- k_B Boltzman constant $1.38 \times 10^{-23} \text{ m}^2\text{kg s}^{-2}\text{K}^{-1}$ ($1.38 \times 10^{-20} \text{ m}^2\text{g s}^{-2}\text{K}^{-1}$)
- η Dynamic viscosity $1 \times 10^{-3} \text{ Kg s}^{-1}\text{m}^{-1}$ ($1.0 \text{g s}^{-1}\text{m}^{-1}$)
- r Radius of the spherical particle (m)
- T Temperature (K)

This means that as both species become more dilute, the average mean free path to reach the interface for each species increases. It can be shown that the mean square displacement from a particular starting position of a particle is proportional to the diffusion coefficient multiplied by time [81]. This linear dependency is shown in equation eq. 28. Therefore if the diffusion coefficient of the PVP is larger than the Pt-NPs than the free polymer chains will increasingly ‘win the race’ to the interface as the concentration of the suspension is decreased.

$$x = \sqrt{q_i D t} \quad \text{eq. 22}$$

Where:

- x displacement
- q_i Numerical constant which depends on dimensionality: $q_i = 2, 4, \text{ or } 6$, for 1, 2, or 3 dimensional diffusion.
- D Diffusion coefficient (usual units are $\text{cm}^2 \text{s}^{-1}$).
- t Time.

It is worth noting that the Stokes–Einstein–Sutherland equation is designed to cope with hard spheres and that the two species in question here are a polymer and a nanoparticle made up of a hard sphere and polymer.

Georges et al use the following law [eq. 27] to calculate the diffusion coefficients for polymeric chains in water [82].

$$D = 1.25(10^{-4})M^{0.55} \quad \text{eq. 23}$$

Where:

M Molecular weight

D Diffusion coefficient

Figure 42 uses the two different equations above (eq. 21 and eq. 23) to plot diffusion coefficient as a function of size for a hard spherical particles and PVP polymeric chains diameter of gyration respectively. The diameter of gyration for the PVP polymer was calculated from the molecular weight using eq. 30

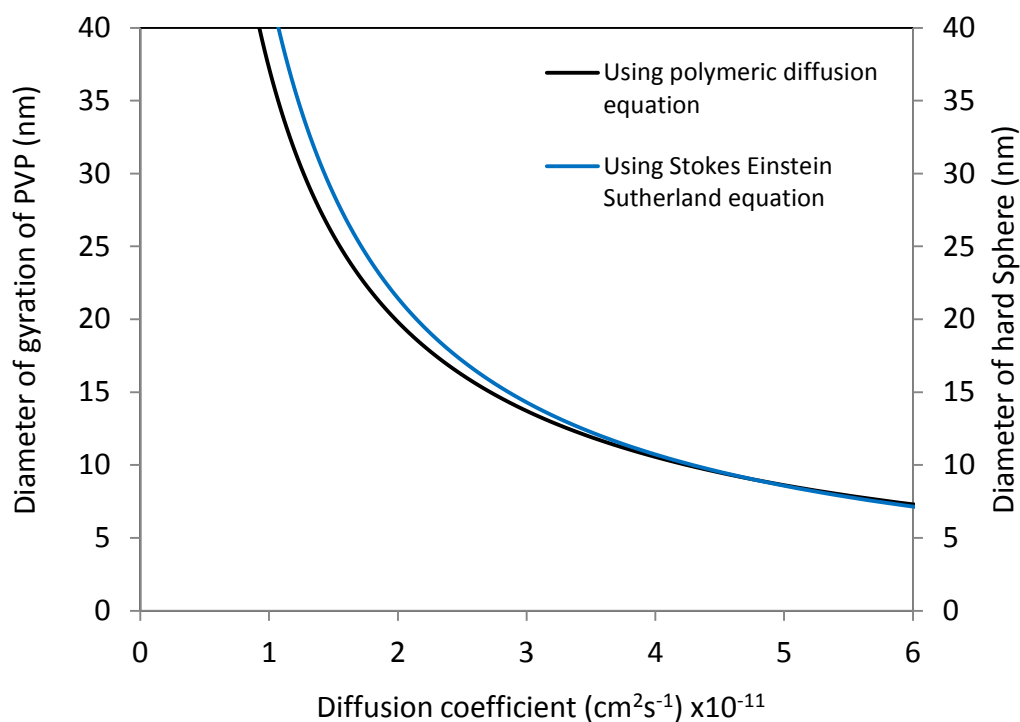


Figure 42 Graph showing spherical hard particle diameter and Polymeric diameter of gyration as a function of diffusion coefficient. Equations eq. 21 and eq. 23 were used to calculate diffusion coefficient for hard spheres and polymeric chains respectively. PVP molecular masses were converted to radius of gyration using equation eq. 30.

Figure 42 shows that there is good agreement between the two equations. At larger diameters the diffusion coefficient for the polymer appears to drop below the diffusion coefficient for the equivalent sized hard particle. However, the equation used to convert the PVP molecular weight to radius of gyration [eq. 30] will have error associated with it because the equation uses a very simple polymer model [see section 5.5.3 for more details].

Both the free polymer and the Pt-NPs consist largely of polymer by volume and certainly have polymer on the exterior. It can be argued therefore that the Pt-NPs behave more like larger polymer entities rather than hard particles. On this basis to obtain approximate values for the diffusion coefficient of both species eq. 23 was used. To obtain a minimum value for diffusion coefficient of the Pt-NP the radius of gyration of a single 40DKa PVP chain was calculated using eq. 30 and this radius was increased by the mean radius of the platinum cores.

Therefore the PVP we are using has molecular weight of 40000 g mol^{-1} . Using eq. 23 we calculate the polymer has a diffusion coefficient of $3.68 \times 10^{-7} \text{ cm}^2 \text{ s}^{-1}$ and from equation eq. 30 a radius of gyration of 5.69 nm. Increasing the radius by half the mean diameter of the Pt cores (1.5nm [Figure 29]), which equates to a diffusion coefficient of $2.84 \times 10^{-7} \text{ cm}^2 \text{ s}^{-1}$ [Figure 42].

This differential between diffusion rates of excess polymeric stabiliser and NPs and its effect on subsequent NP adsorption density is likely to be an inherent issue when attempting to adsorb nanoparticle suspensions which are stabilised by polymeric moieties which are themselves surface active. Typically authors in the literature use a large excess of polymer as stabiliser [Table 1]. Little or no work has been done in reducing this excess without compromising stability. It may be true that the Pt-NP dispersions made in this study using very low concentrations of PVP stabiliser will remain stable for shorter time frames than those synthesised at more typical concentrations (dispersions synthesised using $3.8 \times 10^{-7} \text{ M}$ PVP (0.0015wt%) appear to remain stable for at least a period of 6months). However, our efforts are to keep the particles at very low polymer concentrations stable for long enough for us to run the adsorption process and therefore potential long term instability is not an issue.

It is worth noting that the removal of this excess polymer from the synthesis is not trivial. By definition, the sterically stabilised NPs have the same surface chemistry as the free polymer therefore opportunities to chemically remove the excess polymer are limited. In addition, the small size of both species makes it very hard sediment one species over the other via centrifuge and filtration methods are limited by minimum available pore size and, in most cases, the surface active nature of the polymer.

5.4.5 Rate of adsorption using QCM

If we take the QCM adsorption data in Figure 38 showing adsorption as a function of Pt-NP suspension concentration and zoom into the initial adsorption isotherms we can measure the adsorption rate by measuring the maximum gradient of each isotherm in Figure 43. Figure 44 shows the plot of the rate of adsorption as a function of Pt-NP suspension concentration.

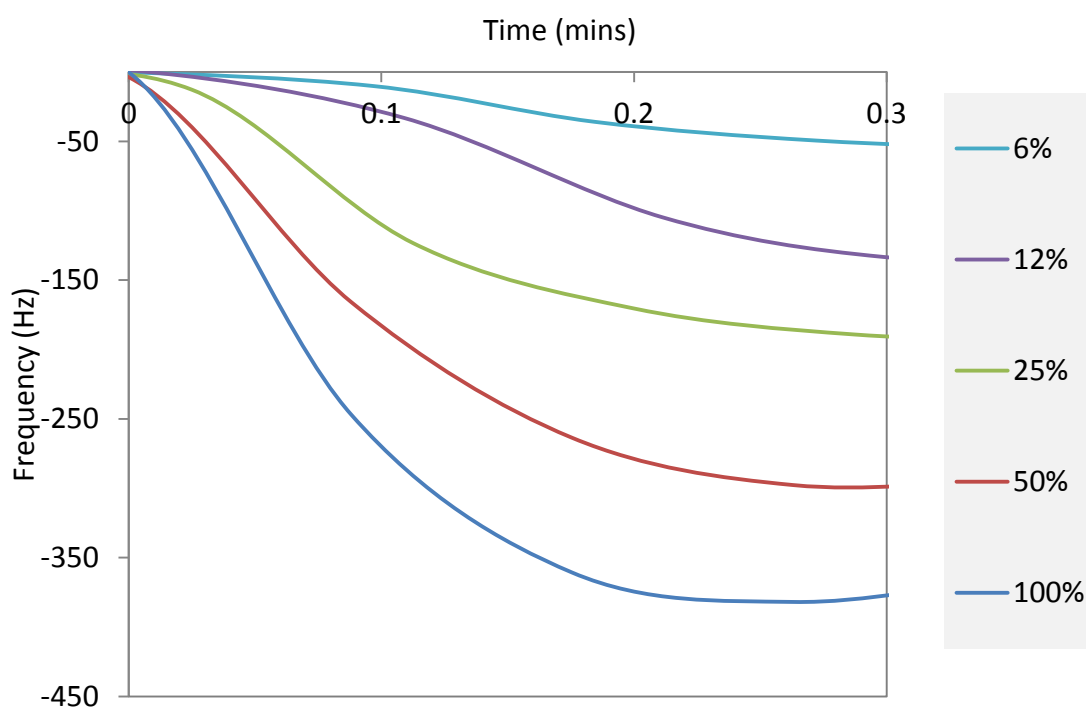


Figure 43 QCM data showing the adsorption rates for different concentrations of the original Pt-NP dispersion at a concentration of $4.6 \times 10^{15} \text{ mL}^{-1}$ (PVP concentration used in Pt-NP synthesis $3.8 \times 10^{-7} \text{ M}$ PVP (0.0015wt%) [3.3.2]).

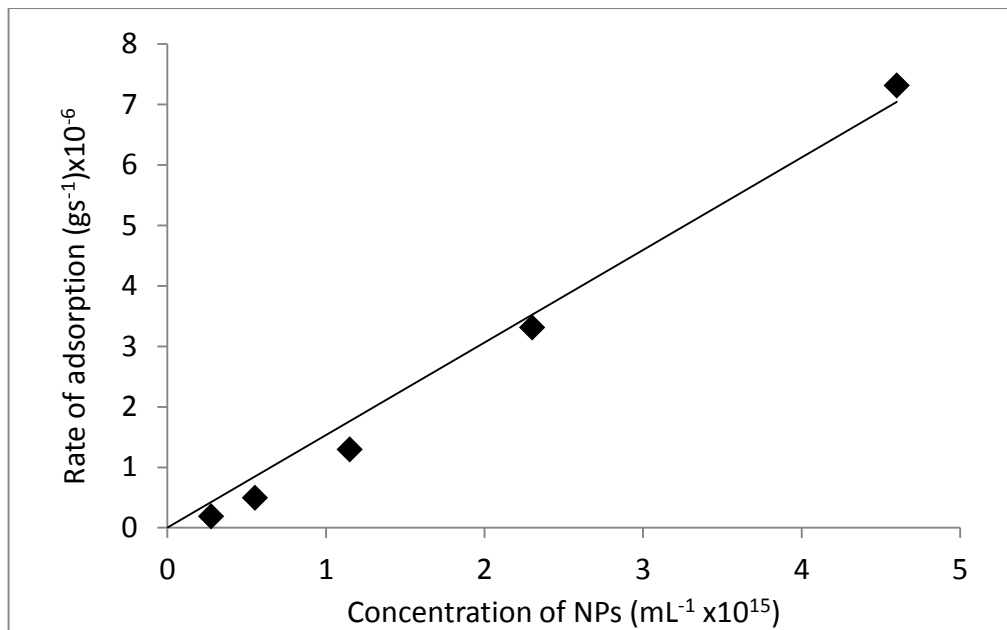


Figure 44 Graph showing rate of adsorption vs concentration of Pt-NP suspension concentration. Adsorption rates were calculated by taking the maximum gradient of the isotherms in Figure 43

We see from Figure 45 that the peak adsorption rate is proportional to the concentration of the Pt-NP suspension in the bulk. We know that the line on this graph must go through the origin. Although the effect is small and could potentially be argued to be within the error of the experiment, we see that at low concentrations the rate of adsorption is slightly less than expected. This is exactly what we should expect to see given the free PVPs ability to diffuse faster than the Pt-NPs. It should be remembered that we are measuring the ‘rate of adsorption’ by measuring the adsorbed mass change per second due to both species in the suspension. Therefore because adsorbed mass per unit area is significantly less for PVP than Pt-NP at low concentrations our measured ‘rate of adsorption’ dips.

5.4.6 Determination of the Langmuir adsorption equilibrium constant and adsorption energy

In this section of the work, an attempt was made to use the QCM adsorption isotherms over a range of Pt-NP dispersion concentrations to analyse both the kinetic adsorption data and the equilibrium adsorption values using standard Langmuir adsorption theories. These data are used to determine a consistent value of the Langmuir adsorption equilibrium constant for the nanoparticle – substrate interaction (Pt-NP suspension – PEMA interface) [40].

The adsorption kinetics of the Pt-NPs are quantified by fitting the QCM adsorption data to the Langmuir isotherm equation [eq. 24]. The Sauerbrey equation [eq. 3] [section 3.2.2] shows that Δf is proportional to the mass adsorbed and therefore to the surface coverage. Therefore, because the units associated with the surface coverage can be said to cancel, we can use Δf at equilibrium and Δf at time (t) for surface coverage $\Gamma(\infty)$ and $\Gamma(t)$ respectively in the following equation [eq. 24]. We are therefore able to estimate values of the rate constant k_{obs} by fitting the data to the Langmuir isotherms collected in the QCM. Figure 45 shows an ideal Langmuir isotherm.

$$\Gamma(t) = \Gamma(\infty)[1 - \exp(-k_{obs}t)] \quad \text{eq. 24}$$

$$k_{obs} = k_a C + k_d \quad \text{eq. 25}$$

$$\Gamma(\infty) = C / (C + k_d / k_a) \quad \text{eq. 26}$$

Where:

- Γ NP surface coverage
- C NP concentration
- k_a Adsorption rate constant
- k_d Desorption rate constant
- t Time

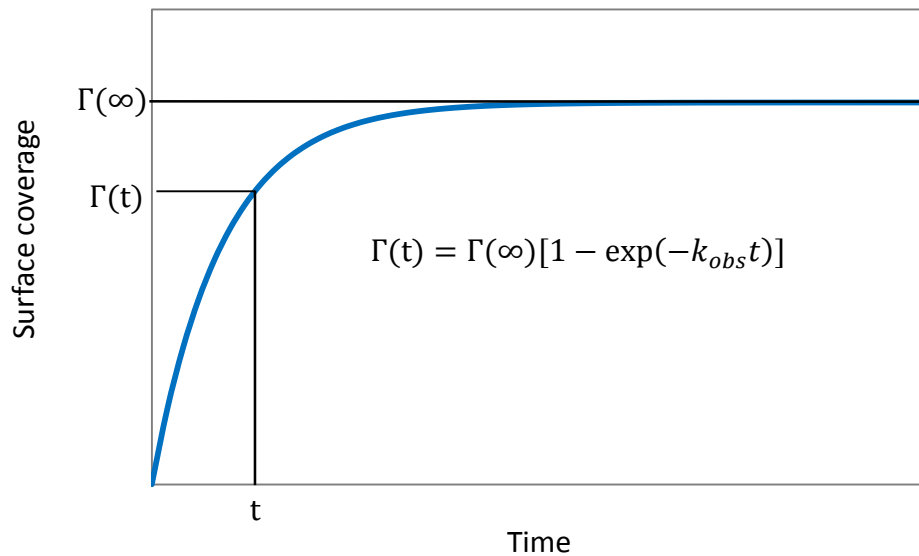


Figure 45 Shows the shape of curve expected for a typical Langmuir isotherm

Plotting k_{obs} as a function of C , we see from equation eq. 25 that the gradient and intercept of the graph correspond to the adsorption (k_a) and desorption (k_d) constants respectively. The adsorption constant (k_a) is a measure of the rate of depletion of the surface active per unit volume of the bulk and the desorption constant (k_d) is simply a rate of desorption of the surface active.

The Langmuir equilibrium constant (K_L) is defined as (k_a/k_d) and is a measure of the depletion per unit volume from the bulk of the surface active. The free energy of NP adsorption can then be found using equation eq. 27 [83].

$$\Delta G_{ads} = -RT \ln K_L \quad \text{eq. 27}$$

Where:

R Gas Constant ($8.314 \text{ J K}^{-1} \text{ mol}^{-1}$)

T Temperature (293K)

Avogadro's number $6.02 \times 10^{23} \text{ mol}^{-1}$ and Boltzmann constant (k) $1.38 \times 10^{-23} \text{ J K}^{-1}$

Pt-NP concentrations were calculated in moles per litre using the mean NP diameters measured from TEM observations [3.4.4]. First the number of NPs in a litre was calculated (N) and then the ratio of this to Avogadro's number (N_A) was used to convert to a moles per litre. 100% dispersion concentration was found to have a nanoparticle concentration of $7.7 \mu\text{mol/L}$. Other papers have used the Beer Lamberts law to calculate NP dispersion concentrations [40]. It seems likely that direct measurement of size distributions via TEM should yield more accurate concentration measurements. Concentration of NPs is regularly expressed as a molarity in the literature. As a colloid scientist it would seem more appropriate to express concentration as number per volume, however, as one moves from molecular to supramolecular to nanoparticulate, where does one draw the line in terms of what can and can't be expressed as a molarity. The theories used here have been developed using these terminologies and therefore we will be using the same in order to compare with the literature data.

Figure 46 shows the Langmuir isotherms for the different Pt-NP concentrations. The dotted lines represent the respective fits for each isotherm from equation eq. 24.

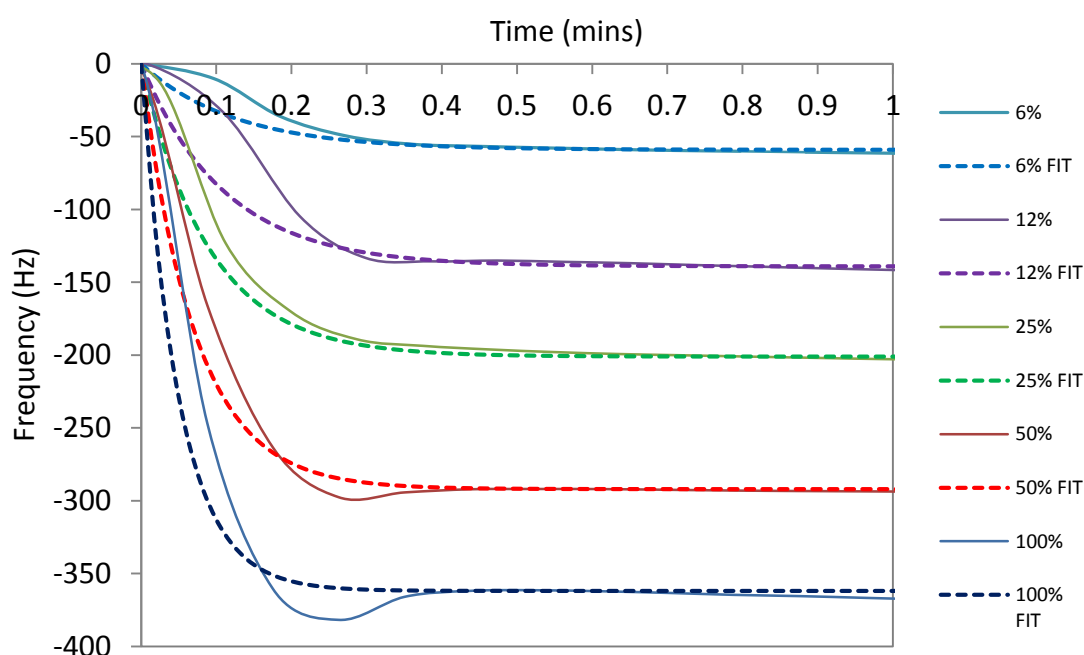


Figure 46 QCM data showing the adsorption isotherms for different concentrations of Pt-NPs (100% concentration equates to 4.6×10^{15} Pt-NPs mL^{-1} . The nanoparticles used were synthesised using $3.8 \times 10^{-7} \text{M}$ PVP (0.0015wt%) [3.3.2].

We can see that the Δf values increase with increasing Pt-NP suspension concentration and the rate of frequency change is greater at higher concentrations. All isotherms plateau in less than 0.5 minutes.

The overshoot in frequency change appears to be due to the pressure wave caused by the inflow of liquid into the QCM cell and onto the crystal. Figure 47 shows the same QCM adsorption data as shown in Figure 46 but with only the low (red squares) and high (blue triangles) concentrations isotherms. The black diamonds show a typical pressure wave for pure water. The dotted lines show what the adsorption isotherms when corrected for the influence of the ‘pressure wave’ would look like.

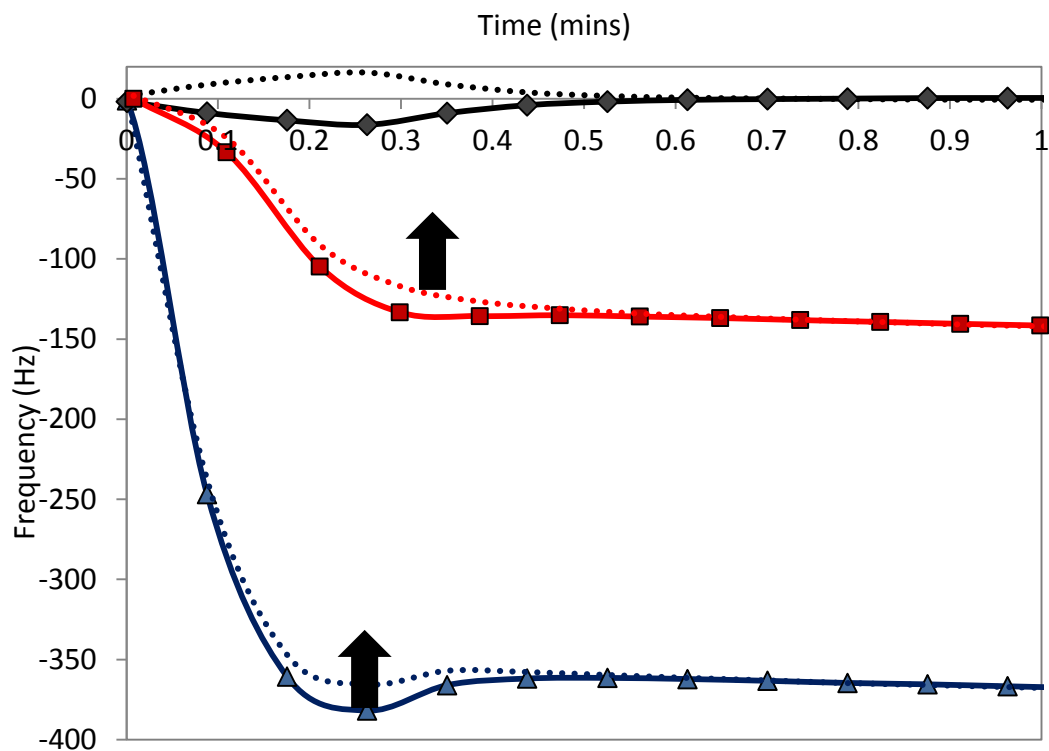


Figure 47 QCM adsorption data for low (red squares) and high (blue triangles) concentrations of Pt-NP suspensions. The black diamonds show a typical pressure wave for pure water. The dotted lines show what the adsorption isotherms when corrected for the influence of the ‘pressure wave’

The dispersion in-flow time is approximately 15 seconds with the valve opening and shutting taking a fraction of a second. Running the QCM with pure water we see a change in frequency of approximately 15 Hz which last 25-30 seconds (Figure 47 black diamonds). The overshoot appears to be somewhat proportional to the dispersion concentration but, on closer inspection, we see that at lower concentrations, because the

adsorption happens more slowly, the contribution to the frequency shift from the pressure wave is buried in the slope. Therefore by the time the adsorption reaches equilibrium the contribution from the pressure wave is over, creating no overshoot.

The size of the pressure wave depends on several variables such as height of pipe inlet, depth of reservoir attached to the pipe inlet and rate at which the valve is opened. In hindsight, it would have been better to correct the data in Figure 46 prior to fitting the lines but this approach was not considered at the time of the experiment and therefore the associated variables were not tightly controlled and average pressure waves plots for pure water were not taken. Although, in hindsight, this is an oversight the overshoot has no effect on the resulting frequency change at equilibrium and has very little effect on the gradient of the adsorption curve and therefore has very little affect on the analysis we undertaken here.

Figure 48 shows the plot of k_{obs} (obtained from fitting the langmuir isotherm) as a function of concentration (C). The line of best fit was generate using the 'least squares' method and provides a gradient and intercept.

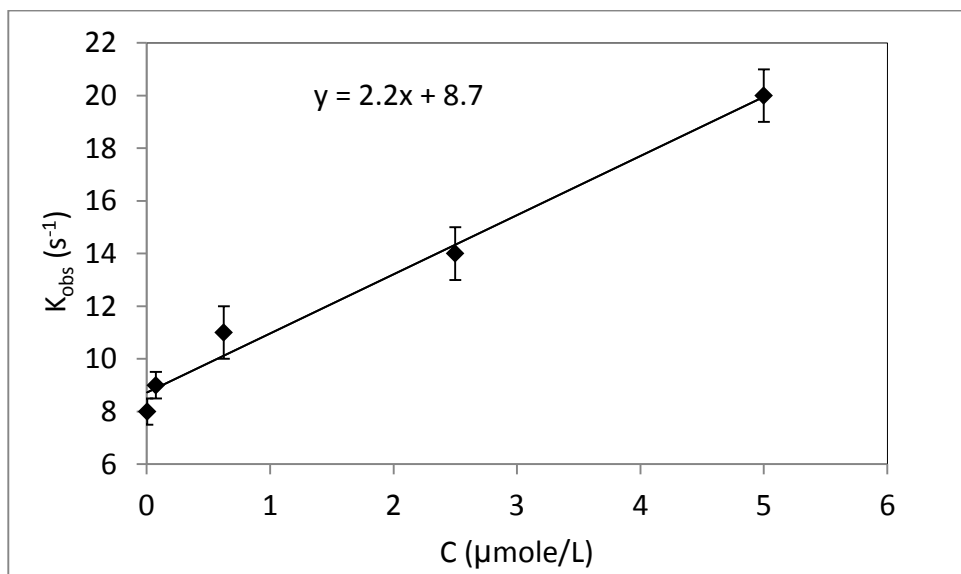


Figure 48 shows a plot of the rate constant as a function of dispersion concentration. The line of best fit is calculated by the 'least squares' method.

The gradient corresponds to the adsorption constant (k_a) and works out at $2.35(\mu\text{mol/L})^{-1}\text{s}^{-1}$ and intercept of the graph corresponds to the desorption constant (k_d) and works out at 8.71 s^{-1} . The Langmuir equilibrium K_L constant (k_a/k_d) is then $0.26\mu\text{mol/L}$. The free energy of nanoparticle adsorption (ΔG_{ads}) therefore works out to be $3.30 \times 10^{-3} \text{ J}/\mu\text{mol}$ [Table 2].

Adsorption rate constant	Desorption rate constant	Langmuir equilibrium constant	Free energy of nanoparticle adsorption	Adsorption energy of a single NP	Background thermal energy	Adsorption energy as a kT multiple
$k_a((\mu\text{mol/L})^{-1}\text{s}^{-1})$	$k_d(\text{s}^{-1})$	$K_L((\mu\text{mol/L})^{-1})$	$\Delta G_{ads}(\text{J}/\mu\text{mol})$	$\Delta G_{ads}(\text{J})$	$kT(\text{J})$	-
2.25	8.71	0.26	3.30×10^{-3}	5.49×10^{-21}	4.04×10^{-21}	1.35

Table 2 shows the numerical results and their associated units for the adsorption and desorption rate constants, the Langmuir equilibrium contact, the free energy of nanoparticle adsorption, the adsorption energy of a single NP, the background thermal energy and finally the ratio of NP adsorption energy to the background thermal energy.

If the free energy of adsorption is converted from J/mol to J, by dividing through by Avogadro's number, one gets a figure of $5.49 \times 10^{-21} \text{ J}$ for the adsorption energy of a single nanoparticle. If this figure is compared to the background thermal energy, Boltzmann constant (k) multiplied by temperature (T), according to these calculations, the energy of adsorption of a nanoparticle is $1.35kT$.

The QCM data shows that over several wash cycles there is no frequency change [Figure 34] and Pt-NP coated capsules are able to undergo 3 wash cycles without a significant reduction in NP surface density [Figure 49]. The adsorption energy of the Pt-NPs must be, at least, several times the background thermal energy. We are therefore forced to conclude that our calculated figure of $1.35kT$ is too low.

Why is the calculated figure for surface adsorption energy so low for this system? Increased mass adsorption at equilibrium as a function of concentrations is typical for a pure system of a surface active molecule/particle which has an adsorption energy which is close to kT . For example, below its critical micelle concentration (CMC), CTAB

exhibits this behaviour [84]. This occurs because the rate of adsorption is a function of concentration and the rate of desorption of individual particles for most concentrations is not. The adsorbed mass at equilibrium is a function of concentration because at higher concentrations for the desorption rate to be equivalent to the adsorption rate there needs to be more mass on the surface to desorb.

The problem with applying this analysis to our data is the assumption that the adsorption isotherms are for a pure Pt-NP dispersion. A pure Pt-NP dispersion with high adsorption energy should reach approximately the same adsorption density at equilibrium for all concentrations of NPs, albeit over longer time frames for lower concentrations. The reason we get this shape with our data is that the system is not pure. We have excess PVP left over from the Pt-NP synthesis which is preferentially adsorbing at the interface at lower concentrations.

In summary, successful Langmuir adsorption studies are regularly made for molecular species which reach adsorption/desorption equilibria at different concentrations. Although the same shaped adsorption isotherms can be found for some particle systems [40, 72, 85]. Care should be taken to discriminate between true equilibrium patterns of adsorption and non-equilibrium patterns. The concentration dependence of adsorbed mass in these systems is likely due to the presence of a second surface active species which has a higher diffusion coefficient.

5.5 Analysis of Pt-NP adsorption density on 3D capsule interface

5.5.1 NP surface density vs NP concentration using TEM (3D)

In the previous sections QCM and TEM were used to look at Pt-NP surface adsorption behaviour on 2D model systems. In this section TEM is employed to directly measure the surface adsorption density of the Pt-NPs onto the polymer shell microcapsule surface.

Similarly to the sections above, where NP surface density was measured on the model 2D polymer surfaces as a function of particle concentration in the bulk, the same adsorption experiments were carried out on the surface of pre-prepared polymer-shell microcapsules. These microcapsules consisted of a toluene core and a PEMA shell and are described in more detail in section 3.3.1. Although the same polymer is used in both the 2D and 3D work the two surfaces are not exactly the same due to the presence of the CTAB stabiliser on the surface of the 3D system. Comparisons between experimentally measured 2D and 3D adsorption densities are made [Figure 53].

Measuring the surface density directly via this method is challenging for the following reasons. Firstly, only capsules smaller than ~500 nm diameter are sufficiently transparent to generate enough contrast between the Pt-NPs and the capsule. Capsules with low Pt-NP surface coverage were also more susceptible to beam damage and were found to change shape under the beam altering the measurements of surface density. In addition, the variation in transmitted light intensity due to the change of thickness across the spherical polymeric capsule [Figure 49] and the overlaid image of both the top and bottom interface of the capsules meant that automated counting software such as image-J proved to be not useful.

As a result, the TEM observations made in these experiments were focused mostly on the suitable small capsules, and the images were subsequently analysed manually. The calculations of NP surface density were then corrected for curvature and transparency.

5.5.1.1 Corrections applied for curvature of the capsules

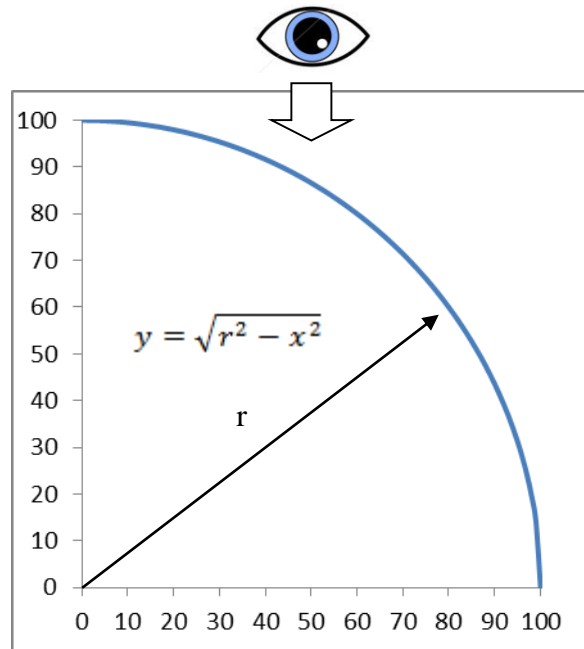


Figure 49 TEM micrograph of a NP coated PEMA capsule highlighting the NP variation across the capsule centre.

When a sphere is observed as an apparent 2D flat surface [Figure 49 TEM micrograph of a NP coated PEMA capsule highlighting the NP variation across the capsule centre.], its actual curvature in the 3 dimensions results in an increasing amount of surface area being projected onto the 2D support from the middle of the sphere to its edges. Therefore, when observing a 2D projection of our microcapsules in the TEM more surface area of the original microcapsule is represented at the edge of the projected circle than in the middle. This means that the apparent NP surface density increases towards the edge of the projected circle and any direct NP surface density needs to be corrected to account for this. As long as adsorption densities are measured for ‘small’ sample boxes on the surface of the capsule at known distance from the observed capsule centre, a mathematical curvature correction could be made in the following way.

The distance from the center of the sphere was noted in each case. Each measurement was then corrected for both surface curvature and halved to compensate for the transparent nature of the capsules (TEM shows NPs on both sides of the capsule). Measurements were then averaged.

Example sphere correction for a circle centered on (0, 0) of radius 100:



$$x^2 + y^2 = r^2$$

$$y = \sqrt{r^2 - x^2}$$

Taking each horizontal unit distance in turn from the centre of the circle to the edge (dx) and calculating the corresponding vertical change (dy), Pythagoras can be used to calculate the corresponding length of tangent which is approximately equal to the length of arc. For example for a circle radius 100, these calculations can be carried out as follows:

For tangential distance for $x_{0 \rightarrow 1}$

$$x = 0 \rightarrow 1$$

$$dx = 1$$

$$dy = \sqrt{100^2} - \sqrt{100^2 - 1^2} = 0.005$$

$$Tx_{0 \rightarrow 1} = \sqrt{0.005^2 + 1^2} = \mathbf{1.00001}$$

For tangential distance for $x_{98 \rightarrow 99}$

$$x = 98 \rightarrow 99$$

$$dx = 1$$

$$dy = \sqrt{100^2 - 99^2} - \sqrt{100^2 - 98^2} = 4.41$$

$$Tx_{98 \rightarrow 99} = \sqrt{4.41^2 + 1^2} = \mathbf{5.52}$$

This tangential length at different distances from the centre can be used as a surface area multiple in order to correct the apparent NP density in a sample area. The blue dotted line in Figure 50 shows how this quantity varies with distance from the centre.

As well as the raw NP density being adjusted for the capsule curvature, the figure also has to be halved to account for the fact that the TEM shows the nano-particulate film on both the top and bottom of the transparent capsule core.

Figure 50 shows the apparent and corrected NP count data as a function of distance from a capsule centre, overlaid over a schematic diagram of a capsule. The dotted blue line plots the surface area relative to a flat surface as a function of sphere radius, the circles show an example of the apparent NP surface density count as a function of sphere radius and the squares show the same data corrected for sphere curvature. Using this technique we are able to obtain a consistent value for NP surface density across the whole surface area.

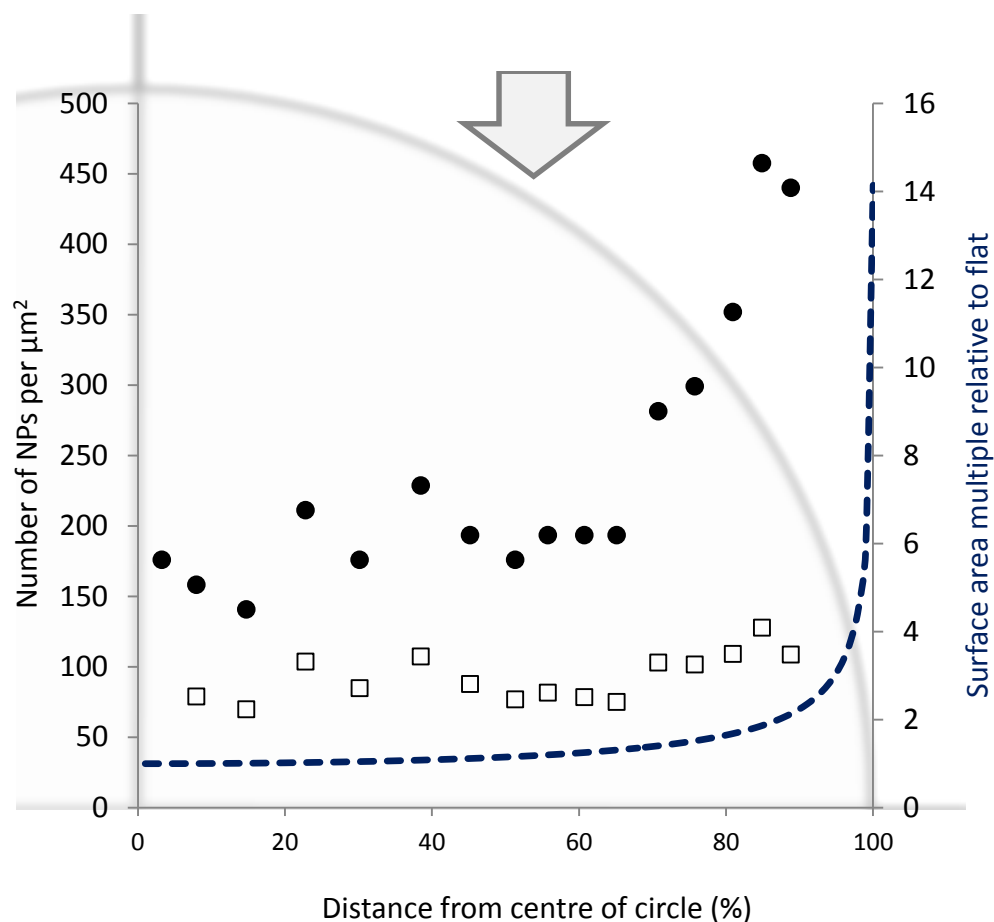


Figure 50 Graph showing how the NP density were corrected for sphere curvature [ref] and sphere transparency. The dotted blue line plots the surface area relative to a flat surface as a function of sphere radius, the circles show an actual example of the apparent NP surface density count as a function of sphere radius and the squares show the same data corrected for sphere curvature. The schematic diagram over which the graph sits is there to aid understanding. The arrow and circle represent the capsule and viewing angle respectively.

5.5.1.2 NPs adsorption densities on polymer shell microcapsules as a function of bulk concentration.

Having defined a specific process to obtain accurate measurements of adsorption densities of Pt NPs on the surface of polymer-shell microcapsules, an experiment was devised to replicate those presented in section 5.4, where NPs densities on the surface of 2D polymer films were investigated as a function of NPs concentration in the bulk.

For this purpose, suspensions of Pt NPs of different concentrations were added to microcapsule suspensions of a constant concentration. 1%wt of the original capsule synthesis were used in all cases [3.3.1].

Figure 51 shows TEM micrographs of the resulting Pt-NP coated microcapsules. Insets to (a) and (d) show corresponding gold coated capsules, both these images were obtained using different electron beam intensity in order to adjust the required contrast between the polymer and gold areas, the location of the gold on the surface was verified via EDX [Figure 52].

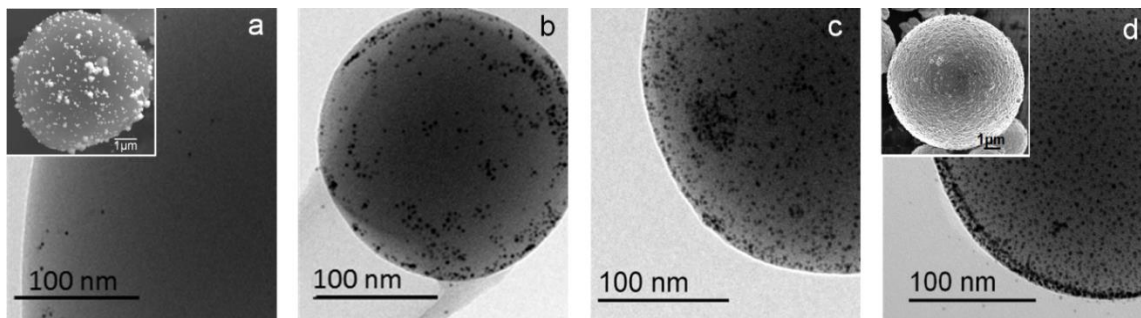


Figure 51 shows representative TEM micrographs of the resulting Pt NPs loaded microcapsules when adding an increasing concentration of Pt NP suspensions to the microcapsules. From (a) to (d) the number of Pt-NP added to the continuous phase was as follows: (a) 1.55×10^{15} , (b) 3.10×10^{15} , (c) 1.26×10^{16} , (d) 1.59×10^{16} . 1%wt of the original capsule synthesis were used [3.3.1]. Insets to (a) and (d) show corresponding gold coated capsules (note that both these images were obtained using different electron beam intensity in order to adjust the required contrast between the polymer and gold areas, the location of the gold on the surface was verified via EDX)

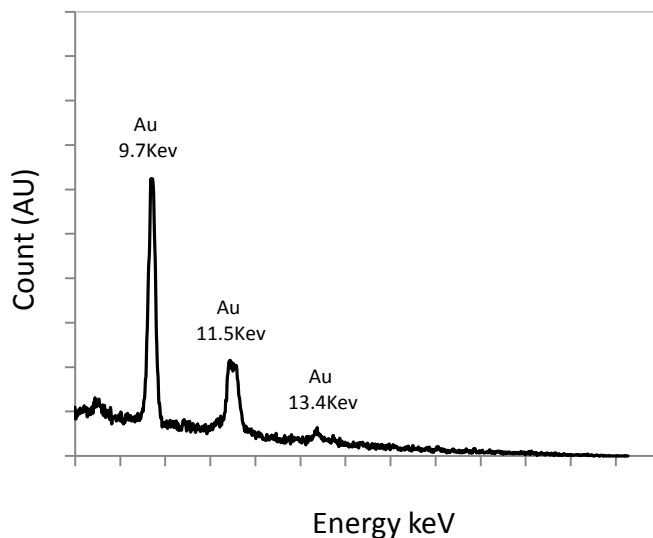


Figure 52 EDX trace showing the presence of gold on the surface of the capsules

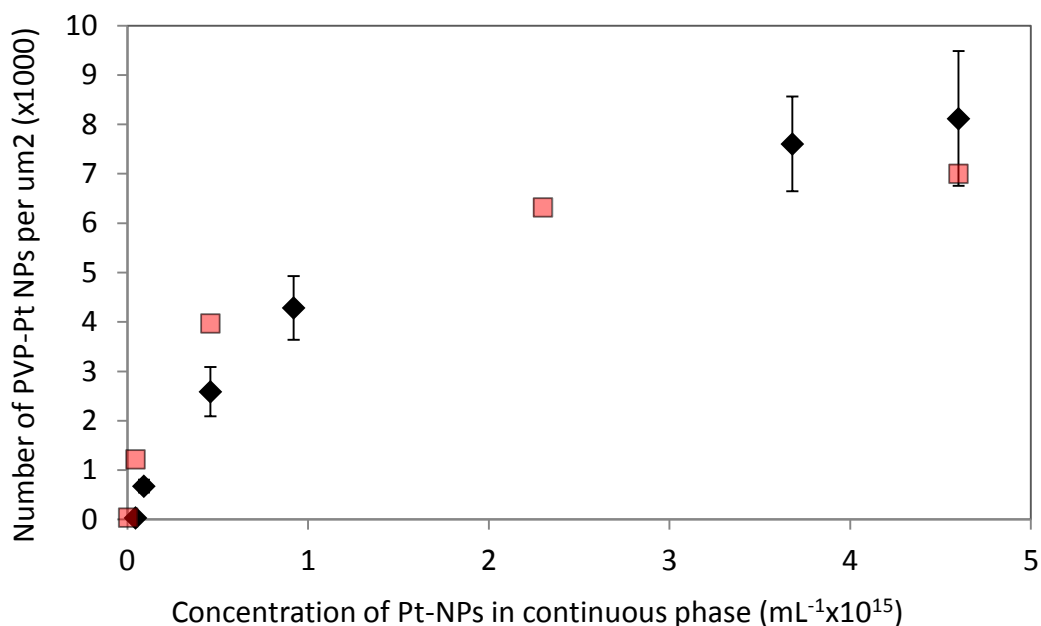


Figure 53 Graph showing Pt-NP adsorption densities on the polymeric microcapsule surfaces as a function of the number of Pt-NP concentration (black diamonds). The (red squares) show the equivalent adsorption data for 2D model substrates from Figure 41.

Figure 51 and Figure 53 show the same relationship between Pt-NP concentration and resulting Pt-NP surface density on the microcapsule surface as was seen for the QCM experiments conducted on the model 2D polymer surfaces. Pt-NP surface density is seen to increase with increasing Pt-NP dispersion concentration. The (red squares) show the equivalent adsorption data for 2D model substrates from Figure 41. We see good comparison between 3D and 2D. It would not be statistically correct to draw conclusions about differences between the two graphs from such a small dataset, more work would be required. It is, however, interesting to note that because of the curvature of the 3D capsule interface we would expect more Pt-NPs to pack per unit surface area.

Figure 54 shows a sphere and a square of ‘same’ surface area. If we assume that we are packing hard spherical particles on hard spherical microcapsules we can say that particles adsorbed on the 3D curved microcapsule interface increase the effective surface area available to them because they effectively sit in a plane one half of their diameter above the capsule surface. Because surface area of a sphere is proportional to the square of the radius this effective surface is larger than the surface of the capsule. It can be shown mathematically that this increase is a function of sphere radius and particle size [eq. 28].

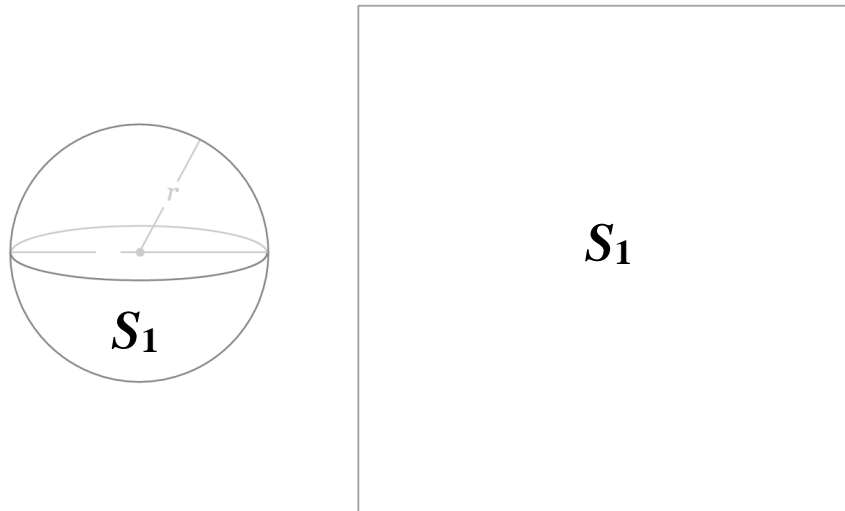


Figure 54 Schematic diagram representing a sphere and a square of equal surface area

Where:

- S_1 Surface area of both the sphere and square
- r Radius of the polymeric capsule
- d_p Diameter of the particle to be adsorbed
- S_2 New surface area at $\frac{1}{2}$ the diameter of the particle above S_1
- $\Delta_{\%}$ Percentage change in effective surface area available to the particles

$$S_1 = 4\pi r^2$$

$$S_2 = 4\pi \left(r + \frac{d_p}{2} \right)^2$$

$$\Delta_{\%} = \frac{100S_1}{S_2} = \frac{4\pi r^2}{4\pi \left(r + \frac{d_p}{2} \right)^2}$$

$$\Delta_{\%} = \frac{100}{1 + \frac{d_p}{r} + \frac{d_p^2}{4r^2}} \quad \text{eq. 28}$$

Therefore the percentage change in effective surface area available to the particles increases with increasing adsorbed particle diameter and decreasing capsule radius [eq. 28]. Therefore for this system the capsule size is $\sim 2\mu\text{m}$ and the adsorbed particle diameter is $\sim 10\text{ nm}$. The percentage increase in effective surface area would therefore be $\sim 2\%$. (The relationship between surface area and NP packing is a linear one, ideal 2D hexagonal close packing takes up 91% of the surface [3.4.3]).

In Figure 55 the calculation of capsule surface area introduced [3.4.1] and used to plot the number of Pt-NPs available per unit surface area of capsules introduced as a function of Pt-NPs introduced to each sample (red squares).

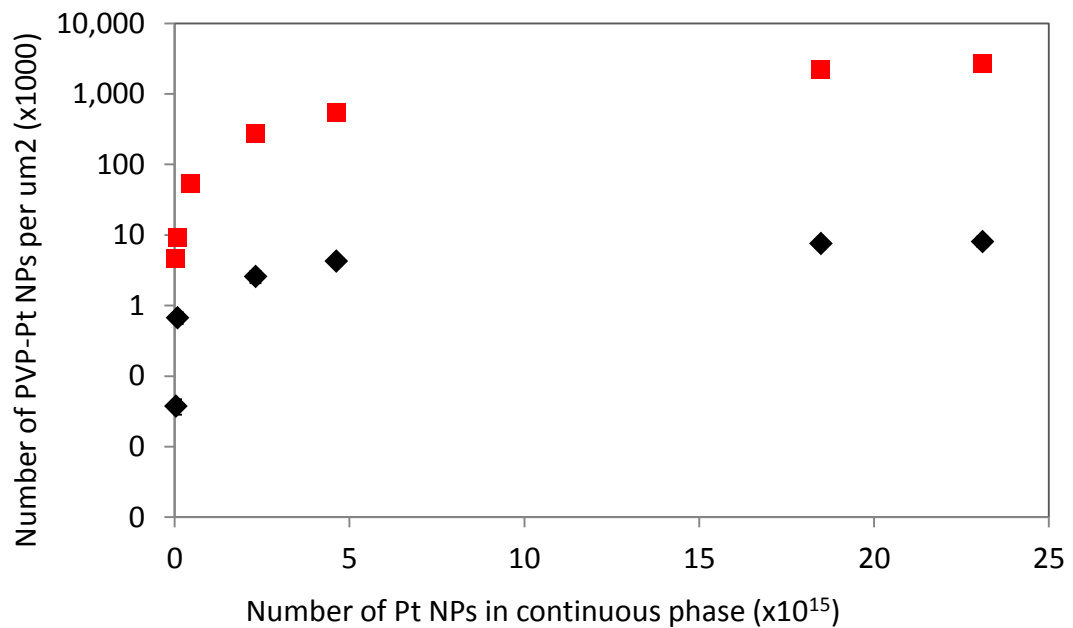


Figure 55 Graph showing number of Pt-NPs available per unit surface area of capsules introduced as a function of Pt-NPs introduced to each sample (red squares) and the measured Pt-NP adsorption densities on the polymeric microcapsule surfaces as a function of Pt-NPs dispersion concentration (black diamonds).

We see that, at all Pt-NP suspension concentrations, the number of Pt-NPs available per unit surface area of capsules introduced is far higher than the measured Pt-NP surface density. Therefore the experimentally measured Pt-NP surface density can't solely be explained by Pt-NP depletion from the continuous phase. At all Pt-NP concentrations

tested there are a large excess of NPs available in the bulk even after the surface has been saturated.

5.5.2 NP Packing Density Analysis

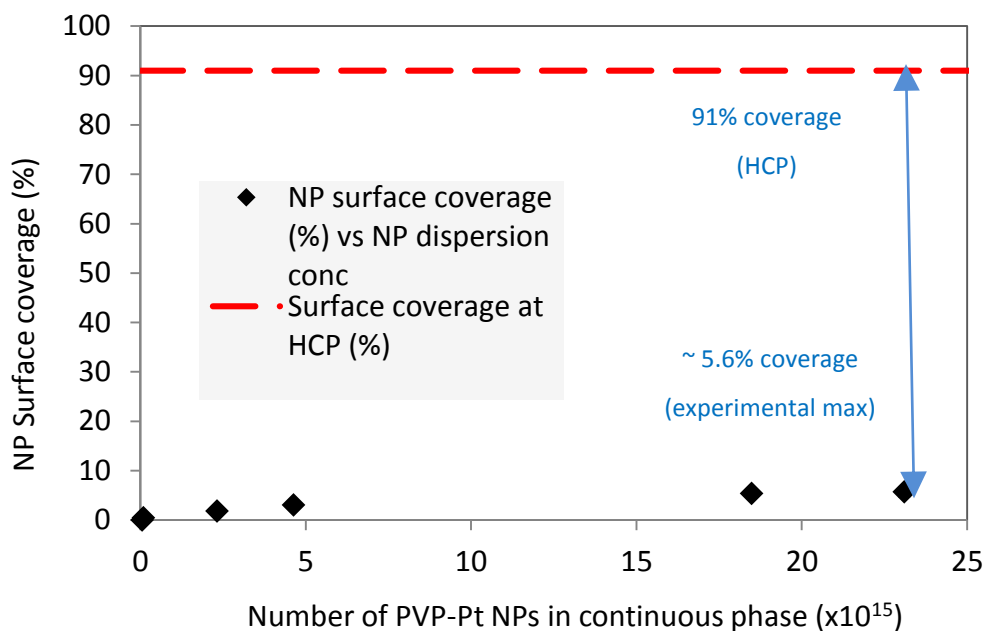


Figure 56 Graph showing the number of NP's per μm^2 needed to achieve hexagonal close packing (HCP) relative to the coverage we are getting. The measured mean size of the NPs using TEM was used to calculate the packing.

If we take the data shown in Figure 53 and, using the mean size of the Pt-NPs [5.3.1], convert the Y-axis into Pt-NP percentage surface coverage. We see that the maximum surface area coverage achieved with this system is $\sim 5.6\%$ [Figure 56] which relates to the SEM micrograph [Figure 51d]. The maximum packing density of equal sized spheres at an interface is 91% [3.4.3].

5.6% surface coverage seems like a relatively sparse surface coverage and doesn't intuitively appear to fit with the TEM images of maximum surface coverage [Figure 58]. However, if we calculate the separation we should expect to see for hexagonal surface packing coverage [eq. 29] we see that the actual ratio of NP separation to NP radius works out to be 0.12 for coverage of 5.6% [Figure 57]. Surface coverage is

proportional to the square of the inverse separation, therefore relatively small separations lead to large reductions in surface coverage.

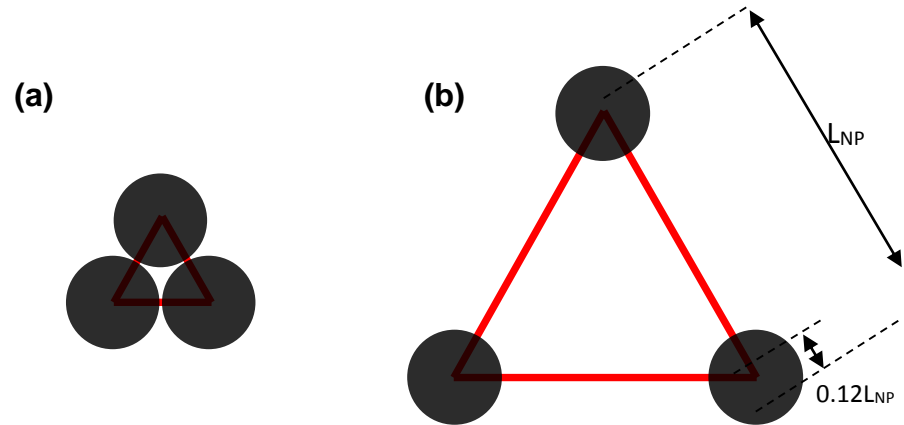


Figure 57 Scaled schematic diagram showing how hexagonal packed sphere separation relates to 2D surface area coverage (a) HCP – 91% surface coverage and (b) 5.6% surface coverage generated from equation eq. 29

Calculation of ratio of hexagonal packed NP separation (L_{NP}) to NP radius (r) for chosen surface area coverage (Γ_{cov}):

Where:

- r NP radius
- Γ_{cov} Surface area coverage
- L_{NP} NP separation
- NP_s NP surface within red triangle
- Δ_s Surface area of the triangle

$$NP_s = \pi r^2 / 2$$

$$\Delta_s = 1/2 L_{NP} \sqrt{L_{NP}^2 - (L_{NP}/2)^2}$$

$$NP_s/\Delta_s = \Gamma_{cov} = \pi r^2 / \left(L_{NP} \sqrt{L_{NP}^2 - (L_{NP}/2)^2} \right)$$

$$L_{NP} \sqrt{L_{NP}^2 - (L_{NP}/2)^2} = \frac{\pi r^2}{\Gamma_{cov}}$$

$$L_{NP}^2 \left(L_{NP}^2 - (L_{NP}/2)^2 \right) = \pi^2 r^4 / \Gamma_{cov}^2$$

$$L_{NP}^4 - L_{NP}^4/4 = \pi^2 r^4 / \Gamma_{cov}^2$$

$$\frac{3L_{NP}^4}{4} = \pi^2 r^4 / \Gamma_{cov}^2$$

$$\frac{r^4}{L_{NP}^4} = \frac{3\Gamma_{cov}^2}{4\pi^2}$$

$$\frac{r}{L_{NP}} = \sqrt[4]{\frac{3\Gamma_{cov}^2}{4\pi^2}} \quad \text{eq. 29}$$

Therefore for 5.6% coverage $\Gamma_{cov} = 0.056$ and $\frac{r}{L_{NP}} = 0.12$

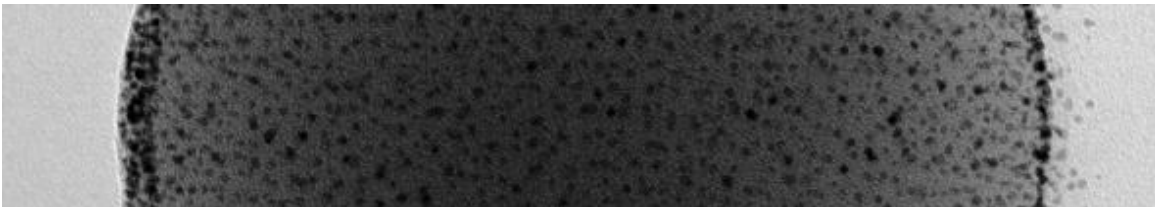


Figure 58 Shows a TEM image of 5.6% surface coverage on a capsule. Note that the image shows both the top and bottom surface. Most NPs appear to be separated from their neighbors instead of being butted up against them.

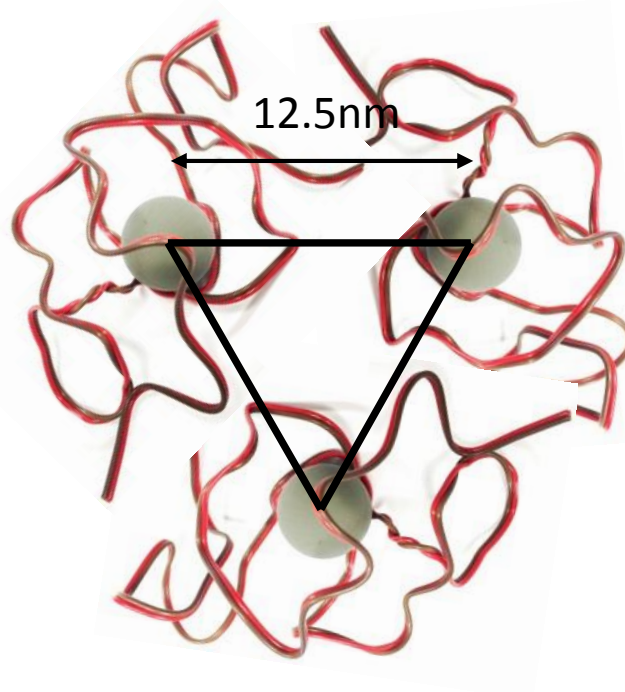


Figure 59 Show a scale ‘model’ of 3 Pt-NPs hexagonally packed at a core separation which represents 5.6% Pt core surface coverage. In this example each Pt core is stabilised by a single 40KDa PVP chain. The ratio of PVP chain length to Pt core diameter is 108:3.

The Pt-NPs used in this work have a mean diameter of ~ 3 nm. At 5.6% surface coverage this translates to a HPC NP core separation of 12.5nm. TEM images of Pt-NPs adsorbed at the maximum surface density onto PEMA coated grids shows that the NPs pack at approximately this calculated separation [Figure 59].

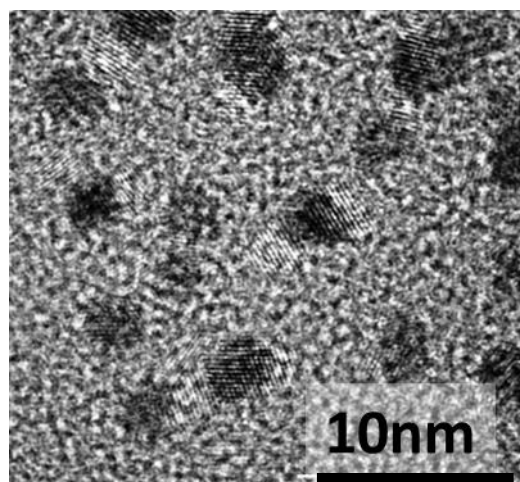


Figure 60 Shows the same NPs adsorbed onto a PEMA coated TEM grid [ref technique] allowing closer inspection. We see a somewhat regular spacing around each adsorbed NP.

Why do the Pt-NPs not butt up against each other in a close packed array but instead tend to have somewhat regular ~12nm spacing around them [Figure 60]? It is known that the hydrocarbon PVP chains do not provide much TEM contrast between the carbon and PEMA film and are therefore largely invisible. We also know that the PVP offers newly synthesised Pt-NPs stability via steric hindrance. It would appear that this steric hindrance also prevents the NPs for approaching too closely when adsorbing onto the polymeric interface.

Interestingly if size the NP dispersion by dynamic light scattering we see that the hydrodynamic diameter is ~10nm [Figure 61] This figure represents the diameter of the platinum core plus the PVP stabiliser in an aqueous phase and better fits with the calculated and observed separation [Figure 57,Figure 58].

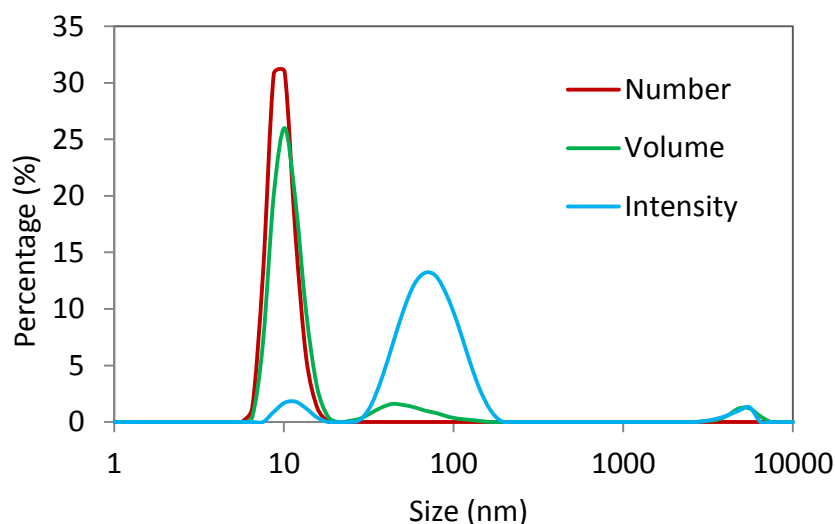


Figure 61 DLS [3.2.4] size data for Pt-NPs showing the percentage of the dispersion by number, volume and intensity.

5.5.3 Pt-NP adsorptions density, morphology and polymeric stabiliser conformation.

From the previous work in this chapter we know that maximum packing density occurs at Pt-NP core separations of approximately 12nm [5.5.2], in addition DLS measurements show the Pt-NP diameters to be approximately 10nm [Figure 61]. We also know that the dispersions used in this chapter have a low ratio of free PVP stabiliser chains to platinum cores [Figure 31]. This, to some extent, restricts the number of possible NP core PVP stabiliser conformations. In this section, the PVP radius of gyration is calculated and, using information gleaned from this chapter, possible NP morphologies are discussed.

The simplest polymer model which considers the sizes of dissolved polymeric chains considers the entire chain as a collection of freely jointed ridged segments. An end to end random walk distance can then be calculated for the chain and through considering the probability distribution of the chain ends a radius of gyration for the polymer can be calculated. Omitting any interactions between monomers, for an ideal chain we get equation eq. 30 [83]:

$$R_g \approx bN^{1/2} \quad \text{eq. 30}$$

Where:

- R_g Radius of gyration
- N Number of monomers
- b Inter-monomer spacing

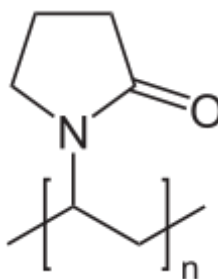


Figure 62 molecular structure of PVP monomer

For our 40KDa PVP chains, N is equal to the total molecular mass divided by the mass of the monomer which, we can see from Figure 62, is 111, therefore $N = 360$. The length of a C-C bond in a hydrocarbon is $\sim 0.15\text{nm}$, therefore $b = 0.3$. Therefore for 40KDa PVP chains the $R_g \sim 5.69\text{nm}$ and the diameter of gyration should be approximately 11.4nm [eq. 30]. Clearly, this figure is very close to our DLS measured diameter of 10nm and the maximum inter-core spacing of $\sim 12\text{nm}$. Can we therefore conclude that our Pt-NPs consist of a platinum nanoparticle core at the centre of a single PVP chain?

Figure 63 shows some simple, approximately to scale, models of possible Pt-NP core / PVP stabiliser conformations. For these scale models, the ratio of NP core diameter to PVP chain length used is 3:108 (3nm mean diameter, 108nm length polymer chain). The length of an extended PVP chain can be calculated, we know that each monomer consists of 2 C-C bonds which are each $\sim 0.15\text{nm}$ long. Therefore, the length of the extended polymer is $0.3 \times 360 \sim 108\text{nm}$.

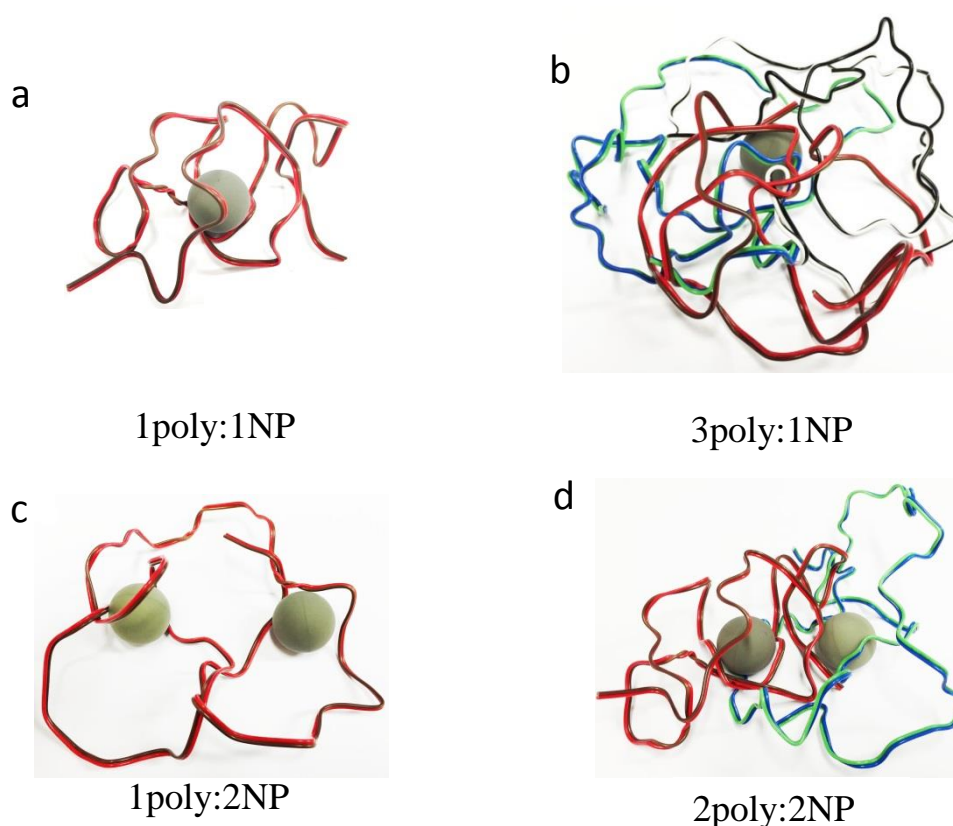


Figure 63 shows some simple, approximately to scale, models of possible Pt-NP core / PVP stabiliser conformations. For these scale models, the ratio of NP core diameter to PVP chain length used is 3:108 (3nm mean diameter, 108nm length polymer chain). The length of an extended PVP chain can be

calculated, we know that each monomer consists of 2 C-C bonds which are each ~0.14nm long.
Therefore, the length of the extended polymer is $0.3 \times 360 \sim 108\text{nm}$.

The following evidence gives credence to the idea that the ratio of number of PVP stabiliser chains per platinum core for an individual NP is approximately 1:1:

- The minimum inter core spacing observed via TEM show an approximate core spacing of 12nm. We know that the radius of gyration of a single PVP chain is approximately 11.4nm. Therefore the confirmation of the PVP chains around the NP cores would have to be significantly smaller if more than one PVP chain were to fit into the achieved close packed NP arrays shown in [Figure 60].
- The ratio of PVP chains to Pt cores used in our NP synthesis has been shown to be close to 1:1 [5.3.2] Pt-NP morphology is most likely to be either 1 core: 1PVP chain or several cores per chain (Figure 63) other ratios of polymer to core would appear to be excluded on the basis of there being not enough PVP in the system.
- PVP has a high affinity for a range of interfaces [75] and stabilises the Pt cores well [64]. However, once a once an approximate monolayer adsorbs to an interface steric hindrance between the adsorbed film of PVP and the free PVP in solution restricts further PVP adsorption [5.4.4]. We would therefore expect the PVP to adsorb as an approximate monolayer on the platinum NP cores. In addition, because of the ratio of size of PVP (~11nm diameter of gyration [5.5.3]) to Pt-NP cores (~3nm diameter [5.3.1]), the geometry only allows for a small number of PVP chains to fit around a single Pt-NP core.

If a proportion of the Pt-NPs are made up of a single platinum nanoparticle core stabilised by a single PVP chain then there are some interesting implications for NP growth mechanisms. It would seem thermodynamically unfavourable for a PVP chain to unfurl from its random walk conformation in order to wrap around newly forming nucleating and growing platinum cores. It seems more likely that the system would

instead keep its Gibbs free energy low by allowing the reduced Pt atoms to nucleate and grow inside individual PVP chains.

5.6 Conclusion

Stable Pt-NP dispersions were synthesised using a range of PVP stabiliser concentrations. Pt-NP core diameters were found to be inversely proportional the log of the concentration of PVP used to stabilise the NP dispersion and vary from ~2.3 to ~3.6nm in diameter. Pt-NP dispersions remained stable and monodisperse down to PVP stabiliser concentrations of 0.0015% wt.

Calculations of ratio of number of NPs to number of PVP chains used in the synthesis of the Pt-NPs were made. Assuming 100% reduction and conversion of the platinum salt to platinum NPs, it was shown that at low PVP stabiliser concentration (less than 0.02wt% PVP:0.23wt% Pt salt) the ratio of number of PVP chains to number of platinum cores was likely to be less than 1:1. Pt-NP dispersions made with less than 0.0015wt% PVP to 0.23wt% Pt salt were found to be unstable and as a result coalesced and sedimented out of the dispersion.

PEMA films with a thickness of ~3nm were successfully spin coated onto QCM crystals and used as a model 2D system for Pt-NP adsorption. NPs were shown to adsorb rapidly reaching equilibrium in less than a minute for all NP concentrations used. Once an approximate nanoparticle monolayer is formed, further adsorption is sterically hindered. QCM and TEM were employed to demonstrate that the Pt-NPs exhibit high adsorption energies.

QCM and TEM were employed to demonstrate that adsorption densities of Pt-NPs on spin coated PEMA films was a function of the concentration of PVP stabiliser used in the original NP synthesis. Reducing the concentration of stabiliser resulted in an increase in Pt-NP adsorption density. Excess PVP left over from the synthesis adsorbs at the interface and sterically hinders further adsorption of Pt-NPs.

QCM and TEM were employed to demonstrate that adsorption densities of Pt-NPs onto spin coated PEMA films was also a function of concentration of the dispersion. Reducing the concentration of the dispersion resulted in a decrease in Pt-NP adsorption density. Free excess PVP chains in the NP dispersion not only adsorb and block potential NP adsorption sites but, even though the ratio of Pt-NPs to PVP remains constant, as the concentration drops the adsorption rate of the PVP increases more relative to the Pt-NP adsorption rate. The larger Pt-NPs diffuse more slowly than the free polymer chains. As both species become more dilute, the average mean free path for each species increases and therefore the smaller polymer chains increasingly 'win the race' to the interface. Adsorption rates (maximum gradient of isotherm) for different Pt-NP concentrations were measured. The peak adsorption rate was found to be proportional to the Pt-NP concentration in the bulk. An overshoot in frequency change observed on the Langmuir isotherms was shown to be due to the pressure wave caused by the inflow of liquid into the QCM cell and onto the crystal.

QCM adsorption isotherms for a range of Pt-NP dispersion concentrations were used to analyse both the equilibrium adsorption and kinetic adsorption data using standard Langmuir adsorption theories. These data were used to determine a consistent value of the Langmuir adsorption equilibrium constant for the nanoparticle – substrate interaction and was found to be $0.26\mu\text{mol/L}$. The Langmuir adsorption equilibrium constant was used to calculate the Gibbs free energy of adsorption, at equilibrium, per mole of Pt-NP and was found to be $3.30 \times 10^{-3} \text{J}/\mu\text{mol}$. Avogadro's number was then used to calculate the adsorption energy of a single Pt-NP and was found to be $5.49 \times 10^{-21} \text{J}$. This figure was compared to the background thermal energy and was found to be $\sim 1.35 \text{kT}$. The adsorption energy of the Pt-NP has been shown experimentally to be many times the background thermal energy. We are therefore forced to conclude that the calculated figure of 1.35kT is too low. We conclude that the concentration dependence of adsorbed mass in these systems is due to the presence of a second surface active species, in this case PVP, which has a higher diffusion coefficient. Successful Langmuir adsorption studies are regularly made for molecular species which reach adsorption/desorption equilibria at different concentrations. Although the same shaped adsorption isotherms can be found for some particle systems, care should be taken to make sure the system is pure before applying this analysis.

A technique was developed and employed to take account of the curvature and transparency of polymeric microcapsules in order to measure Pt-NP adsorption densities on capsule surfaces via TEM. The same relationship as observed in the 2D model system between Pt-NP concentration and resulting Pt-NP surface density was observed on the 3D microcapsule surface. Pt-NP surface density increased with dispersion concentration and was shown to plateau. Calculations of available capsule surface area and number of Pt-NPs in the continuous phase were made. The number of Pt-NPs available per unit surface area of capsules introduced was shown to be significantly greater than that of the measured Pt-NP surface density. Therefore the observed variation in Pt-NP surface density can't solely be explained by Pt-NP depletion from the bulk. This lends weight to the argument that free PVP chains are adsorbing at the interface at the expense of the Pt-NPs in the suspension.

Comparisons were made using TEM between 2D NP adsorption densities on model PEMA surfaces and 3D NP adsorption density on PEMA capsules. Adsorption densities compared well. An equation was derived to calculate the percentage increase in packing density when a 2D interface is changed into spherical particulate interface of equal interfacial area. The change in packing density was shown to be dependent on the capsule size and the size of the NPs to be adsorbed. For the system used in this study the capsule size was $\sim 2\mu\text{m}$ and the adsorbed particle diameter was $\sim 10\text{nm}$. The percentage increase in available packing due to the curved interface was calculated at $\sim 2\%$.

The maximum NP surface area coverage achieved was shown to be $\sim 5.6\%$. TEM images showed that NP metallic cores adsorbed in semi-regular hexagonal packing patterns and exhibited regular gaps of $\sim 12\text{nm}$ between cores. Dynamic light scattering showed the NP hydrodynamic diameter to be $\sim 10\text{nm}$. The NP core interspacing can therefore be explained by the steric hindrance of the adsorbed PVP polymeric stabilizer.

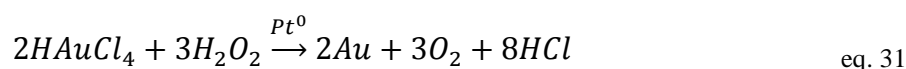
The radius of gyration, in an aqueous environment, of 40KDa PVP chains was calculated to be 5.69nm (11.38nm diameter). DLS was used to measure the diameter of the Pt-NPs and was found to be $\sim 10\text{nm}$ which fitted well with the observed minimum inter-core spacing of $\sim 12\text{nm}$ seen on TEM. This information coupled with the

calculated low ratio of PVP chains to number of platinum cores in the Pt-NP dispersions used in these experiments leads us to conclude that our Pt-NPs may consist of a platinum nanoparticle core at the centre of a single PVP chain.

6 Secondary metallic film morphology, growth and properties

6.1 Synopsis

Thin films of solid gold can be grown directly onto adsorbed Pt-NP films using electroless plating [See section 2.2.2 for more detailed description of mechanisms][64]. This method utilizes the platinum as a catalyst and nucleation site for gold growth in the presence of a reducing agent for the metal ions [eq. 31].



The presence of the nanoparticles localizes the deposition of solid gold, which limits further precipitation in the continuous phase. Once all the catalytic platinum sites are covered the gold film can continue to grow, albeit at a slower rate, as gold also acts to promote the reduction of gold on gold through an autocatalytic process.

The previous chapter has demonstrated an understanding and good control of the catalytic nanoparticle adsorption densities. Therefore, this chapter will focus on using these nanoparticle films as catalysts for the growth of secondary metal and explore the influence of variables such as temperature and time on the resulting metal film morphology [Figure 64d]. 2D polymeric spin coated glass slides [3.2.3] were used as a model system in order to analyse, using AFM and SEM, the secondary metal film thickness and roughness as a function of time and temperature. In order to characterise the secondary metal films on 3D microcapsule surfaces, capsules were microtomed and observed using TEM [3.2.7]. In addition, FIB epitaxy was used to cut sections through the capsules which were then observed via SEM [3.2.6].

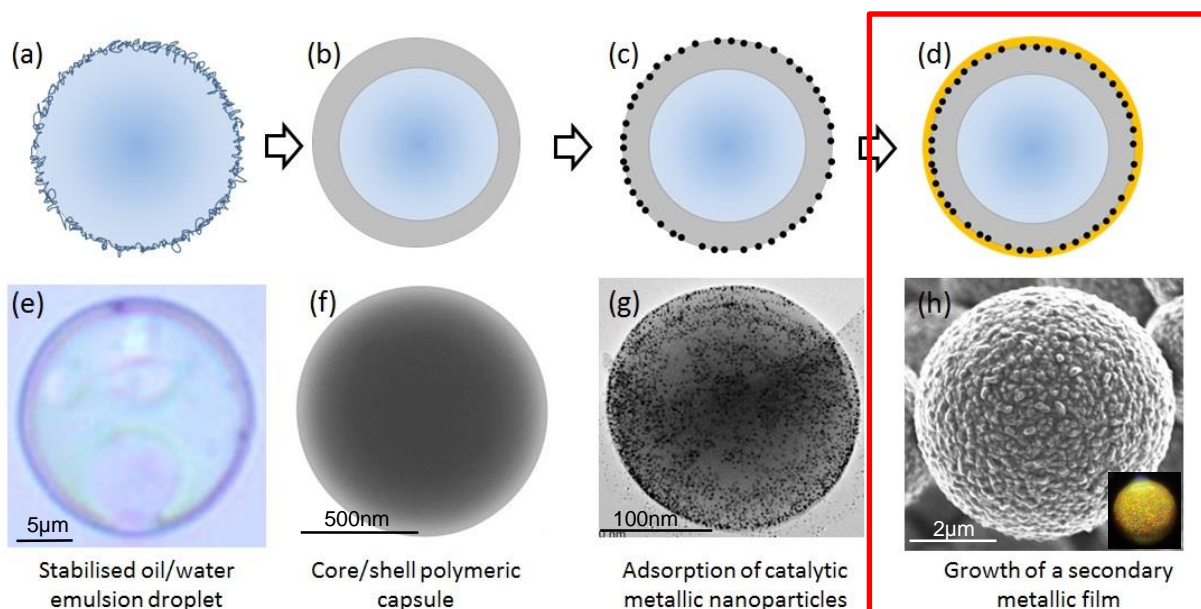


Figure 64 Schematic diagrams (a-d) and corresponding optical and electron microscopy images (e-h) of the different phases from emulsion droplet to gold coated capsule (a) emulsion droplet, (b) capsule, (c) capsule with adsorbed NPs, (d) Gold coated capsule, (e) emulsion droplet (optical microscopy), (f) capsule (TEM), (g) capsule with adsorbed NPs (TEM), (h) Gold coated capsule (SEM) (inset gold coated capsule under visible light). Red box highlights the part of the process discussed in this chapter.

In this part of the work, catalytic Pt-NPs are used to grow continuous secondary gold films via electroless deposition. The synthesis of the Pt-NPs is described in section [3.3.2] and the standard gold plating technique is described in section [3.3.4]. Any variations from these standard methodologies will be described within this chapter.

As described in the aims of this work, this project has focused on developing the methodology with good control over the deposited metal films, which was made possible by using a well understood metal combination and translating the knowledge provided by the literature to deposition of similar films onto polymeric microcapsule shells. On this basis we justify the use of this combination of Noble metals. We know this is a potential challenge with respect to translating the methodology to commercial products because of the costs associated with using these metals in the manufacturing process. Our research group is separately focusing on developing this methodology for more cost effective metal combinations such as palladium catalysing the growth of continuous copper or nickel secondary films.

Irrespective of chosen metal combination, to limit costs and provide an affordable solution to the encapsulation of small active ingredients thin, smooth, complete

secondary films are required. In addition, triggered release of actives from the capsule core is envisaged to be through mechanical breakage and therefore control over metal film thickness would allow for the production of capsules with different rupture strengths.

It will also be beneficial to control surface roughness of the secondary metallic film as this has been shown to effect the resulting achievable adsorption density of biological moieties for potential targeted therapeutic pharmaceutical drug delivery [86] and may also effect the rupture strength of the capsule.

6.2 Metal film morphology on 2D model polymeric substrates

In order to minimise the number of variables and the associated error and observe the metal film growth kinetics in detail, metal film growth was analysed in 2D on polymer-coated glass slides using atomic force microscopy (AFM) and SEM. Polymeric thin films were first spin-coated onto glass slides [3.2.3]. Knowledge gained in chapter 5 was then used to adsorb known surface densities of Pt-NPs onto the coated slides. Metal films were grown to test the influence of several variables associated with the process.

Figure 65 shows an SEM image of the spin coated PEMA film on a glass substrate with a gold film grown on top. It was found that light scraping with a plastic pipette tip removed only the gold film (A) and light scraping with a scalpel removed both the PEMA and the gold film but left the glass substrate intact (B). The spin-coating technique was the same used to spin-coat quartz crystals in section 5.4.1 and resulted in PEMA films approximately 3nm thick.

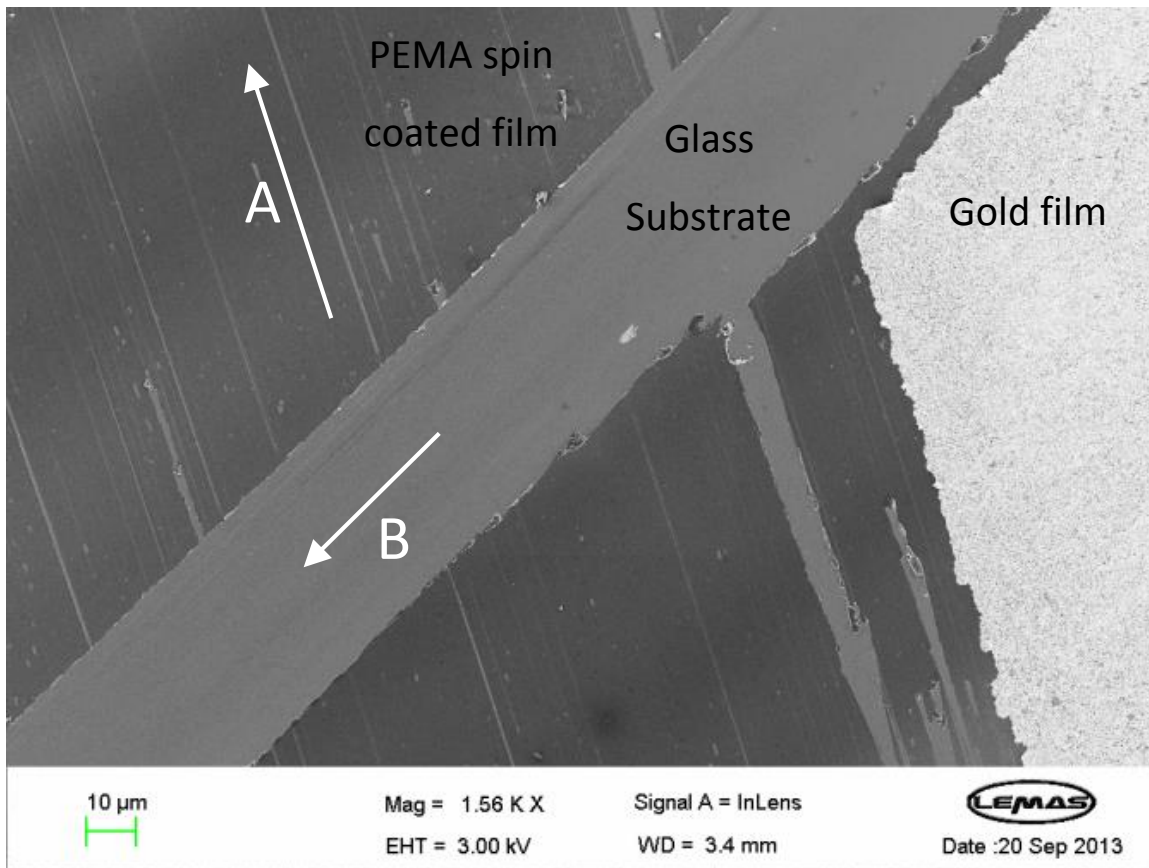


Figure 65 SEM image of spin-coated PEMA film on a glass substrate with a gold film grown on top. The arrows show (A) a relatively light scrape with a plastic pipette tip removes only the gold film and (B) light scraping with a scalpel removes both the PEMA and the gold film. The PEMA film is ~3nm thick [5.4.1].

In order to measure the metal film thickness multiple scalpel score lines were made across the sample. AFM scans were then made of the score line and height profile lines were drawn across the PEMA/gold film boundary. Figure 66a shows an example of the data obtained for a typical height profile. Each profile was split manually into the line sections representing the PEMA film height and the gold film height [Figure 66b] and the equation of each new line was found automatically by the excel software by the ‘least squares’ method [Figure 66c]. Although the gradients of the two lines of best fit differ slightly and therefore the further from the divide one goes the less accurately the ‘perpendicular’ distance between the two lines reflects the film thickness. Therefore, the mid-point of the divide and the average of the inverse of the two line gradients were then used to generate a third ‘perpendicular’ line which went through the mid-point [Figure 66d]. This line was then intersected with the other two lines to find the

coordinates of the two intersect points and Pythagoras was used to calculate the perpendicular distance between the two lines at the mid-point. This was done for 10 profiles on each sample and then averaged.

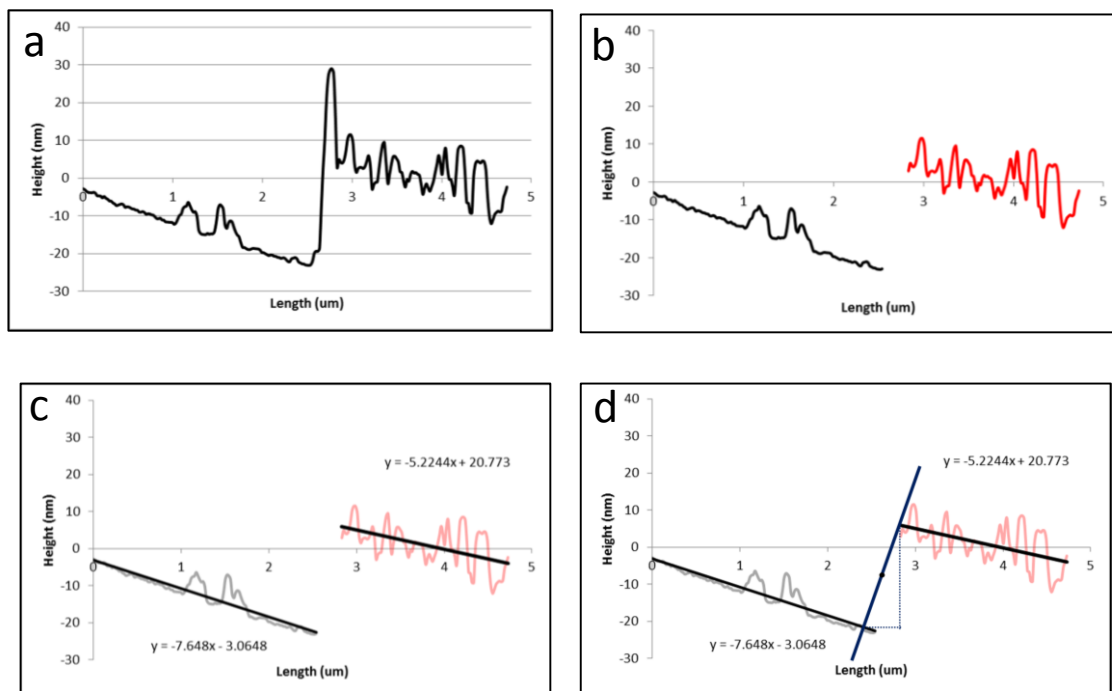


Figure 66 shows how AFM height profiles were analysed to measure the thickness of the metal films (a) shows the data for a single profile (b) shows two new line made when the profile was split (c) the equation of each new line was found and (d) the mid-point of the divide and the average of the inverse of the two lines gradient was used to generate a third line.

In the previous chapter, QCM adsorption data on PEMA spin coated silica crystals and direct TEM micrographs of dip coated PEMA films on TEM grids both show that Pt-NP saturate PEMA interfaces in minutes to forming complete monolayers [5.4.2]. An assumption was made that the Pt-NP would interact in the same way with PEMA spin coated glass slides. Therefore by choosing to work with constant particle concentrations and adsorption times a further assumption was made that the NP density would remain constant for all the samples tested.

6.2.1 AFM analysis of 2D film thickness and roughness as a function of temperature and time

Using the procedure described above, mean film thickness was measured as a function of temperature and time. Film roughness was also measured for each of the samples. Roughness was measured by comparing the expected area of the flat AFM raster scan surface to the actual surface area of the scan [3.2.1].

To create the metal-coated surfaces for these experiments, Pt-NPs were first adsorbed onto the spin coated PEMA films at a reproducible known density [5.4.4] (Pt-NP concentration in the bulk $4.6 \times 10^{15} \text{ mL}^{-1}$ resulting in a Pt-NP surface adsorption density of $7 \times 10^3 \mu\text{m}^{-2}$). The NP-coated surfaces were then washed several times to remove any excess NP from the system. They were subsequently dipped into electroless plating solutions for a range of times at various temperatures and then immediately rinsed with Milli-Q water.

Figure 67 and Figure 68 show graphs of mean gold film thickness as a function of time and temperature.

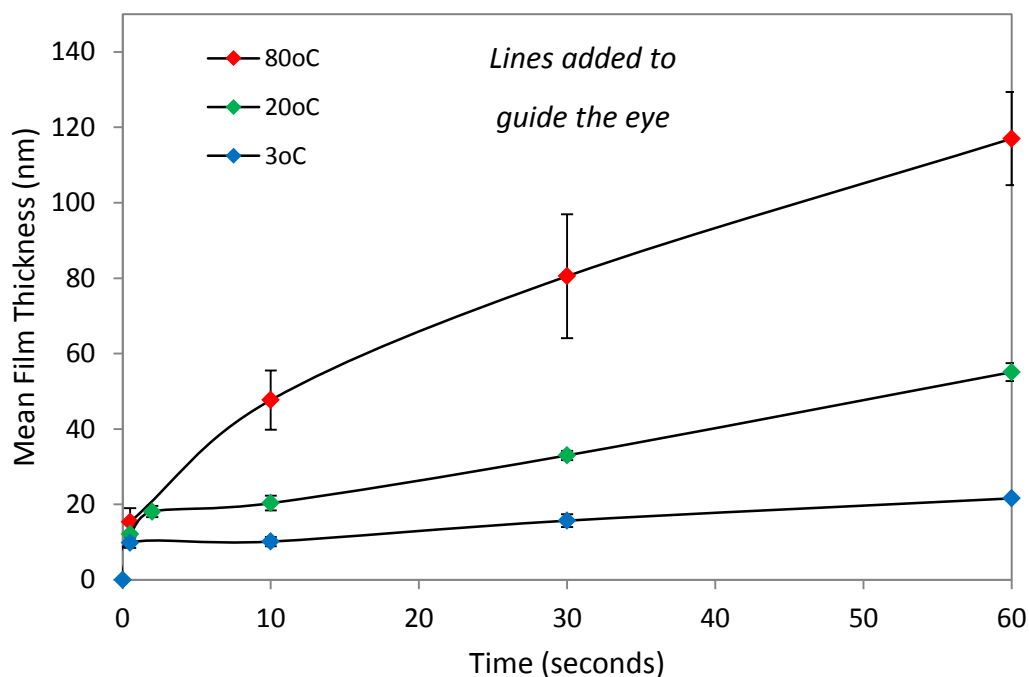


Figure 67 Graph showing how mean secondary metal film thickness varies with time and temperature..

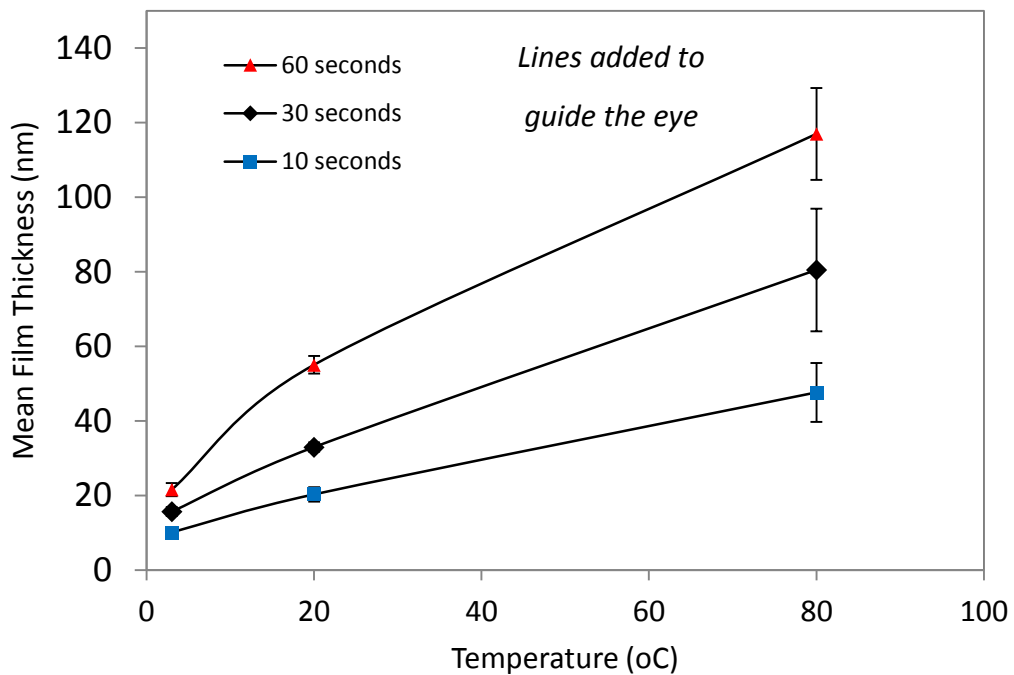


Figure 68 Graph of mean metal film thickness as a function of temperature at 10, 30 and 60 seconds plating time.

The mean film thickness increases over time for all temperatures [Figure 67] and the rate of film thickness growth is greater at higher temperatures [Figure 68]. The standard deviation on thickness at 80°C is higher because of the increased surface roughness at elevated temperature.

Figure 67 shows that two distinct growth phases were observed. In the primary phase the growth rate is high and non-linear, in the secondary phase the growth rate slows and the relationship between film thickness and time appears to become linear. Early growth rates are difficult to practically measure due to the relatively large error associated with the time the samples are dipped into the plating solution. However, we can choose any temperature and look at the change in film thickness in the first 10 seconds compared to the thickness at 60 seconds. For example at 20°C, the mean film thickness is ~20nm after 10 seconds. If this rate were to continue we would expect the thickness at 60 seconds to be ~160 nm, instead it is only ~55 nm. This two stage growth rate is likely to be caused by the catalytic Pt-NP surface initially promoting rapid gold film growth followed by slower autocatalytic gold on gold film growth. Horiuchi et al. report similar findings for gold grown on Pt-NPs and interestingly when they go on to grow gold on

gold nanoparticles they show a near linear relationship between thickness and time with no second phase [64].

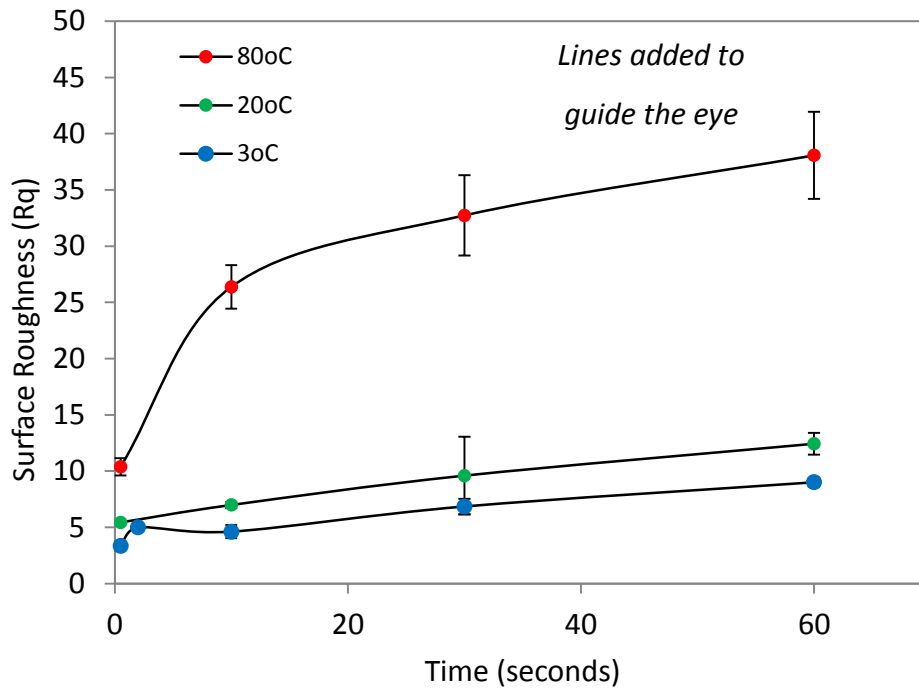


Figure 69 Graph showing how mean secondary metal film surface roughness varies with time

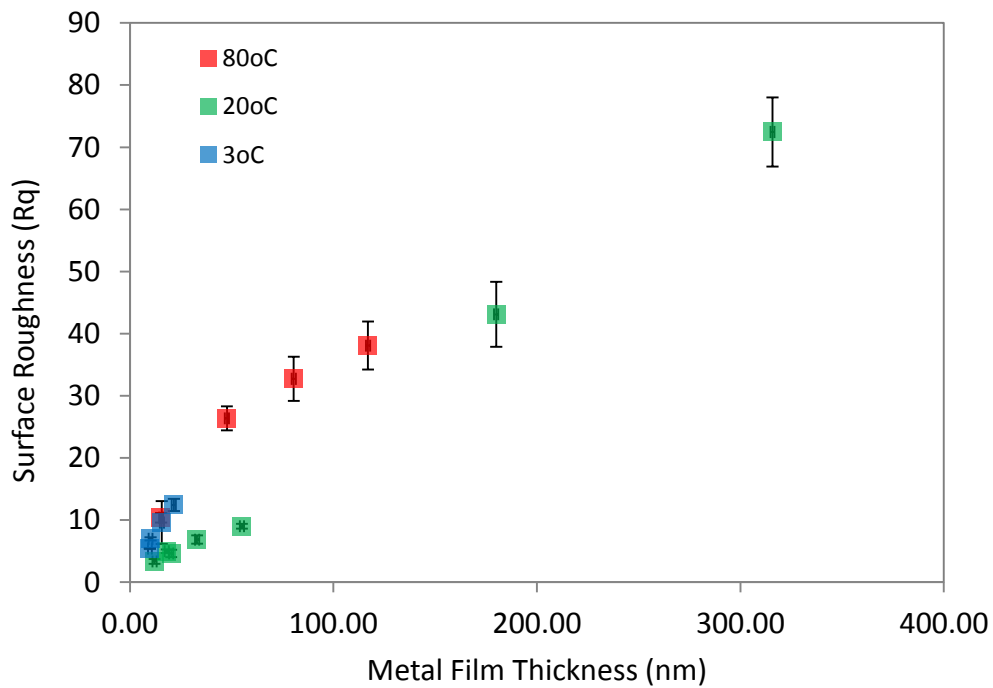


Figure 70 showing how mean secondary metal film thickness varies with roughness

Figure 69 shows a graph of surface roughness as a function of time for a series of temperatures. The roughness increases over time for all temperatures and the rate of increase is greater at higher temperatures.

Plotting surface roughness as a function of mean metal film thickness shows that there is little variation between temperatures [Figure 70]. It seems likely that although the films become rougher and thicker more quickly at higher temperature the relationship between surface roughness and film thickness is linear.

Figure 71a-d show AFM raster scan height profiles in plan as a function of time. In addition, Figure 71e-h show 3D projections of the same samples. It is evident from these AFM data that both the surface roughness and 'grain' size increase with time. This phenomenon has also been observed in previous literature data.

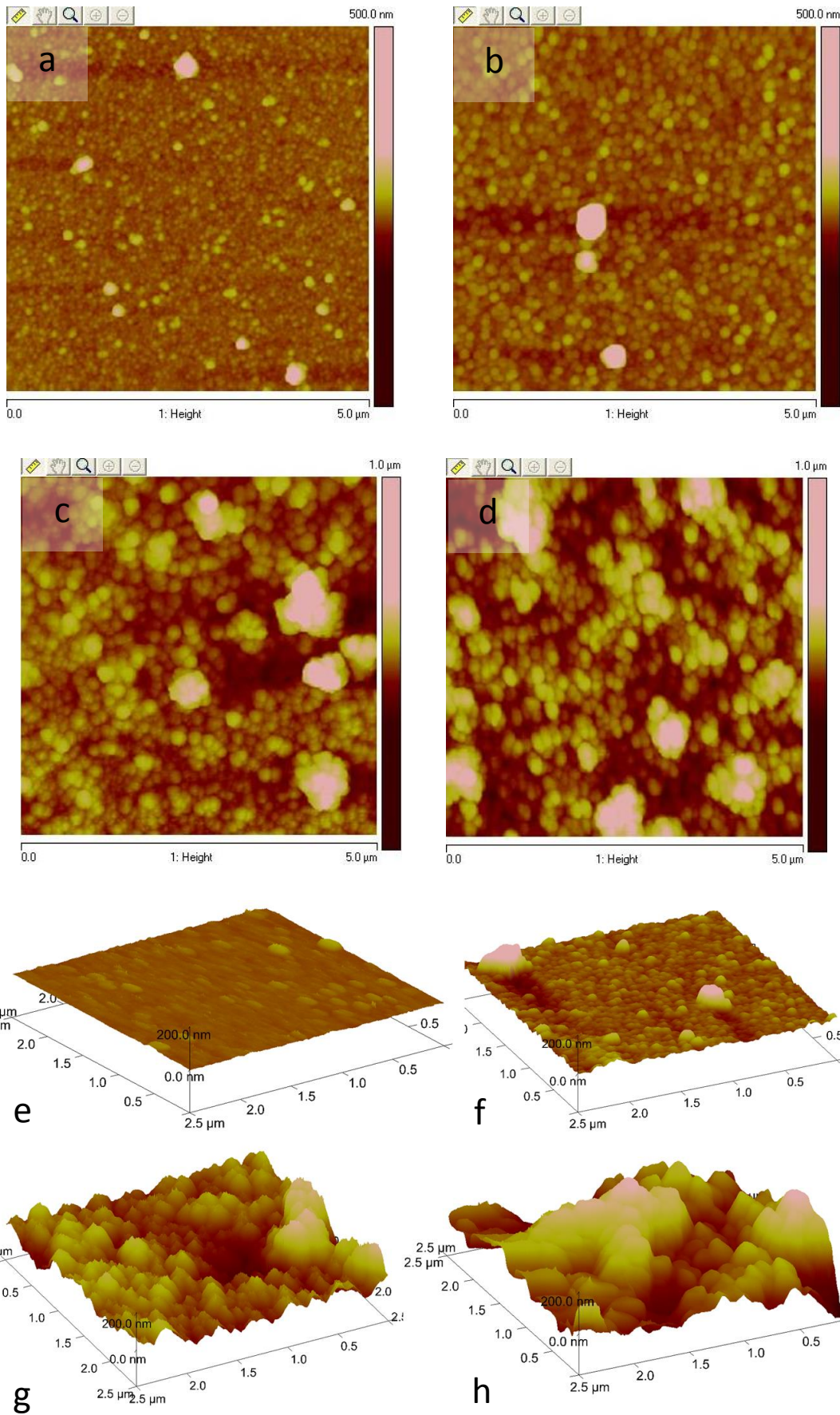


Figure 71 AFM images showing increasing roughness and 'grain' size with time (a-d) height profiles in plan for times 0.5, 10, 60 and 600sec respectively, (e-h) 3D projections of the same samples.

For example, Porter et al grew noble metals on germanium surfaces via galvanic displacement and also observed the ‘grain size’ and surface roughness increasing with plating time [59]. In addition, these authors noticed that the lustre or shine of the surfaces decreased with increasing film thickness, which correlates well with the roughness increasing in parallel to thickness.

Figure 72 shows a schematic diagram of the proposed mechanism for the growth of the secondary metal film on the nanoparticle substrate.

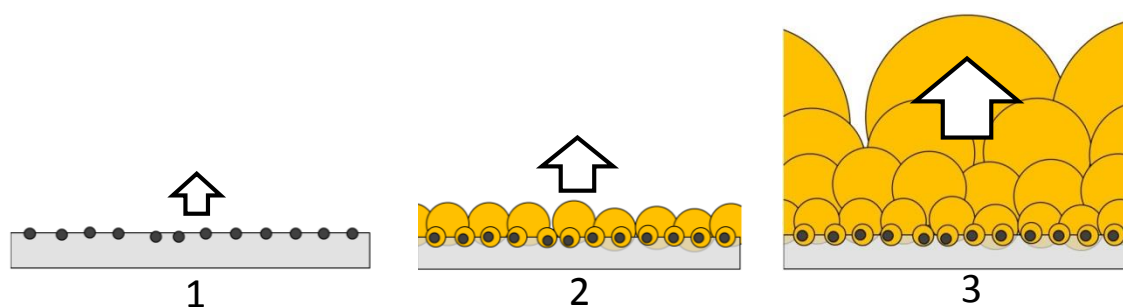


Figure 72 shows a schematic diagram of the proposed mechanism for secondary metallic film growth on a NP film.

Figure 70 shows surface roughness increasing with film thickness and Figure 71a-d show that the surface consists of increasingly large nodules of gold as the film thickness increases. The height/vertical resolution of the AFM used in these studies is on the order of 1nm however the lateral/horizontal resolution is far lower and therefore it is not possible to resolve the Pt-NPs or the initial gold growth phase. However, if we make the assumption that this trend continues and the nodular nature of the films continues to reduce in size as the gold films get thinner one can speculate that the polycrystalline film originally forms on the scale of the underlying Pt-NP adsorption density [Figure 74]. It seems likely that the film grows by a form of competition between growing nodules and that no new nucleation occurs. If this is the case and the nodules were found to be single crystals the implication would be that each large nodule on the surface of the gold film is in fact a single crystal grown from a single Pt-NP on the polymeric interface.

6.3 Metal film morphology on microcapsule 3D surfaces

6.3.1 Further evidence of Gold film growth mechanism

Analysis of model 2D gold film growth via AFM showed that films roughness increased with time and film thickness [6.2.1]. A mechanism was proposed to explain the increase in roughness observed in Figure 72.

Figure 73 shows an SEM image of a broken capsule. The edge of the metal film at the break is rolled back in a way that it is possible to image both the interior surface and exterior surface.

If we zoom in on the image we can see evidence of grain size variation from the inside to the outside, the grain size increases from the interior to the exterior. The initial secondary metal grain size appears to be comparable to the dimensions of the original adsorbed Pt-NP film. The, to scale, inset in Figure 73 is a TEM micrograph of 2D model Pt-NP adsorption density of the equivalent Pt-NP film used. The Pt-NP surface density is on the same scale as the initial crystalline gold growth on the underside of the film. This fits well with the proposed mechanism for the growth of the secondary metal film on the nanoparticle substrate described in section 6.2.1 of this chapter.

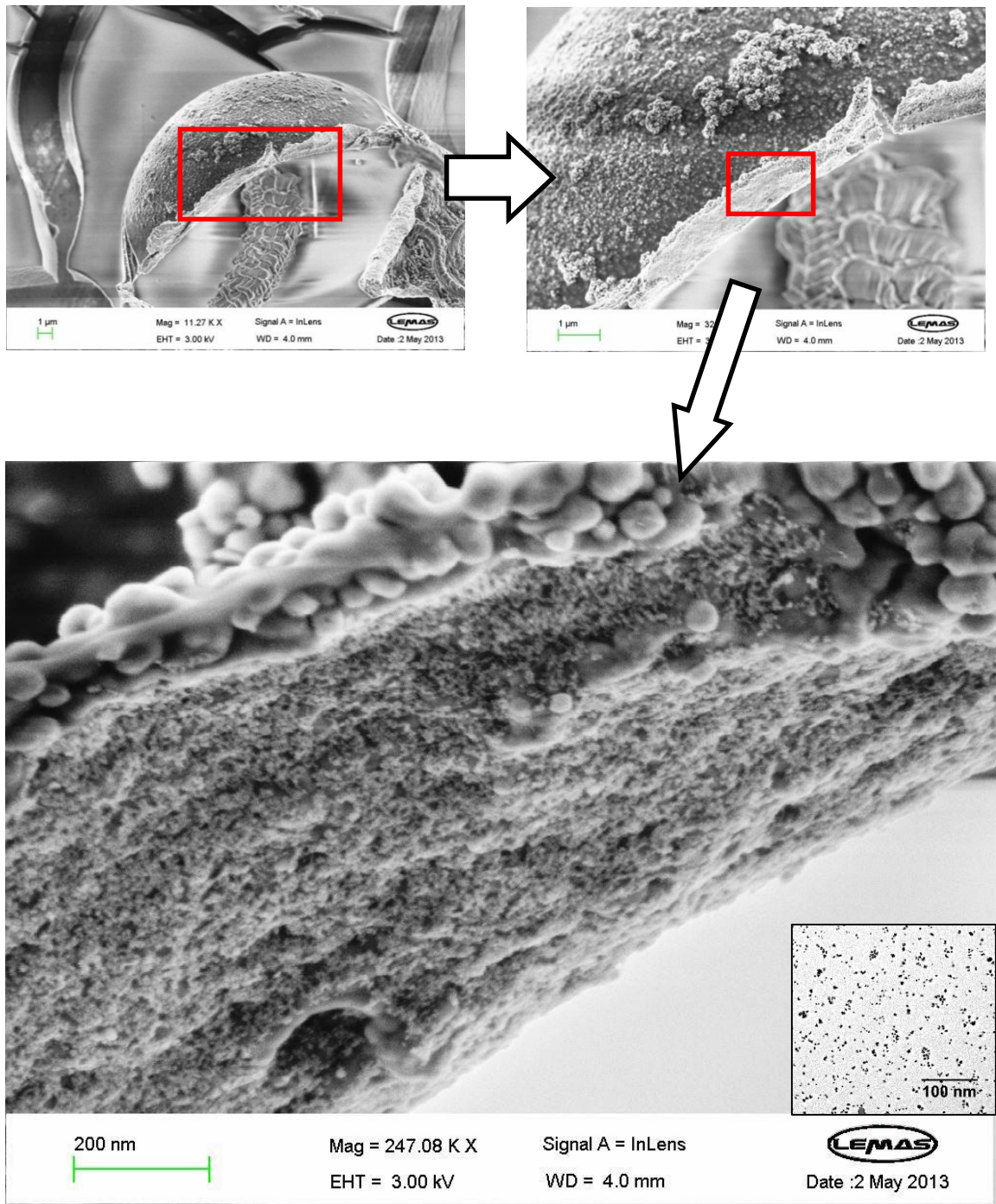


Figure 73 shows SEM evidence for grain size variation on a broken capsule. The grain size increases from the interior out and initial secondary metal gain size appears to be comparable to the dimensions of the original adsorbed Pt-NP film. Inset shows 2D model Pt-NP adsorption density of the equivalent Pt-NP film used.

6.3.2 Measuring metal film thickness from microtome capsules

Initial attempts to mechanically break the capsules via freeze fracturing were successful. ~0.5mL samples of the gold coated capsules in an aqueous continuous phase were dipped into liquid nitrogen for 30 seconds and then crushed between two glass slides (the glass slides had been precooled in the nitrogen). However, the shell morphology proved difficult to assess. Although the gold films were clearly visible, only a very small proportion of the broken capsules were oriented in such a way as to make good shell thickness measurements possible and many of the edges were folded over or twisted [Figure 74].

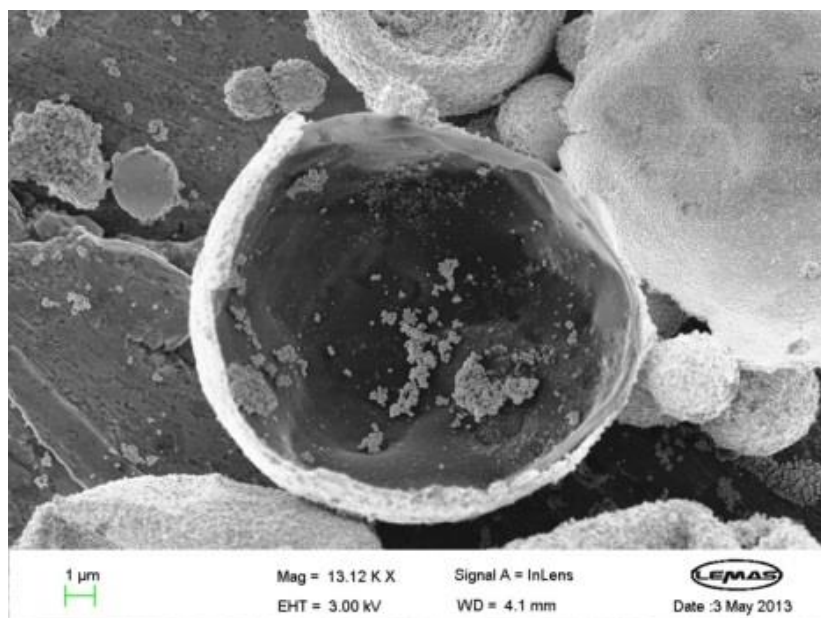


Figure 74 shows an SEM micrograph of a freeze fractured capsule showing how the gold film edges can fold and twist which prevents accurate measurement of thickness

A microtome was therefore used to observe thin slices of capsules under TEM. The gold coated capsules were suspended in ethanol and subsequently mixed into a liquid epoxy resin which was allowed to harden. The solid epoxy resin block was then microtomed to produce ~100nm thick slices which revealed the gold wall structure on each microcapsule [3.2.7]. The films were then mounted onto TEM grids.

In addition to the microtoming, focused ion beam (FIB) and electron microscopy were used to incrementally, 100nm at a time, slice through the epoxy resin block of metal coated capsules [3.2.6] and take SEM micrographs of the section through the capsules prior to each new cut.

6.3.2.1 Dealing with the four variables associated with microtome samples

Microtoming the capsules proved very successful [Figure 75]. However measuring metal film thickness was not simply a matter of measuring the mean thickness of capsules visible in the microtomed slice. The film thickness of a metal coated capsule depends on how far from the diameter the capsule is sliced. Because of the spherical shape of the metal shell, the further from the capsule equatorial diameter the slice is made the thicker the film appears to be [Figure 78]. If the sample is monodisperse it is possible to use the apparent diameter to mathematically correct for this phenomenon in a microtomed sample, however, the PEMA/Tol capsules used in this study have a polydisperse size distribution.

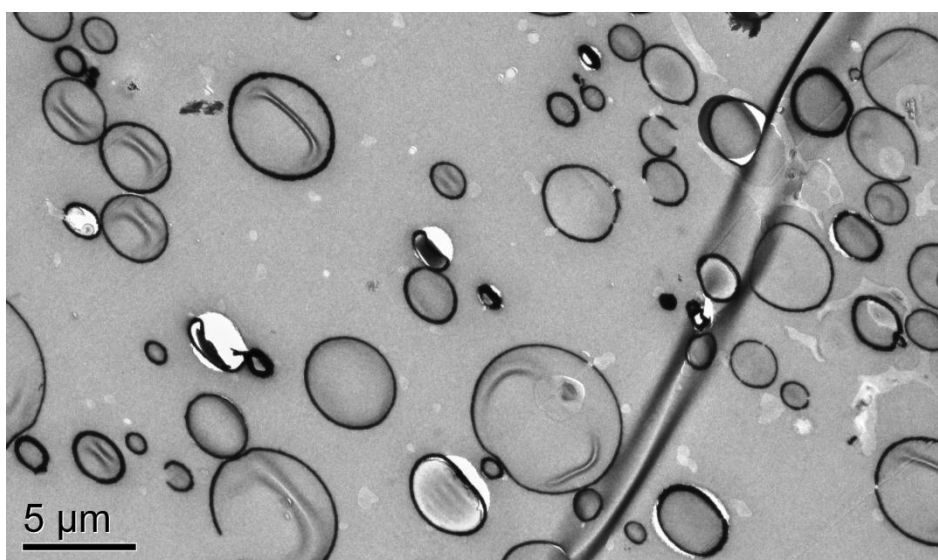


Figure 75 TEM image of a 100nm thick microtome slice through metal coated capsules set in an epoxy resin block [3.2.7].

Figure 76 shows TEM images of microtomed capsules with a range of apparent secondary metallic film thicknesses. Even in an ‘ideal’ sample where all capsules are coated with the same film thickness, variation of apparent film thickness within the sample is observed because of the variation of both capsule size and slice position.

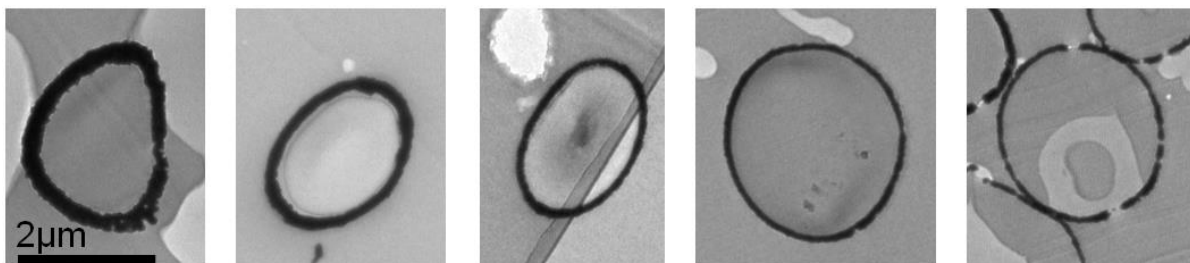


Figure 76 TEM images of microtomed capsules from the same sample showing a range of apparent secondary metallic film thicknesses. A range such as this can be found within a single sample due to the polydisperse capsule size and random capsule slice position.

If it were possible to grow exactly the same thickness metal films on all of the capsules within a polydisperse dispersion one could simply estimate the true metal film thickness as the lowest film thickness from the measured distribution of thicknesses. However, there are two other variables, which make this impossible. Firstly, the metal film has a significant roughness as compared to its thickness (since the aim here is to achieve thicknesses below 100nm) and secondly, due to inhomogeneous mixing during the electroless plating phase, there is a variation of film thickness from capsule to capsule Figure 77.

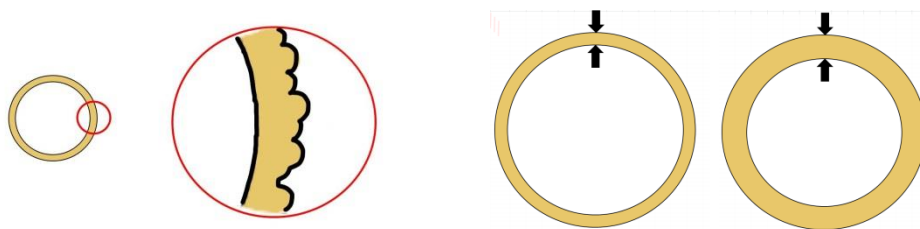


Figure 77 Schematic diagrams representing shell roughness and shell thickness between capsules, the two variables which have the action of spreading the theoretical thickness frequency distribution for a single ‘microtome’ shell.

6.3.2.2 Finding a mean shell thickness using microtome

In order to obtain a representative statistic of the metal shell thickness distribution while overcoming the above challenges, one needs to deal with 4 variables 1) the cut position relative to the equatorial diameter, 2) the polydisperse capsule size distribution, 3) the surface roughness and 4) the variation in thickness due to inhomogeneous mixing during the electroless plating phase. The paragraphs below tackle each of these variables in turn and show that it is still possible to obtain a representative mean shell thickness from the TEM measurements of the microtomes capsules.

The observed film thickness can be calculated at different distances from the equatorial diameter for an ideal metal coated capsule [Figure 78]. The radius can be divided into 1000 equal parts and the apparent film thickness can be calculated for all positions using [eq. 32]. On this basis, a plot of the frequency distribution of apparent thickness (d_{app}) for a particular capsule size (r_{cap}) and metal shell thickness (d_g) can be plotted.

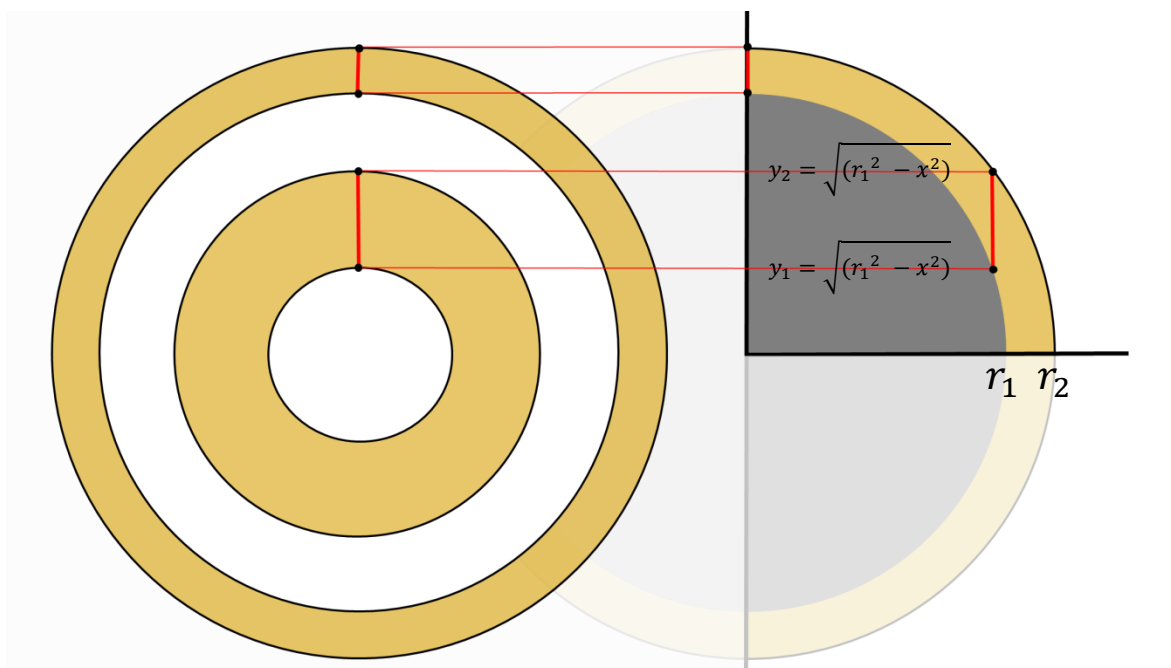


Figure 78 Schematic diagram showing that the observed film thickness of an ideal metal coated capsule depends on how far from the diameter the capsule is sliced.

Where:

r_{cap} Radius of the polymer capsule

d_g The metal film thickness

d_{app} The apparent metal film thickness

x Distance from the centre of the capsule in the x direction

y_1 Distance to the polymer capsule surface from position x in the y direction

y_2 Distance to the metal film surface from position x in the y direction

$$y_1 = \sqrt{r_{cap}^2 - x^2}$$

$$y_2 = \sqrt{(r_{cap} + d_g)^2 - x^2}$$

$$d_{app} = y_2 - y_1$$

Therefore:

$$d_{app} = \sqrt{r_{cap}^2 + d_g^2 - x^2 + 2r_{cap}d_g} - \sqrt{r_{cap}^2 - x^2} \quad \text{eq. 32}$$

Figure 79 shows the theoretical shell thickness frequency distribution for two capsules of radius 100nm and 40nm and shell thickness 5nm. It is found that, for an ideal capsule, its thickness is given by the peak of the frequency distribution curve or the 'mode'. This is because the true thickness occurs more frequently than any other apparent thickness (NB the peak appears to occur at a slightly increased thickness in Figure 79 but if enough measurements are taken and the bin limits are small enough this skewing of the data will not be observed).

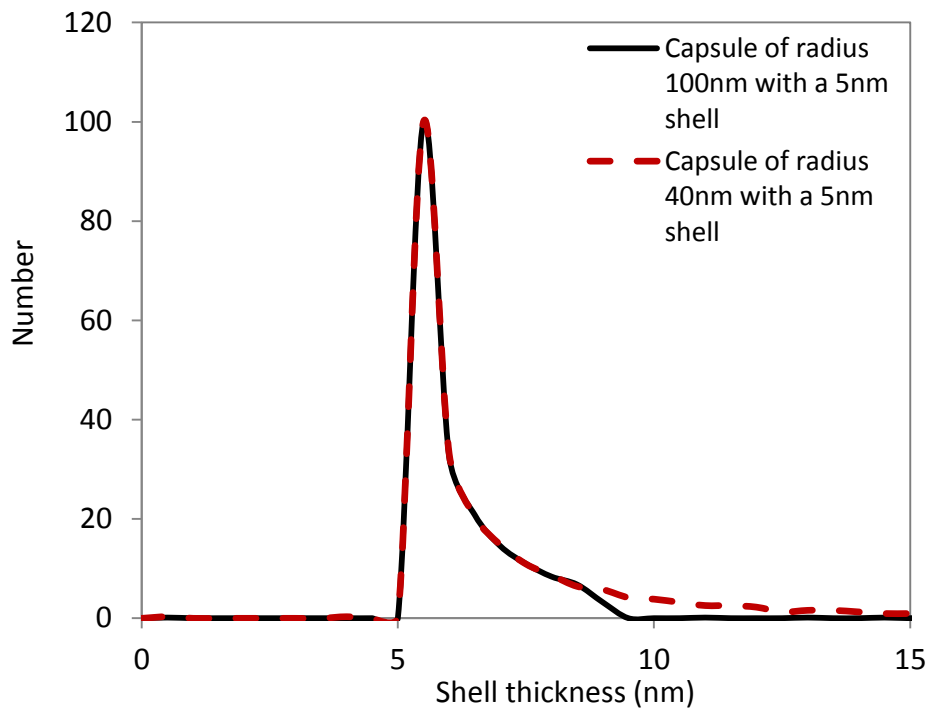


Figure 79 Theoretical shell thickness frequency distribution for spheres of radii 100 and 40nm both with a 5nm shell.

Is it therefore appropriate to simply plot an observed apparent film thickness frequency distribution for a particular microtome sample and read off the thickness at the mode and record that as our mean film thickness?

Figure 80 shows actual frequency data for one of our samples. We can see that although the characteristic expected theoretical shape due to the cut position is present, it has been spread out somewhat and the initial sharp rise observed in the theoretical plot is lost.

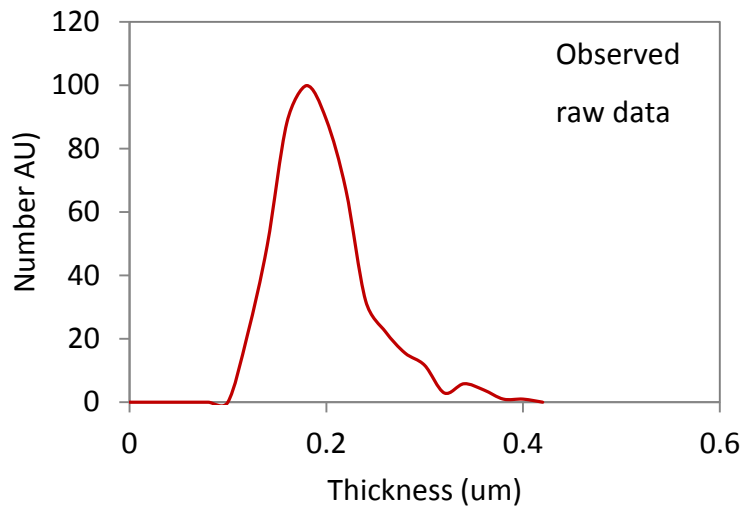


Figure 80 shows experimental frequency distribution data for a polydisperse microtome capsule sample.

We know from the theoretical work described above that variation of capsule size does not act to spread the curve. Metal film roughness and the variation of film thickness due to inhomogeneous mixing during the electroless deposition phase will both act to spread out the thickness distribution curve. However, both of these variables contribute a ‘normal’ distribution curve to the underlying data and do not skew the data or shift the peak of the curve in either a positive or negative direction.

In summary then, to measure the mean thickness of our metal films, we can ignore all 4 variables and, by simply plotting a frequency distribution of shell thickness, take the mode as the mean.

In order to further check that the microtome technique is valid, focused ion beam (FIB) and electron microscopy were used to incrementally slice through the same sample of metal coated capsules [3.2.6]. By imaging each slice, we were able to construct a video of the cut progression through the block [Figure 81].

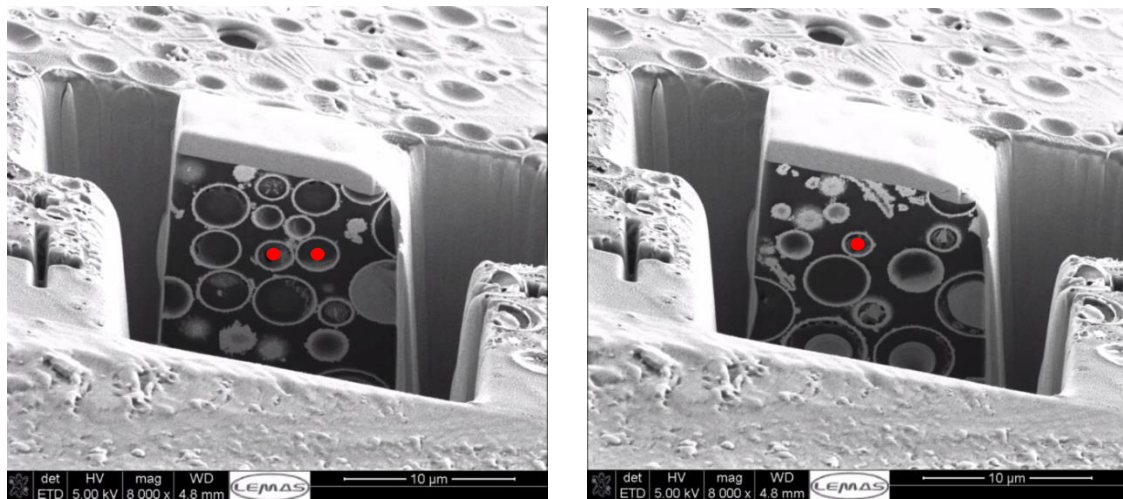


Figure 81 SEM images of different slices of a block of capsules set in epoxy resin. The red dots in show capsules in a different volume of the sample that have been cut through the diameter

Unlike for the microtomed sample observation via TEM, here it was possible to determine each capsule equatorial diameter and therefore remove the characteristic curve formed when cuts are made randomly through the sphere at different positions away from the equatorial diameter. The red dots in Figure 81 show capsules, for which the depth of observation (i.e. the extent at which the FIB had slices through the sample) corresponds to the equatorial diameter of the capsules. The frequency distribution for the FIB data is now purely due to the variation in shell thickness and roughness across the sample and is not a function of cut position. Figure 82 shows an overlay of the frequency distribution for the FIB data and the microtome data measured and calculated for the same sample using the methods described. As expected here, the thickness distribution peak has not shifted, which confirms that surface roughness and shell thickness do not affect the position of the peak.

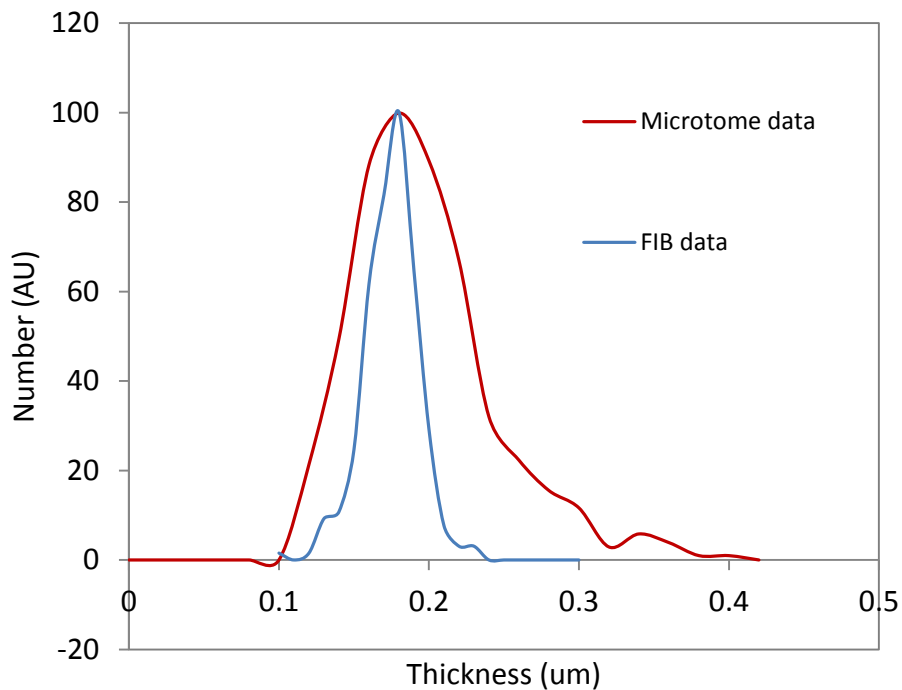


Figure 82 Frequency distribution of gold film thickness of a sample of microcapsules formed in a 0.73M gold salt plating solution. The two distributions compare data from 100nm thick microtomed capsules samples [3.2.7] and thickness measurements taken directly from FIB [3.2.6].

FIB is a relatively expensive and time consuming method for analysing capsule cross-sections. In addition to this, sampling is limited to a relatively small number of capsules. Microtoming is less expensive, less time consuming and provides a relatively large number of capsules for sampling. From this point, measurements of microcapsule metal shell thickness via microtome and TEM will be considered a reliable technique and be used to obtain this information and to compare data when investigating the influence of synthesis variables.

6.3.3 Microcapsule gold film thickness as a function of plating solution concentration (PEMA/Toluene core capsules)

The microtoming technique, described above, was used to measure gold film thicknesses as a function of metal salt plating solution. Toluene core, PEMA shell microcapsules [3.3.1] were coated in a Pt-NP film using the standard coating method [3.3.3]. In order to maximise the Pt-NP adsorption density, NPs synthesised with using

0.015wt% of PVP stabiliser were used in excess at a concentration of $4.6 \times 10^{15} \text{mL}^{-1}$ [5.4.4]. The Pt-NP density is therefore expected to be comparable to Figure 51d in the previous chapter.

The reducing agent concentration and the percentage of the original capsule dispersion being metal coated was kept constant, which ensured capsule number and capsule total surface area used remained the same. In this case, only gold salt concentration was varied.

Each sample was then processed for microtoming and 100 nm thick slices of capsules were observed using TEM. Wide field TEM micrographs of the microtomed capsules were used. Images approximately $50 \mu\text{m}$ square were used to measure gold film thickness [Figure 83]. Five thickness measurements were taken from each capsule in the slice, these 5 thicknesses were then averaged for each capsule.

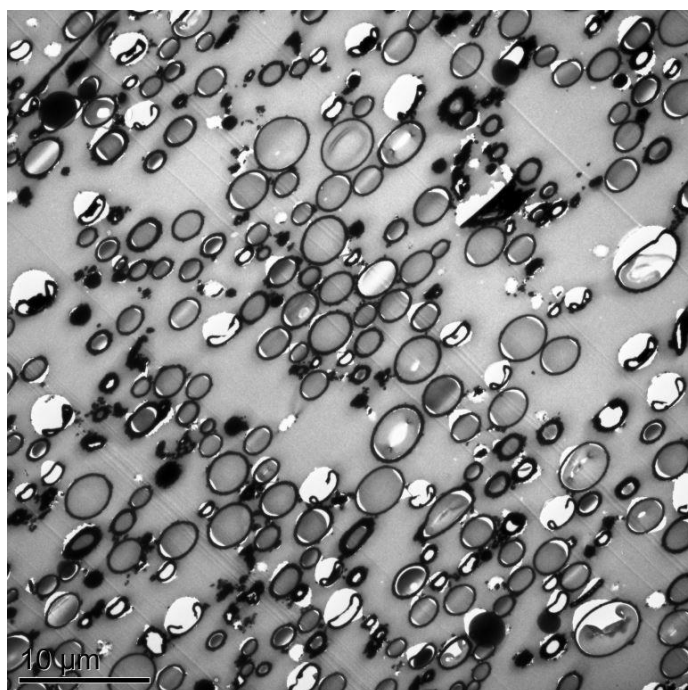


Figure 83 Typical wide field TEM micrograph of $\sim 100 \text{nm}$ thick microtome gold coated capsules in epoxy resin [3.2.7].

As described in section [6.3.2.2], the frequency distributions for each gold salt concentration were plotted and the mode of each distribution was taken as the mean thickness. Mean shell thickness was then plotted as a function of gold salt concentration [Figure 84]. Using the standard deviation of the raw data doesn't take account of the variation in film thickness due to the variation of the cut position relative to the equatorial position. Standard deviation was therefore calculated by taking the standard deviation of the raw film thickness measurements and subtracting the standard deviation of the theoretical data used to generate the theoretical shell thickness frequency distribution at the same peak shell thickness. In other words the standard deviation due to the cut position was removed.

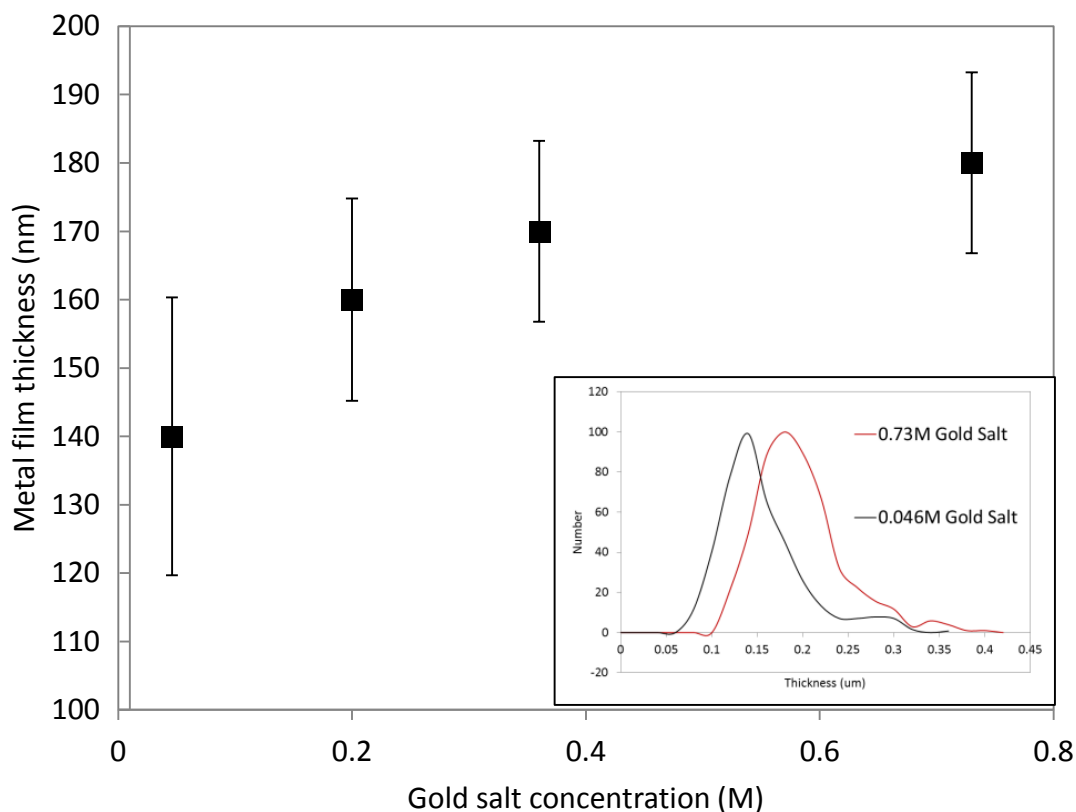


Figure 84 Microtome data showing gold film thickness as a function of gold salt concentration used on the electroless plating solution.

Figure 84 shows mean metal film thickness increasing with increasing gold salt concentration in the plating solution. As the salt concentration drops to zero we know that the film thickness also drops to zero and therefore any fitted curve must pass

through the origin. Therefore the relationship between gold salt in the plating solution and the resulting capsule metal film thickness was shown to exponentially approach a plateau.

The volume of gold introduced can be calculated from the volume of gold salt introduced and the concentration. We can then use this volume and the calculated surface area of capsules introduced [4.1.2] to calculate the expected gold film thickness if 100% of the gold salt introduced were to be converted to solid gold film. In Figure 85 the gold film thickness at 100% conversion of gold salt is plotted as a function of gold salt concentration and is overlaid on the actual measured gold film thicknesses for the different gold salt concentrations.

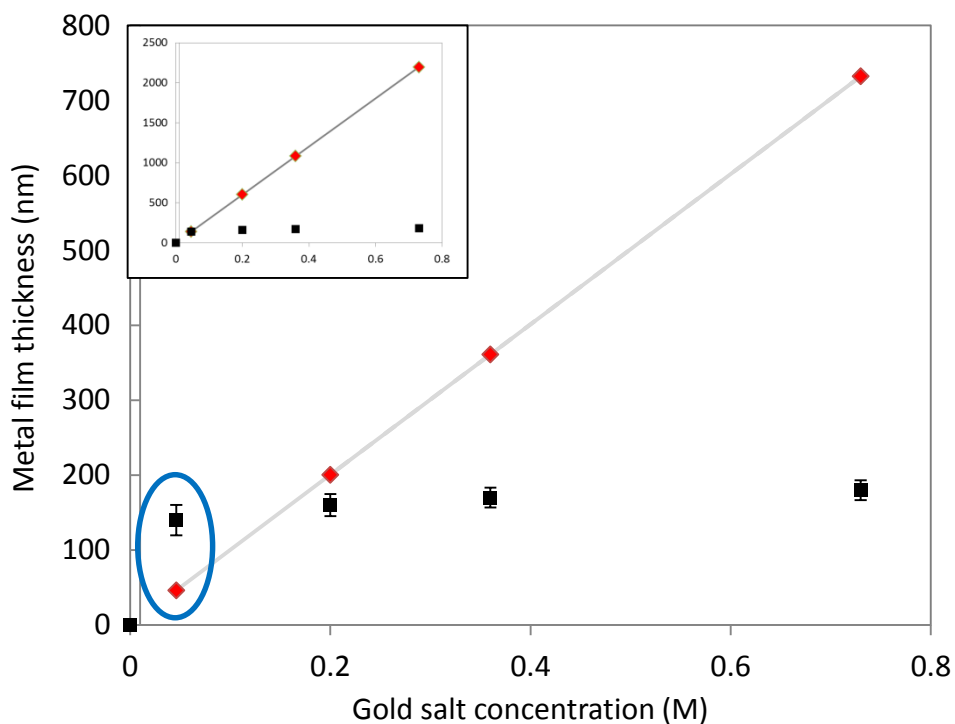


Figure 85 shows the calculated gold film thickness at 100% conversion of gold salt, plotted as a function of introduced gold salt concentration (red diamonds) and is overlaid on the actual measured gold film thicknesses for the different gold salt concentrations (black squares). The inset shows the same graph but with the calculated film thickness corrected for a 2/3 loss of capsules during the synthesis wash cycles.

Figure 85 shows that the calculated gold film thickness (assuming 100% conversion of gold salt to gold film) varies linearly with introduced gold salt concentration. Interestingly, at a concentration of 45mM (Figure 85 circled in blue) the calculated

maximum possible film thickness is a factor of 3 less than the actual measured film thickness. The method of synthesis used to make these gold coated capsules required 6 separate wash cycles, 3 after capsule formation [3.3.1] and 3 after the Pt-NP adsorption phase [3.3.3]. The explanation is that we are losing at least 2/3 of the available surface area during the wash cycles (The slower settling rate of smaller capsules which contribute to the overall surface area relative to their volume, are more easily lost, therefore we can't for certain say that we are losing 2/3 of the actual capsules).

If the calculated thickness measurements are increased by a factor of 3 [Figure 85 inset] it is clear that at all but the lowest gold concentration there is a large excess of gold which is not used to make the films. The plateauing of the measured gold film thickness can't therefore be attributed to depletion of the gold salt from the continuous phase and, in all but the lowest gold salt concentrations used in this study, the gold is being used inefficiently.

With this system we demonstrated successful coating of polymer capsules with a thick metallic shell however, initial attempts to characterize release from these capsules highlighted challenges with small core volumes when using toluene as a core therefore we didn't minimize the shell thickness for this system but instead developed capsules with a new core (hexyl salicylate [3.3.1]).

6.5 Oil core release and gold film thickness as a function of temperature (Hexyl salicylate core capsules)

6.5.1 Oil core release study (Hexyl salicylate core capsules)

The potential of metallic shell capsules for “permanently” encapsulating low molecular weight, volatile molecules within a continuous phase that can dissolve the encapsulated actives is demonstrated in this section.

Polymer capsules are porous and are known to allow diffusion of the core into the external environment, particularly if there is a high solubility of the core in the continuous phase. Here, the potential of the developed metal shell capsules for retaining a volatile oil within their core is compared to that of the precursor polymer-shell capsules. The procedure for monitoring the release of the oil from both sets of capsules is described in section [3.3.5] As previously mentioned, toluene proved to be a suitable system to test the nanoparticle adsorption and subsequent secondary metal film growth, its relatively high solubility in water ($\sim 0.52 \text{ g}\cdot\text{L}^{-1}$ at $25 \text{ }^\circ\text{C}$) prevented its use for release testing. Thus, the oil used here is hexyl salicylate. It has poor water solubility ($\sim 9 \times 10^{-4} \text{ g}\cdot\text{L}^{-1}$ at $25 \text{ }^\circ\text{C}$) which is advantageous as compared to the use of toluene. This ensures maximum core retention through the precursor polymer capsules preparation and washing procedure before porosity testing (at $40 \text{ }^\circ\text{C}$) in 4:1 ethanol/water mixtures.

In this case, polymer capsules produced from an oil emulsion template [3.3.1] were coated with Pt-NPs and a secondary continuous film of gold, as described in sections [3.3.3] and [3.3.4.1] respectively. Characterization of the release of hexyl salicylate was performed using gas chromatography for both sets of capsules.

Figure 86 shows that the bare polymer capsules release their entire contents into the ethanol–water mix within 20 min. When a gold film is grown on the surface of the precursor polymer capsules, only a small fraction of the initially encapsulated oil is

released, (typically smaller than the error associated with the measurement) over the 21 day test period. By mechanically fracturing the metal-coated capsules (as demonstrated in the inset of Figure 86) and testing the sample again for core release, we measured a release of 49% of the initial hexyl salicylate oil present in the precursor polymeric capsules, thus confirming the presence of encapsulated oil within the metal shell microcapsules. The fact that not all of the oil was recovered from the mechanically fractured capsules is likely due to loss of material during the fracturing procedure and because not all capsule shells were successfully broken.

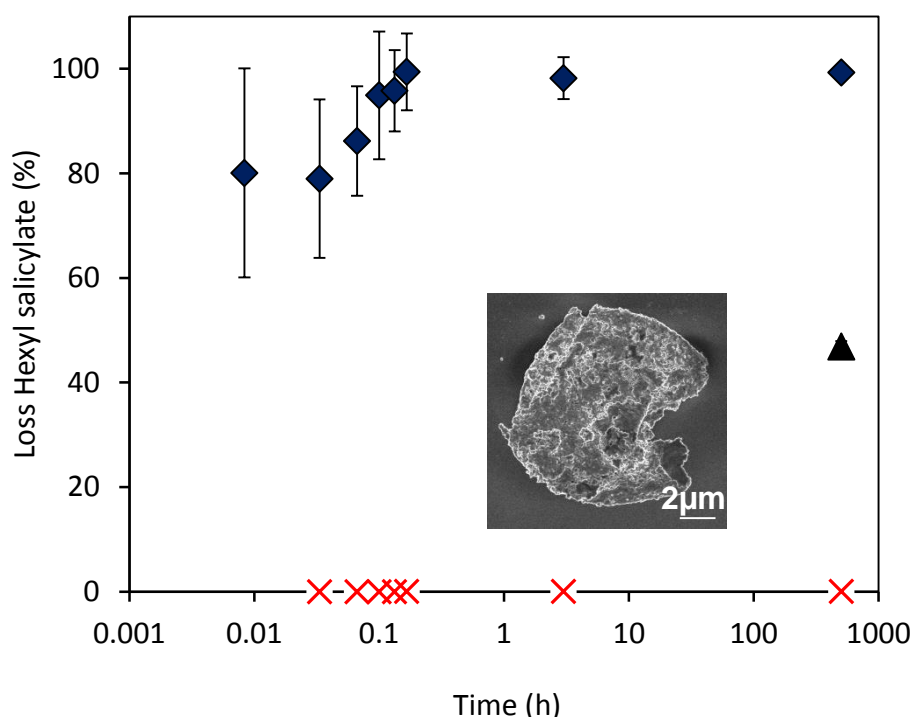


Figure 86 Hexyl salicylate release profile from PMMA capsules (◆) and gold coated PMMA capsules (x), placed in 4:1 ethanol:water at 40°C. The level of encapsulated oil released from mechanically fractured gold coated capsules (after residing in ethanol:water mixture for 7 days) is indicated by ▲. Inset – An SEM image of a mechanically fractured gold coated PMMA capsule with hexyl salicylate core. These data were not collected experimentally by myself but are part of the overall effort of our research group to demonstrate this technology on polymer microcapsules, however they have been published in the article placed in appendix [87] [Appendix section 9].

Long term encapsulation of small, volatile molecules was one of the primary aims of this thesis and therefore the successful encapsulation of hexyl salicylate demonstrated here is important.

6.5.2 Gold film thickness as a function of temperature (Hexyl salicylate core capsules)

This part of the work investigates the effect of the electroless plating reaction temperature over the shell thickness of the metal film produced and its resulting permeability. By reducing the reaction temperature for the metal growth, it is expected that we will obtain thinner metal films as a consequence of a slower reaction rate [88]. Growth of thinner metal films is a potential cost advantage with regards to a manufacturing process provided the capsule impermeability can be retained.

Figure 87 shows that as the temperature is decreased, the measured shell thickness (via TEM of microtomed samples and subsequent image processing [3.2.7]) does decrease significantly from 150nm to 60nm. However, above 60 °C, the film thickness appears to reach a plateau.

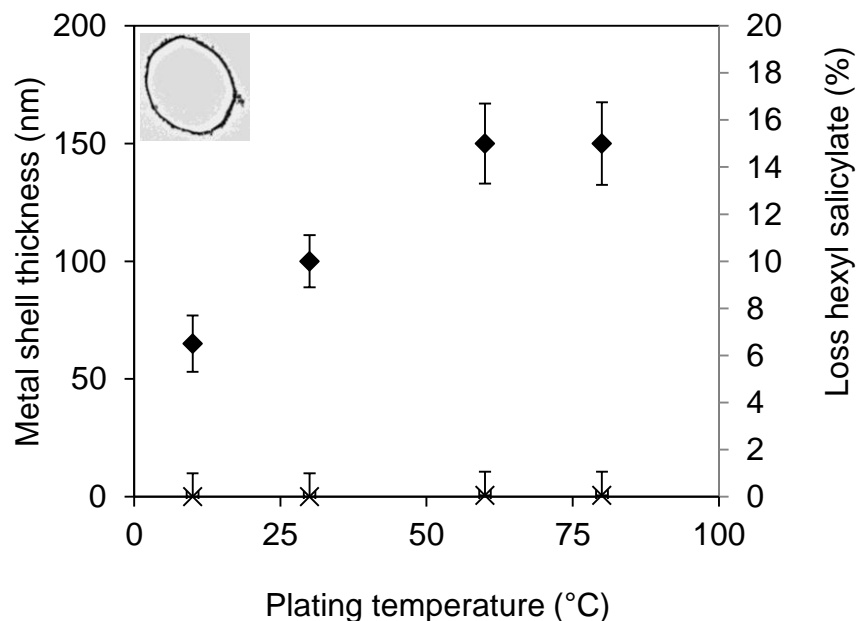


Figure 87 Thickness of metal shell as a function of plating temperature (◆), measured from microtome images using TEM, and release of core as a function of plating temperature (4:1 ethanol:water mixture for 7 days at 40°C) (X). Inset – A TEM image showing a microtomed capsule from which shell thicknesses are measured. These data were not collected experimentally by myself but are part of the overall effort of our research group to demonstrate this technology on polymer microcapsules, however they have been published in the article placed in appendix

Release studies conducted for the four samples of capsules obtained by varying the film growth temperature all show no significant release (a maximum of 0.1wt%, which is within experimental error) of the encapsulated oil into the water/ethanol bulk phase. The full retention of the core oil implies that a complete impermeable shell is formed in all cases independently of its thickness. It is expected that further optimisation of the metal film growth conditions could lead to sub 10 nm impermeable films.

6.6 Conclusion

Continuous homogeneous metal films were successfully grown on both 2D model systems (PEMA films) and 3D polymeric microcapsules (Toluene core/PEMA shell). In both cases platinum nanoparticulate films of known high surface density were used as a catalyst for the electroless deposition of complete secondary metallic films of gold.

For the 2D model system, PEMA films with a thickness of ~3nm were successfully spin coated onto glass slides and used as substrates for metal film growth. AFM and SEM were successfully used to analyse the effect of time and temperature on the secondary metallic films morphology. Film thickness and roughness were both shown to increase with time and temperature. A two stage growth rate was observed, the catalytic Pt-NP surface initially promoted rapid gold film growth followed by slower autocatalytic gold on gold film growth.

The increase in film roughness as films increased in thickness was shown via SEM and AFM to be due to increasing gold nodule size. Capsule freeze fracture was used to image the interior surface of a formed gold film via SEM. Initial gold nodule size and spacing was shown to be on the same order as the underlying nanoparticles in the Pt-NP film.

A technique was developed and employed to measure gold film thickness on polymeric capsules via microtome and TEM. It was shown that although the thickness of the microtomed capsule sections were subject to several variables, the median or peak of film thickness distribution curves was a good measure of the mean thickness of the

sample. Mean metal film thickness was shown to increase with increasing gold salt concentration in the plating solution. The relationship between gold salt in the plating solution and the resulting capsule metal film thickness was shown to exponentially approach a plateau.

Expected gold film thickness at 100% conversion of gold salt was calculated from gold salt concentration and calculated available capsule surface area. It was shown that calculations of capsule surface area were at least a factor of 3 too high due to unaccounted for losses during wash cycles. It was shown that in all but the lowest gold concentrations used, a large excess of gold salt is used to make the films. Therefore the plateauing of the measured gold film thickness can't be attributed to depletion of the gold salt from the continuous phase.

In order to validate the method used to measure film thicknesses using the technique developed to analyse microtome samples, FIB and SEM were used to incrementally slice through the same samples of metal coated capsules. A video of the cut progression through the block was constructed and therefore capsule equatorial diameter could be found and film thicknesses at that diameter could be measured and averaged. Film thickness measurements found using this method fitted well with measurements made from the same sample using the technique developed to analyse microtome samples.

Hexyl salicylate core, PEMA shell microcapsules were used to demonstrate the potential of metallic shells for 'permanently' encapsulating low molecular weight, volatile molecules within a continuous phase that can dissolve the encapsulated actives. Bare polymer capsules release their entire contents into the ethanol-water mix within 20 min. When a gold film was grown on the surface of the precursor polymer capsules, only a small fraction of the initially encapsulated oil is released over the 21 day test period. By mechanically fracturing the metal-coated capsules and testing the sample again for core release, 49% of the initial hexyl salicylate oil present in the precursor polymeric capsules was measured, thus confirming the presence of encapsulated oil within the metal shell microcapsules.

The hexyl salicylate core, PEMA shell microcapsules were used to measure secondary metal film thickness as a function of gold plating solution temperature. As the temperature is decreased, the measured shell thickness decreases significantly from 150nm to 60nm. Above 60 °C, the film thickness appears to reach a plateau. Release studies conducted for the samples of capsules obtained by varying the film growth temperature all show no significant release of the encapsulated oil into the water/ethanol bulk phase. The full retention of the core oil implies that a complete impermeable shell is formed in all cases independently of its thickness. It is expected that further optimisation of the metal film growth conditions could lead to sub 10nm impermeable films.

7 Metal films grown directly on emulsion droplet surfaces

7.1 Synopsis

This relatively short chapter describes an exploratory method for growing a complete gold film around a Pt-NP stabilised hexadecane emulsion droplet and describes the evolution of the method. This work was only possible because of the knowledge gained in chapter 0 understanding how and why Pt-NPs adsorb at an interface.

The explanations for the success of this work are currently somewhat speculative due to the lack of a fully systematic study. Nonetheless, ethanol stability studies are used here to successfully demonstrate the permanent encapsulation of an oil phase in water using this technique; demonstrating that a complete secondary metallic shell has been formed. Although preliminary, this work warrants inclusion in this thesis.

In order to stabilise an oil-in-water emulsion with Pt-NPs creating a nano-particulate Pickering emulsion onto which a metal coating can be grown, we need to consider the following.

- The NPs must have an affinity for the oil water interface. In addition, the energy of adsorption must be significantly larger than the background thermal energy (kT) because the Pickering emulsion needs to be stable even when there are little or no Pt-NPs in the continuous phase (i.e. after washing [3.3.3.2]). This is necessary to limit the precipitation/reduction of gold on excess Pt-NP's in the continuous phase.
- There needs to be little excess PVP polymeric stabiliser left over from the Pt-NP synthesis in order to maximise the adsorption of Pt-NPs and minimise the adsorption of the free PVP polymer [5.3.1].

- The NP dispersion needs to be sufficiently concentrated. Chapter 5 [section 5.4.4] shows that a low concentration favours the diffusion of the bare PVP over the Pt-NP and therefore should favour bare PVPs adsorption at the oil water interface.
- The individual droplets in the resulting Pickering emulsion need to be robust enough to remain coated with a full film of NPs during likely turbulent flow during agitation/washing and droplet / droplet interaction when the emulsion creams (there are little or no NPs in the continuous phase to ‘plug’ any gaps). This may favour smaller droplets.

7.2 Pickering emulsions formed using high purity Pt-NP dispersions

Attempts to grow secondary metallic films on oil/water emulsions stabilised with Pt-NPs which were synthesised with relatively high PVP concentrations (commonly used in the literature) were unsuccessful. This was thought to be due to the excess PVP in the dispersion adsorbing at the oil water interface instead of the Pt-NPs which results in poor secondary film coatings due to the low surface density of catalytic NPs.

Pt-NPs dispersions synthesised with very low excess PVP stabiliser at high concentrations were shown to successfully stabilise oil in water emulsions [Figure 88].

The Pt-NPs which proved successful were synthesised with 0.0015wt% PVP and 0.23wt% Pt salt and therefore had little excess PVP left over from the synthesis [5.3.2]. 0.1mL of hexadecane was homogenised with 10mL of the Pt-NP dispersion for 2 minutes [3.3.2]. The resulting Pickering emulsion creamed in minutes and was then washed to remove the excess Pt-NPs [3.3.3.2]. The emulsion was then redispersed and electroless plated using the standard plating solution [3.3.4.3].

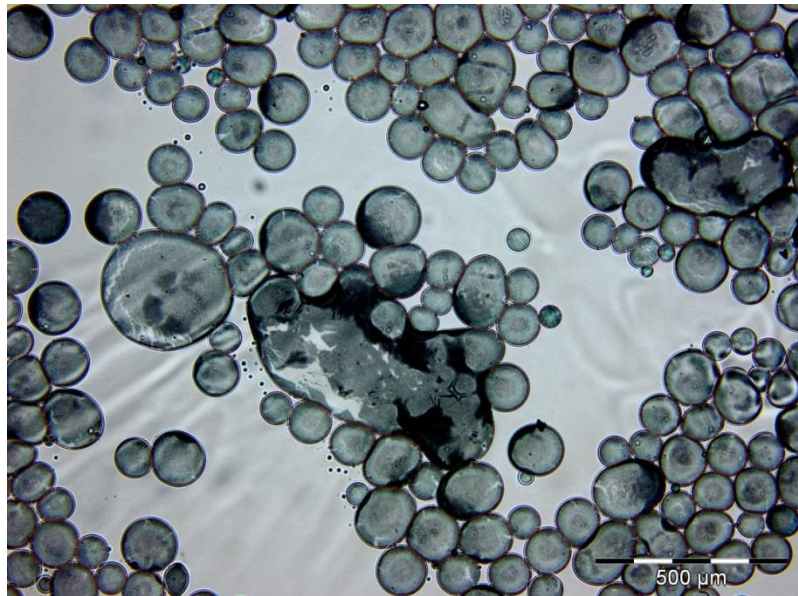


Figure 88 Optical microscopy of Pt-NP stabilised hexadecane emulsion droplets (pre secondary metal growth stage). Homogenised at 15Krpm for 2 min and then gentle agitated by hand for 30 seconds [3.3.3.2].

The resulting emulsion was large (~140 μ m diameter). After the wash cycle, under optical microscopy, cracks could be seen in the Pt-NP surface on a high proportion of the emulsion droplets. Electroless plating did not result in microcapsules with continuous secondary metallic films due to the lack of Pt-NPs in the cracks. Ethanol stability studies [3.3.5.1] showed 95% release of the hexadecane.

7.2.1 Reducing the emulsion size distribution to increase droplet stability

Small emulsion droplets have a higher surface area volume ratio than larger droplets. Therefore, although the surface tension/energy between the two phases is the same any change from a spherical shape has a higher energetic cost. Put another way, altering the shape of a large emulsion droplet costs less energy per unit volume than a small droplet. In order to make the emulsion droplets more robust and less prone to surface cracking the homogenisation speed was therefore increased from 15Krpm to 23Krpm in order to reduce the size of the resulting emulsion.

Figure 89 shows optical micrographs of Pt-NP stabilised emulsion droplets homogenized at 15Krpm and 23Krpm.

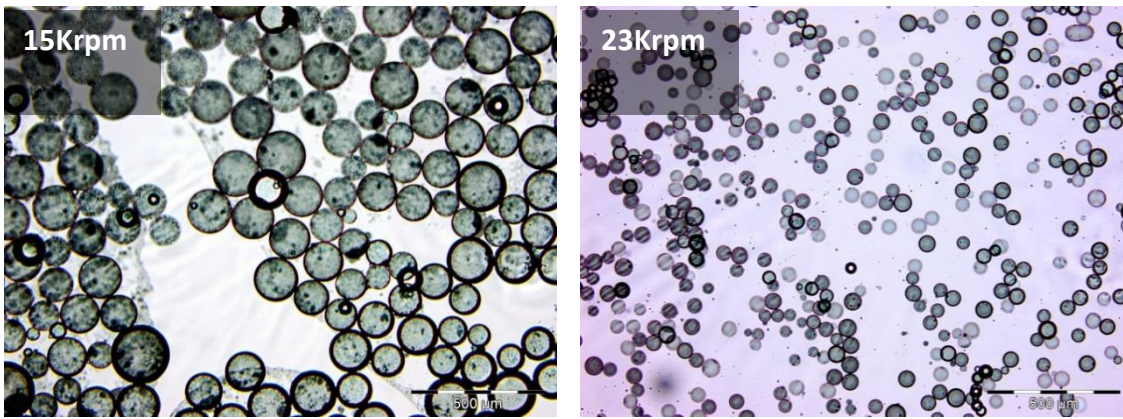


Figure 89 Optical microscopy of Pt-NP stabilised emulsion droplets. Images show emulsion droplets homogenized at a) 15Krpm 5 min and b) 23Krpm for 5 min.

The resulting, smaller, more robust emulsion droplets showed little or no surface cracking even after several wash cycles and good secondary metal films formed during the electroless plating step [Figure 90a].

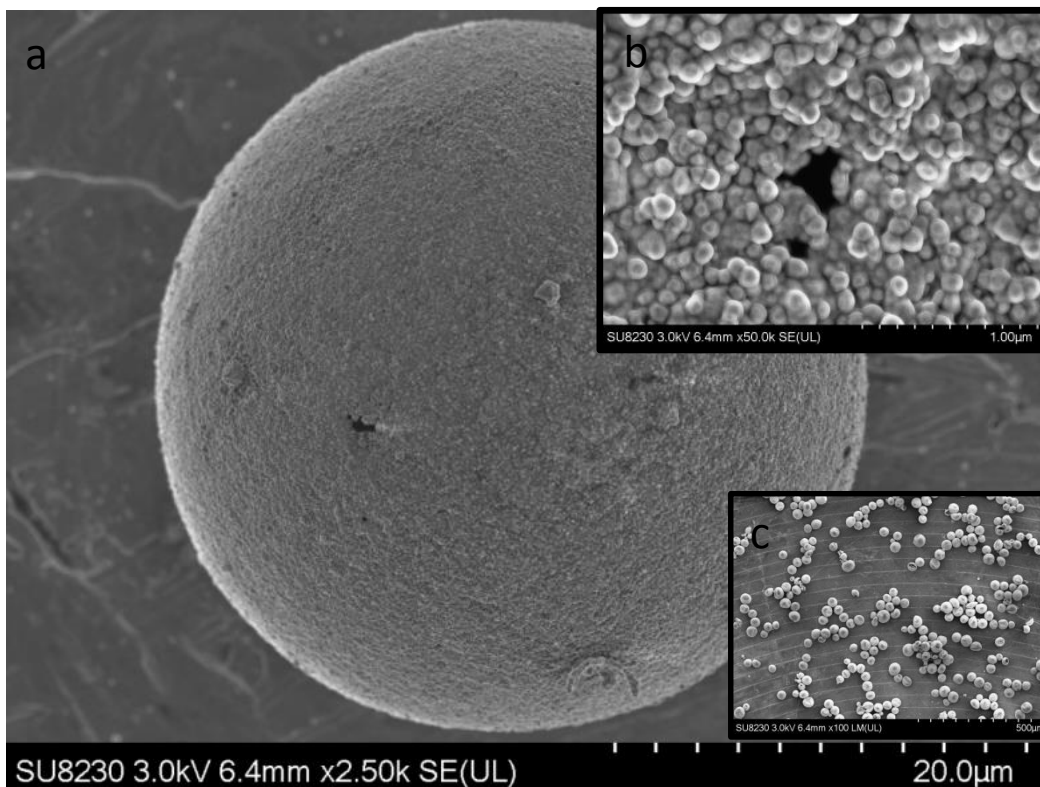


Figure 90 SEM micrograph of (a) a representative gold coated emulsion droplet showing pinholes in the metal film and (b) a zoomed in micrograph of one of the pin holes and (c) a wide field image of the capsules.

However, SEM images revealed small semi-regular spaced holes in the secondary metal film [Figure 90b]. These holes were thought to be due to damage caused to the primary Pt-NP film at droplet-droplet contact points when the emulsion creamed after each wash cycle. It seems likely that the buoyancy of the hexadecane core is sufficient to 'compress' the creamed layer such that the steric stability provided by the PVP on the Pt-NP film, on the surface of the emulsion droplet, is overcome. As a result Pt-NP on adjacent Pickering emulsion droplets come into close contact and adsorb to one another. When the cream is redispersed the Pt-NP film becomes punctured at these points.

Ethanol stability tests showed approximately 80% release of the oil phase from these capsules. The implication being that 20% of the capsules have complete secondary metal films and kept the hexadecane core from dissolving in the ethanol phase. This was therefore encouraging, the following work was carried out to further improve the capsules.

7.2.2 Pickering emulsion 'aging'

It was subsequently found that emulsions formed by emulsifying at 23K rpm, when left on a carousel for 24 hours with excess Pt-NPs in the continuous phase [3.3.3.2] underwent a form of limited coalescence coupled with Pt-NP film multi-layering. This is potentially combined with an Ostward ripening process however this is expected to be small because the variation in size of the emulsions is relatively small.

Figure 91 shows the change that occurs when the newly made Pickering emulsion is left on the carousel for 24 hours. The emulsions size increases and becomes more polydisperse. Several of the droplets become non spherical.

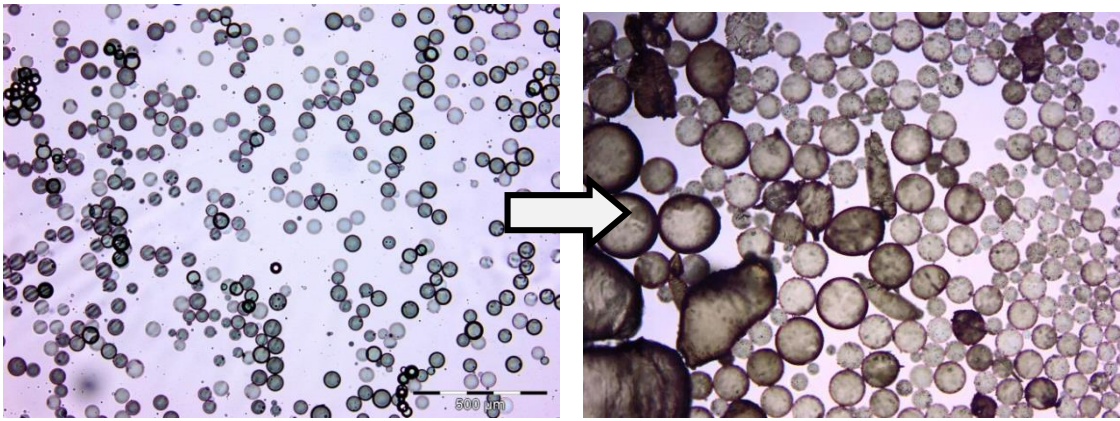


Figure 91 Optical microscopy showing the difference in capsule size and morphology when left on the carousel for 24 hours in excess NP dispersion – multi-layering and size distribution becomes larger.

Figure 92 shows a zoomed image of a single emulsion droplet that has undergone this ‘aging’ process. The stabilizing NP film clearly shows some multi-layering. It was also noticed that the Pt-NP films remained stable as films even when emulsion droplets were broken with glass slides and the films themselves became free of the oil/water interface.

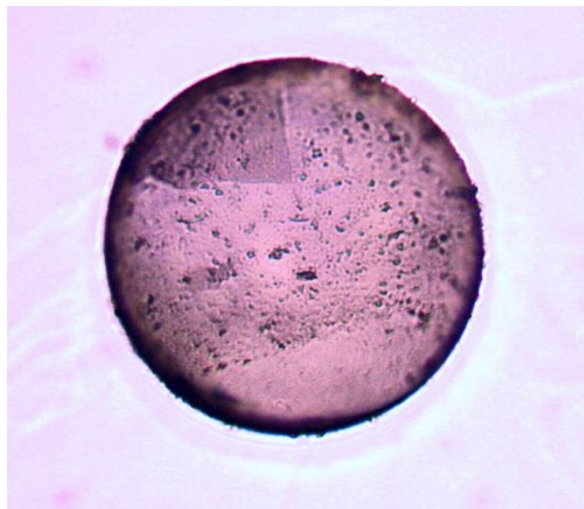


Figure 92 shows a single Pt-NP stabilized emulsion droplet that has undergone limited coalescence. The stabilizing NP film clearly shows some multi-layering

7.2.2.1 Is limited coalescence occurring in our system?

Limited coalescence is a mechanism whereby one phase (usually oil) is dispersed, via some form of homogenisation, in a continuous phase (usually water) containing a particulate stabiliser. In some cases the initial homogenisation step creates a sufficiently large surface area emulsion that the stabilising particles are insufficient in number to completely coat the emulsion droplets. In this case the resulting Pickering emulsion droplets coalesce, in a limited way, so as to lower the total surface area of the emulsion to the point at which the total surface is completely covered with particles. This gives rise to highly stable Pickering emulsions with relatively low size polydispersity [89].

Our system coalesces during the 24 hour aging phase, the size distribution increases and some droplets become non spherical. Can this aging process be described as limited coalescence?

It would appear that during the aging process two mechanisms are occurring simultaneously. Droplets are coalescing to form larger, often non spherical emulsion droplets and the Pt-NP films are becoming thicker due to multi-layering [Figure 91 and Figure 92].

Post homogenisation excess NPs were clearly present in the continuous phase, it remained dark and only cleared approximately 3 hours into the aging process. A requirement of limited coalescence is that there are an insufficient number of particles in the continuous phase to stabilise the emulsion drop surface post homogenisation.

The size distribution would appear to be increasing through coalescence of the emulsion droplets. However, upon detachment from the emulsion droplet surface Pt-NPs remain as stable NP sheets and do not redisperse. A requirement of true limited coalescence is that the particle stabiliser is able to reorganise, as a particle and not a stable film, on coalescing particles surfaces. Detached Pt-NP films are also able to 're-adsorb' to other emulsion droplets forming multilayers [Figure 92].

It would seem then that the system is not undergoing true limited coalescence during this aging phase.

The fact that once formed the Pt-NP films remain stable as films, even on detachment from the emulsion droplet surface, justifies the use of the term colloidosome when describing the Pt-NP stabilised emulsion droplets.

7.2.2.2 What is the mechanism for multi-layered stable film growth?

Figure 93 shows optical micrographs of multilayer Pt-NP films which have built up over a period of 48 hours at a hexadecane / Pt-NP dispersion interface. The photo graph of the vial shows the vial from which the film was taken. In order to collect the sample a small spatula is dipped into the Pt-NP dispersion and then is drawn back through the oil/water interface.

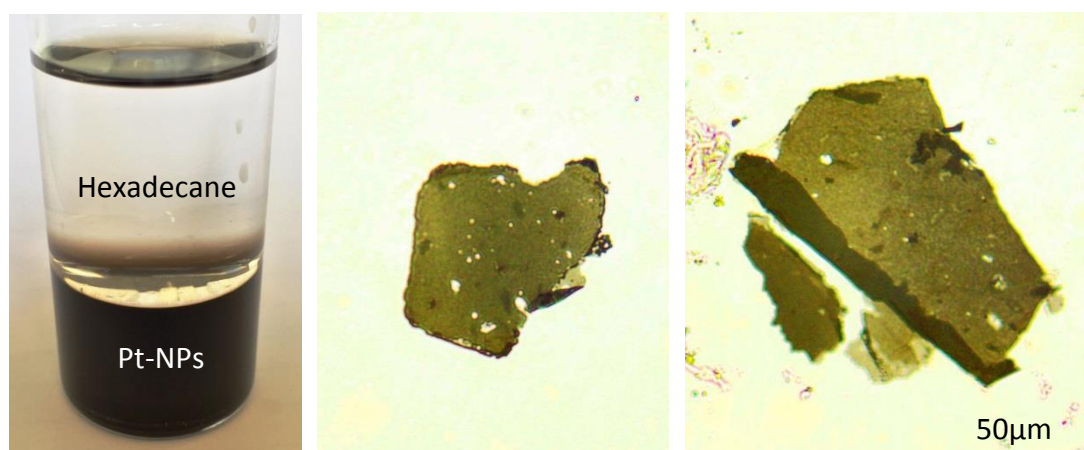


Figure 93 Show optical micrographs of multilayer Pt-NP films which have built up over a period of 48 hours at a hexadecane / Pt-NP dispersion interface. The photo graph of the vial shows the vial from which the film was taken.

Pt-NP films at 2D oil / water interfaces, over time, grow into multilayer films, these 2D films remain stable even after detachment from the interface. Films also remain stable on detachment from the 3D emulsion droplet oil / water interface, remaining as fragments of film in the continuous phase, the constituent Pt-NPs do not redisperse.

How are Pt-NPs that are able to remain stable in a dispersion though steric hindrance able to a) form films which remain stable upon detachment into the aqueous phase and

b) are able to form multilayers either on a nanoparticle by nanoparticle basis [Figure 93] or by two films joining together [Figure 92]?

The steric hindrance the individual Pt-NPs exert on each other when in an aqueous dispersion is somehow overcome once they adsorb at the oil/water interface. Not only do they attach to each other in the film plane but they also allow further adsorption perpendicular to the plane creating multilayers. Further work is needed to understand this little understood process however, the following speculative explanations are worth making:

- The energy of adsorption of the Pt-NPs at the oil/water interface coupled with the limited surface of each emulsion droplet and the ability of the Pt-NP to move in the plane of the interface acts to create a pressure between individual NPs in the film which overcomes steric hindrance and allows the Pt-NPs to get sufficiently close that they entangle/adsorb to each other via general Van der Waal type interactions?
- The insolubility of the PVP stabiliser in the oil phase causes the polymer on the platinum nanoparticle core surface to collapse onto the Pt cores in the oil phase thereby reducing the steric hindrance between Pt-NPs in the plane of the interface allowing Pt-NPs to approach and entangle/adsorb via general Van der Waal type interactions?
- This same effect may allow the Pt-NPs to 'sink' into the oil phase which over time may reduce steric hindrance to secondary Pt-NP adsorption from the aqueous phase. The repetition of the process over time could potentially account for the apparent overcoming of steric hindrance forces during the formation of multilayer films.

7.2.3 Proof of a complete non porous metallic shell

7.2.3.1 Ethanol stability test using GC

Pt-NP Pickering emulsion droplets which had been synthesised at 24Krpm and allowed to ripen for 24 hours and were then gold coated [3.3.3.2] and tested for permeability using the standard ethanol stability test via gas chromatography [3.3.5.1]. Figure 94 shows a graph GC data showing release of hexadecane into ethanol over a period of 7 days.

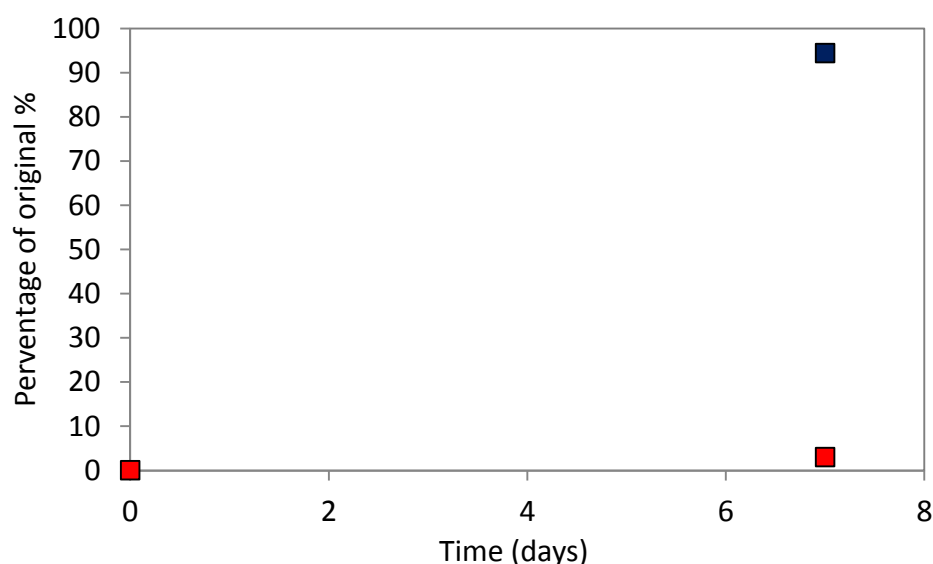


Figure 94 Gas chromatography data showing stability in ethanol/water (80/20) for 7 days. Red squares show the percentage loss hexadecane into the ethanol after 7 days. The blue point shows subsequent 94% release on mechanical breakage by crushing [3.3.5.1].

Figure 94 shows that only ~3% of the hexadecane core in ethanol is released over 7 days. This demonstrates that the majority of the emulsion droplets have been coated in a full non permeable metal shell with no pin holes. We see that on crushing we are able to release, and detect using GC, over 90% of the expected hexadecane volume. The aging process has therefore been successful in preventing pin hole formation.

7.2.3.2 Oil soluble fluorophore encapsulation in an ethanol continuous phase

Attempts were made to encapsulate a fluorophore in the core phase. Perylene, an oil soluble fluorophore, was dissolved in hexadecane and used as the oil phase in the formation of gold coated capsules via the standard technique described above. The continuous phase was then swapped out for an ethanol phase via centrifugation. The capsules were left for 24 hours in the ethanol. The capsules were then crushed with a glass rod and observed in visible and ultraviolet light.

Figure 95 a,b show the Pt-NP stabilised emulsion droplets in an aqueous environment under visible and UV light respectively. Figure 95 c,d show the the corresponding gold coated capsules in an ethanol continuous phase under visible and UV light and Figure 95 e,f show the same capsuels after crushing under visible and UV light.

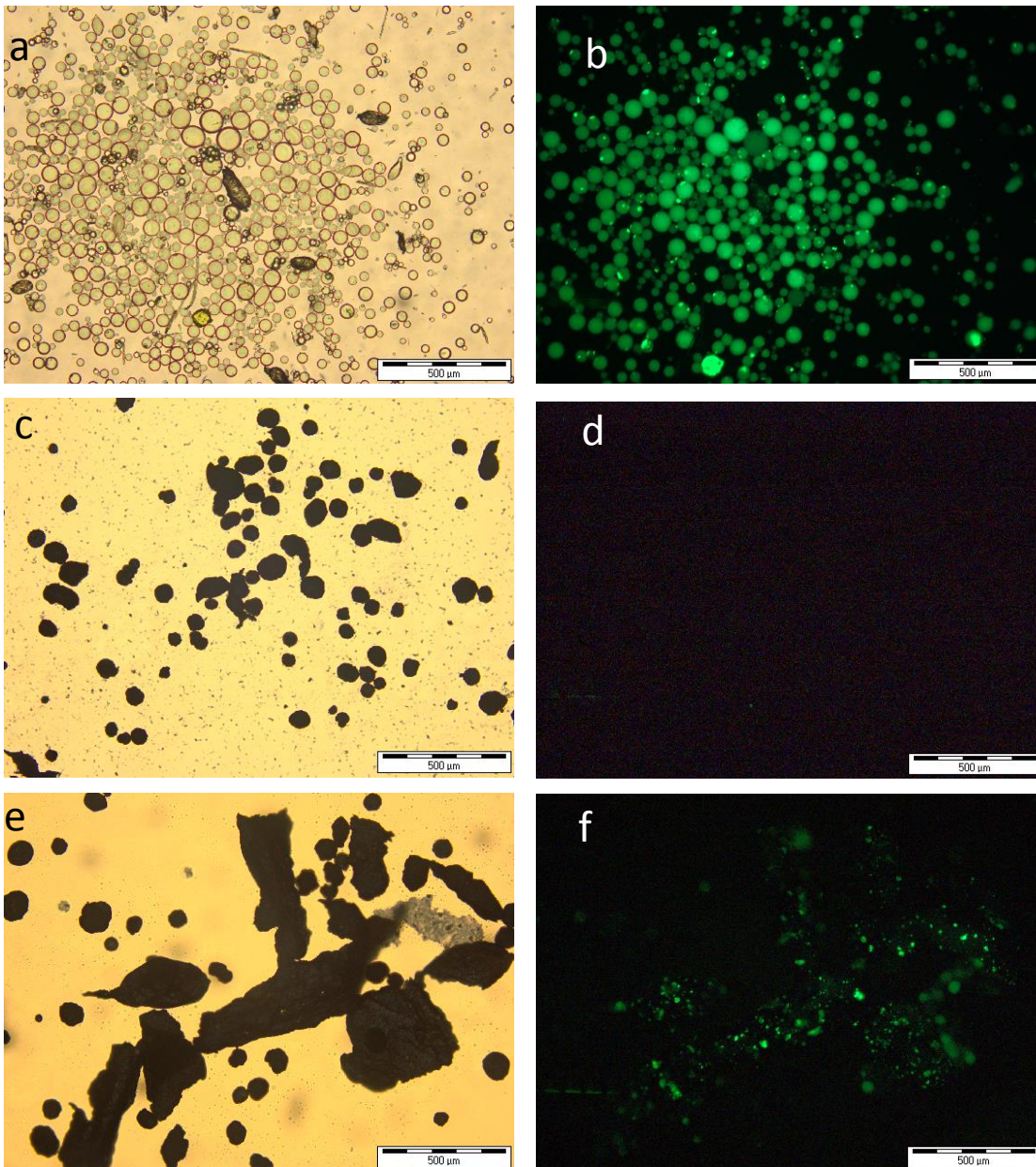


Figure 95 (a,b) stabilised emulsion under visible and UV light, (b,c) crystalline coated microcapsules under visible and UV light and (e,f) crushed capsules under visible and UV light

Figure 95 c,d shows that an oil soluble fluorescent dye has been successfully encapsulated in the core of metal coated microcapsules. No fluorescence was detected under appropriate UV stimulating wavelengths of light. The fluorescence was shown to be blocked (not quenched) by the crystalline shell [Figure 95d].

No release of fluorescent dye was observed over a 24 hour period in the ethanol continuous phase. Mechanical rupturing, of the capsules after 24 hours, with a glass rod revealed the fluorescent core which quickly dissolved into the ethanol phase [Figure 95e,f].

7.3 Further improvement using ultrasonic homogenisation?

Previous work in this chapter showed that increasing the homogenisation speed from 15-24Krpm in order to reduce droplet size resulted in the formation of more robust Pickering emulsion droplets which were less prone to the formation of surface defects in the stabilising Pt-NP film. However, the smaller Pickering emulsions still proved to be leaky due to pin hole formation in the Pt-NP layer which were presumed to be formed during the creaming/wash phase of the synthesis. This problem was solved by aging the Pickering emulsions in excess Pt-NP in order to form NP multilayers thereby making the emulsion droplets more stable. These capsules showed good oil core retention in ethanol stability tests [7.2.3.1]. Apart from the pin holes gold coated capsules formed at 24Krpm appear to be perfect under SEM [Figure 90].

It was therefore thought that further reducing the emulsion droplets in size by homogenising using an ultrasonic probe might allow for the production of non-leaky gold capsules without the need for the 24hour aging step.

0.4mL of hexadecane was sonic probe homogenised (UP200S Ultrasonic Processor (Scimed)) with 10mL of Pt-NPs (0.006wt%)[3.3.2] at 30% amplitude for 1min. The resulting 'colloidosomes' were then washed twice and coated with gold [3.3.4.3].

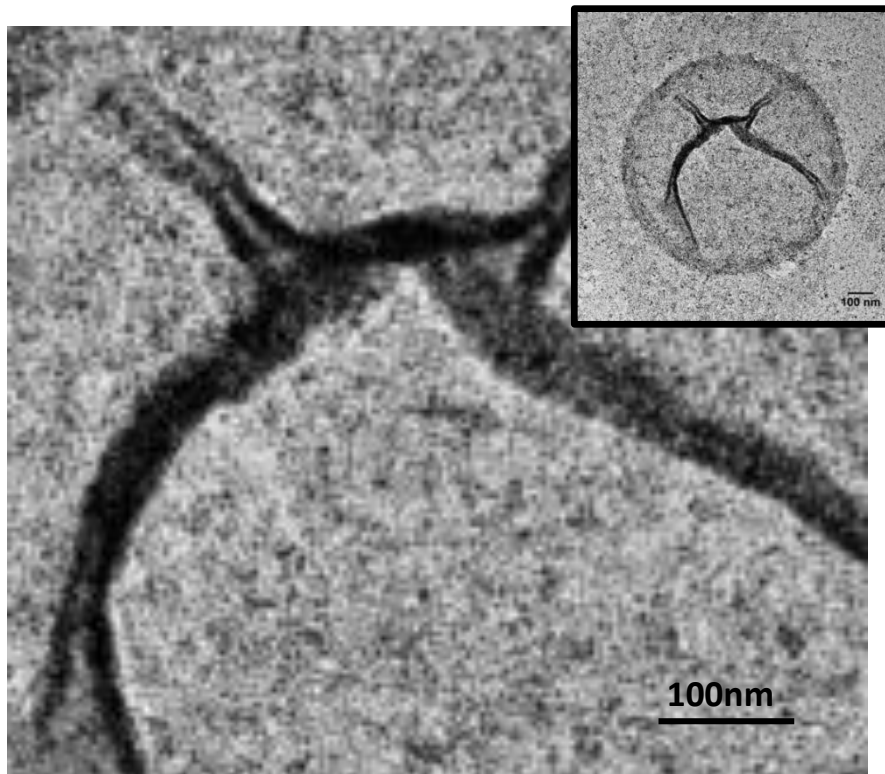


Figure 96 TEM micrographs of collapsed Pt-NP colloidosomes formed by ultrasonic probe homogenization [3.3.3.2].

TEM images of collapsed colloidosomes formed by ultrasonic probe homogenization show good surface structure [

Figure 96]. Although some cracking can be seen along the line of the wrinkle in the surface, no other visible cracking or pinholes can be seen in the rest of the colloidosome surface indicating that the cracks were formed as the colloidosome collapsed on drying and were not originally present.

Figure 97 shows an optical micrograph of the resulting gold coated capsules. The insets show the relative size of emulsions formed via homogenisation with ultraturrax at 15Krpm and 23Krpm.

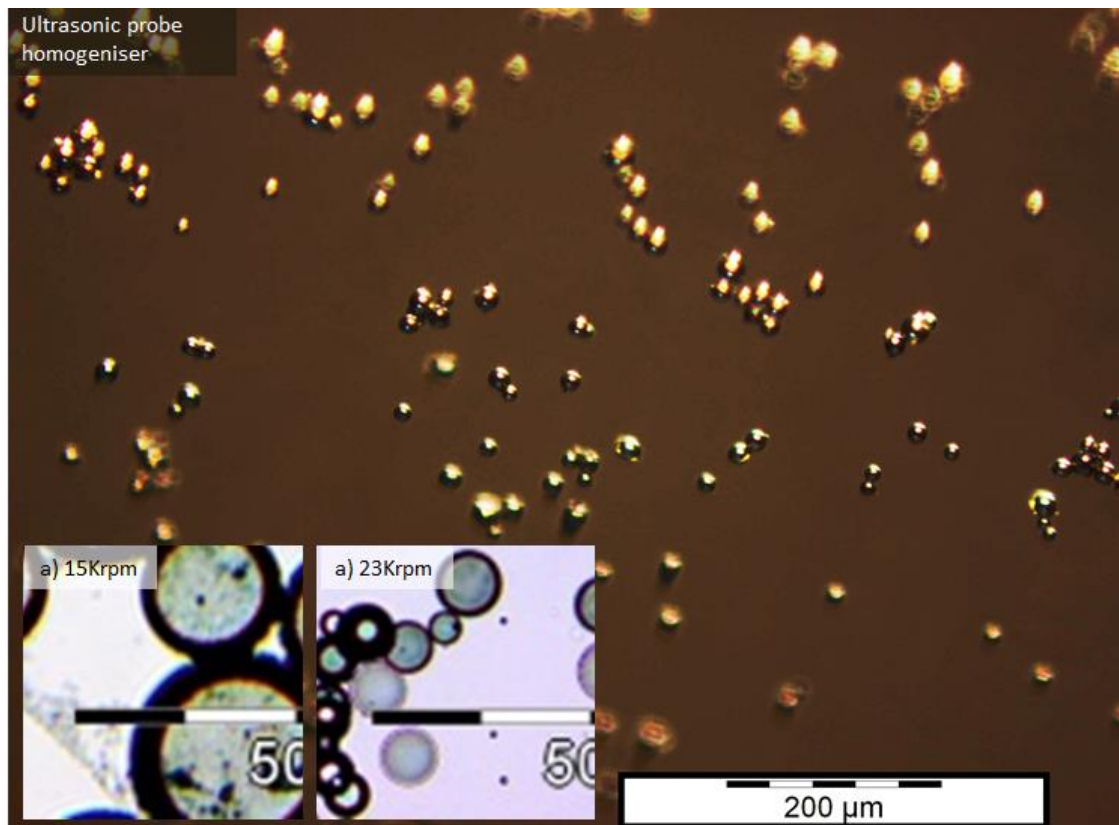


Figure 97 shows an optical micrograph of the ultrasonic probe homogenized colloidosomes [3.3.3.2] coated with gold [3.3.4.3]. The insets show the relative size of emulsions formed via homogenisation with ultraturrax at 15Krpm and 23Krpm.

The capsules formed from the ultrasonic homogenized emulsions are significantly smaller than those formed using homogenization by Ultraturrax [Figure 97]. All of the capsules collapsed/popped when dried out. However, SEM revealed no visible pin holes in the gold surface Figure 98. The concentration of gold salt was the same for this experiment as for previous work [2.2.4] in which capsules did not collapse [Figure 90c]. The collapse of these capsules in air was put down to thinner gold film growth due to the large increase in surface area due to the reduced size (the volume of hexadecane used was the same). Future work will hopefully show that the gold coated emulsion droplets formed by ultrasonic homogenization show good release data and negate the requirement for the secondary ‘aging’ stage.

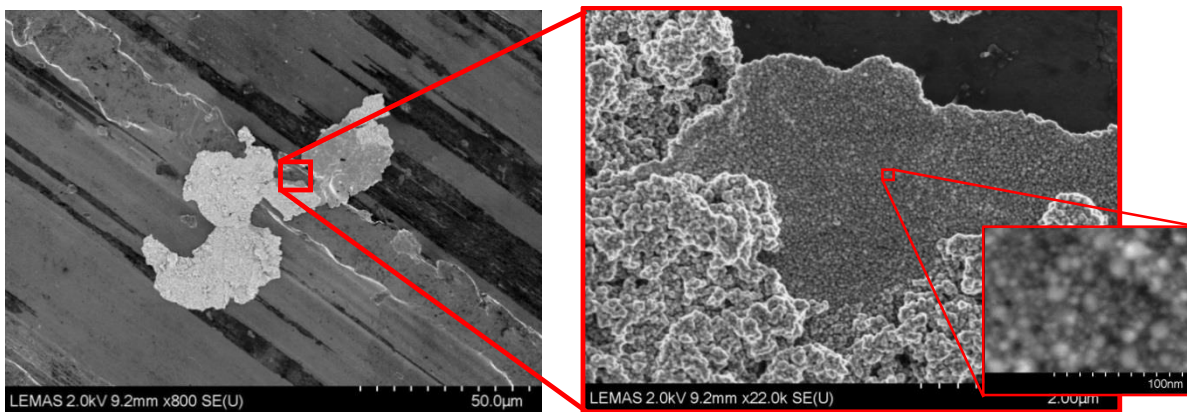


Figure 98 SEM micrograph of a capsule from the sample shown in Figure 97. All the capsules cracked open under vacuum.

The broken capsules provided a good opportunity to image the interior surface. As the gold films grow directly on the Pt-NP stabilised emulsion droplet surface, and not a polymeric interface, the interior of broken capsules reveal the morphology of the initial gold film. Confirmation that the gold does indeed initially grow as a polycrystalline film on the scale of the underlying Pt-NP adsorption density as predicted in previous sections [6.2.1 and 6.3.1] was able to be made.

Figure 99a show a schematic diagram of the proposed gold film growth mechanism, (a1, a2 and a3) are ‘to scale’ and show a TEM micrograph of the underlying Pt-NP film, an SEM image of the interior gold surface and an SEM micrograph of the external surface of the gold film respectively. (b) and (c) show ‘to scale’ zoomed micrographs of the Pt-NP film and the interior gold film surface demonstrating that the spacing of Pt-NP and gold ‘crystals’ is similar.

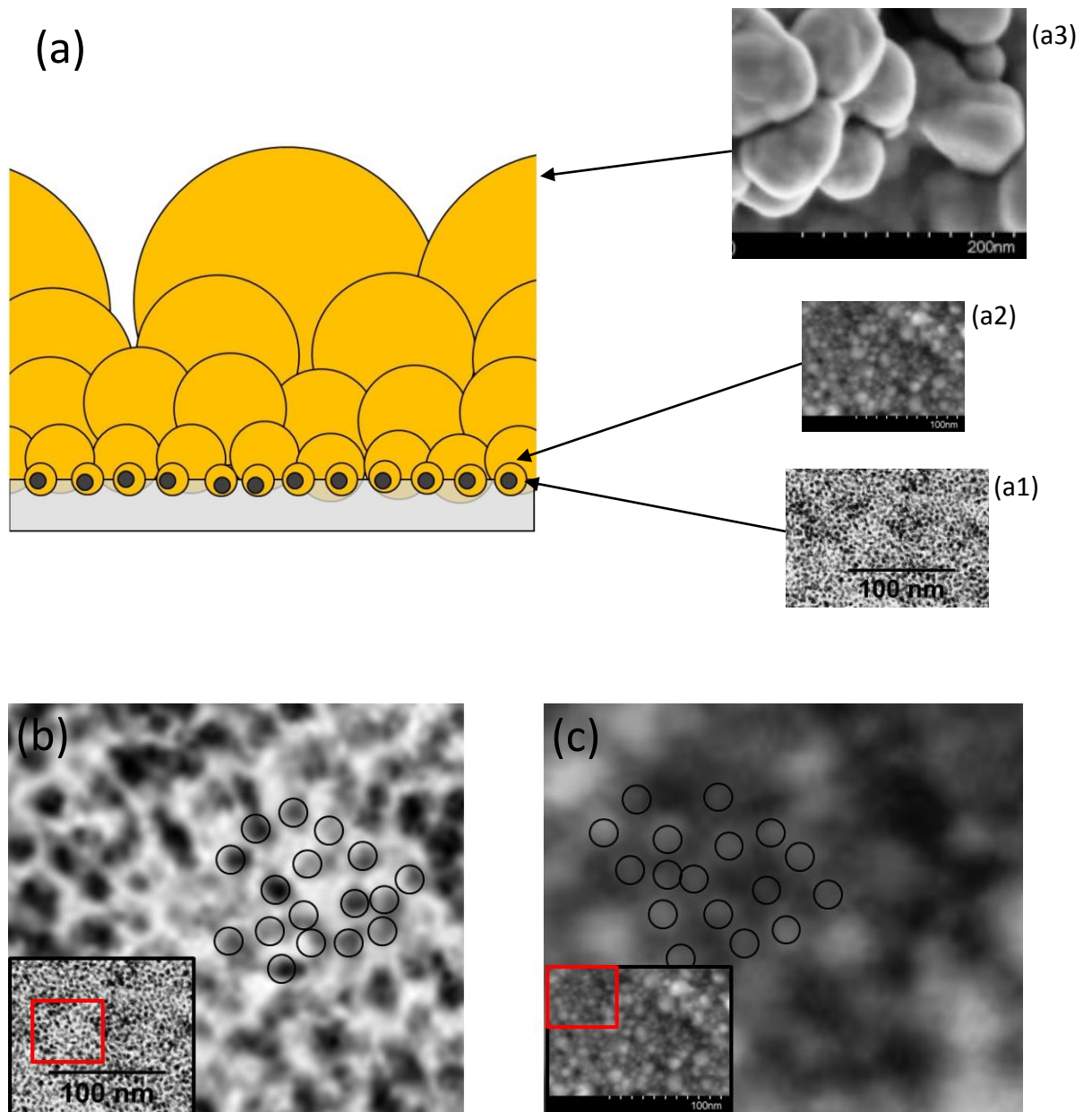


Figure 99 (a) Schematic diagram showing the proposed gold film growth mechanism, (a1, a2 and a3) are to scale and show a TEM micrograph of the underlying Pt-NP film, an SEM image of the interior gold surface and an SEM micrograph of the external surface of the gold film respectively. (b) and (c) show to scale zoomed micrographs of the Pt-NP film and the interior gold film surface.

7.5 Conclusions

Pt-NPs synthesised using low concentrations of PVP are able to directly stabilise hexadecane emulsion droplets in an aqueous continuous phase. The resulting Pickering emulsions remain stable on washing and can be subsequently used to grow complete secondary gold films to form gold capsules containing ~100% oil cores.

Issues with incomplete/cracked NP films on the emulsion drop interface causing incomplete secondary metal films was solved by increasing the homogenisation speed from 15Krpm to 23Krpm using Ultraturrax. This reduced the size of the Pickering emulsion droplets providing a more stable interface for the Pt-NP film formation. In addition, the emulsion was allowed to ‘age’ over 24hours in a dispersion of excess Pt-NPs.

Emulsion droplets which had undergone the ‘aging’ process showed clear evidence of multilayering in the Pt-NP stabilising film. The multilayering was shown to occur for two reasons. Firstly, NP films which detach from the emulsion droplet surface are able to remain as stable films in the continuous phase and can reattach over the top of existing Pt-NP stabilised emulsion droplets. Secondly Pt-NP films at oil / water interfaces were shown to grow into multilayer films over time. Several reasons were proposed to explain this behaviour.

- The energy of adsorption of the Pt-NPs at the oil/water interface coupled with the limited surface of each emulsion droplet and the mobility of the Pt-NP in the plane of the interface may act to create a pressure between individual NPs in the film which overcomes the steric hindrance between Pt-NPs allowing them to approach sufficiently closely that they entangle/adsorb to each other via general Van der Waal type interactions
- The insolubility of the PVP stabiliser in the oil phase causes the polymer collapses on to the Pt core surface thereby reducing the steric hindrance between Pt-NPs in the plane of the interface allowing Pt-NPs to approach and entangle/adsorb.

The fact that Pt-NP films remained stable as films even when emulsion droplets were broken with glass slides and the films themselves became free of the oil/water interface justified the use of the term ‘colloidosomes’ when describing the NP stabilised emulsion droplets

Emulsions formed by emulsifying at 23K rpm and ageing for 24hours [3.3.3.2] were used to successfully demonstrate the potential of metallic shells for significantly prolonging the release of encapsulated, low molecular weight, volatile molecules within a continuous phase that can dissolve the encapsulated actives. Gas chromatography data showed stability in ethanol/water (80/20) for 7 days. By mechanically fracturing the metal-coated capsules and testing the sample again for core release, a 94% release of the hexadecane present in the precursor colloidosomes was detected.

Ultrasonic probe homogenisation was used to further improve colloidosome stability with a view to potentially negating the requirement of the aging step in the synthesis. TEM images of collapsed colloidosomes showed good Pt-NP surface structure with no cracking or pinholes visible. SEM of the resulting gold coated capsules also showed good surface structure with no pinholes visible. It is hoped that subsequent GC testing will show these capsules to be ‘impermeable’ to small, volatile molecules.

SEM micrographs of broken capsules provided a good opportunity to image the interior surface. Gold films grow directly on the Pt-NP stabilised emulsion droplet surface and therefore, the interior reveal the morphology of the initial gold film. Confirmation that the gold does indeed initially grow as a polycrystalline film on the scale of the underlying Pt-NP adsorption density as predicted in previous sections [6.2.1 and 6.3.1] was able to be made.

Any metal that can be stabilised by PVP should adsorb at an oil / water interface in the same way as Pt-NPs. Therefore, as long as the primary metallic catalytic NPs can be stabilised by PVP other electroless deposition / metal pairings should work using this technique (see section 0 for potential alternative metal pairings).

8 Appendix 1 - Future work

8.1 Potential Papers

- 1 *Control of nanoparticle density on polymeric microcapsules* – data has been gathered which shows good control over nanoparticle adsorption densities on both capsule surfaces and 2D model interfaces. Good control over the nanoparticle adsorption density is key for controlling the morphology of the secondary complete metallic film.
- 2 *Controlling the morphology of metal films on polymeric microcapsules and emulsion droplets with a view to breakage via electromagnetic radiation and/or ultrasound* – data has been gathered showing how variables such as temperature, primary nanoparticle density and electroless plating solution constitution affect the rate of growth and resulting morphology of the secondary complete metallic film. This is important because the morphology of the film affects the resulting capsules structural integrity and is key to the potential heating or breakage of the capsules using particular wavelengths of light and/or ultrasound.
- 3 *Controlled core release from metal coated polymeric microcapsules* - Sufficiently reducing the thickness of the secondary metal shell results in nano-sized pin holes. This opens up the opportunity to tune the porosity of the shell and control the release of actives via size exclusion. We have release data from capsules with different shell morphologies and are working to add non-metallic particles into the metal shell to act as portals with porosity which could be controlled by environmental triggers.
- 4 *Mono-disperse metal microcapsules for use in photonic arrays*
- 5 *Mono-disperse metal microcapsules for use in next generation metal composite foams*

- 6 *Using tissue transparent light to enhanced plasmon response of size/film thickness tuned gold micro-capsules*
- 7 *Size and shell thickness tuning of metal shell microcapsules to enhance ultrasonic interaction for an efficient drug delivery system*
- 8 *Surface modified gold capsules as an efficient drug delivery system*
- 9 *The effect of metal coated microcapsules size, surface morphology and chemistry on cell ingestion and toxicity*

8.2 Pharmaceuticals

Existing micro-encapsulation methods tend to be leaky due to the use of semi-porous polymeric shells; our gold films act as a barrier to virtually any molecule and prevent leakage. Gold is inert and provides a surface for the attachment of biological moieties and therefore our capsules are ideal for targeted delivery of drugs without any release until activated.

Biocompatibility/ targeting / cell ingestion of capsules – the following papers may be useful sources of information if one was to attempt to attach biological material to the surface of the capsules in order to promote biocompatibility, cell targeting/ingestion:

- Control over the surface roughness control the density of adsorbed biological moieties [86]
- Biomedical Applications of Gold Nanoparticles: Opportunity and Challenges - Look at drug delivery section [90].
- Review paper on functionalising metal NPs for bio apps - [91].
- Lui et al. discuss and demonstrate the adsorption and testing of HD-DNA on gold surfaces on QCM [86]

Release mechanisms- The metal film characteristics should be optimised for remote capsule breakage via laser or ultra-sound. Using our capsules Professor Sukhorukov (Queen Mary University of London) has already demonstrated remote breakage via laser and ultra-sound. This fits very well with Professor Freear's (University of Leeds) work in this area. One could attempt to tune the shell morphology to maximise response to tissue transparent wavelengths of sound /light in order to maximise tissue penetration. The following papers may be useful sources of information for this area:

- Tzur-Balter et al. have demonstrated in vivo and in vitro dissolution of nanostructured porous silica. Introducing these biodegradable portals into the metal film may enable a timed release of the capsule core within the body [92].
- Sukhorukov et al. used ultrasound to fracture polymeric capsules [93].
- Wang et al. – photo-thermal (laser excitation) of gold nanorods for cancer treatment (Astbury group Leeds) [94].
- Tommy Horozov [84, 95] and Binks et al. have looked at stabilising emulsion droplets and 2D liquid/liquid interfaces with a mixture of Silica NPs and cationic surfactant (CTAB) [96].

8.3 Advanced materials photonics/plasmonics and metal micro foam composites

Photonics/Plasmonics/Metal micro-foam composites – There is potential to use metal nano/micro-foams as photonic arrays for use in photovoltaics, optics, photo-catalysts or metal composite foams with unusual structural qualities. The following papers may be useful sources of information for this area of work:

- Jiang et al. developed a technique for depositing a monolayer of silver shelled NPs for photonics [97].
- Paper makes Silver shells for photonic crystal fabrication [74].
- Lovely monodisperse SiO₂ particle photonic crystals [98].
- Growing different shaped NPs – may be transferrable to the Au surface [21].
- Constructing opal structure of monodisperse silver coated silica particles [97]

Growth of quantum dot/nano-wires on metallic surface There may be some merit in growing secondary nanostructured inorganic or even hybrid organic/ inorganic photo-active components on the surface of the metal microcapsules for use in solar cells. Metallic films provide good opportunity for the surface growth of nano-structures [85] The huge microcapsule surface area could potentially allow for increase efficiencies over equivalent flat 2D interfaces. He et al. grow gold nanowires from adsorbed Au-NPs if these could be swapped for Pt and grown on the surface of a capsule it may exhibit a high level of catalytic activity [99] .

8.4 Metal bubbles for low density materials with unusual thermal

Pt-NPs can be shown to form films at water/air interface [Figure 100]. It may be possible to use Pt-NPs to stabilise bubbles with a view to growing secondary films to form metal bubbles. The following papers may be useful sources of information for this area of work:

- Mechanics of hollow sphere foams [100].
- Manufacture, characterisation and application of cellular metals and metal foams [101].

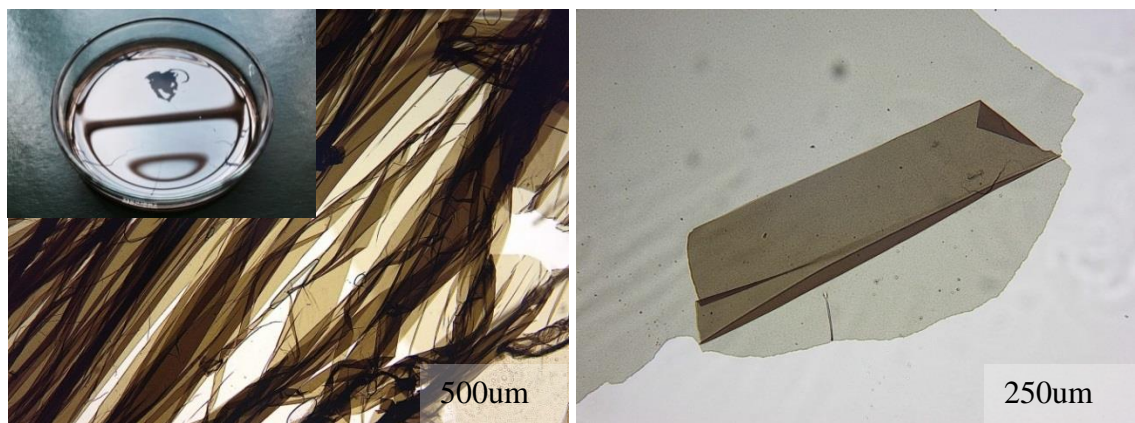


Figure 100 Microscopy images of the film of NP's formed at an air water interface after several weeks. Very robust, appears to be more than one NP thick. Maybe NP's behave differently at an oil-water

(liquid-liquid) interface than they do at a water-polymer (liquid-solid) interface NB move this to future work bubble section I have an experiment running to show growth at and oil water interface

8.5 Minimising the use of secondary metal

8.5.1 Producing smooth thin secondary metal films

Much work has been undertaken in the metal plating industry to achieve smooth crystalline growth. Usually additives are used during the plating process which restrict crystalline growth in certain planes allowing for uniform complete films (mostly this is done to improve lustre). Taking advantage of some of this technology may allow for the production of smoother gold films and therefore improve efficiency.

8.5.2 PVP stabilised silica with interstitial Pt-NPs

Using ‘large’ non porous PVP stabiled SiO_2 particles as a stabilier for a Pickering emulsion and then adsorbing PVP stabilised Pt-NPs to the interstitial liquid-liquid interface between the SiO_2 particles may allow for the growth of secondary metal only in these sites. Steric hindrance between the polymer on the SiO_2 particles and the NP’s should restrict adsorption onto the silica. SiO_2 particles would have to be relatively large for there to be enough space between them for NP adsorption to take place. Bollhorst et al. look at tailoring the inter-particle pore size in sub-micron Pickering emulsions and colloidosomes [40].

8.5.3 Amorphous/crystalline nonporous glasses as shells

Look into the possibility of growing non-porous amorphous or crystalline NP glasses such as SiO_2 in aqueous solution. Attempt to grow films on polymeric shells or SiO_2 Pickering emulsions to ‘plug the gaps’. High quality Al_2O_3 films are grown on silica in an aqueous environment in the following paper [102].

8.6 Alternative metals shell synthesis

8.6.1 Alternative combinations / methods

Deposition of nickel growth on palladium - The following papers may be useful sources of information for this area of work:

- Growth of Palladium NP on PS-Latex particles – for catalysis (Suuki-type for formation of carbon-carbon bonds) [103].
- Lin et al. grow Ni shells on polyelectrolyte-modified PMMA beads using direct Ni^+ ion adsorption and reduction – very simple [70].
- Electrolytic adsorption and insitu-reduction of palladium ions - Palladium ions from a palladium salt will adsorb onto a polyelectrolyte brush (negatively charged polymer). These ions can then be reduced insitu to produced stabilized palladium nanoparticles [61].
- Kondo et al. photo-chemically deposit Pd(0) from adsorbed Pd(II) ions – used to grow copper on 2D printed circuit boards but could be used for Ni [104].

Deposition of gold/copper on platinum/silver - The following papers may be useful sources of information for this area of work:

- Sanlés-Sobrido et al. adsorb Pt-NPs onto and into submicron sized particles to create highly active nanoreactors [62].
- The following paper describes electroless copper growth Copper on silver NPs 2D [105].
- Adsorbing / embedding pH destabilised NP's on polymeric capsules - Prepare polymeric capsules, via co solvent precipitation, in the presence of destabilised PAA-Pt (Adapt the following technique [55]). PAA-Pt are negatively charged and destabilise in an acidic environment in order to adsorb them onto a polymeric interface. The following paper provides information about the interplay between PAA-Pt and the raw PAA[96].

- Tin ions can be used as a catalyst for atomic platinum growth - Use of 'atomic' platinum as a catalyst. Adapt a technique which uses Tin-Porphyrin to create silica/platinum - core/shell particles [106, 107]. These methods could be transferred onto 3D silica nanoparticle Pickering emulsions. Alternatively 3D negatively charged polymeric capsules could be formed [106, 107].
- The following paper describes the use of a Tin - Porphyrin complex as a Photocatalyst for Platinum deposition [107].

Deposition of silver on gold - The following papers may be useful sources of information for this area of work:

- Larson-smith et al. use thiol-terminated polyethylene glycol (PEG) chain stabilised gold nanoparticles to form Pickering emulsions [49]. Silver films could be grown directly on the picking emulsion surface.
- Yamanaka et al. form water in oil Pickering emulsions stabilized with mercaptocarboxylated Au nanoparticles [48]. Silver films could be grown directly on the picking emulsion surface.
- Metallic Ligand - Lee et al.1 successfully use Crown ether derivatives to precipitate out gold at an oil/water interface [47].

Deposition of copper growth on copper - The following papers may be useful sources of information for this area of work:

- Haas, I., Shanmugam, S., Gedanken, A. Pulsed sonoelectrochemical synthesis of size-controlled copper nanoparticles stabilized by poly(N-vinylpyrrolidone) (2006) Journal of Physical Chemistry B, 110 (34), pp. 16947-16952. Cited 79 times.
- Jianfeng, Y., Guisheng, Z., Anming, H., Zhou, Y.N. Preparation of PVP coated Cu NPs and the application for low-temperature bonding (2011) Journal of Materials Chemistry, 21 (40), pp. 15981-15986. Cited 20 times.

Deposition of copper growth on Palladium - The following papers may be useful sources of information for this area of work:

- Reduction of catalyst in ion form on surface - Patchan et al. – Sn – Pd - Nickel method [72]
- Kondo et al. photo-chemically deposit Pd(0) from adsorbed Pd(II) ions – used to grow copper [104].

8.6.2 Nickel-Boron hard low friction microcapsules/particles

It may be possible to grow nickel-boron alloy on the surface of microcapsules/emulsion droplets or particles. The following papers may be useful sources of information for this area of work:

- Riddel et al. demonstrate an improved method for 2D growth Ni-B via electroless deposition [108]. Used for composite materials, for example, SiO₂ core Ni-B shell particles for friction reduction? Also [109].
- Electroless Ni–B coatings: preparation and evaluation of hardness and wear resistance [110].
- Corrosion resistance of electrodeposited Ni–B and Ni–B–Si₃N₄ composite coatings [111].

8.8 Variable flow buoyancy pinning using a controlled flow environment

One could potentially create a 'one pot' continuous flow environment in which NP adsorption, washing and secondary metal film growth can be carried out. This would potentially allow for a very gentle environment for synthesis of, for example, metal coated bubbles or thin coated emulsion droplets (no creaming or violent wash steps). Tailored flow would allow for the selection of emulsion droplets/bubbles with mono disperse size distributions for use in, for example, photonic arrays. Figure 101 shows a schematic diagram of potential rig.

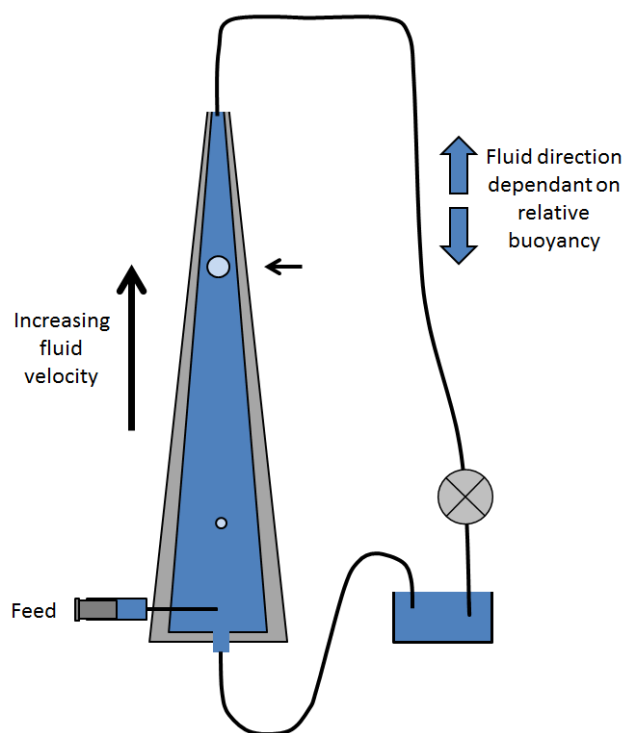
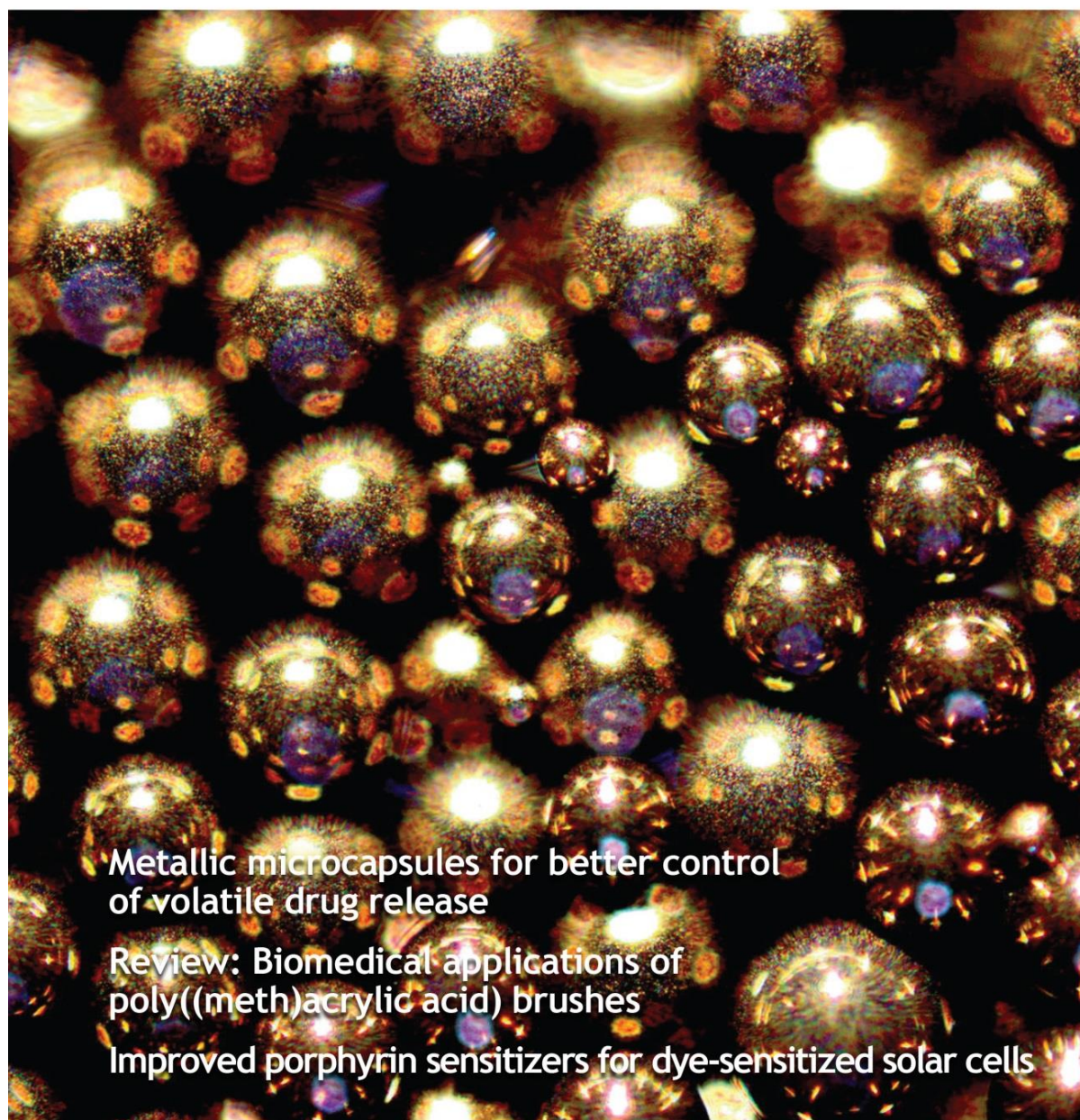


Figure 101 Schematic diagram for a variable flow buoyancy pinning using a controlled flow environment

8.9 Self-healing materials

Generally the requirements of microcapsules for use in self-healing materials are that they do not leak but will break as and when a micro crack moves through the material surrounding them. Often the released 'healing' material is a two part epoxy type material which only hardens on the mixing of both parts residing in different cores. Alternatively, one of the parts can reside in the continuous phase. Non porous metal capsules may be well suited to this application [112].

9 Appendix 2 - Paper

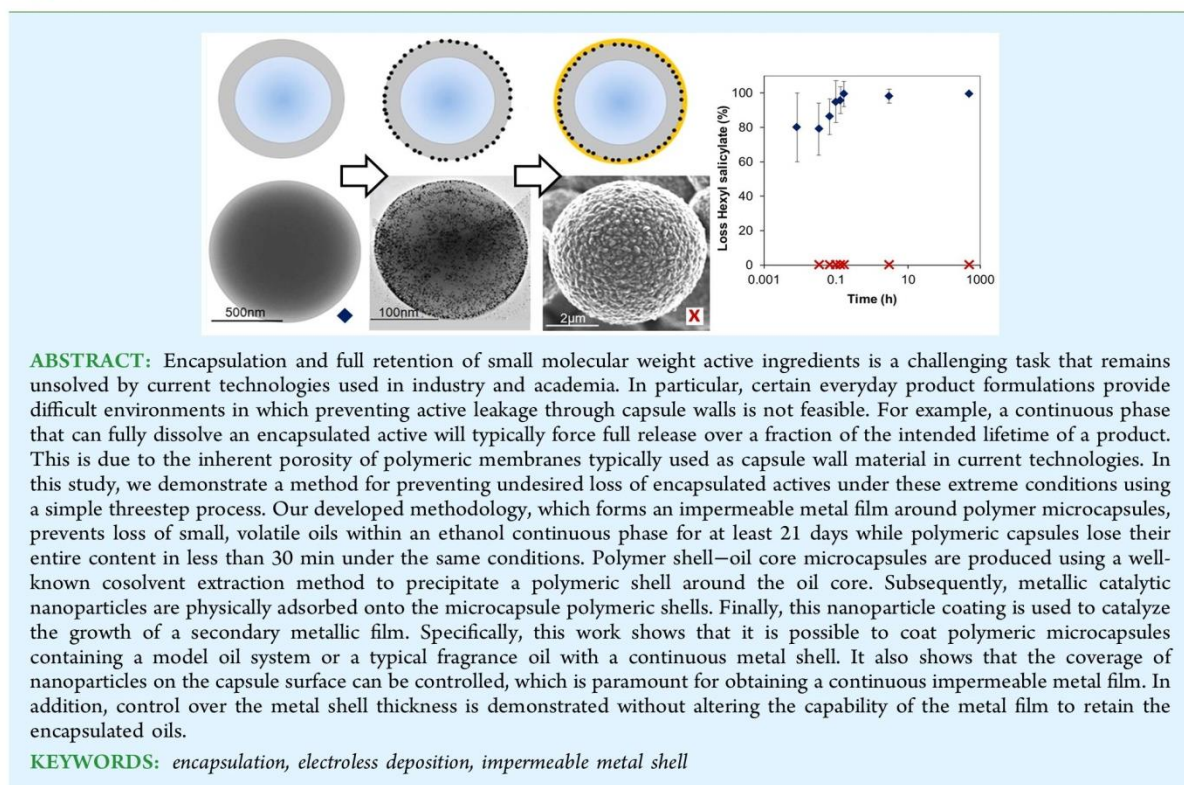


**Metallic microcapsules for better control
of volatile drug release**

**Review: Biomedical applications of
poly((meth)acrylic acid) brushes**

Improved porphyrin sensitizers for dye-sensitized solar cells

Long-Term Retention of Small, Volatile Molecular Species within Metallic Microcapsules

James P. Hitchcock,[†] Alison L. Tasker,[†] Elaine A. Baxter,[‡] Simon Biggs,[†] and Olivier J. Cayre^{*†}[†]School of Chemical and Process Engineering, University of Leeds, Woodhouse Lane, Leeds LS2 9JT, United Kingdom[‡]Procter & Gamble, Greater London Innovation Centre, Egham, Surrey TW20 9NW, United Kingdom Supporting Information

1. INTRODUCTION

The efficient encapsulation of active chemicals with an associated controlled (and targeted) delivery is increasingly important to a range of industries.^{1–6} The targeted delivery of actives using microcapsules provides potential benefits for many applications, for example, in pharmaceutical or agrochemical formulations by lowering the required dose in the final product. This has obvious cost benefits and, importantly, lower doses can reduce or eliminate detrimental side effects. While microencapsulation techniques are increasingly used for specific actives such as fragrances in personal care products, insecticides in agrochemicals, nutraceuticals in foods, and drugs in pharmaceuticals, there remain significant limitations for both

the types of actives that can be encapsulated and the characteristics of the release profile that can be achieved.

Numerous methodologies for encapsulating and delivering specific actives (cancer drugs, pesticides, etc.) have been reported in the academic literature.^{2,7–13} The proposed methodologies have yielded increasingly functional microcapsules but often the complexity of the synthesis processes involved is a significant barrier to the implementation of these advanced delivery technologies in every day products. A particular area requiring improvement concerns the encapsu-

Received: April 10, 2015

Accepted: June 16, 2015

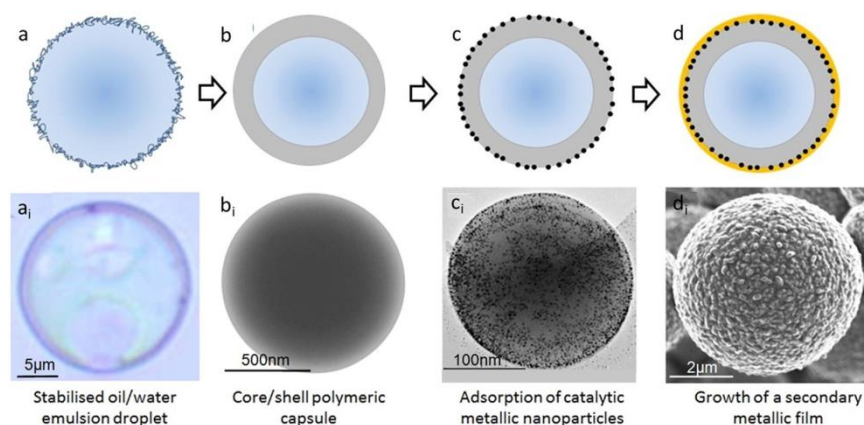


Figure 1. (a–d) Schematic diagrams and corresponding optical and (a_i–d_i) electron microscopy images of the different phases from emulsion droplet to metal coated capsule: (a) emulsion droplet, (b) capsule, (c) capsule with adsorbed NPs, (d) metal (Au) coated capsule, (a_i) emulsion droplet (optical microscopy), (b_i) capsule (TEM), (c_i) capsule with adsorbed NPs (TEM), and (d_i) metal-coated capsule (SEM). The micrographs correspond to different samples and are chosen to illustrate the evolution of the systems over the different steps.

lation and delivery of small molecules to which most typical microcapsule membranes (i.e., polymeric/particulate/lipid-based membranes) are highly permeable. In particular, small volatile compounds present a significantly difficult challenge when designing methods for controllably delivering such actives within formulated products. This is of specific relevance to the incorporation of fragrance oils and other small actives in personal care products, cosmetics, and home care products, for example. It is also important in a wide range of other areas (pharmaceuticals, foods) where the delivery of small actives (e.g., drugs, vitamins) is important. Arguably, the key challenge to using microencapsulation as an efficient delivery route for such small, volatile actives is the ability to retain them within the carrier capsule without leaching or potentially damaged by interaction with the environment. In this work, we propose a method that tackles this challenge in an environment (i.e., the continuous phase in which the capsules are dispersed) that can also dissolve the encapsulated active.

Several methods exist for significantly reducing the release rate of small, volatile actives from microcapsules, and those have been applied on the basis of standard laws of diffusion through membranes. Fickian laws of diffusion are typically used to describe the diffusion rate of an active ingredient permeating across a membrane as a function of time.¹⁴ In the case of diffusion of an encapsulated active through a shell into an immiscible continuous phase, the following equation can be used as a general basis for understanding the microcapsule characteristics that control the release rate.

$$\frac{d_c}{d_t} = \frac{AHD(C_{\text{int}} - C_{\text{ext}})}{x} \quad (1)$$

where A is the surface area, H is the partition coefficient, D is the diffusion coefficient, C is the active concentration, and x is the shell thickness.

Here, the partition coefficient, H , defines the solubility of the core in the shell and, as such, is fixed for a particular core material. The diffusion coefficient, D , describes the diffusion of the core phase through the shell material. According to eq 1, the diffusion rate, d_c/d_t , can be significantly reduced by minimizing the relative solubility of the dispersed phase within

the continuous phase.¹² Reducing the concentration difference between the capsule core and the continuous phase can also lead to drastically slower diffusion rates, but this does, of course, obviate the value of encapsulation. Thicker capsule shells will also have a beneficial effect but typically at the cost of reducing the volume of the capsule core, leading to smaller encapsulation efficiencies.¹²

Such measures are often considered/applied but typically do not lead to complete retention of active species. In particular, when the active ingredients have high vapor pressures, the diffusion rates tend to be dictated by the volatility of the species and are typically very high.¹⁵ The successful long-term encapsulation of volatile molecules requires different materials than currently used (organic shells) to create impermeable barriers that can arrest the diffusion of actives from the capsule core. For example, polymeric materials produce diffusion coefficients in the order of $10^{-8} \text{ cm}^2 \cdot \text{s}^{-1}$ for highly volatile small molecules.¹⁶ These relatively high diffusion coefficients render most currently implemented encapsulation methods inappropriate to achieve full retention of such actives, particularly in an environment that is capable of dissolving them. For example, microcapsules for which the release of a specific active is tested (e.g., a dye with suitable solubility characteristics) typically demonstrate a full release of the encapsulated species within days, more often within hours.^{12,17,18} Recently, Zieringer et al. have demonstrated significantly low release rate of a dye molecule ($>300 \text{ g} \cdot \text{mol}^{-1}$) and a divalent electrolyte in water across a fluoropolymer (PFPE) shell.¹⁹ In this case, the poor wetting of the polymer shell by the solvent facilitates a very low permeability (for release tested over a period of 4 weeks). However, when the wetting is slightly improved by placing the capsules in an organic solvent, a sustained release of a dye initially dissolved in the toluene core was observed.

In this study, we hypothesize that the long-term retention of highly volatile small molecules can be possible in any environment when using amorphous/crystalline metals or inorganic crystals with very low diffusion coefficients (e.g., $10^{-15} \text{ cm}^2 \cdot \text{s}^{-1}$ for hydrogen atoms diffusing across a metal film) as the shell material.^{20,21} Films of these materials are considered impermeable due to their crystalline nature.²² While atomic

B

DOI: 10.1021/acsami.5b03116
ACS Appl. Mater. Interfaces XXXX, XXX, XXX–XXX

species can permeate through a crystalline metal surface,²³ a hydrocarbon chain larger than the interstitial spacing within the crystal is unlikely to be able to move through the lattice. Thus, metal films in the order of tens of nanometres in thickness should render the movement of small volatile molecules across the membranes negligible over the relevant time scales (i.e., those of product manufacturing, storage and use). Enabling the encapsulation of such small compounds could have very significant impact across many industries where active retention during product storage and triggered release during use (through mechanical action in this case) would be beneficial.

Here, we report a simple method to encapsulate low molecular weight volatile oils, as a proof of concept for the use of metallic microcapsule shells. Importantly, the microcapsules produced are capable of retaining a small aromatic hydrocarbon with negligible leakage upon changing the continuous phase from water to ethanol (which provides an environment where the encapsulated oil is fully soluble). The method we describe here uses an oil-in-water emulsion as the precursor for a polymeric microcapsule. Extraction of a cosolvent from the oil dispersed phase induces precipitation of a polymer (initially dissolved in the oil phase), which forms a shell of the resulting microcapsules.^{24,25} This method typically allows for the production of systems with good control over shell thickness. Such microcapsules are not suitable for long-term retention of small, volatile actives. The prepared polymer microcapsules dispersed in water are the basis for the next steps in our procedure, which creates impermeable microcapsule shells through the electroless deposition of a metal film. The second step in the procedure consists of metallic nanoparticle adsorption onto the microcapsule polymeric shells. In a third step, this nanoparticle coating is used to catalyze/nucleate the growth of a secondary metallic film reduced in situ from the continuous phase.²⁶ Here, the catalytic nanoparticles on the surface of the polymer microcapsules reduce the energy barrier for the metal salt reduction and thereby serve to localize the reduction of the metal salt on the microcapsule surface, which also drastically limits precipitation of solid metal in the continuous phase.

Figure 1 shows a schematic diagram of the complete production process (a–d) and corresponding optical and electron micrographs of examples of microcapsules produced in each stage (a₁–d₁).

While there are methods available in the existing literature, to apply a metal coating to colloidal objects (mostly solid particles),^{27–32} the simple three-step method proposed here allows for a full metal coating to efficiently encapsulate small volatile actives in their liquid form. Two other recent articles also report the use liquid core objects to deposit a metal coating.^{33,34} In the first example, Patchan et al. sequentially adsorb multiple layers of polyelectrolyte, followed by tin and palladium ions before the target surface is suitable for metal deposition.³³ The method we propose here requires fewer synthetic steps to deposit the metal coating, which offers significant advantages with respect to the viability of an eventual manufacturing process. In the second example, Nocera et al. describe a method that requires the doping of a polymer membrane (surrounding an oil core) with metal ions and subsequent reduction of further ions in the continuous phase.³⁴ Although the primary aim of these experiments was to create core-shell structures with specific optical properties (the authors do not investigate the permeability of the metal films), this study creates a precedent to the methodology we describe

here. However, the method described in Nocera et al. requires specific conditions, including a 2 h reaction time to deposit a layer of polydopamine for subsequent adsorption of the metal ions. In our case, the preparation of the surface for electroless deposition of the metal only requires adsorption of the nanoparticles, a step that can be completed within 10 min. Additionally, PVP-stabilized nanoparticles can be adsorbed to a broad range of surfaces and interfaces (including polymeric and charged surfaces) as a result of the polarity of the polymer stabilizer.³⁵

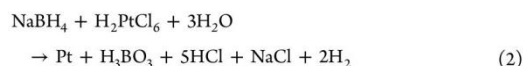
In this study, we demonstrate that by metal coating polymer microcapsules, the release of a volatile oil from the core is effectively prevented, as compared to the core release observed with bare polymeric capsules. We also demonstrate an ability to control the nanoparticle surface density on the polymer, which plays a critical role in ensuring that the metal coating is continuous and impermeable. Finally, we also show control over the metal shell thickness by varying the reaction temperature for the metal growth step without affecting the release characteristics of the resulting microcapsules.

2. EXPERIMENTAL SECTION

2.1. Materials. Poly(methyl methacrylate) (PMMA) (120 kDa), cetyltrimethylammonium bromide (CTAB) 98%, toluene 99%, dichloromethane (DCM) >99%, poly(vinyl pyrrolidone) (PVP) (40 kDa), chloroplatinic acid (H₂PtCl₆) 99%, chloroauric acid (HAuCl₄) 99.99%, 35% hydrogen peroxide, hexyl salicylate, 99%, and sodium borohydride were obtained from Sigma-Aldrich. All solutions were prepared using ultrapure Milli-Q water (resistivity of 18.2 MΩ·cm).

2.2. Methods. **2.2.1. Synthesis of Polymeric Capsules with Oil Core.** PMMA (5–10g) was dissolved in DCM (76–81g). The oil to be encapsulated (14g) was added and mixed until a single phase formed. This was used as the emulsion dispersed phase. CTAB (0.28g) was dissolved into 100 mL Milli-Q water to form the emulsion continuous phase. The dispersed phase (7 mL) and continuous phase (7 mL) were added to a glass vial and emulsified (using IKA T25 Ultra-Turrax) at 15 000 rpm for 2 min. The emulsion was then stirred magnetically at 400 rpm while a further 86 mL of continuous phase was poured in slowly. The diluted emulsion was then stirred at 400 rpm for 24 h at room temperature to allow capsule formation to occur—this stage allows for extraction of DCM into the continuous phase and subsequent evaporation, which forces precipitation of the polymer onto the emulsion droplet surface. The resulting capsules underwent three washing steps via centrifugation (Heraeus Megafuge R16) at 4000 rpm for 5 min, during which the supernatant was removed and replaced with fresh Milli-Q water. Finally, the capsules were redispersed in 50 mL Milli-Q water. Colloidal stability of the prepared capsules was verified over the time scale of the procedure through light scattering measurements.

2.2.2. Preparation of Platinum Nanoparticles. H₂PtCl₆·6H₂O (0.23 g) was added to an aqueous solution of PVP (100 mL, 1.56 μM) and stirred to dissolve. An aqueous solution of NaBH₄ (0.4 mL, 0.5 mM) was added to the platinum salt–PVP solution with vigorous stirring for 2 min. The mixture immediately turned dark brown, suggesting formation of solid platinum (as illustrated in eq 2), and was left to stand overnight for the formation of PVP-Pt nanoparticles to complete.²⁶



The resulting suspensions were characterized through TEM and light scattering measurements, confirming the formation of Pt nanoparticles 2–4 nm in diameter.

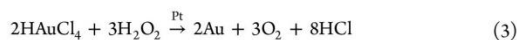
2.2.3. Adsorption of PVP-Stabilized Pt Nanoparticles. PMMA capsules (1.0 mL, 2 wt %) were added to the PVP-Pt nanoparticle suspension (5 mL), and mixed for 10 min at 30 rpm. Immediately

C

DOI: 10.1021/acsami.5b03116
ACS Appl. Mater. Interfaces XXXX, XXX, XXX–XXX

after, the capsules were washed by centrifugation at 4000 rpm for 5 min, three times. The capsules were subsequently redispersed in 30 mL Milli-Q water. Colloidal stability of the resulting Pt-loaded microcapsules was verified through light scattering measurements.

2.2.4. Au Film Growth. HAuCl₄ (1 mL, 40 mM), hydrogen peroxide (1 mL, 60 mM) and poly(vinyl pyrrolidone) (1 mL, 0.05 mM; used in this procedure as a polymeric stabilizer to provide colloidal stability to the resulting microcapsules) formed the electroless plating solution, which was heated to 60 °C. Pt-loaded polymer capsules (3 mL, 0.6 wt %) pre-heated to 60 °C were added dropwise to the plating solution and stirred vigorously for 5 min, during which the gold ions were reduced to solid gold, as shown in eq 3. The capsules were subsequently washed by centrifugation at 4000 rpm for 5 min, three times.



The resulting metallic-shell microcapsules were subsequently characterized through a range of methods described below.

2.3. Characterization. **2.3.1. Microscopy.** The morphology of the microcapsules was studied using an Olympus BX51 optical microscope, a LEO 1530 Gemini field emission gun scanning electron microscopy (FEGSEM), and an FEI Tecnai TF20 field emission transmission gun electron microscopy (FEGTEM) fitted with a HAADF detector and Gatan Orius SC600A CCD camera. Prior to TEM analysis, samples were dispersed on a TEM grid (holey carbon film, 400 Cu Mesh from Agar Scientific). Chemical compositions of the metal-coated microcapsules were analyzed using an Oxford Instruments INCA 350 energy dispersive X-ray spectroscopy (EDX) with 80 mm X-Max SDD detector, within the FEGTEM and FEGSEM instruments. To analyze metal shell thickness, cross sections of the capsules were taken using microtomy, prior to being studied by FEGTEM and analyzed using ImageJ image processing software.

2.3.2. Release Rate of Hexyl Salicylate Using Gas Chromatography (GC). In all our release experiments, we compared the metal-coated capsules against standard polymer-shell capsules. An equal portion of polymer capsules was removed from the sample undergoing the coating procedure. The polymer capsules were subjected to the same washing steps as the metal coated capsules to ensure equivalent losses of encapsulated oil (although minimal over the time scale of the experiment) from the capsule cores through the various stages of the process. Release rates in different solvent conditions were measured using gas chromatography as follows.

In a typical experiment, a known volume of metal-coated capsules was centrifuged to remove the supernatant. A corresponding sample of polymer-shell capsules was also centrifuged to remove the supernatant.

Each sample was dispersed in 2 mL of Milli-Q water and heated to 40 °C. Then, 8 mL of absolute ethanol at 40 °C was added to each sample and the capsules were redispersed and placed in a water bath at 40 °C. This procedure was chosen for compliance with industry standard tests. One milliliter (1 mL) of each agitated suspension was taken at known time intervals over a period of 21 days. The extracted capsule samples were centrifuged at 7000 rpm for 1 min and the supernatant analyzed via GC.

Samples were run on a PerkinElmer Clarus 580GC using the following method and column. GC column: Elite-1 capillary column; length, 30 m; internal diameter, 0.25 mm. The column temperature was programmed from 50 to 300 °C at 20 °C/min at a flow rate of 2 mL/min.

All data were compared against a calibration curve of the encapsulated oil determined in the same continuous phase of 4:1 ethanol–water mixture.

2.3.3. Measuring Nanoparticle Density on Capsule Surfaces Using TEM. TEM was employed to measure the surface adsorption density of PVP-Pt NPs on the capsule surface. Only capsules smaller than ~500 nm diameter were sufficiently transparent to gather enough contrast between the NPs and the capsules to provide enough information for particle counting. Assumptions were made that no effects of curvature during the nanoparticle adsorption process were to be expected and that capsules of all sizes were coated with Pt

nanoparticles to the same degree. The variation of intensity across the spherical capsules meant that automated counting software such as imageJ proved to be inadequate. Instead, once suitable small capsules were found, images were analyzed manually. The sample area distance from the center of the sphere was noted in each case. Each measurement was corrected for both surface curvature and the transparent nature of the capsules (as nanoparticles on both sides of the capsules were detectable, while only one hemisphere is being accounted for).

3. RESULTS AND DISCUSSION

3.1. Synthesis of Gold-Coated PMMA Capsules Containing a Toluene Core.

For proof of principle that a polymer capsule can be coated with a metal film, a model system is used, where toluene is the core material and poly(methyl methacrylate) (PMMA) is the precipitated microcapsule polymer shell. Toluene is a small, volatile oil, which provides a good model for typical fragrance oils. In these experiments, PMMA shell microcapsules were formed from an initial oil-in-water emulsion template via the following steps. The emulsion-dispersed phase contained PMMA dissolved in DCM, a volatile good solvent for the polymer, and toluene, both a poor solvent for the polymer and the model encapsulate. Upon dilution of the emulsion in water, the DCM is extracted from the dispersed droplets, which induces precipitation of the polymer. Under the correct wetting conditions, as DCM is fully extracted (and evaporated), the polymer precipitates at the droplet surface, thus forming a complete shell around the oil core.^{25,36,37}

The key variables affecting the capsule morphology and properties are the composition of the emulsion dispersed phase, the type and concentration of stabilizer used, and the method of emulsification. The stabilizer choice is a key determinant in the resulting capsule morphology.^{25,36} By varying the “core” phase composition, it is possible to control the resulting polymer shell thickness in relation to the core.³⁸ For example, using the dispersed phase composition of PMMA 10 wt %, DCM 76 wt % and core oil 14 wt %, we obtain capsules with a 32% shell volume and, correspondingly, a 68% core volume. The size of the final capsules is dependent on the emulsification step, for which a number of routine methods exist for controlling droplet size and size distribution.³⁹

Figure 2a shows a scanning electron micrograph of a typical sample of PMMA shell–toluene core microcapsules formed by ultraturax homogenization.

Platinum nanoparticles are a known catalyst for electroless gold salt reduction and can be tailored to efficiently adsorb onto polymer substrates.²⁶ In our case, CTAB is used as the stabilizer during the synthesis of the polymer microcapsules and results in a net positive charge to the capsule surfaces (typical measured zeta potential of the polymer capsules is ~ +60 mV). Such surfaces are thus suitable substrates for adsorption of both negatively charged and uncharged polymer-stabilized nanoparticles. In the example shown in Figure 2b, platinum nanoparticles stabilized with PVP are adsorbed onto the surface of PMMA microcapsules, under similar conditions to those reported by Nakao et al.⁴⁰ In brief, the nanoparticles were adsorbed by introducing a known quantity of PVP-stabilized Pt nanoparticles to the microcapsule suspension followed by a 10 min mixing step. This was found to be a sufficient time for the nanoparticles to efficiently adsorb to the capsule surface, as demonstrated in Figure 2b. However, careful consideration must be given to the ratio of PVP to platinum salt when preparing the nanoparticle suspension, as excess PVP in the

D

DOI: 10.1021/acsami.5b03116
ACS Appl. Mater. Interfaces XXXX, XXX, XXX–XXX

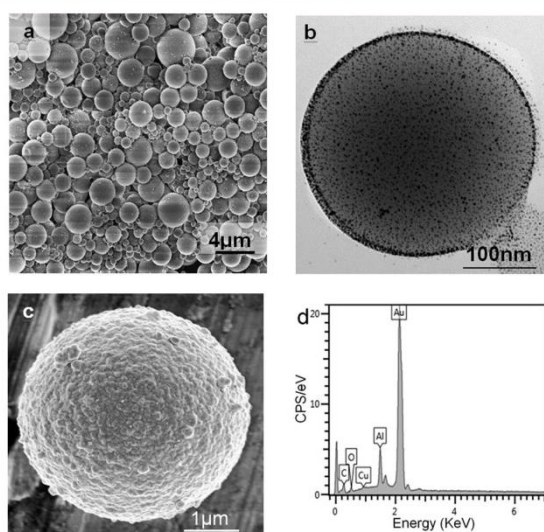


Figure 2. Example of toluene core microcapsules obtained for each step of the process leading to metal coated polymer capsule. (a) Scanning electron micrograph of PMMA microcapsules. (b) Transmission electron micrograph of PVP-stabilized Pt nanoparticle adsorbed onto PMMA microcapsules (note that the TEM observations are specifically focused on the smallest capsules to visualize the Pt nanoparticles throughout the whole shell). (c) Scanning electron micrograph of gold-coated PMMA microcapsules. (d) EDX analysis of metal-coated polymer microcapsules obtained during SEM observation.

system will compete with the PVP-stabilized Pt nanoparticles for surface adsorption sites on the capsule surfaces. This is the subject of further more systematic studies and will be reported separately.

A thin film of solid gold can be grown directly onto the adsorbed platinum nanoparticle layer using electroless plating. This method utilizes the platinum as a catalyst and nucleation site for gold growth in the presence of a reducing agent for the metal ions. By introducing the capsules to the electroless plating solution described in section 2.2.4 at 60 °C, and allowing the reaction to occur under mixing for 5 min, a continuous gold film can be deposited on the PVP-Pt-loaded polymer capsules. It is worth noting here that the presence of the nanoparticles localizes the deposition of solid gold onto the surface of the capsules, which limits further precipitation in the

continuous phase. Once all the catalytic platinum sites are covered, the gold film can continue to grow, as gold nanoparticles also act as a catalyst for the decomposition of hydrogen peroxide, although this is a slower process.⁴¹ The reaction is much faster at higher temperatures and so the platinum catalytic sites are used up rapidly, followed by autocatalytic gold growth at a faster rate than under ambient conditions.

The scanning electron micrograph and EDX graph in Figure 2c,d give evidence of the successful growth of the gold film on the capsule surface using this method.

3.2. Controlling the Density of Nanoparticles Adsorbed to the Capsule Surface. Surface adsorption homogeneity, surface density, and energy of adsorption of the catalytic PVP-Pt NP layer onto the microcapsule polymeric shells are important variables which can affect the quality of subsequent secondary metallic film growth via electroless deposition. This part of the work concentrates on the possibility of obtaining films of PVP-Pt nanoparticles of different surface densities, which is likely to affect the quality (i.e., the permeability) and thickness of the metal films.

By changing the concentration of PVP-Pt nanoparticles in the dispersion, it is possible to control the 2D density of the nanoparticles adsorbed onto the surface of the polymer capsules, as shown in Figures 3 and 4. When comparing the

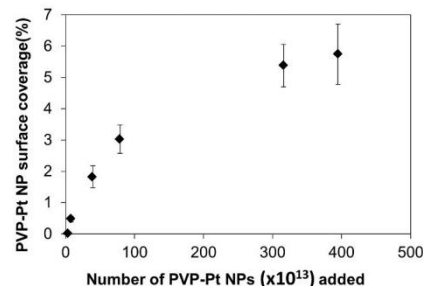


Figure 4. TEM data showing how the concentration of PVP-Pt NPs in the continuous phase affects the resulting adsorption density of the NPs on the polymeric microcapsule surface (conversion of number NPs per μm^2 to percentage surface coverage used mean diameter of NPs).

insets in Figure 3a and d, it is clear that the metal film growth is limited to the surface of the primary nanoparticles. Therefore, it is possible to conclude here that if the 2D density of the

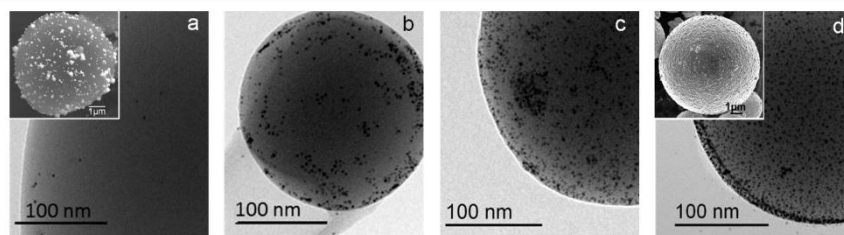


Figure 3. Transmission electron micrographs showing NP adsorption densities on the polymeric microcapsule surfaces as a function of the number of PVP-Pt nanoparticles added to 2 wt % polymer capsules. (a) 1.55×10^{15} , (b) 3.10×10^{15} , (c) 1.26×10^{16} , (d) 1.59×10^{16} . (a and d, insets) Corresponding gold-coated capsules (note that both these images were obtained using different electron beam intensity in order to adjust the required contrast between the polymer and gold areas; the location of the gold on the surface was verified via EDX).

E

DOI: 10.1021/acsami.5b03116
ACS Appl. Mater. Interfaces XXXX, XXX, XXX–XXX

primary nanoparticle catalyst on the polymer capsule surface is sufficiently low (as shown in Figure 3a), the secondary metal film cannot grow on the full capsule surface. The maximum nanoparticle surface coverage achieved was measured at $\sim 5\%$ of the total surface area of the capsules (Figure 3d). This level of surface coverage is equivalent to a 2D hexagonal close packed PVP-Pt NP core–core separation of ~ 12 nm. However, it is worth noting here that the measurement only takes into account the platinum core of the nanoparticles and not the surrounding stabilizing PVP shell, as only the high-density Pt is resolved in the TEM. Indeed, close inspection of the nanoparticles on the capsule surface shows that the nanoparticles are not in close contact, which is consistent with other observations of sterically stabilized nanoparticle adsorption on surfaces.⁴² Taking account of the stabilizing PVP layer, the observed 5% surface coverage (of the Pt cores) most likely corresponds to the maximum surface coverage. As seen in Figure 4, at higher nanoparticle concentrations, the surface coverage plateaus at this $\sim 5\%$ coverage. Such a low surface coverage is in agreement with surface adsorption of nanoparticles, where the spacing between the adsorbed particles can be influenced by the presence of a large polymer stabilizer or charged species on the surface of the nanoparticles.⁴³

3.3. Encapsulation of a Fragrance Oil within an Impermeable Metallic Shell. The potential of metallic shell capsules for “permanently” encapsulating low molecular weight, volatile oils within a continuous phase that can dissolve the encapsulated actives is demonstrated in this section. Polymer capsules are porous and are known to allow diffusion of the core into the external environment,⁸ particularly if there is a high solubility of the core in the continuous phase. Here, the potential of the developed metal shell capsules for retaining a volatile fragrance oil within their core is compared to that of the precursor polymer-shell capsules. The procedure for monitoring the release of the fragrance oil from both sets of capsules is described in section 2.3.2.

Although toluene proved to be a suitable system to test the nanoparticle adsorption and subsequent secondary metal film growth, its relatively high solubility in water (~ 0.52 g·L⁻¹ at 25 °C) prevented its use for release testing. Thus, the fragrance oil used here is hexyl salicylate, an oil routinely used as a component of formulated products. It has poor water solubility ($\sim 9 \times 10^{-4}$ g·L⁻¹ at 25 °C) which is advantageous as compared to the use of toluene. This ensures maximum core retention through the precursor polymer capsules preparation and washing procedure before porosity testing (at 40 °C) in 4:1 ethanol/water mixtures. In this case, polymer capsules produced from an oil emulsion template initially containing 10 wt % PMMA were coated with Pt nanoparticles and a film of solid gold, as described in sections 2.2.3 and 2.2.4.

Characterization of the release of hexyl salicylate was performed with gas chromatography for both sets of capsules. Figure 5 shows that the bare polymer capsules release their entire contents into the ethanol–water mix within 20 min.

When a gold film is grown on the surface of the precursor polymer capsules (at a reaction temperature of 60 °C), only a small fraction of the initially encapsulated oil is released, (typically smaller than the error associated with the measurement) over the 21 day test period.²² By mechanically fracturing the metal-coated capsules (as demonstrated in the inset of Figure 5) and testing the sample again for core release, we measured a release of 49% of the initial hexyl salicylate oil present in the precursor polymeric capsules, thus confirming

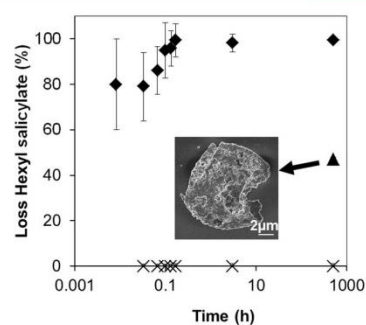


Figure 5. (◆) Hexyl salicylate release profile from PMMA capsules and (×) gold coated PMMA capsules, placed in 4:1 ethanol–water at 40 °C. (▲) Release of encapsulated oil observed from mechanically fractured gold coated capsules (after residing in ethanol–water mixture for 7 days). (Inset) SEM image of a mechanically fractured gold coated PMMA capsule with hexyl salicylate core.

the presence of encapsulated oil within the metal shell microcapsules. The fact that not all of the oil was recovered from the mechanically fractured capsules is likely due to loss of material during the fracturing procedure and because not all capsule shells were successfully broken.

3.4. Controlling Metal Shell Quality. This part of the work investigates the effect of the electroless plating reaction temperature over the shell thickness of the metal film produced and its resulting permeability. By reducing the reaction temperature for the metal growth, it is expected that we will obtain thinner metal films as a consequence of a slower reaction rate.⁴⁴ Growth of thinner metal films are a potential cost advantage with regards to a manufacturing process provided the capsule impermeability can be retained.

Figure 6 shows that as the temperature decreases, the measured shell thickness (via transmission electron microscopy

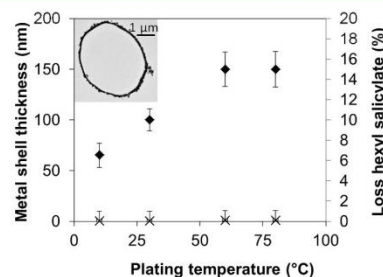


Figure 6. (◆) Thickness of metal shell as a function of plating temperature, measured from microtome images using TEM, and (×) release of core as a function of plating temperature (4:1 ethanol–water mixture for 7 days at 40 °C). (Inset) TEM image showing a microtomed capsule from which shell thicknesses are measured. A high-magnification image of part of this cross section is shown in the Supporting Information.

of microtomed samples and subsequent image processing) decreases significantly from 150 to 60 nm. However, above 60 °C, the film thickness appears to reach a plateau. This phenomenon is potentially linked to the gold salt supply being fully depleted due to the faster rate of reaction at higher temperatures leading to metal formation in the bulk solution.

F

DOI: 10.1021/acsami.5b03116
ACS Appl. Mater. Interfaces XXXX, XXX, XXX–XXX

Release studies conducted for the four samples of capsules obtained by varying the film growth temperature show no significant release (a maximum of 0.1 wt %, which is within experimental error) of the encapsulated oil into the water/ethanol bulk phase. The full retention of the core oil implies that a complete impermeable shell is formed in all cases independently of its thickness. It is expected that further optimization of the metal film growth conditions could lead to sub-10 nm impermeable films.

4. CONCLUSIONS

In this work, we have successfully demonstrated that a polymeric microcapsule containing a small, volatile oil, can be coated with an impermeable metal shell preventing significant release of the core material over days. The nanoparticle density on the polymeric capsule surface can be controlled, which can be used to vary the final metal film thickness and structure. By reducing the electroless plating reaction temperature we can achieve thinner, continuous films that retain their impermeability. This control provides advantages with respect to cost efficiency and operating conditions, both of which have positive implications for manufacturing. The use of expensive metal components in this demonstrated example can be justified when using these systems in high-margin products such as perfumes, but further work will investigate different catalysts and metal coatings such as silver, copper, and nickel, which will open up the potential of this platform technology for the delivery of a large range of other active ingredients.

■ ASSOCIATED CONTENT

■ Supporting Information

High-magnification TE micrograph showing part of a cross section of a typical hexyl salicylate core-PMMA shell-gold capsule at a plating temperature of 30 °C (full cross section shown in the inset of Figure 6). The Supporting Information is available free of charge on the ACS Publications website at DOI: 10.1021/acsami.5b03116.

■ AUTHOR INFORMATION

■ Corresponding Author

*E-mail: o.j.cayre@leeds.ac.uk.

■ Notes

The authors declare no competing financial interest.

■ ACKNOWLEDGMENTS

The authors acknowledge the EPSRC for grant numbers EP/J500458/1 and EP/K503836/1, providing us with the funding to complete this work. We also acknowledge the funding received from Procter and Gamble. We would like to express our gratitude to Martin Fuller for preparation of the microtome samples. Data in this work are patent pending.

■ REFERENCES

- (1) Bône, S.; Vautrin, C.; Barbesant, V.; Truchon, S.; Harrison, I.; Geffroy, C. Microencapsulated Fragrances in Melamine Formaldehyde Resins. *Chimia* **2011**, *65* (3), 177–181.
- (2) Cao, J.; Su, T.; Zhang, L.; Liu, R.; Wang, G.; He, B.; Gu, Z. Polymeric Micelles with Citraconic Amide as Ph-Sensitive Bond in Backbone for Anticancer Drug Delivery. *Int. J. Pharm.* **2014**, *471* (1–2), 28–36.
- (3) Chang, W. T. H.; Chen, H. Y.; Wang, Y. C. Microcapsule Composition for Inhibiting an Ethylene Response in Plants, Method

for Preparing Microcapsules, and Method Using the Microcapsule Composition. US 08461086, Jun 11, 2013.

- (4) Gibbs, B. F.; Kermasha, S.; Alli, I.; Mulligan, C. N. Encapsulation in the Food Industry: A Review. *Int. J. Food Sci. Nutr.* **1999**, *50* (3), 213–224.

- (5) Mao, Z.; Song, M.; Zhong, Y.; Xu, H.; Zhang, L. Microcapsule-Supported Binuclear Manganese Complex as an Efficient and Reusable Oxidation Catalyst. *Chem. Eng. J.* **2014**, *240*, 116–123.

- (6) Park, K. M.; Sung, H.; Choi, S. J.; Choi, Y. J.; Chang, P.-S. Double-Layered Microparticles with Enzyme-Triggered Release for the Targeted Delivery of Water-Soluble Bioactive Compounds to Small Intestine. *Food Chem.* **2014**, *161*, 53–59.

- (7) Cai, S.; Zhao, M.; Fang, Y.; Nishinari, K.; Phillips, G. O.; Jiang, F. Microencapsulation of Lactobacillus Acidophilus Cgmcc1.2686 Via Emulsification/Internal Gelation of Alginate Using Ca-Edta and Caco3 as Calcium Sources. *Food Hydrocolloids* **2014**, *39*, 295–300.

- (8) Bergek, J.; Trojer, M. A.; Mok, A.; Nordstierna, L. Controlled Release of Microencapsulated 2-*n*-Octyl-4-Isothiazolin-3-One from Coatings: Effect of Microscopic and Macroscopic Pores. *Colloids Surf. Physicochem. Eng. Aspects* **2014**, *458*, 155–167.

- (9) Caruso, F.; Trau, D.; Mohwald, H.; Renneberg, R. Enzyme Encapsulation in Layer-by-Layer Engineered Polymer Multilayer Capsules. *Langmuir* **2000**, *16* (4), 1485–1488.

- (10) Dai, L.; Li, J.; Zhang, B.; Liu, J.; Luo, Z.; Cai, K. Redox-Responsive Nanocarrier Based on Heparin End-Capped Mesoporous Silica Nanoparticles for Targeted Tumor Therapy in Vitro and in Vivo. *Langmuir* **2014**, *30* (26), 7867–77.

- (11) Dong, L.; Peng, H.; Wang, S.; Zhang, Z.; Li, J.; Ai, F.; Zhao, Q.; Luo, M.; Xiong, H.; Chen, L. Thermally and Magnetically Dual-Responsive Mesoporous Silica Nanospheres: Preparation, Characterization, and Properties for the Controlled Release of Sophoridine. *J. Appl. Polym. Sci.* **2014**, *131* (13).

- (12) Dowding, P. J.; Atkin, R.; Vincent, B.; Bouillot, P. Oil Core/Polymer Shell Microcapsules by Internal Phase Separation from Emulsion Droplets. II: Controlling the Release Profile of Active Molecules. *Langmuir* **2005**, *21* (12), 5278–5284.

- (13) Giovagnoli, S.; Palazzo, F.; Di Michele, A.; Schoubben, A.; Blasi, P.; Ricci, M. The Influence of Feedstock and Process Variables on the Encapsulation of Drug Suspensions by Spray-Drying in Fast Drying Regime: The Case of Novel Antitubercular Drug-Palladium Complex Containing Polymeric Microparticles. *J. Pharm. Sci.* **2014**, *103* (4), 1255–1268.

- (14) Vasisht, N. Applications of Mass and Heat Transfer in Microencapsulation Processes. In *Microencapsulation in the Food Industry*, Gaonkar, A. G., Vasisht, N., Khare, A. R., Sobel, R., Eds. Academic Press: San Diego, 2014; Chapter 3, pp 25–32.

- (15) Hui, Y. H.; Chandan, R. C.; Clark, S.; Cross, N. A.; Dobbs, J. C.; Hurst, W. J.; Nollet, L. M. L.; Shimoni, E.; Sinha, N.; Smith, E. B. *Handbook of Food Products Manufacturing*, 2 Vol. Set. John Wiley & Sons: Hoboken, NJ, 2007.

- (16) Ponitsch, M.; Gotthardt, P.; Gruger, A.; Brion, H. G.; Kirchheim, R. Diffusion of Small Molecules in Glassy Polymers. *J. Polym. Sci., Part B: Polym. Phys.* **1997**, *35* (15), 2397–2408.

- (17) Mallepally, R. R.; Parrish, C. C.; Mc Hugh, M. A.; Ward, K. R. Hydrogen Peroxide Filled Poly(methyl methacrylate) Microcapsules: Potential Oxygen Delivery Materials. *Int. J. Pharm.* **2014**, *475* (1–2), 130–137.

- (18) Trojer, M. A.; Andersson, H.; Li, Y.; Borg, J.; Holmberg, K.; Nyden, M.; Nordstierna, L. Charged Microcapsules for Controlled Release of Hydrophobic Actives. Part III: The Effect of Polyelectrolyte Brush- and Multilayers on Sustained Release. *Phys. Chem. Chem. Phys.* **2013**, *15* (17), 6456–6466.

- (19) Zieringer, M. A.; Carroll, N. J.; Abbaspourrad, A.; Koehler, S. A.; Weitz, D. A. Microcapsules for Enhanced Cargo Retention and Diversity. *Small* **2015**, DOI: 10.1002/smll.201403175.

- (20) Cussler, E. L.; Moggridge, G. D. *Chemical Product Design*. Cambridge University Press: Cambridge, U.K., 2001.

- (21) Prins, W.; Hermans, J. J. Theory of Permeation through Metal Coated Polymer Films. *J. Phys. Chem.* **1959**, *63* (5), 716–720.

G

DOI: 10.1021/acsami.5b03116
ACS Appl. Mater. Interfaces XXXX, XXX, XXX–XXX

- (22) Marko, J. *Mass Transfer in Chemical Engineering Processes*. InTech: Rijeka, Croatia, 2011.
- (23) Smithells, C. J.; Ransley, C. E. The Diffusion of Gases through Metals. II. Diffusion of Hydrogen through Aluminium. *Proc. R. Soc. London, Ser. A* **1935**, *152* (877), 706–713.
- (24) Dowding, P. J.; Atkin, R.; Vincent, B.; Bouillot, P. Oil Core–Polymer Shell Microcapsules Prepared by Internal Phase Separation from Emulsion Droplets. I. Characterization and Release Rates for Microcapsules with Polystyrene Shells. *Langmuir* **2004**, *20* (26), 11374–11379.
- (25) Loxley, A.; Vincent, B. Preparation of Poly(methyl methacrylate) Microcapsules with Liquid Cores. *J. Colloid Interface Sci.* **1998**, *208* (1), 49–62.
- (26) Horiuchi, S.; Nakao, Y. Platinum Colloid Catalyzed Etchingless Gold Electroless Plating with Strong Adhesion to Polymers. *Surf. Coat. Technol.* **2010**, *204* (23), 3811–3817.
- (27) Lin, K.-J.; Wu, H.-M.; Yu, Y.-H.; Ho, C.-Y.; Wei, M.-H.; Lu, F.-H.; Tseng, W. J. Preparation of Pmma-Ni Core–Shell Composite Particles by Electroless Plating on Polyelectrolyte-Modified Pmma Beads. *Appl. Surf. Sci.* **2013**, *282*, 741–745.
- (28) Karagoz, B.; Sirkecioglu, O.; Bicak, N. Surface Rejuvenation for Multilayer Metal Deposition on Polymer Microspheres via Self-Seeded Electroless Plating. *Appl. Surf. Sci.* **2013**, *285*, 395–402.
- (29) Kim, B. C.; Park, J. H.; Lee, S. J. Preparation of Composite Particles via Electroless Nickel Plating on Polystyrene Microspheres and Effect of Plating Conditions. *Polymer (Korea)* **2010**, *34* (1), 25–31.
- (30) Bicak, N.; Sungur, S.; Tan, N.; Bensebaa, F.; Deslandes, Y. Metalization of Polymer Beads via Polymer-Supported Hydrazines as Reducing Agents. *J. Polym. Sci., Part A: Polym. Chem.* **2002**, *40* (6), 748–754.
- (31) Lee, J.-H.; Oh, J. S.; Lee, P. C.; Kim, D. O.; Lee, Y.; Nam, J.-D. Fabrication of Nickel/Gold Multilayered Shells on Polystyrene Bead Cores by Sequential Electroless Deposition Processes. *J. Electron. Mater.* **2008**, *37* (10), 1648–1652.
- (32) Mandal, S.; Sathish, M.; Saravanan, G.; Datta, K.; Ji, Q.; Hill, J. P.; Abe, H.; Honma, I.; Ariga, K. Open-Mouthed Metallic Microcapsules: Exploring Performance Improvements at Agglomeration-Free Interiors. *J. Am. Chem. Soc.* **2010**, *132* (41), 14415–14417.
- (33) Patchan, M. W.; Baird, L. M.; Rhim, Y.-R.; LaBarre, E. D.; Maisano, A. J.; Deacon, R. M.; Xia, Z.; Benkoski, J. J. Liquid-Filled Metal Microcapsules. *ACS Appl. Mater. Interfaces* **2012**, *4* (5), 2406–2412.
- (34) Nocera, G. M.; Ben M'Barek, K.; Bazzoli, D. G.; Fraux, G.; Bontems-Van Heijenoort, M.; Chokki, J.; Georgeault, S.; Chen, Y.; Fattaccioli, J. Fluorescent Microparticles Fabricated through Chemical Coating of O/W Emulsion Droplets with a Thin Metallic Film. *RSC Advances* **2014**, *4* (23), 11564–11568.
- (35) Haaf, F.; Sanner, A.; Straub, F. Polymers of N-Vinylpyrrolidone: Synthesis, Characterization and Uses. *Polym. J.* **1985**, *17* (1), 143–152.
- (36) Yow, H. N.; Routh, A. F. Formation of Liquid Core-Polymer Shell Microcapsules. *Soft Matter* **2006**, *2* (11), 940–949.
- (37) Trojer, M. A.; Li, Y.; Abrahamsson, C.; Mohamed, A.; Eastoe, J.; Holmberg, K.; Nyden, M. Charged Microcapsules for Controlled Release of Hydrophobic Actives. Part I: Encapsulation Methodology and Interfacial Properties. *Soft Matter* **2013**, *9* (5), 1468–1477.
- (38) Cayre, O. J.; Biggs, S. Hollow Microspheres with Binary Colloidal and Polymeric Membrane: Effect of Polymer and Particle Concentrations. *Adv. Powder Technol.* **2010**, *21* (1), 19–22.
- (39) Manga, M. S.; Cayre, O. J.; Williams, R. A.; Biggs, S.; York, D. W. Production of Solid-Stabilised Emulsions through Rotational Membrane Emulsification: Influence of Particle Adsorption Kinetics. *Soft Matter* **2012**, *8* (5), 1532–1538.
- (40) Nakao, Y.; Kaeriyama, K. Preparation of Noble Metal Sols in the Presence of Surfactants and Their Properties. *J. Colloid Interface Sci.* **1986**, *110* (1), 82–87.
- (41) Quintanilla, A.; Garcia-Rodriguez, S.; Dominguez, C. M.; Blasco, S.; Casas, J. A.; Rodriguez, J. J. Supported Gold Nanoparticle Catalysts for Wet Peroxide Oxidation. *Appl. Catal., B* **2012**, *111*, 81–89.
- (42) Lu, Y.; Liu, G. L.; Lee, L. P. High-Density Silver Nanoparticle Film with Temperature-Controllable Interparticle Spacing for a Tunable Surface Enhanced Raman Scattering Substrate. *Nano Lett.* **2004**, *5* (1), 5–9.
- (43) Park, J. J.; Lacerda, S. H. D. P.; Stanley, S. K.; Vogel, B. M.; Kim, S.; Douglas, J. F.; Raghavan, D.; Karim, A. Langmuir Adsorption Study of the Interaction of CdSe/ZnS Quantum Dots with Model Substrates: Influence of Substrate Surface Chemistry and Ph. *Langmuir* **2009**, *25* (1), 443–450.
- (44) Iacovangelo, C. D. Autocatalytic Electroless Gold Deposition Using Hydrazine and Dimethylamine Borane as Reducing Agents. *J. Electrochem. Soc.* **1991**, *138* (4), 976–982.

H

DOI: 10.1021/acsami.5b03116
ACS Appl. Mater. Interfaces XXXX, XXX, XXX–XXX

10 References

- [1] S. Bône, C. Vautrin, V. Barbesant, S. Truchon, I. Harrison, and C. Geffroy, "Microencapsulated Fragrances in Melamine Formaldehyde Resins," *CHIMIA*, vol. 65, pp. 177-181, // 2011.
- [2] J. Cao, T. Su, L. Zhang, R. Liu, G. Wang, B. He, *et al.*, "Polymeric micelles with citraconic amide as pH-sensitive bond in backbone for anticancer drug delivery," *International journal of pharmaceuticals*, vol. 471, pp. 28-36, 2014-Aug-25 2014.
- [3] W. T. H. Chang, H. Y. Chen, and Y. C. Wang, "Microcapsule composition for inhibiting an ethylene response in plants, method for preparing microcapsules, and method using the microcapsule composition," US 08461086, 2013.
- [4] B. F. Gibbs, S. Kermasha, I. Alli, and C. N. Mulligan, "Encapsulation in the food industry: a review," *International Journal of Food Sciences and Nutrition*, vol. 50, pp. 213-224, May 1999.
- [5] Z. Mao, M. Song, Y. Zhong, H. Xu, and L. Zhang, "Microcapsule-supported binuclear manganese complex as an efficient and reusable oxidation catalyst," *Chemical Engineering Journal*, vol. 240, pp. 116-123, Mar 15 2014.
- [6] K. M. Park, H. Sung, S. J. Choi, Y. J. Choi, and P.-S. Chang, "Double-layered microparticles with enzyme-triggered release for the targeted delivery of water-soluble bioactive compounds to small intestine," *Food chemistry*, vol. 161, pp. 53-59, Oct 15 2014.
- [7] S. Cai, M. Zhao, Y. Fang, K. Nishinari, G. O. Phillips, and F. Jiang, "Microencapsulation of *Lactobacillus acidophilus* CGMCC1.2686 via emulsification/internal gelation of alginate using Ca-EDTA and CaCO₃ as calcium sources," *Food Hydrocolloids*, vol. 39, pp. 295-300, Aug 2014.
- [8] J. Bergek, M. A. Trojer, A. Mok, and L. Nordstierna, "Controlled release of microencapsulated 2-n-octyl-4-isothiazolin-3-one from coatings: Effect of microscopic and macroscopic pores," *Colloids and Surfaces a: Physicochemical and Engineering Aspects*, vol. 458, pp. 155-167, Sep 20 2014.
- [9] F. Caruso, D. Trau, H. Mohwald, and R. Renneberg, "Enzyme encapsulation in layer-by-layer engineered polymer multilayer capsules," *Langmuir*, vol. 16, pp. 1485-1488, Feb 22 2000.
- [10] L. Dai, J. Li, B. Zhang, J. Liu, Z. Luo, and K. Cai, "Redox-responsive nanocarrier based on heparin end-capped mesoporous silica nanoparticles for targeted tumor therapy in vitro and in vivo," *Langmuir*, vol. 30, pp. 7867-77, 2014-Jul-8 2014.
- [11] L. Dong, H. Peng, S. Wang, Z. Zhang, J. Li, F. Ai, *et al.*, "Thermally and Magnetically Dual- Responsive Mesoporous Silica Nanospheres: Preparation, Characterization, and Properties for the Controlled Release of Sophoridine," *Journal of Applied Polymer Science*, vol. 131, Jul 5 2014.
- [12] P. J. Dowding, R. Atkin, B. Vincent, and P. Bouillot, "Oil core/polymer shell microcapsules by internal phase separation from emulsion droplets. II: Controlling the release profile of active molecules," *Langmuir*, vol. 21, pp. 5278-5284, Jun 7 2005.
- [13] S. Giovagnoli, F. Palazzo, A. Di Michele, A. Schoubben, P. Blasi, and M. Ricci, "The Influence of Feedstock and Process Variables on the Encapsulation of Drug Suspensions by Spray-Drying in Fast Drying Regime: The Case of Novel Antitubercular Drug-Palladium Complex Containing Polymeric Microparticles," *Journal of Pharmaceutical Sciences*, vol. 103, pp. 1255-1268, Apr 2014.
- [14] N. Vasisht, "Chapter 3 - Applications of Mass and Heat Transfer in Microencapsulation Processes," in *Microencapsulation in the Food Industry*, A. G. Gaonkar, N. Vasisht, A. R. Khare, and R. Sobel, Eds., ed San Diego: Academic Press, 2014, pp. 25-32.

- [15] Y. H. Hui, R. C. Chandan, S. Clark, N. A. Cross, J. C. Dobbs, W. J. Hurst, *et al.*, *Handbook of Food Products Manufacturing, 2 Volume Set*: John Wiley & Sons, 2007.
- [16] M. Ponitsch, P. Gotthardt, A. Gruger, H. G. Brion, and R. Kirchheim, "Diffusion of small molecules in glassy polymers," *Journal of Polymer Science Part B: Polymer Physics*, vol. 35, pp. 2397-2408, Nov 15 1997.
- [17] R. R. Mallepally, C. C. Parrish, M. A. Mc Hugh, and K. R. Ward, "Hydrogen peroxide filled poly(methyl methacrylate) microcapsules: Potential oxygen delivery materials," *International Journal of Pharmaceutics*, vol. 475, pp. 130-137, Nov 20 2014.
- [18] M. A. Trojer, H. Andersson, Y. Li, J. Borg, K. Holmberg, M. Nyden, *et al.*, "Charged microcapsules for controlled release of hydrophobic actives. Part III: the effect of polyelectrolyte brush- and multilayers on sustained release," *Physical Chemistry Chemical Physics*, vol. 15, pp. 6456-6466, 2013.
- [19] E. L. Cussler and G. D. Moggridge, *Chemical Product Design*: Cambridge University Press, 2001.
- [20] W. Prins and J. J. Hermans, "Theory of Permeation through Metal Coated Polymer Films," *The Journal of Physical Chemistry*, vol. 63, pp. 716-720, 1959/05/01 1959.
- [21] A. Guerrero-Martínez, S. Barbosa, I. Pastoriza-Santos, and L. M. Liz-Marzán, "Nanostars shine bright for you: Colloidal synthesis, properties and applications of branched metallic nanoparticles," *Current Opinion in Colloid & Interface Science*, vol. 16, pp. 118-127, 2011.
- [22] C. J. Smithells and C. E. Ransley, "The Diffusion of Gases through Metals. II. Diffusion of Hydrogen through Aluminium," *Proceedings of the Royal Society of London, Series A; Mathematical and Physical Sciences*, vol. 152, pp. 706-713, 1935.
- [23] G. R. A Brenner, "Nickel plating on steel by chemical reduction," *National Bureau of Standards* vol. 37, 1946.
- [24] P. J. Dowding, R. Atkin, B. Vincent, and P. Bouillot, "Oil core-polymer shell microcapsules prepared by internal phase separation from emulsion droplets. I. Characterization and release rates for microcapsules with polystyrene shells," *Langmuir*, vol. 20, pp. 11374-11379, Dec 21 2004.
- [25] A. Loxley and B. Vincent, "Preparation of poly(methylmethacrylate) microcapsules with liquid cores," *Journal of Colloid and Interface Science*, vol. 208, pp. 49-62, Dec 1 1998.
- [26] S. Horiuchi and Y. Nakao, "Platinum colloid catalyzed etchingless gold electroless plating with strong adhesion to polymers," *Surface & Coatings Technology*, vol. 204, pp. 3811-3817, Aug 25 2010.
- [27] F. Hof, S. L. Craig, C. Nuckolls, and J. J. Rebek, "Molecular Encapsulation," *Angewandte Chemie International Edition*, vol. 41, pp. 1488-1508, 2002.
- [28] S. Gibbs Bf Fau - Kermasha, I. Kermasha S Fau - Alli, C. N. Alli I Fau - Mulligan, and M. CN, "Encapsulation in the food industry: a review," *Int J Food Sci Nutr*, vol. 50, pp. 213-24, 1999.
- [29] I. Aranberri, K. J. Beverley, B. P. Binks, J. H. Clint, and P. D. I. Fletcher, "How Do Emulsions Evaporate?," *Langmuir*, vol. 18, pp. 3471-3475, 2002/04/01 2002.
- [30] M. A. Zieringer, N. J. Carroll, A. Abbaspourrad, S. A. Koehler, and D. A. Weitz, "Microcapsules for Enhanced Cargo Retention and Diversity," *Small*, 2015.
- [31] W. Z. Jin-Mei Wang , Qing-Wen Song , Hong Zhu , Ying Zhou, "Preparation and Characterization of Natural Fragrant Microcapsules," *JFBI* vol. 1, 2009.
- [32] A. Madene, M. Jacquot, J. Scher, and S. Desobry, "Flavour encapsulation and controlled release – a review," *International Journal of Food Science & Technology*, vol. 41, pp. 1-21, 2006.
- [33] C. I. Beristain, A. Vazquez, H. S. Garcia, and E. J. Vernon-Carter, "Encapsulation of Orange Peel Oil by Co-crystallization," *LWT - Food Science and Technology*, vol. 29, pp. 645-647, 1996.

- [34] J. Risch Sara, "Encapsulation: Overview of Uses and Techniques," in *Encapsulation and Controlled Release of Food Ingredients*. vol. 590, ed: American Chemical Society, 1995, pp. 2-7.
- [35] M. Antonietti and S. Förster, "Vesicles and Liposomes: A Self-Assembly Principle Beyond Lipids," *Advanced Materials*, vol. 15, pp. 1323-1333, 2003.
- [36] Y.-C. Horng, P.-S. Huang, C.-C. Hsieh, C.-H. Kuo, and T.-S. Kuo, "Selective encapsulation of volatile and reactive methyl iodide," *Chemical Communications*, 2012.
- [37] A. Benichou, A. Aserin, and N. Garti, "Double emulsions stabilized with hybrids of natural polymers for entrapment and slow release of active matters," *Advances in Colloid and Interface Science*, vol. 108–109, pp. 29-41, 2004.
- [38] O. D. Velev, K. Furusawa, and K. Nagayama, "Assembly of Latex Particles by Using Emulsion Droplets as Templates. 1. Microstructured Hollow Spheres," *Langmuir*, vol. 12, pp. 2374-2384, 1996/01/01 1996.
- [39] O. J. Cayre, J. Hitchcock, M. S. Manga, S. Fincham, A. Simoes, R. A. Williams, *et al.*, "pH-responsive colloidosomes and their use for controlling release," *Soft Matter*, vol. 8, pp. 4717-4724, 2012.
- [40] T. Bollhorst, T. Grieb, A. Rosenauer, G. Fuller, M. Maas, and K. Rezwan, "Synthesis Route for the Self-Assembly of Submicrometer-Sized Colloidosomes with Tailorable Nanopores," *Chemistry of Materials*, vol. 25, pp. 3464-3471, 2013/09/10 2013.
- [41] P. J. Dowding, R. Atkin, B. Vincent, and P. Bouillot, "Oil Core/Polymer Shell Microcapsules Prepared by Internal Phase Separation from Emulsion Droplets. I. Characterization and Release Rates for Microcapsules with Polystyrene Shells," *Langmuir*, vol. 20, pp. 11374-11379, 2011/10/25 2004.
- [42] H. N. Yow and A. F. Routh, "Formation of liquid core-polymer shell microcapsules," *Soft Matter*, vol. 2, pp. 940-949, 2006.
- [43] E. Donath, G. B. Sukhorukov, F. Caruso, S. A. Davis, and H. Möhwald, "Novel Hollow Polymer Shells by Colloid-Templated Assembly of Polyelectrolytes," *Angewandte Chemie International Edition*, vol. 37, pp. 2201-2205, 1998.
- [44] W. Chen and T. J. McCarthy, "Layer-by-Layer Deposition: A Tool for Polymer Surface Modification," *Macromolecules*, vol. 30, pp. 78-86, 1997/01/01 1997.
- [45] C. N. R. Rao, G. U. Kulkarni, P. J. Thomas, V. V. Agrawal, and P. Saravanan, "Films of Metal Nanocrystals Formed at Aqueous–Organic Interfaces†," *The Journal of Physical Chemistry B*, vol. 107, pp. 7391-7395, 2003/07/01 2003.
- [46] C. N. R. Rao, G. U. Kulkarni, V. V. Agrawal, U. K. Gautam, M. Ghosh, and U. Tumkurkar, "Use of the liquid–liquid interface for generating ultrathin nanocrystalline films of metals, chalcogenides, and oxides," *Journal of Colloid and Interface Science*, vol. 289, pp. 305-318, 2005.
- [47] K. Y. Lee, Y. Bae, M. Kim, G.-W. Cheong, J. Kim, S. S. Lee, *et al.*, "Crown ether derivatives-mediated self-assembly of nanoparticles at the liquid/liquid interface," *Thin Solid Films*, vol. 515, pp. 2049-2054, 2006.
- [48] K. Yamanaka, S. Nishino, K. Naoe, and M. Imai, "Preparation of highly uniform Pickering emulsions by mercaptocarboxylated gold nanoparticles," *Colloids and Surfaces A: Physicochemical and Engineering Aspects*, vol. 436, pp. 18-25, 2013.
- [49] K. Larson-Smith and D. C. Pozzo, "Pickering Emulsions Stabilized by Nanoparticle Surfactants," *Langmuir*, vol. 28, pp. 11725-11732, 2012/08/14 2012.
- [50] J. Tian, J. Jin, F. Zheng, and H. Zhao, "Self-Assembly of Gold Nanoparticles and Polystyrene: A Highly Versatile Approach to the Preparation of Colloidal Particles with Polystyrene Cores and Gold Nanoparticle Coronae," *Langmuir*, vol. 26, pp. 8762-8768, 2010/06/01 2010.
- [51] V. Kozlovskaya, E. Kharlampieva, S. Chang, R. Muhlbauer, and V. V. Tsukruk, "pH-Responsive Layered Hydrogel Microcapsules as Gold Nanoreactors," *Chemistry of Materials*, vol. 21, pp. 2158-2167, 2009/05/26 2009.

- [52] B. G. De Geest, A. G. Skirtach, T. R. De Beer, G. B. Sukhorukov, L. Bracke, W. R. Baeyens, *et al.*, "Stimuli-Responsive Multilayered Hybrid Nanoparticle/Polyelectrolyte Capsules," *Macromolecular rapid communications*, vol. 28, pp. 88-95, 2007.
- [53] A. A. Antipov, G. B. Sukhorukov, Y. A. Fedutik, J. Hartmann, M. Giersig, and H. Möhwald, "Fabrication of a novel type of metallized colloids and hollow capsules," *Langmuir*, vol. 18, pp. 6687-6693, 2002.
- [54] D. Liu, X. Jiang, and J. Yin, "One-Step Interfacial Thiol–Ene Photopolymerization for Metal Nanoparticle-Decorated Microcapsules (MNP@MCs)," *Langmuir*, vol. 30, pp. 7213-7220, 2014/06/24 2014.
- [55] O. J. Cayre and S. Biggs, "Hollow microspheres with binary porous membranes from solid-stabilised emulsion templates," *Journal of Materials Chemistry*, vol. 19, pp. 2724-2728, 2009.
- [56] G. O. Mallory and J. B. Hajdu, *Electroless plating: fundamentals and applications*: William Andrew, 1990.
- [57] J. R. Ross, *Heterogeneous catalysis: fundamentals and applications*: Elsevier, 2011.
- [58] P. W. Atkins and J. A. Beran, *General chemistry*: Scientific american books, 1992.
- [59] L. A. Porter, H. C. Choi, A. E. Ribbe, and J. M. Buriak, "Controlled Electroless Deposition of Noble Metal Nanoparticle Films on Germanium Surfaces," *Nano Letters*, vol. 2, pp. 1067-1071, 2002/10/01 2002.
- [60] F. Li, F. Li, J. Song, J. Song, D. Han, and L. Niu, "Green synthesis of highly stable platinum nanoparticles stabilized by amino-terminated ionic liquid and its electrocatalysts for dioxygen reduction and methanol oxidation," *Electrochemistry Communications*, vol. 11, pp. 351-354, 2009.
- [61] Y. Mei, Y. Lu, F. Polzer, M. Ballauff, and M. Drechsler, "Catalytic Activity of Palladium Nanoparticles Encapsulated in Spherical Polyelectrolyte Brushes and Core–Shell Microgels," *Chemistry of Materials*, vol. 19, pp. 1062-1069, 2007/03/01 2007.
- [62] M. Sanlés-Sobrido, M. Pérez-Lorenzo, B. Rodríguez-González, V. Salgueiriño, and M. A. Correa-Duarte, "Highly Active Nanoreactors: Nanomaterial Encapsulation Based on Confined Catalysis," *Angewandte Chemie International Edition*, vol. 51, pp. 3877-3882, 2012.
- [63] C. Deraedt, L. Salmon, S. Gatard, R. Ciganda, R. Hernandez, J. Ruiz, *et al.*, "Sodium borohydride stabilizes very active gold nanoparticle catalysts," *Chemical Communications*, vol. 50, pp. 14194-14196, 2014.
- [64] S. Horiuchi and Y. Nakao, "Platinum colloid catalyzed etchingless gold electroless plating with strong adhesion to polymers," *Surface and Coatings Technology*, vol. 204, pp. 3811-3817, 2010.
- [65] K.-J. Lin, H.-M. Wu, Y.-H. Yu, C.-Y. Ho, M.-H. Wei, F.-H. Lu, *et al.*, "Preparation of PMMA-Ni core-shell composite particles by electroless plating on polyelectrolyte-modified PMMA beads," *Applied Surface Science*, vol. 282, pp. 741-745, Oct 1 2013.
- [66] B. Karagoz, O. Sirkecioglu, and N. Bicak, "Surface rejuvenation for multilayer metal deposition on polymer microspheres via self-seeded electroless plating," *Applied Surface Science*, vol. 285, pp. 395-402, 2013.
- [67] B. C. Kim, J. H. Park, and S. J. Lee, "Preparation of Composite Particles via Electroless Nickel Plating on Polystyrene Microspheres and Effect of Plating Conditions," *Polymer-Korea*, vol. 34, pp. 25-31, Jan 2010.
- [68] N. Bicak, S. Sungur, N. Tan, F. Bensebaa, and Y. Deslandes, "Metalization of polymer beads via polymer-supported hydrazines as reducing agents," *Journal of Polymer Science Part a: Polymer Chemistry*, vol. 40, pp. 748-754, Mar 15 2002.
- [69] J.-H. Lee, J. S. Oh, P. C. Lee, D. O. Kim, Y. Lee, and J.-D. Nam, "Fabrication of nickel/gold multilayered shells on polystyrene bead cores by sequential electroless deposition processes," *Journal of Electronic Materials*, vol. 37, pp. 1648-1652, Oct 2008.

- [70] K.-J. Lin, H.-M. Wu, Y.-H. Yu, C.-Y. Ho, M.-H. Wei, F.-H. Lu, *et al.*, "Preparation of PMMA-Ni core-shell composite particles by electroless plating on polyelectrolyte-modified PMMA beads," *Applied Surface Science*, vol. 282, pp. 741-745, 10/1/ 2013.
- [71] Z. Wang, M. Chen, and L. Wu, "Synthesis of Monodisperse Hollow Silver Spheres Using Phase-Transformable Emulsions as Templates," *Chemistry of Materials*, vol. 20, pp. 3251-3253, 2008/05/01 2008.
- [72] M. W. Patchan, L. M. Baird, Y.-R. Rhim, E. D. LaBarre, A. J. Maisano, R. M. Deacon, *et al.*, "Liquid-Filled Metal Microcapsules," *ACS Applied Materials & Interfaces*, vol. 4, pp. 2406-2412, 2012/05/23 2012.
- [73] G. M. Nocera, K. Ben M'Barek, D. G. Bazzoli, G. Fraux, M. Bontems-Van Heijenoort, J. Chokki, *et al.*, "Fluorescent microparticles fabricated through chemical coating of O/W emulsion droplets with a thin metallic film," *Rsc Advances*, vol. 4, pp. 11564-11568, 2014 2014.
- [74] G. M. Nocera, K. B. M'Barek, D. G. Bazzoli, G. Fraux, M. Bontems-Van Heijenoort, J. Chokki, *et al.*, "Fluorescent microparticles fabricated through chemical coating of O/W emulsion droplets with a thin metallic film," *RSC Advances*, vol. 4, pp. 11564-11568, 2014.
- [75] F. Haaf, A. Sanner, and F. Straub, "Polymers of N-vinylpyrrolidone: synthesis, characterization and uses," *Polymer Journal*, vol. 17, pp. 143-152, 1985.
- [76] M. Oćwieja, M. Morga, and Z. Adamczyk, "Self-assembled silver nanoparticles monolayers on mica-AFM, SEM, and electrokinetic characteristics," *Journal of Nanoparticle Research*, vol. 15, pp. 1-14, 2013/02/09 2013.
- [77] I. Pastoriza-Santos and L. M. Liz-Marzán, "Formation of PVP-Protected Metal Nanoparticles in DMF," *Langmuir*, vol. 18, pp. 2888-2894, 2002/04/01 2002.
- [78] S. P. Jiang, L. Li, Z. Liu, M. Pan, and H. L. Tang, "Self-Assembly of PDPA-Pt Nanoparticle/Nafion Membranes for Direct Methanol Fuel Cells," *Electrochemical and Solid-State Letters*, vol. 8, pp. A574-A576, 2005.
- [79] S. P. Jiang, L. Li, Z. Liu, M. Pan, and H. L. Tang, "Self-Assembly of PDPA-Pt Nanoparticle/Nafion Membranes for Direct Methanol Fuel Cells," *Electrochemical and Solid-State Letters*, vol. 8, pp. A574-A576, 2005.
- [80] A. Leeson, "Polymer adsorption on 2D interfaces using QCM - As yet unpublished data," As yet unpublished data, Leeds University IPSE 2015.
- [81] G. Seisenberger, M. U. Ried, T. Endress, H. Büning, M. Hallek, and C. Bräuchle, "Real-time single-molecule imaging of the infection pathway of an adeno-associated virus," *Science*, vol. 294, pp. 1929-1932, 2001.
- [82] J. Georges, "Investigation of the diffusion coefficient of polymers and micelles in aqueous solutions using the Soret effect in cw-laser thermal lens spectrometry," *Spectrochimica Acta Part A: Molecular and Biomolecular Spectroscopy*, vol. 59, pp. 519-524, 2003.
- [83] P. J. Flory and M. Volkenstein, "Statistical mechanics of chain molecules," *Biopolymers*, vol. 8, pp. 699-700, 1969.
- [84] A. D. Law, D. M. A. Buzza, and T. S. Horozov, "Two-Dimensional Colloidal Alloys," *Physical Review Letters*, vol. 106, p. 128302, 03/24/ 2011.
- [85] B. H. Kim and J. W. Kwon, "Metal Catalyst for Low-Temperature Growth of Controlled Zinc Oxide Nanowires on Arbitrary Substrates," *Sci. Rep.*, vol. 4, 03/14/online 2014.
- [86] S.-f. Liu, J.-R. Li, and L. Jiang, "Surface modification of platinum quartz crystal microbalance by controlled electroless deposition of gold nanoparticles and its enhancing effect on the HS-DNA immobilization," *Colloids and Surfaces A: Physicochemical and Engineering Aspects*, vol. 257-258, pp. 57-62, 5/5/ 2005.
- [87] J. P. Hitchcock, A. L. Tasker, E. A. Baxter, S. Biggs, and O. J. Cayre, "Long-Term Retention of Small, Volatile Molecular Species within Metallic Microcapsules," *ACS Applied Materials & Interfaces*, vol. 7, pp. 14808-14815, 2015/07/15 2015.

- [88] C. D. Iacovangelo, "Autocatalytic electroless gold deposition using hydrazine and dimethylamine borane as reducing agents," *Journal of the Electrochemical Society*, vol. 138, pp. 976-982, Apr 1991.
- [89] S. Arditty, C. P. Whitby, B. P. Binks, V. Schmitt, and F. Leal-Calderon, "Some general features of limited coalescence in solid-stabilized emulsions," *The European Physical Journal E*, vol. 12, pp. 355-355, 2003/10/01 2003.
- [90] U. K. Parida and P. Nayak, "Biomedical Applications of Gold Nanoparticles: Opportunity and Challenges," *World Journal of Nano Science and Technology*, vol. 1, pp. 10-25, 2012.
- [91] N. T. Thanh and L. A. Green, "Functionalisation of nanoparticles for biomedical applications," *Nano Today*, vol. 5, pp. 213-230, 2010.
- [92] A. Tzur-Balter, Z. Shatsberg, M. Beckerman, E. Segal, and N. Artzi, "Mechanism of erosion of nanostructured porous silicon drug carriers in neoplastic tissues," *Nat Commun*, vol. 6, 02/11/online 2015.
- [93] B. G. De Geest, A. G. Skirtach, A. A. Mamedov, A. A. Antipov, N. A. Kotov, S. C. De Smedt, *et al.*, "Ultrasound-Triggered Release from Multilayered Capsules," *Small*, vol. 3, pp. 804-808, 2007.
- [94] F. Wang, Y. Shen, W. Zhang, M. Li, Y. Wang, D. Zhou, *et al.*, "Efficient, dual-stimuli responsive cytosolic gene delivery using a RGD modified disulfide-linked polyethylenimine functionalized gold nanorod," *Journal of Controlled Release*, vol. 196, pp. 37-51, 2014.
- [95] A. D. Law, M. Auriol, D. Smith, T. S. Horozov, and D. M. A. Buzza, "Self-assembly of two-dimensional colloidal clusters by tuning the hydrophobicity, composition, and packing geometry," *Physical review letters*, vol. 110, p. 138301, 2013.
- [96] B. P. Binks, J. A. Rodrigues, and W. J. Frith, "Synergistic Interaction in Emulsions Stabilized by a Mixture of Silica Nanoparticles and Cationic Surfactant," *Langmuir*, vol. 23, pp. 3626-3636, 2007/03/01 2007.
- [97] Y. Jiang, C. Whitehouse, J. Li, W. Y. Tam, C. T. Chan, and P. Sheng, "Optical properties of metallo-dielectric microspheres in opal structures," *Journal of Physics: Condensed Matter*, vol. 15, p. 5871, 2003.
- [98] P. Jiang, J. Bertone, K. Hwang, and V. Colvin, "Single-crystal colloidal multilayers of controlled thickness," *Chemistry of Materials*, vol. 11, pp. 2132-2140, 1999.
- [99] J. He, Y. Wang, Y. Feng, X. Qi, Z. Zeng, Q. Liu, *et al.*, "Forest of Gold Nanowires: A New Type of Nanocrystal Growth," *ACS Nano*, vol. 7, pp. 2733-2740, 2013/03/26 2013.
- [100] W. S. Sanders and L. J. Gibson, "Mechanics of hollow sphere foams," *Materials Science and Engineering: A*, vol. 347, pp. 70-85, 4/25/ 2003.
- [101] J. Banhart, "Manufacture, characterisation and application of cellular metals and metal foams," *Progress in Materials Science*, vol. 46, pp. 559-632, // 2001.
- [102] S. M. George, "Atomic layer deposition: an overview," *Chemical reviews*, vol. 110, pp. 111-131, 2009.
- [103] S. Fujii, S. Matsuzawa, Y. Nakamura, A. Ohtaka, T. Teratani, K. Akamatsu, *et al.*, "Synthesis and Characterization of Polypyrrole-Palladium Nanocomposite-Coated Latex Particles and Their Use as a Catalyst for Suzuki Coupling Reaction in Aqueous Media," *Langmuir*, vol. 26, pp. 6230-6239, 2010/05/04 2010.
- [104] K. Kondo, F. Ishikawa, N. Ishida, and M. Irie, "Photochemical Deposition of Pd (0) from Adsorbed Pd (II)-Complex Ions," *Journal of The Electrochemical Society*, vol. 139, pp. 2815-2817, 1992.
- [105] Y. Fujiwara, "Adsorption Promotion of Ag Nanoparticle Using Cationic Surfactants and Polyelectrolytes for Electroless Cu Plating Catalysts," *Electrochemical Society*, 2010.
- [106] Y. Kobayashi, V. Salgueiriño-Maceira, and L. M. Liz-Marzán, "Deposition of Silver Nanoparticles on Silica Spheres by Pretreatment Steps in Electroless Plating," *Chemistry of Materials*, vol. 13, pp. 1630-1633, 2001/05/01 2001.

- [107] H. Wang, Y. Song, Z. Wang, C. J. Medforth, J. E. Miller, L. Evans, *et al.*, "Silica–Metal Core–Shells and Metal Shells Synthesized by Porphyrin-Assisted Photocatalysis," *Chemistry of Materials*, vol. 20, pp. 7434-7439, 2008/12/23 2008.
- [108] Y. Riddle and T. Bailerare, "Friction and wear reduction via an Ni-B electroless bath coating for metal alloys," *JOM*, vol. 57, pp. 40-45, 2005.
- [109] V. Vitry, A. Sens, A.-F. Kanta, and F. Delaunois, "Experimental study on the formation and growth of electroless nickel–boron coatings from borohydride-reduced bath on mild steel," *Applied Surface Science*, vol. 263, pp. 640-647, 12/15/ 2012.
- [110] K. Krishnaveni, T. S. Narayanan, and S. Seshadri, "Electroless Ni–B coatings: preparation and evaluation of hardness and wear resistance," *Surface and Coatings Technology*, vol. 190, pp. 115-121, 2005.
- [111] K. Krishnaveni, T. S. Narayanan, and S. Seshadri, "Corrosion resistance of electrodeposited Ni–B and Ni–B–Si 3 N 4 composite coatings," *Journal of Alloys and Compounds*, vol. 480, pp. 765-770, 2009.
- [112] T. S. Coope, U. F. J. Mayer, D. F. Wass, R. S. Trask, and I. P. Bond, "Self-Healing of an Epoxy Resin Using Scandium(III) Triflate as a Catalytic Curing Agent," *Advanced Functional Materials*, vol. 21, pp. 4624-4631, 2011.